Maneuver Detection and Reconstruction in Data Sparse Systems with an Optimal Control Based Estimator

by

Daniel P. Lubey

B.S., The Pennsylvania State University, 2011

M.S., University of Colorado, 2013

A thesis submitted to the
Faculty of the Graduate School of the
University of Colorado in partial fulfillment
of the requirements for the degree of
Doctor of Philosophy
Department of Aerospace Engineering Sciences
2015

This thesis entitled:
Maneuver Detection and Reconstruction in Data Sparse Systems with an Optimal Control Based Estimator
written by Daniel P. Lubey
has been approved for the Department of Aerospace Engineering Sciences

Daniel J. Scheeres

Prof. George Born

Prof. John Hauser

Prof. Jeffrey Parker

Date ____________

The final copy of this thesis has been examined by the signatories, and we find that both the content and the form meet acceptable presentation standards of scholarly work in the above mentioned discipline.

Lubey, Daniel P. (Ph.D., Aerospace Engineering Sciences)

Maneuver Detection and Reconstruction in Data Sparse Systems with an Optimal Control Based Estimator

Thesis directed by Prof. Daniel J. Scheeres

The Big Sky Theory once posited that the volume of Earth's orbital environment is so large that the chance of a collision ever occurring is effectively negligible. However, since 1996 six accidental collisions have been recorded in orbit, contributing thousands of trackable debris objects to this environment and possibly hundreds of thousands to millions more that are too small to track with current assets. Much of this debris persists to today. Access to this environment has become critical in our society, thus we need methods to ensure safe and continued access to it. Part of ensuring this is obtaining better information on its dynamics and its population. This research focuses on developing an automated approach to detecting and understanding the presence of mismodeled dynamics for orbital applications in order to provide more information on the objects in Earth orbit. We develop an algorithm called the Adaptive Optimal Control Based Estimator, which automatically tracks a target given observations, detects the presence of dynamic uncertainty, and reconstructs that mismodeling as an optimal control policy. These control policies may then be used to better understand the source of the mismodeling. Outside of a specific astrodynamics application, this algorithm attempts to fulfill a specific hole in the existing literature: automated, real-time estimation in dynamically mismodeled systems with data sparse and non-cooperative observation sets while obtaining information about the mismodeling. The development of this algorithm is shown, and several astrodynamics-based simulations demonstrate its ability to automatically detect and reconstruct dynamic mismodeling while maintaining tracking of the target.

Dedication

To the great teachers I have had throughout my life that have helped me become who I am today. Most notably, my parents, who have taught me since birth; Barbra Abell, who showed me what I could accomplish if I dedicated myself; and Robert Melton, who showed me the great effect an educator can have.

Acknowledgements

First, I would like to thank my advisor, Dr. Daniel Scheeres, for his guidance throughout my time at CU. I would also like to thank the other member of my dissertation committee: Dr. George Born, Dr. John Hauser, Dr. Jeffrey parker, Dr. Jay McMahon, and Dr. Marcus Holzinger. Their insightful feedback on this research really helped strengthen it into its final version. I would also like to thank Dr. Hanspeter Schaub, Dr. Alireza Doostan, and Dr. Brandon Jones for their collaboration on additional projects.

I would like to thank AFOSR and the NASA Space Technology Research Fellowship for providing for their support of this work. As an NSTRF fellow I had the privilege to conduct onsite research experiences in addition to my primary research. I would like to thank my mentors from each of my three experiences: Dr. John Ruppert, Dr. Richard Erwin, and Dr. Rob Haw (and the entire SMAP navigation team).

One of the best parts of graduate school is sharing that time with your peers. I would like to than the other members of CSML for enriching my experiences at CU. I would also like to thank the students, faculty, and staff in CCAR. I'd specifically like to mention Sarah Melssen and Steve Hart, who on more than one occasion saved all of my work from permanent deletion.

Finally, I would like thank my friends and family. Most importantly, I want thank my wife Antonella Albuja. Having her to go through graduate school with has been greatest support I could imagine. The fact that she was so supportive while were both so stressed makes that even more meaningful.

Contents

Chapter

1 Introduction 1

1.1 History and Development of Space Situational Awareness 1

1.2 Overview of Research 4

1.3 Previous Work 6

1.3.1 Estimation Theory and Orbit Determination 6

1.3.2 Maneuver Detection and Reconstruction 9

1.3.3 Control Distance Metrics 13

1.4 Contributions 14

1.5 Publications 16

1.5.1 Journal Publications 16

1.5.2 Conference Papers and Presentations 16

1.5.3 Abstracts, Posters, and Presentations 18

1.6 Thesis Organization 18

2 Background Material 21

2.1 Optimization of Bolza-Type Cost Function 21

2.2 Control Distance Metrics 25

2.3 Dynamical Models for Space Situational Awareness 27

2.3.1 State dynamics 28

2.3.2 Adjoint Dynamics 31

2.4 Measurement Models for Space Situational Awareness 32

2.4.1 Range and Range-Rate Measurements 33

2.4.2 Optical Measurements 33

3 The Optimal Control Based Estimator 35

3.1 Cost Function of the OCBE 36

3.2 The Nonlinear OCBE 39

3.2.1 Equations of the Nonlinear OCBE 40

3.2.2 Existence of a Solution 42

3.3 The Generalized Linear OCBE 46

3.3.1 Equations of the GL-OCBE 46

3.3.2 Analysis of GL-OCBE 48

3.4 The Ballistic Linear OCBE 52

3.4.1 Ballistic Properties 52

3.4.2 Equations of the BL-OCBE 54

3.4.3 Special Properties of the BL-OCBE 56

3.5 The OCBE Smoother 61

3.5.1 Nonlinear OCBE Full Smoother 62

3.5.2 GL-OCBE Full Smoother 63

3.5.3 BL-OCBE Smoother 64

3.6 Conclusions 66

4 Applications of the Optimal Control Based Estimator 68

4.1 Mass-Spring-Damper System with Dynamical Mismodeling 68

4.1.1 Example I: Mass-Spring-Damper with Unmodeled Perturbation 69

4.1.2 Example II: Spring-Mass-Damper with Mismodeled Natural Dynamics 72

4.2 Tracking a Spacecraft in LEO with Mismodeled Drag and an Unknown Maneuver . . 75

4.2.1 Tracking with the BL-OCBE 76
4.2.2 Tracking with the Nonlinear OCBE 81
4.3 Tracking a Spacecraft in GEO with Unknown Stationkeeping Maneuvers 85
4.3.1 Tracking with the BL-OCBE 85
4.3.2 Tracking with the Nonlinear OCBE 90
4.4 Conclusions 93

5 Maneuver Detection and Reconstruction with the OCBE 95
5.1 Nonlinear OCBE Distance Metrics 95
5.2 Maneuver Detection with OCBE Distance Metrics 98
5.3 GL-OCBE Distance Metrics 100
5.4 BL-OCBE Distance Metrics 104
5.5 Natural Dynamics Estimation with Optimal Control Policies 108
5.5.1 Comparison of Optimal and Natural Dynamics 108
5.5.2 Estimating Natural Dynamics Using OCPs 110
5.6 Sample Natural Dynamics Estimation Applications 115
5.6.1 Simulation I: Biased Dynamics 116
5.6.2 Simulation II: Biased Dynamics and Unmodeled Maneuver 121
5.7 Sample Maneuver Detection and Reconstruction with the OCBE 124
5.7.1 Tracking a Spacecraft in LEO with Mismodeled Drag and an Unknown Maneuver 124
5.7.2 Tracking a Spacecraft in GEO with Unknown Stationkeeping Maneuvers . . . 128
5.8 Conclusions 132

6 Adaptive Optimal Control Based Estimator 134
6.1 OCBE Automation Algorithm 135
6.1.1 Automation Criterion 135
6.1.2 Existence of a Solution 137

6.1.3 Solution Method . . . 140
6.1.4 When Automation Should be Employed . . . 142
6.1.5 Adaptive OCBE Algorithm Summary . . . 143
6.2 Sample Applications of the Adaptive OCBE . . . 146
6.2.1 Tracking a target in LEO with Mismodeled Drag and an Unknown Maneuver 146
6.2.2 Tracking a target in GEO with Unknown Stationkeeping Maneuvers . . . 149
6.3 Conclusions . . . 153

7 Conclusions and Future Work 154
7.1 Conclusions . . . 154
7.2 Future Work . . . 158

Bibliography 161

Appendix

A Derivation of the GL-OCBE State, Adjoint and Control Estimates 167
A.1 State Estimate at the Measurement Epoch . . . 167
A.2 State Estimate at the a priori Epoch . . . 170
A.3 Adjoint and Optimal Control Estimates . . . 171

B Uncertainty Properties of the GL-OCBE 173
B.1 Uncertainty of the Propagated a priori State . . . 173
B.2 Propagated a priori State Quasi-Covariance . . . 176
B.3 Uncertainty of the State Estimate at the a priori Epoch . . . 177
B.4 Uncertainty of the State Estimate at the Measurement Epoch . . . 180
B.5 Uncertainty of the Control Estimate . . . 181
B.6 Numerical Implementation of Process Noise Terms . . . 184

Tables

Table

2.1 Gravitational Dynamics Parameters 29
2.2 Atmospheric Drag Dynamics Parameters 29
2.3 Solar Radiation Pressure Constant Dynamics Parameters 30
2.4 Third Body Gravitational Dynamics Parameters 31

4.1 True System Parameters and Initial Conditions for Mass-Spring-Damper Simulation 69
4.2 True System Parameters and Initial Conditions for LEO Simulation 76
4.3 LEO Tracking RMS Values with the BL-OCBE 80
4.4 LEO Tracking RMS Values with the Nonlinear OCBE 84
4.5 LEO Tracking squared weighted RMS values with the BL-OCBE and the Nonlinear OCBE 84
4.6 GEO Tracking RMS Values with the BL-OCBE 89
4.7 GEO Tracking RMS Values with the Nonlinear OCBE 92
4.8 GEO Tracking squared weighted RMS values with the BL-OCBE and the Nonlinear OCBE 93

5.1 True Object Parameters for LEO and GEO Simulations 116
5.2 Initial Keplerian orbital elements for LEO and GEO cases in Simulation I 116
5.3 Timing and Impulse Values for Test Case IV 122

Figures

Figure

4.1 Smoothed state tracking results (deviations relative to truth) with varied assumed dynamic uncertainty (σ_Q). 70

4.2 Smoothed uncertainty in state estimates with varied assumed dynamic uncertainty (σ_Q). 71

4.3 Smoothed control estimates against true input acceleration with varied assumed dynamic uncertainty (σ_Q). 71

4.4 (Top) Control Estimate using correct dynamic uncertainty and the true mismodeling. (Bottom) Deviation between these control estimates and the true mismodeling with a 1-σ envelope. 72

4.5 Smoothed state tracking results (deviations relative to truth) with varied assumed dynamic uncertainty (σ_Q). 73

4.6 Smoothed uncertainty in state estimates with varied assumed dynamic uncertainty (σ_Q). 74

4.7 Smoothed control estimates against true natural mismodeling with varied assumed dynamic uncertainty (σ_Q). 75

4.8 (Top) Control Estimate with correct dynamic uncertainty and the true mismodeling. (Bottom) Deviation between these control estimates and the true mismodeling with a 1-σ envelope. 75

4.9 Postfit measurement residuals with 3-σ bounds after running BL-OCBE ($\sigma_Q = 10^{-12}$ m/s^2). 77

4.10 Zoomed-in postfit measurement residuals after accounting for drag mismodeling ($\sigma_Q = 2 \times 10^{-8}$ m/s^2) 77

4.11 Postfit measurement residuals after accounting for drag mismodeling and maneuver . 78

4.12 ECI state estimate deviations relative to truth with a 3-σ envelope after accounting for drag mismodeling and maneuver 78

4.13 Hill frame control estimate magnitudes after accounting for drag mismodeling and maneuver 79

4.14 ECI smoothed state estimate deviations relative to truth with a 3-σ envelope after accounting for drag mismodeling and maneuver 80

4.15 Hill frame smoothed control estimate magnitudes after accounting for drag mismodeling and maneuver 80

4.16 Nonlinear OCBE postfit measurement residuals after accounting for drag mismodeling and the cross-track maneuver 81

4.17 Nonlinear OCBE ECI state estimate deviations relative to truth with a 3-σ envelope after accounting for drag mismodeling and the cross-track maneuver 82

4.18 Nonlinear OCBE Hill frame control estimate magnitudes after accounting for drag mismodeling and the cross-track maneuver 82

4.19 Nonlinear OCBE ECI state estimate deviations relative to truth with a 3-σ envelope after accounting for drag mismodeling and the cross-track maneuver 83

4.20 Nonlinear OCBE Hill frame control estimate magnitudes after accounting for drag mismodeling and the cross-track maneuver 83

4.21 BL-OCBE postfit measurement residuals with a 3-σ envelope when processing GEO observations with $\sigma_{Q,NF} = 10^{-10}$ m/s^2. 86

4.22 BL-OCBE postfit measurement residuals with a 3-σ envelope after accounting for first observed maneuver. 86

4.23 BL-OCBE postfit measurement residuals with a 3-σ envelope after accounting for both observed maneuvers. 87

4.24 BL-OCBE state estimate deviations relative to truth with a 3-σ envelope after accounting for both observed maneuvers. 88

4.25 BL-OCBE control estimates magnitude in a Hill frame after accounting for both observed maneuvers. 88

4.26 BL-OCBE smoothed state estimate deviations relative to truth with a 3-σ envelope after accounting for both observed maneuvers. 89

4.27 BL-OCBE smoothed control estimates magnitude in a Hill frame after accounting for both observed maneuvers. 89

4.28 Nonlinear OCBE postfit measurement residuals with a 3-σ envelope after accounting for both observed maneuvers. 90

4.29 Nonlinear OCBE state estimate deviations relative to truth with a 3-σ envelope after accounting for both observed maneuvers. 91

4.30 Nonlinear OCBE control estimates magnitude in a Hill frame after accounting for both observed maneuvers. 91

4.31 Nonlinear OCBE smoothed state estimate deviations relative to truth with a 3-σ envelope after accounting for both observed maneuvers. 92

4.32 Nonlinear OCBE smoothed control estimates magnitude in a Hill frame after accounting for both observed maneuvers. 92

5.1 Optimal control policy with mismodeled atmospheric drag and SRP for true boundary states. (Top) Missing dynamics and OCP magnitudes. (Bottom) Alignment of OCP with missing dynamics 109

5.2 Optimal control policy with mismodeled atmospheric drag and SRP for dispersed boundary states. (Top) Missing dynamics and OCP magnitudes (Middle) Alignment of OCP with missing dynamics. (Bottom) Magnitude of differenced OCP and missing natural dynamic accelerations. 110

5.3 Nonlinear dispersed boundary state analysis with comparison to analytical covariance envelopes (1-3 σ). 113

5.4 Long and short arc Drag and SRP parameter estimates from each pair of observation epochs for a tracked LEO object with mismodeled drag and SRP perturbations. The true parameters, initial modeled values, and batch estimates are indicated. 118

5.5 Percent error in the drag parameter estimate over time for LEO simulation. Blue represents the error of the actual estimates in these simulations and black represents the 3-σ envelope associated with these estimates. Long and short arcs are represented by solid and dashed lines, respectively. 119

5.6 SRP parameter estimate histogram for GEO Simulation with long (top) and short (bottom) arcs. The true parameters, initial modeled values, and batch estimates are indicated. 120

5.7 Percent error in the drag parameter estimate over time for GEO simulation. Blue represents the error of the actual estimates in these simulations and black represents the 3-σ envelope associated with these estimates. Long and short arcs are represented by solid and dashed lines, respectively. 121

5.8 Drag and SRP parameter estimates for each pair of observation epochs for a tracked LEO object with mismodeled Drag and SRP perturbations and an unmodeled impulsive maneuver. True parameters, initial modeled values, and the batch estimate are indicated. 122

5.9 Control distance metrics between each measurement epoch for LEO simulation with unmodeled maneuver. Metrics from before estimation are provided (top) as well as from after parameter estimation (bottom). 123

5.10 Distance metric to metric threshold ratio when running the BL-OCBE with $\sigma_Q = 10^{-12}$ m/s^2. 125

5.11 Distance metric to metric threshold ratio when running the BL-OCBE with $\sigma_Q = 2 \times 10^{-8}$ m/s^2. 125

5.12 Distance metric-to-threshold ratio when running the BL-OCBE after accounting for the drag mismodeling and the remaining maneuver 126

5.13 Distance metric-to-threshold when running the BL-OCBE after accounting for the drag mismodeling and the remaining maneuver. All ratios are taken with respect to an assumed dynamic uncertainty of $\sigma_Q = 2 \times 10^{-8}$ m/s^2 126

5.14 Distance metric-to-threshold ratio when running the Nonlinear OCBE after accounting for the drag mismodeling and the remaining maneuver. 127

5.15 Distance metric-to-threshold when running the Nonlinear OCBE after accounting for the drag mismodeling and the remaining maneuver. All ratios are taken with respect to an assumed dynamic uncertainty of $\sigma_Q = 2 \times 10^{-8}$ m/s^2 128

5.16 Distance metric to metric threshold ratio when running the BL-OCBE with $\sigma_Q = 10^{-10}$ m/s^2. 129

5.17 Distance metric to metric threshold ratio when running the BL-OCBE after accounting for the first maneuver. 129

5.18 Distance metric-to-threshold ratio when running the BL-OCBE after accounting for the drag mismodeling and the remaining maneuver 130

5.19 Distance metric-to-threshold when running the BL-OCBE after accounting for the drag mismodeling and the remaining maneuver. All ratios are taken with respect to an assumed dynamic uncertainty of $\sigma_Q = 10^{-10}$ m/s^2 130

5.20 Distance metric-to-threshold ratio when running the Nonlinear OCBE after accounting for the drag mismodeling and the remaining maneuver. 131

5.21 Distance metric-to-threshold when running the Nonlinear OCBE after accounting for the drag mismodeling and the remaining maneuver. All ratios are taken with respect to an assumed dynamic uncertainty of $\sigma_Q = 10^{-10}$ m/s^2. 131

6.1 OCBE control distance metric, mean, and ratios as function of the assumed dynamic uncertainty for a case where the adaptive solution exists. 137

6.2 OCBE control distance metric, mean, and threshold as functions of the assumed dynamic uncertainty for a case where the adaptive solution does not exist. 138

6.3 BL-OCBE distance metric, mean, and threshold as a function of the assumed dynamic uncertainty for a case where the adaptive solution exists. 139

6.4 BL-OCBE distance metric, mean, and threshold ratios as functions of the assumed dynamic uncertainty for a case where the adaptive solution does not exist. 139

6.5 Flowchart illustrating how the Adaptive OCBE operates. 144

6.6 Flowchart illustrating how the Assumed Dynamic Uncertainty is automatically calculated in the Adaptive OCBE. 145

6.7 Distance metric-to-metric threshold ratio relative to dynamic noise floor when applying the Adaptive OCBE. 147

6.8 Distance metric to metric threshold ratio relative the adaptive assumed dynamic uncertainty when applying the Adaptive OCBE. 147

6.9 Magnitude of estimated controls in Hill frame when applying the Adaptive OCBE. . 148

6.10 Cartesian state estimate deviations from truth against measurement index with a 3-σ envelope (red) when applying the Adaptive OCBE. 148

6.11 Distance metric-to-metric threshold ratio relative to dynamic noise floor when applying the Adaptive OCBE. 150

6.12 Distance metric to metric threshold ratio relative the adaptive assumed dynamic uncertainty when applying the Adaptive OCBE. 150

6.13 Magnitude of estimated controls in Hill frame when applying the Adaptive OCBE. . 151

6.14 Cartesian state estimate deviations from truth against measurement index with a 3-σ envelope (red) when applying the Adaptive OCBE. 152
6.15 Distance metric-to-metric threshold ratio relative to the dynamic noise floor when applying the Adaptive OCBE with angles-only observation. 152

Chapter 1

Introduction

In this chapter we introduce the central topic of this research - the Optimal Control Based Estimator (OCBE). The estimator incorporates an optimal control criterion into an estimator, such that it reconstructs mismodeled dynamics as an optimal control policy. These estimated control policies may be analyzed to determine the presence of dynamic mismodeling and characterize the mismodeling. This chapter focuses on setting up the context for the OCBE by illuminating the motivation behind this research, discussing what hole it fills within the existing literature, and outlining how this thesis will present this research. We start with an overview of Space Situational Awareness (SSA), which informs the discussion of the motivation behind this work. Next we define the research problem, and then discuss where that research fits in the existing literature. Finally, we call out the main contributions of this research, define the previous publications associated with this research, and finish with an outline of how the reset of this thesis is organized.

1.1 History and Development of Space Situational Awareness

Before October 4, 1957, Earth's orbital environment was untouched by humans. It was composed of sparse amounts of natural bodies like meteoroids and a lot of empty space. This all changed with the launch of Sputnik-1 by the Soviet Union, which triggered the Cold War space race with the United States. This led to a new era for mankind - The Space Age. 58 years later, we are currently tracking in Earth Orbit 16,925 objects greater than 10 cm in diameter, with upwards of 90% of those objects being pieces of uncontrolled, manmade debris [64]. Though we are currently unable to accurately track objects smaller than this cutoff, we are able to estimate that the debris problem only gets worse with around 500,000 objects between 1 cm and 10 cm in size, and hundreds of millions of other objects below this size cutoff [69]. These objects in orbit are a testament to some of mankind's greatest triumphs as well as our many failures.

Our successes in space have created a society that is dependent on continued access to Earth orbit, but the failures that led to debris accumulation are threatening this access for manned and robotic missions alike. This has not always been the case. In the early years of space race, there were only two nations launching satellites into space: the United States and the Soviet Union. Less than 4 years after the first manmade satellite was put in Earth orbit, the first breakup event occurred - increasing the population of objects in Earth's orbit by over 400%. The United States's Transit 4A R/B spacecraft experienced a propulsion failure, which contributed 296 pieces of trackable debris (of which 176 remain as of 2011) [32, 49]. Many more breakup events would follow - not all of which were accidental.

While propulsion-based breakups are the most common type of breakup, intentional destruction of payloads have created a large portion of the debris population. Between 1964 and 2007, 56 satellites were intentionally destroyed in orbit by three different nations: 51 satellites by Russia / Soviet Union, 4 satellites by the United States, and 1 by China [32]. Not much data is available on the reasons for why all of the Soviet Union's satellites were intentionally destroyed, but the reasons varied from a payload failure to intentional destruction through testing of their Anti-Satellite (ASAT) weapons program [21]. These self destructions were usually initiated at low altitudes, so much of the resulting debris (numbering as much as 248 trackable pieces for a single destruction) quickly reentered the atmosphere - though, those that were initiated at higher altitudes still have remaining pieces of debris in orbit almost forty years later. The United States intentionally destroyed one satellite at a low altitude to test structural loading limits in orbit (AS-203), and the other three were demonstrations of ASAT Weapons - the trackable debris from which persisted until 2002 [21]. The U.S. destroyed an additional satellite via ASAT in 2008 in order to prevent the spread of hydrazine on the ground as the failed satellite began to reenter, but the destruction took place at a low altitude providing only debris with a short lifespan [51]. Though China intentionally destroyed the fewest number of satellites, they have created the biggest problem in terms of debris. Their destruction of the Fengyun 1-C satellite via an ASAT weapon has contributed over 3,312 pieces of debris greater than 10 cm in size (with upwards of 150,000 smaller pieces) to a popular orbital altitude where debris does not quickly reenter the atmosphere [48]. It remains the most orbital debris-creating event in history.

As the debris population in Earth orbit has evolved, so too has our attitude toward it. In the early days of space-faring, the general approach to space debris and payloads in general was the "Big Sky Theory" [68]. This approach (borrowed from the field of aviation), basically surmised that the total volume of the inhabited sky is so large that the probability of any chance collision is essentially negligible. This theory was disproved in 1996 when the French Cerise spacecraft was hit by a piece of space debris [32]. This was just the first in a series of six accidental collisions that have happened to date. The most significant of these events was the collision of Iridium 33 (an active U.S. payload) and Cosmos 2251 (a decommissioned Russian payload) on February 10, 2009. This event led to the creation of 2,201 pieces of debris larger than 10 cm in size with many more pieces that are smaller, the majority of which remain in orbit to date [36]. This event effectively ended any remaining hope in the Big Sky Theory and brought Space Situational Awareness (SSA) to the forefront.

SSA focuses on better understanding Earth's orbital environment and its population with one of its chief aims being the mitigation of the orbital debris problem. Better understanding this environment includes providing higher fidelity and more accurate dynamical models, more robust and precise tracking algorithms, and more reliable and computationally efficient algorithms for trajectory and uncertainty propagation. The algorithms may be combined to better understand the past, present, and future motions of all objects in orbit as well as their coupled motions. In the end, this allows for more accurate prediction of collisions - one of the central goals of SSA.

The success of research in SSA is important to continued access to earth orbit, which is vital to today's society. If the orbital debris problem is left unchecked, then eventually runaway collisions between debris and active payloads could make this vitally important environment too costly for even robotic missions. We have already seen these effects with the destruction of Russia's BLITS satellite through a collision with a piece of debris that is widely believed to have come from the destruction of Fengyun 1-C [37]. By addressing this issue early enough the problem is far more manageable, and it may even be solvable given sufficient time, attention, and resources. Aiding this cause is an upgrade to the United State's sensing abilities through the upcoming S-band Space Fence as well as similar upgrades in Russia and Europe [88]. This new suite of sensors uses shorter wavelengths for observation, which will allow us to track objects below the current 10 cm cutoff. Estimates put the fence's capabilities at tracking 200,000 objects with 1.5 million observations a day [23]. This sudden flood of information will present its own challenges, but by focusing on computationally efficient algorithms the SSA community will be able to more accurately characterize the debris problem and avoid the problems associated with rising population in Earth orbit.

1.2 Overview of Research

The effects of the debris problem in Earth orbit have already been felt through the six incidental collisions that have occurred so far and the countless number of propellant-draining debris avoidance maneuvers that active payloads have had to execute. These events have motivated a stronger interest in SSA as a means to mitigate the problems associated with rising population in Earth orbit so that this invaluable environment (and areas beyond) can remain open to mankind for all generations to come.

SSA is a complex and dense field that no single research project can cover. This research specifically focuses on the tracking problem within SSA - more specifically, estimation in dynamically mismodeled systems. Earth's orbital environment is fraught with sources of dynamical mismodeling due to uncertainties in several different perturbations. These mismodelings can include both natural dynamics and controlled dynamics if observing an active payload. While the dominant gravitational accelerations are well understood object-dependent natural dynamics are often poorly modeled. The most dominant object-dependent perturbations are atmospheric drag and solar radiation pressure. For both, the natural mechanisms are not fully understood due to the complex solar dynamics, and the addition of vehicle mismodeling introduces even more error. SSA surveys are typically non-cooperative meaning the measurements are obtained passively (i.e., without any links with the observed object). This makes object identification difficult at times, which only exacerbates dynamic mismodeling since complicated object-dependent dynamical models are not possible when dealing with an unidentified object. When the object being observed is an active payload the situation is complicated further due to the possibility of active maneuvers being performed. Without having *a priori* knowledge of the vehicle's actuated capabilities the entire maneuver is completely unknown to the observer.

Beyond dynamic mismodeling, estimation in SSA is further complicated by the data sparse nature of the observations. Given the large number of objects in orbit and the limited sensing resources the number of dedicated observations per object is often quite small. Generally several orbital periods can pass with no observation - this can extend to days or weeks. As such, the information content is quite low, thus estimation methods need to be robust to this.

Putting this all together, the larger problem this research seeks to address is estimation in dynamically mismodeled systems with data sparse and non-cooperative observation while obtaining information about any mismodeling. We specifically focus on application to astrodynamics in a SSA context, but the algorithms are written generally to promote application to any type of system. This research goal is formally summed up into the following thesis statement:

> Combining an optimal control criterion with the pieces of information available to a sequential state estimator, an estimation method that is robust to dynamic mismodeling, data sparse information, and non-cooperative observation may be obtained. This method simultaneously outputs state and control estimates such that the state trajectory is continuous across the observation gap while the control estimates provide a representation of the mismodeling in the system. These resulting estimates may be used to reveal the presence of mismodeled dynamics, provide time-series representations of those maneuvers, and estimate underlying mismodeled natural dynamics.

The algorithm developed to address these research goals is called the Optimal Control Based

Estimator (OCBE). It is a state estimator infused with an optimal control process that is meant to replicate the effects of dynamic mismodeling. These control policies may then be analyzed to identify the presence of mismodeling, characterize the mismodeling, and reconstruct the mismodeling. This thesis will focus on developing this algorithm, examining its properties, and demonstrating its utility through application to sample astrodynamics-based tracking simulations. In the next subsection we will focus on what work has been done to address aspects of this research statement as well as address where the OCBE fits in with the larger collection of existing literature.

1.3 Previous Work

In this section, a comprehensive examination of the existing literature related to this research is examined. It starts with an overview of estimation theory as a whole and how that has been specifically applied to orbit determination. Next, there is an overview of existing methods for maneuver detection and reconstruction as applied to astrodynamics as well as other applications. Finally, there is an overview of a specific method called control distance metrics. These form the basis of the Optimal Control Based Estimator, thus we focus on them to provide insight on the foundations of the research discussed in this paper.

1.3.1 Estimation Theory and Orbit Determination

The field of Estimation Theory focuses on how to take measurements of a system that are infused with sensor error, and turn them into optimal parameter and/or state estimates for a given system. Optimal in this sense means the estimate minimizes or maximizes some meaningful objective. The topic is central to both science and engineering since perfect observations are impossible to obtain, and our knowledge of systems is completely based on our ability to observe them. Methods must exploit statistics to obtain results that minimize observation error and other sources of error such that the estimates approach truth with the continual addition of new information.

Optimal estimation is generally seen to have begun with the advent of Least Squares. Least squares is a statistical estimation method that estimates states or system parameters while minimizing the summed squares of the measurement residuals. In the late 18^{th} to early 19^{th} century the method was developed independently by Karl Friedrich Gauss [19] and Adrien-Marie Legendre [44]. There is much debate on who developed the method first. Legendre published it in 1805 while Gauss published in 1809, but Gauss argued he had been using the method since 1795 and discussed it before 1805 with several other astronomers. His claim is further supported by several notations made in earlier work, and his results from a study of the French Meridian Arc problem in 1799 [72]. Additionally, an American named Robert Adrain published the method in 1808 as applied to surveying problems [2], though it is possible it was influenced by Legendre's work [72]. In general, it is believed that Gauss developed the method and provided the most formal statistical presentation of it, but it was Legendre who popularized the method.

The next leap in statistical methods for estimation was the work of Thomas Bayes [8]. Bayes' rule (also called inverse probability) deals with conditional probability saying that the probability of an estimate conditioned on measurements is proportional to the probability of the measurements conditioned on the estimate. Essentially, it is a formal method for how to update belief when incorporating new information. While Bayes's paper was published well before Least Squares (1763 versus 1805), the method was not well known until Laplace popularized it in his own works in 1812 [38, 73]. This method has been adapted into what we call Bayesian estimators, and it is widely applied today [83, 65, 86].

Though Bayesian estimators are widely used, they are not without their critics. Chief among them is Ronald Fisher, who brought about another leap in estimation methods. Fisher argued that Bayesian estimators were arbitrary because when you parametrize the estimate you obtain contrary results [24]. He introduced his own method in 1912 [15], which was unaffected by this parameterization issue. Over the next 10 years he would solidify his theory and formally name it the Maximum Likelihood Estimator (MLE) [16, 5]. This method does not require inverse probability, rather it chooses the estimate that maximizes the likelihood of the obtained measurements. For linear systems where the noises are normally distributed the MLE and Bayesian estimate are identical, since the mode and mean of a Gaussian distribution are identical. Only when the linear and Gaussian assumptions are invalidated do these estimators produce different results.

The next leap in estimation theory came from Rudolf Kalman in 1960, who treated sequential state estimation in dynamical systems [34]. The Kalman Filter operates in linear, discrete, time-invariant systems where measurements are processed as the come in, and they update the state trajectory in a manner that minimizes the variance of the estimate, is unbiased, and may also be shown to be a weighted least squares solution. There is much debate over who deserves credit for this estimator, though. Research has found that Thorvald Thiele first derived an equivalent state estimator in 1880 [39, 40]. His work seems to have gone unnoticed by English-speaking statisticians due to a lack of communication during his time, which ironically mirrors his reluctance to cite his references in his own work [31]. After Thiele, Peter Swerling provided the next development of what would would become known as the Kalman Filter, focusing specifically on problems of Orbit Determination [79]. Additionally, the work of Ruslan Stratonovich [75, 74, 76, 77] is a nonlinear estimator that is actually a generalization of the Kalman Filter. After Kalman's first paper formalizing the estimator, his subsequent work with Bucy formalized the approach for continuous time systems [35].

The Kalman Filter was derived at a perfect time for application to space-based problems. Right after its publication, Stanley Schmidt of NASA Ames Research Center invited Kalman out for a visit [22]. It was here that both sides realized that this estimator was a perfect fit for navigation of the Apollo missions, which had just recently been started. Schmidt's group developed the algorithm for application and along the way made the algorithm more robust, and one of the first groups to develop and apply the Extended Kalman Filter (EKF) [67, 22]. The EKF is a non-optimal implementation of the Kalman Filter to nonlinear systems, and has the problem of divergence if the dynamics are mismodeled. Despite this, these algorithms have revolutionized navigation in the aerospace industry as well as many other fields. They form the basis of what is known as Statistical Orbit Determination - estimation theory applied to astrodynamics problems.

Since the original development of the Kalman Filter and the EKF in the 1960s for the Apollo missions, improvements have been made that reflect the improved computational power of today. An improved nonlinear version of the Kalman Filter that retains its optimality known as the Unscented Kalman Filter was developed in 1997 by Julier and Uhlmann [33]. This algorithm nonlinearally propagates several points in the vicinity of the *a priori* state estimate in order to capture higher order moments of the underlying probability distribution. The optimality it provides is balanced against the increased amount of computational time and tuning it requires. An even more nonlinear algorithm is the particle filter. This algorithm operates on a Monte Carlo-like basis, where it propagates many samples of the state trajectory and provides an estimate that is optimal in a Bayesian sense. The estimator had existed in several heuristic forms since the mid-20th century, but it had not been formalized until Pierre Del Moral's publication in 1996 [56]. This method is computationally intense, so its application is often limited, unlike the Kalman Filter and its variants.

The OCBE is a sequential estimator in the same vein as a Kalman Filter. It differs from the Kalman Filter in that it is a nonlinear filter, it is derived from a least squares context, it segregates *a priori* state and dynamic uncertainties, and it provides a means to compensate for mismodeled dynamics and reconstruct them through estimated optimal control policies that are imbued within the estimator. Its specific purpose is to address estimation in dynamically mismodeled systems, which is not addressed in the algorithms listed in this section. We address that existing literature in the next section.

1.3.2 Maneuver Detection and Reconstruction

Given that estimation in dynamically mismodeled systems is the focus of this thesis we will now provide a focused review of methods to deal with dynamic mismodeling. Each of the methods discussed in this section deal at least with one of the following fields: (1) identification of mismodeled dynamics (i.e.,, maneuver detection), (2) compensation for mismodeled dynamics, and (3) estimation of mismodeled dynamics (i.e,. maneuver characterization and reconstruction).

Typical methods for dealing with uncertain dynamics in the state estimation process include adding process noise to the system, Dynamic Model Compensation (DMC), or appending dynamics parameters to the state vector [83, 30, 46]. Process noise [63], while effective at preventing divergence due to mismodeling, only masks the problem. It provides no method for estimating the mismodeling or detecting its presence, it does not have a strong physical significance, and the uncertainty it injects in the system limits the accuracy of the state estimates. DMC requires a significant amount of tuning, and though the functional form is significant in a statistical sense it does not have a strong physical significance for arbitrary systems [29, 80]. Appending dynamics parameters to the state can be an effective method for recovering dynamics, but it requires a known model for those mismodeled dynamics.

Beyond these classical methods, the problems of dynamic mismodeling identification (maneuver detection) and mismodeling estimation (maneuver characterization/reconstruction and natural dynamics estimation) have been addressed for different systems. Generally, algorithms have been developed for highly dynamical systems (e.g., missile tracking and guidance) that are data-rich (i.e., observations taken throughout a maneuver). Methods such as Bar-Shalom and Birmiwal's Variable Dimension Filter [7], Chan, Hu, and Plant's Input Estimation Method [11], and Goff, Black, and Beck's variable dimension approach [20] directly append accelerations to the state vector for estimation when a maneuver is detected through residuals, but such methods require observation throughout a continuous maneuver. Patera's space event detection method [57] focuses more on quick events in an astrodynamics context, so it tends to neglect smaller maneuvers and natural dynamics mismodeling as well as being limited in application. Hill's detection method [27], though effective, is based solely on optical tracklets, which limits its application to certain tracking problems. Lemmens and Krag [45] addressed maneuver detection for LEO orbits with a Two-Line-Element-based method. Aaron [1] and Folcik, Cefola, and Abbot [18] addressed maneuver detection for Geosynchronous (GEO) orbits with a method based on application of the Extended Semianalytic Kalman Filter (ESKF). These three methods produce promising maneuver detection results for astrodynamics applications, but they provide no information about the underlying maneuvers. Aside from DMC and appending parameters to the state vector in Kalman filtering, a method for estimating dynamics parameters is provided by Mandankan, Singla, Singh, and Scott [52]. This method relies on polynomial chaos. It provides both state and parameter estimates, but just like other methods it requires a model for mismodeled perturbations and it does not have maneuver detection properties. Each of the methods described does not fully address the problem of detecting and estimating mismodeled dynamics in data-sparse systems. We seek an algorithm that will fully address the entirety of this problem in as automatic a fashion as possible.

Estimation in mismodeled systems is known in some academic circles as System Identification. This is a large field, with many treatments including the seminal work of Ljung [50]. While there are many different methods within this larger field, system identification essentially uses a system's inputs and outputs and tries to identify the mechanism in between them - the system model (e.g., dynamical model). Examples of this method at work include Ahmed, Coppola, and Bernstein's inertia matrix identification method [4] where they develop an asymptotically stable tracking control law that is completely robust to inertia matrix mismodeling, because it uses the control inputs and the sensed outputs to reconstruct the inertia matrix. Similarly, Chandresekhar and Bernstein's acceleration identification method [12] addresses unknown system dynamics, but in this case it constructs an acceleration based model that is observed with unknown biases. As with the previous paper, his method requires both input and output information, and in general it requires that the user exercises a degree of control over the system. This is not the case with SSA observation, thus these types of methods (which characterize much of system identification) cannot be applied to the central research topic covered in this thesis.

Not all system identification methods require direct knowledge of the inputs, though. Wang and Haldar's method [87] is identified as system identification with few observations and no input information. While this is true with respect to other system identification techniques, the method still requires too many observations to be applicable to SSA. Additionally, it seems too directed toward structural problems, and it requires active observation rather than the type of relatively "spotty" coverage typical in SSA. Brincker, Zhang, and Andersen [10] discuss a frequency based system identification method that also does not require knowledge of the inputs. Rather, the method focuses on identifying the modes of a system that indicate the natural dynamics of the system. This method does require much observation and it focuses exclusively on natural dynamics mismodeling, thus it does not fully cover the research problem addressed here. In general, system identification methods that do not require knowledge of the inputs are frequency based, and as such are not well posed to the nonlinear state-space systems typical of SSA. Viberg [85] provides a review of existing subspace-based system identification methods that are better adapted to state-space models, but like other system identification methods these generally require a lot of observations and control over the system. One of the most applicable system identification methods to an SSA-type problem are methods like Stubberud and Kramer's [78]. This method adaptively adjusts weights on a neural network to continually adjust the dynamics in the system in a Kalman filter implementation. The method still requires more than data-sparse observation, though, and it limits the maneuvers and mismodeled dynamics to being represented by the polynomials in a neural network, which is not always physically meaningful.

Another area of study that is adapted for estimation in dynamically mismodeled systems is Multiple Model Estimation. This, like system identification, is a large field of study, but Li and Jilkov provided a substantial review of the existing literature in 2005 [47]. Multiple model estimation works by providing a bank of filters with different models in them, and then an estimate is generated by combining the results in a way that illuminates what is the most likely model. One multiple model based approach is Hanlon and Maybeck's Multiple Model Adaptive Estimator [25], which uses a bank of Kalman Filters each with a different dynamical model. The results from each filter are combined in a manner to weight the solution toward the most likely model, such that the method automatically adjusts to changing dynamics or failures in the system. Lee and Hwang's multiple model estimation based method [43] senses maneuver's based on orbital element changes using a series of user predefined maneuvers. It then determines which maneuver mode is most likely. Multiple model estimation, as a field of study, is a great way to attack certain systems with dynamic mismodeling, but because it requires you to discretize different maneuvers it loses the ability to deal with general maneuvers where no *a priori* information is available. Additionally, the added computation time limits real-time applicability, and its method are not designed to address data sparse systems. As such it is not the best method to approach the research problem of this thesis.

What is missing in all of this literature is an automated method that estimates in dynamically mismodeled systems using any type of observation for any type of system (assuming the situation is observable) with non-cooperative and data sparse observations while obtaining information about the mismodeling. Different methods mentioned here cover certain aspects of the problem, but no one method covers it all. The Adaptive OCBE, as will be developed in the following chapters, is designed to fill this hole so that it can be implemented as a real-time state estimator and maneuver detection algorithm for SSA applications. Its general form will expand its applicability to many other systems too.

1.3.3 Control Distance Metrics

The problems of object correlation, maneuver detection, and maneuver characterization in data sparse environments were addressed by Holzinger, Scheeres, and Alfriend [28] with a distance metric approach that is based on optimal control policies. They develop a concept called control distance metrics that measure the integrated control effort that connects two states at different times with a given dynamical model. This metric may be used to probabilistically determine the likelihood that a given measurement is properly associated with a given target or if that target has mismodeled dynamics. A more detailed summary of this method is provided in Chapter 2.

Work with this control distance metric framework has been limited to object correlation, maneuver detection, and characterization. We seek to advance this research into a full estimation algorithm that estimates a system's state, detects mismodeled dynamics (maneuvers), compensates for mismodeled dynamics, and estimates those mismodeled dynamics. The algorithm should be highly automated, and it should be designed to work in data-sparse environments with noncooperative observations. With the problem and motivation fully defined for this research we present the following summary of contributions that this thesis as a whole will provide.

1.4 Contributions

The main contribution of this thesis is the Optimal Control Based Estimator and its companion algorithms. Each of the specific pieces of this larger contribution are identified below.

(1) **The Nonlinear Optimal Control Based Estimator (OCBE)**:

A nonlinear estimator with a meaningful cost function that accounts for *a priori* state error, measurement error, and dynamic mismodeling in a least squares sense. The nonlinear estimator consists of a set of necessary conditions for state and adjoint trajectories that must be solved via a nonlinear root finder. The estimator outputs both state and control trajectories, the latter of which represents the mismodeling in the system. The estimated dynamics represent the minimum amount of dynamics necessary to connect the boundary states under the assumed dynamical model.

(2) **The Generalized Linear Optimal Control Based Estimator (GL-OCBE)**:

A linearized version of the OCBE that uses arbitrary nominal initial state and initial adjoint. The method is designed such that it may be iterated to solve the nonlinear OCBE equations. In addition to state and control estimates, it provides measures of uncertainty in these estimates through a covariance.

(3) **The Ballistic Linear Optimal Control Based Estimator (BL-OCBE)**:

A special version of the GL-OCBE that limits the nominal state and adjoint trajectories to be ballistic - meaning the nominal adjoint is zero for all time (i.e., there is no nominal optimal control policy). Since the method does not have an arbitrary nominal initial adjoint it cannot be iterated to solve the nonlinear OCBE necessary equations. However, the algorithm has special properties including the automatic inclusion of dynamic uncertainty in a manner that is completely equivalent to continuous process noise, a state estimate and covariance at the measurement epoch that are equivalent to the Kalman Filter state estimate and covariance, and a state estimate and covariance at the *a priori* epoch that are equivalent to the smoothed Kalman Filter state estimate and covariance. As such, the BL-OCBE is shown to be a generalization of the Kalman Algorithm that also provides information on dynamic mismodeling through the estimated optimal control policies.

(4) **OCBE Maneuver Detection Method**:

A method that leverages the estimated states and optimal control policies that come out of the OCBE to determine whether those control policies represent deterministic mismodeling within the estimator. The method uses a control distance metric framework to identify whether the optimal control policies are statistically significant, and if they are then the control policies represent a reconstruction of the mismodeled dynamics.

(5) **Optimal Control Based Dynamics Parameter Estimation Method**:

If the estimated optimal control policies are deemed to represent deterministic mismodeling in the system, then this parameter estimation method may be used to estimate dynamics parameter from the control policies themselves. The method chooses parameters that minimize the residuals of the estimated controls and a basis of the estimated forces. The method specifically focuses on application to atmospheric drag and solar radiation pressure parameter estimation due to similarities in the functional forms of the controls and those specific object-dependent orbital perturbations.

(6) **OCBE Full Smoother**:

A smoothing algorithm that recursively incorporates the information from all measurements to the entire observation arc. The method produces a smoothed state trajectory starting at the initial time through all measurement epochs such that it provides a continuous state trajectory in time and an associated optimal control policy informed by all measurements. The state trajectory is forced to be continuous due to the presence of the non-impulsive smoothed control estimates.

(7) **Adaptive Optimal Control Based Estimator**:

An automated version of the OCBE that uses maneuver detection results to adaptively select the assumed dynamic uncertainty parameter at each epoch. This processes all measurements without user input at each epoch, thus allowing for automated real-time state estimation, maneuver detection, and maneuver reconstruction.

1.5 Publications

In this section, a complete list of publications and conference presentations completed during the student's graduate studies is provided. These papers and presentations form the basis of the material presented in this thesis.

1.5.1 Journal Publications

(1) **Lubey, D.P.** & Scheeres, D.J., "Combined State and Dynamics Estimation for Dynamically Mismodeled Systems: The Optimal Control Based Estimator," Journal of Guidance, Control, and Dynamics. (In Preparation)

(2) **Lubey, D.P.** & Scheeres, D.J., "State and Dynamics Estimation with the Optimal Control Based Estimator," IEEE Transactions on Automatic Control. (Submitted)

(3) **Lubey, D.P.** & Scheeres, D.J., "Identifying and Estimating Mismodeled Dynamics via Optimal Control Problem Distance Metrics," Journal of Guidance, Control, and Dynamics, Vol. 37, No. 5, (2014), pp. 1512-1523. doi: 10.2514/1.G000369

1.5.2 Conference Papers and Presentations

(1) Baresi, N., **Lubey, D.P.**, & Scheeres, D.J., "Model Estimation Using Hovering Satellites About Asteroids," Proceedings of the 66th International Astronautical Conference, October 2015.

(2) **Lubey, D.P**. & Scheeres, D.J., "Towards Real-Time Maneuver Detection: Automatic State and Dynamics Estimation with the Adaptive Optimal Control Based Estimator," Proceed-

ings of the 2015 Advanced Maui Optical and Space Surveillance Technologies Conference, September 2015.

(3) **Lubey, D.P.** & Scheeres, D.J., “Automated State and Dynamics Estimation in Dynamically Mismodeled Systems with Information From Optimal Control Policies,” Proceedings of the 18^{th} International Conference on Information Fusion, July 2015.

(4) **Lubey, D.P.**, Scheeres, D.J., & Erwin, R.S., “Maneuver Detection and Reconstruction of Stationkeeping Spacecraft at GEO Using the Optimal Control-Based Estimator,” Proceedings of the 2015 Workshop on Advanced Control and Navigation for Autonomous Aerospace Vehicles, June 2015.

(5) **Lubey, D.P.**, Doostan, A., & Scheeres, D.J., “Estimating Object-Dependent Natural Orbital Dynamics with Optimal Control Policies: A Validation Study,” Proceedings of the 2015 AAS/AIAA Space Flight Mechanics Meeting, January 2015.

(6) **Lubey, D.P.** & Scheeres, D.J., “Robust Tracking and Dynamics Estimation with the Automated Optimal Control Based Estimator,” Proceedings of the 2015 AAS/AIAA Space Flight Mechanics Meeting, January 2015.

(7) **Lubey, D.P.** & Scheeres, D.J., “Supplementing State and Dynamics Estimation with Information from Optimal Control Policies,” Proceedings of the 17th International Conference on Information Fusion, July 2014.

(8) **Lubey, D.P.** & Scheeres, D.J., “Combined Optimal Control and State Estimation for the Purposes of Maneuver Detection and Reconstruction,” Proceedings of the 2014 American Control Conference, Portland, OR, 2014.

(9) **Lubey, D.P**. & Scheeres ,D.J., “An Optimal Control Based Estimator for Maneuver and Natural Dynamics Reconstruction,” Proceedings of the 2013 Advanced Maui Optical and Space Surveillance Technologies Conference, September 2013.

(10) **Lubey, D.P.** & Scheeres, D.J., “An Optimal Control Based Estimator for Maneuver Detection and Reconstruction,” Proceedings of the 2013 AAS/AIAA Astrodynamics Specialists Meeting, August 2013.

(11) **Lubey, D.P.** & Scheeres, D.J., “Identifying and Quantifying Mis-Modeled Dynamics via Optimal Control Problem Distance Metrics,” Proceedings of the 2012 AIAA/AAS Astrodynamics Specialists Meeting, August 2012.

1.5.3 Abstracts, Posters, and Presentations

(1) **Lubey, D.P.**, “Achieving Real Time Maneuver Detection: The Adaptive Optimal Control Based Estimator,” 5th Annual Smead Symposium, May 2015.

(2) **Lubey, D.P.**, “Maneuver Detection and Reconstruction in Data Sparse Systems with an Optimal Control Based Estimator,” 4th Annual Smead Symposium, May 2014.

(3) **Lubey, D.P.**, “Dynamics Estimation and Maneuver Reconstruction Using Optimal Control Policies,” 3rd Annual Smead Symposium, April 2013.

(4) **Lubey, D.P.**, “Identifying and Quantifying Mis-Modeled Dynamics via Optimal Control Policies,” NASA Technology Days, November 2012.

(5) **Lubey, D.P.**, “Dynamics Estimation Using Optimal Control Policies,” 2nd Annual Smead Symposium, May 2012.

1.6 Thesis Organization

This thesis focuses on developing, understanding, and applying the OCBE and its companion algorithms. The thesis is ordered to show the development of the basic theory of the estimator first, and then it focuses on the companion algorithms that are used to understand the dynamic mismodeling in the system.

Chapter 2 includes an overview of necessary background information that will be referred to throughout the rest of the thesis. This includes: the mathematics behind control distance metrics as developed by Holzinger, Scheeres, and Alfriend [28]; the necessary conditions that accompany functional optimization of a standard Bolza-type cost function; and the state and adjoint dynamical models that will be used in the simulations that follow throughout the remainder of the thesis. This provides the basis for how to form the cost function of the OCBE, and how to optimize that cost function to create the estimator.

Chapter 3 provides a full development of the OCBE and its linear counterparts. It starts with the definition of the of the OCBE cost function, the resulting necessary conditions of the OCBE, and a proof of its existence under certain conditions. Next, there is a treatment of the GL-OCBE including the full linearization method, simplification, and calculation of associated covariances. Next, the focus is on the BL-OCBE. This includes special properties of ballistic trajectories, how to simplify the GL-OCBE into this form, and discussions of its noise propagation properties, smoothing properties, and its relation to the Kalman Filter. Next, a method is developed to smooth the results of the OCBE across more than one observation gap, such that a final smooth state trajectory can be obtained with associated controls. Finally, a concluding discussion is provided to illuminate the key discoveries and important takeaways.

Chapter 4 focuses on the application of the OCBE and its linear counterparts to sample tracking applications. This includes a discussion on how to implement the algorithm computationally, and then scenarios where the the nonlinear OCBE and BL-OCBE are implemented to track Low Earth Orbit (LEO) and Geosynchronous Earth Orbit (GEO) based satellites that have some degree of dynamic mismodeling (natural and / or active dynamical mismodeling). Following is a conclusion discussing the effectiveness of the OCBE as applied to these tracking scenarios.

Chapter 5 discusses the application of maneuver detection algorithms to the OCBE, and what the reconstructions of the mismodeled dynamics can tell us. It starts with a discussion of how control distance metrics may be implemented into the GL-OCBE framework, and the associated hypothesis testing that can be done to identify if the measurement corresponds to a detected maneuver. Next, this GL-OCBE maneuver detection development is simplified for application to the BL-OCBE. Next, an algorithm that estimates dynamics parameters (specifically related to atmospheric drag and solar radiation pressure) using the estimated optimal control policies is developed and discussed with relation to the OCBE. Following this are sample applications of the maneuver detection algorithms to the same simulations from the previous chapter. Finally, a discussion of the algorithms' effectiveness concludes the chapter.

Chapter 6 combines the OCBE and the maneuver detection algorithm to create a fully adaptive estimator that automatically detects, compensates for, and reconstructs mismodeled dynamics. This discussion of the automation of the OCBE specifically focuses on the automation criterion, the existence of a solution to this criterion, how to obtain the solution if it does exist, and a formal overview of how the adaptive OCBE should be implemented. Some sample applications of the algorithm to tracking scenarios is provided, and then the chapter is concluded with a discussion of the adaptive algorithm and its abilities.

Chapter 7 concludes this thesis with a summary and discussion of the most important developments, as well as a discussion of avenues for future research and development of the OCBE and its companion algorithms.

Chapter 2

Background Material

Before deriving the Optimal Control Based Estimator, the central algorithm of this thesis, it is important to first cover some important background information. This includes an overview of how a Bolza-type cost function is optimized via functional optimization since this will define necessary conditions for the OCBE, an overview of control distance metrics as they motivate the creation of the OCBE, and defining the dynamical and measurement models that we will be applying these algorithms to throughout this thesis. This chapter will cover each of these topics as they relate the OCBE. This will setup the derivation and application of the OCBE in the subsequent chapters.

2.1 Optimization of Bolza-Type Cost Function

The process of deriving an Optimal Control Policy using a generic cost function is summarized below, as it plays a crucial role in our filter derivation. More detailed accounts are provided by Lawden [41, 42], Marec [53], Stengel [70], and Prussing [60, 59] among others.

An arbitrary cost function may be written in the Bolza form shown in Eq. 2.1. In this notation the Lagrangian portion of the cost ($\mathcal{L}$) is evaluated across the entire time of flight, whereas the boundary costs (K_0 and K_f) are evaluated only at the initial and/or final epochs. In this notation $\vec{x}$ refers to the state of the system, $\vec{u}$ refers to control input into the system, and the subscripts indicate at what epoch the values are evaluated (0 = initial epoch and f = final epoch).To fully define the system, we make the following definitions: $t \in \mathbb{R}$, $\vec{x} \in \mathbb{R}^n$; $\vec{u} \in \mathcal{U} \subset \mathbb{R}^m$; and K_0, K_f, and

$\mathcal{L}$ are scalar functions. $\mathcal{U}$ is a compact set with at most finite discontinuities.

$$\mathcal{J}(t_0, \vec{x}_0, t_f, \vec{x}_f, \vec{u}(t)) = K_0(\vec{x}_0, t_0) + K_f(\vec{x}_f, t_f) + \int_{t_0}^{t_f} \mathcal{L}\left(\vec{x}(\tau), \vec{u}(\tau), \tau\right) d\tau \tag{2.1}$$

In addition to these soft constraints, hard constraints are imposed via Lagrange multipliers ($\vec{\mu}_0$,$\vec{\mu}_f$, and $\vec{p}(t)$). The first two hard constraints force the initial and final times and states to lie on given manifolds ($\left\{g_0(\vec{x}_0, t_0) = \vec{0}\right\} : \mathbb{R}^n x\mathbb{R} \to \mathbb{R}^q$ and $\left\{g_f(\vec{x}_f, t_f) = \vec{0}\right\} : \mathbb{R}^n x\mathbb{R} \to \mathbb{R}^s$). The final hard constraint enforces the state dynamics to adhere to a given function of the state, control, and time ($\dot{\vec{x}}(t) = \vec{f}\left(\vec{x}(t), \vec{u}(t), t\right)$). We make the additional constraint that the state dynamics are affine in the control, and any multipliers on the control are not state dependent ($\vec{f}\left(\vec{x}(t), \vec{u}(t), t\right) = \vec{f}_n\left(\vec{x}(t), t\right) + B(t)\vec{u}(t)$). The following derivation does not necessitate this assumption, but it simplifies the approach. It should be noted that other known controls may be put into the state dynamics, but this does not affect the following analysis. The Lagrange multiplier that enforces this dynamic constraint ($\vec{p}(t) \in \mathbb{R}^n$) is termed the system's adjoint or costate. The adjoined cost function is provided in Eq. 2.2.

$$\begin{aligned} &\mathcal{J}_A(t_0, \vec{x}_0, \vec{\mu}_0, t_f, \vec{x}_f, \vec{\mu}_f, \vec{u}(t), \vec{p}(t)) = \\ &= \left[K_0(\vec{x}_0, t_0) + \vec{\mu}_0^T g_0(\vec{x}_0, t_0)\right] + \left[K_f(\vec{x}_f, t_f) + \vec{\mu}_f^T g_f(\vec{x}_f, t_f)\right] \\ &+ \int_{t_0}^{t_f} \left[\mathcal{L}\left(\vec{x}(\tau), \vec{u}(\tau), \tau\right) + \vec{p}(\tau)^T \left(\vec{f}\left(\vec{x}(\tau), \vec{u}(\tau), \tau\right) - \dot{\vec{x}}(\tau)\right)\right] d\tau \end{aligned} \tag{2.2}$$

The system as defined may be defined via a Hamiltonian formulation as shown in Eq. 2.3. This provides a more compact form for optimization as well as useful properties (such as the symplectic state transition matrix), which are used later in analytical manipulation.

$$\mathcal{H}\left(\vec{x}(t), \vec{u}(t), \vec{p}(t), t\right) = \mathcal{L}\left(\vec{x}(t), \vec{u}(t), t\right) + \vec{p}(t)^T \vec{f}\left(\vec{x}(t), \vec{u}(t), t\right) \tag{2.3}$$

Freeing up the boundary times and states when taking the first variation of the cost we obtain the necessary conditions for optimality (Eqs. 2.4-2.10) subject to the Hamiltonian definition.

$$\hat{u}(t) = \underset{\vec{u} \in \mathcal{U}}{\operatorname{argmin}} \left(\mathcal{H}\left(\vec{x}(t), \vec{u}(t), \vec{p}(t), t\right)\right) \tag{2.4}$$

$$\dot{\vec{x}}(t) = \frac{\partial \hat{\mathcal{H}}}{\partial \vec{p}}^T = \vec{f}\left(\vec{x}(t), \hat{u}(t), t\right) = \vec{f}_n\left(\vec{x}(t), t\right) + B(t)\hat{u}(t) \tag{2.5}$$

$$\dot{\vec{p}}(t) = -\frac{\partial \hat{\mathcal{H}}}{\partial \vec{x}}^T = -\frac{\partial \mathcal{L}}{\partial \vec{x}}^T - \frac{\partial \vec{f}}{\partial \vec{x}}^T \vec{p}(t) \tag{2.6}$$

$$\hat{\mathcal{H}}_0 = \frac{\partial K_0(\vec{x}(t_0), t_0)}{\partial t} + \vec{\mu}_0^T \frac{\partial g_0(\vec{x}(t_0), t_0)}{\partial t} \tag{2.7}$$

$$\vec{p}(t_0) = -\frac{\partial K_0(\vec{x}(t_0), t_0)}{\partial \vec{x}}^T - \frac{\partial g_0(\vec{x}(t_0), t_0)}{\partial \vec{x}}^T \vec{\mu}_0 \tag{2.8}$$

$$\hat{\mathcal{H}}_f = -\frac{\partial K_f(\vec{x}(t_f), t_f)}{\partial t} - \vec{\mu}_f^T \frac{\partial g_f(\vec{x}(t_f), t_f)}{\partial t} \tag{2.9}$$

$$\vec{p}(t_f) = \frac{\partial K_f(\vec{x}(t_f), t_f)}{\partial \vec{x}}^T + \frac{\partial g_f(\vec{x}(t_f), t_f)}{\partial \vec{x}}^T \vec{\mu}_f \tag{2.10}$$

The first necessary condition (Eq. 2.4) defines the optimal control policy ($\vec{u}(t)$) in terms of the state and adjoint using the result from the Pontryagin Minimum Principle. The next two necessary conditions (Eqs. 2.5 and 2.6) provide equations of motion for the state and adjoint, respectively. The final four necessary conditions (Eqs. 2.7 - 2.10) are the transversality conditions, which set boundary conditions on the initial and final times and adjoints. In these equations $\mathcal{H}_0$ and $\mathcal{H}_f$ represent the Hamiltonian evaluated at the initial and final epoch, respectively. The hat above a quantity signifies this is the optimal solution for the given variable.

Integrating the state and adjoint dynamics to an arbitrary epoch t given initial conditions t_{k-1}, $\vec{x}_{k-1}$, and $\vec{p}_{k-1}$ we define the solution in the form of a solution flow as shown below.

$$\phi_x(t; t_{k-1}, \vec{x}_{k-1}, \vec{p}_{k-1}) = \vec{x}_{k-1} + \int_{t_{k-1}}^{t} \dot{\vec{x}}(\tau, \vec{x}, \vec{p}) d\tau \tag{2.11}$$

$$\phi_p(t; t_{k-1}, \vec{x}_{k-1}, \vec{p}_{k-1}) = \vec{p}_{k-1} + \int_{t_{k-1}}^{t} \dot{\vec{p}}(\tau, \vec{x}, \vec{p}) d\tau \tag{2.12}$$

It should be noted that we do not explicitly account for the control vector in this propagation because the results of the Pontryagin Minimum Principle create a direct mapping between the control and the state and adjoint.

Furthermore, we define motion in the vicinity of this solution via a linear expansion where the state and adjoint partials are quadrants of the state transition matrix. The full state transition matrix is defined in Eq. 2.13. The dynamics of this matrix and initial conditions are defined in Eqs. 2.14 and 2.15 where $\vec{z}$ is the combined state and adjoint vector ($\vec{z} = [\vec{x}^T, \vec{p}^T]^T$).

$$\begin{aligned} \Phi(t_k, t_{k-1}) &= \begin{bmatrix} \Phi_{xx}(t_k, t_{k-1}) & \Phi_{xp}(t_k, t_{k-1}) \\ \Phi_{px}(t_k, t_{k-1}) & \Phi_{pp}(t_k, t_{k-1}) \end{bmatrix} \\ &= \left. \begin{bmatrix} \frac{\phi_x(t_k)}{\partial \vec{x}_{k-1}} & \frac{\phi_x(t_k)}{\partial \vec{p}_{k-1}} \\ \frac{\phi_p(t_k)}{\partial \vec{x}_{k-1}} & \frac{\phi_p(t_k)}{\partial \vec{p}_{k-1}} \end{bmatrix} \right|_{(t_k; t_{k-1}, \vec{x}_{k-1}, \vec{p}_{k-1})} \end{aligned} \tag{2.13}$$

$$\begin{aligned} \dot{\Phi}(t, \tau) &= A(t)\Phi(t, \tau) \\ \Phi(\tau, \tau) &= I_{2nx2n} \end{aligned} \tag{2.14}$$

$$A(t) = \left. \frac{\partial \dot{\vec{z}}}{\partial \vec{z}} \right|_{(t, \vec{x}(t), \vec{p}(t))} \tag{2.15}$$

As mentioned, the symplectic nature of the STM falls out of the Hamiltonian Formulation of the dynamical system [58]. This results in the relations between the quadrants of the STM as described in Eq. 2.16.

$$\begin{gathered} \Phi_{xx}(t, \tau)^T \Phi_{px}(t, \tau) = \left(\Phi_{xx}(t, \tau)^T \Phi_{px}(t, \tau)\right)^T \\ \Phi_{pp}(t, \tau)^T \Phi_{xp}(t, \tau) = \left(\Phi_{pp}(t, \tau)^T \Phi_{xp}(t, \tau)\right)^T \\ \Phi_{xx}(t, \tau)^T \Phi_{pp}(t, \tau) - \Phi_{px}(t, \tau)^T \Phi_{xp}(t, \tau) = I_{nxn} \end{gathered} \tag{2.16}$$

These linear dynamics will be used to find a solution to this nonlinear optimization problem, as well as prove its existence. Beyond this, these definitions will be relied upon to define the linear estimator during the development of the OCBE in Chapter 3. Having defined notation for optimization and linearization of the system, we now proceed to a discussion about control distance metrics, which inform the development of the OCBE and its accompanying maneuver detection capabilities.

2.2 Control Distance Metrics

Control distance metrics, as defined by Holzinger, Scheeres, and Alfriend [28], may be used to quantify the level of mismodeling within a system. The metric takes two time, state, and covariance triplets ($a = (t_a, \vec{x}_a, P_a)$ and $b = (t_b, \vec{x}_b, P_b)$) from different epochs along with an assumed dynamical model. A control policy that minimizes Eq. 2.17 is then generated to absolutely connect the nominal states from each triplet. This control policy integrated in the same objective it minimizes defines the control distance metric (Eq. 2.17).

$$D_C(a,b) = \inf_{\vec{u} \in \mathcal{U}} \left[\int_{t_a}^{t_b} \frac{1}{2} \vec{u}(\tau)^T \vec{u}(\tau) d\tau \right] \tag{2.17}$$

In terms of maneuver detection, these metrics may be used to quantify state distances in a far more meaningful way than a typical metric like a Mahalonobis distance. Specifically, it quantifies the minimum amount of extra dynamics needed to connect the nominal state estimates when constraining the dynamical model as discussed. As such the metric may be used to assess how far states are from one another in a dynamics space, which is meaningful for maneuver-based analysis. Given that the states in the triplets are uncertain estimates with known covariances, the metrics themselves are random variables. As such, the associated maneuver detection method is probabilistic. Linearized about a nominal state and adjoint trajectory, the metric may be rewritten in a linear form that allows for quantification of its distribution. This linearized form is summarized in Eqs. 2.18 - 2.23 where $\tilde{u}(t)$ is the control on the nominal state and adjoint trajectories.

$$\begin{aligned} D_C(a,b) &= \tilde{D}_C(a,b) + \vec{\omega}(t_b,t_a)^T \delta\vec{X} + \delta\vec{X}^T \Omega(t_b,t_a) \delta\vec{X} \qquad (2.18) \\ &= \tilde{D}_C(a,b) + D_U \end{aligned}$$

$$\tilde{D}_C(a,b) = \int_{t_a}^{t_b} \frac{1}{2} \tilde{u}(\tau)^T \tilde{u}(\tau) d\tau \tag{2.19}$$

$$\vec{\omega}(t_b,t_a) = \int_{t_a}^{t_b} \Lambda(\tau,t_a)^T B(\tau) \tilde{u}(\tau) d\tau \tag{2.20}$$

$$\Omega(t_b,t_a) = \frac{1}{2} \int_{t_a}^{t_b} \Lambda(\tau,t_a)^T B(\tau) B(\tau)^T \Lambda(\tau,t_a) d\tau \tag{2.21}$$

$$\Lambda(t,t_a) = \begin{bmatrix} \Phi_{px}(t,t_a) - \Phi_{pp}(t,t_a)\Phi_{xp}(t_b,t_a)^{-1}\Phi_{xx}(t_b,t_a) & \Phi_{pp}(t,t_a)\Phi_{xp}(t_b,t_a)^{-1} \end{bmatrix} \tag{2.22}$$

$$\delta\vec{X} = \begin{bmatrix} \delta\vec{x}_a \\ \delta\vec{x}_a \end{bmatrix} \tag{2.23}$$

The resulting mean and variance of this linearized metric is defined in Eqs. 2.24 and 2.25 where P_X is the covariance of the random vector $\delta\vec{X}$.

$$\mu_C(a,b) = \int_{t_a}^{t_b} \frac{1}{2}\tilde{u}(\tau)^T\tilde{u}(\tau)d\tau + \mathrm{Tr}\left[\Omega(t_b,t_a)P_X\right] \tag{2.24}$$

$$\sigma_C^2(a,b) = \vec{\omega}(t_b,t_a)^T P_X \vec{\omega}(t_b,t_a) + 2\mathrm{Tr}\left[\Omega(t_b,t_a)P_X\Omega(t_b,t_a)P_X\right] \tag{2.25}$$

Knowing the statistical form of the distance metric, the probability that the calculated metric represents deterministic mismodeling may be obtained via a hypothesis test. To perform this test the deterministic portion of the metric is compared against the distribution of the stochastic portion. The probability that the metric represents deterministic mismodeling is assessed as the probability that the calculated metric ($\tilde{D}_C$) exceeds the stochastic error (D_U). This forms the basis of the hypothesis testing done in the OCBE maneuver detection process.

Singh, Horwood, and Poore [66] adapted the Control Distance Metric approach by using a minimum-fuel cost function, which yields impulsive control policies rather than smooth continuous controls. This makes the method far more numerical than the quadratic control policy approach, but it demonstrates a different application of this metric formulation.

This thesis uses the control distance metric as a foundation, and then builds on it to create a combined state estimator, maneuver detection, and maneuver reconstruction algorithm. A modified version of this metric is used to construct the OCBE cost function, which combines three pieces of information (i.e. a priori state estimate, measurement, and confidence in the dynamical model) into a simultaneous minimization procedure. The resulting algorithm simultaneously outputs state estimates at both epochs along with an optimal control policy that represents mismodeling within the system. Using a hypothesis test similar to the one described above, the statistical significance of the estimated mismodeling is then determined to assess whether it represents a deterministic error. This process is then automated using the maneuver detection algorithm to allow for real-time application to complex systems.

While the OCBE will be derived for application to an arbitrary mechanical system, the focus will be on application to SSA problems. As such, we define the dynamics for these type of systems in the following section, since they will be used for all applications within this thesis.

2.3 Dynamical Models for Space Situational Awareness

With the primary application of the OCBE being SSA, it is important to define the dynamics of the system. Specifically, orbital dynamics in Earth orbit. The dynamical models used in the simulations throughout this paper are not overly complex, as they are just meant to demonstrate the algorithm under representative dynamics rather than too specific a situation. Adding more perturbations generally does not affect the results unless the perturbation is mismodeled within the estimator. In this section we provide models for the following specific forces: two-body gravitation, a non-spherical gravity term (J_2: Oblateness), atmospheric drag, solar radiation pressure, and third-body gravitational effects. These models are based on those presented in Tapley, Schutz, and Born [83], Vallado [84], and Curtis [13]. We start with a description of the state dynamics, then derive the resulting adjoint dynamics.

This section focuses on the natural dynamics, which are only time and state dependent. As defined previously, the dynamics are affine in the control with a time-dependent gain on the control vector. For all SSA applications in this paper we use the following control gain matrix.

$$B(t) = \begin{bmatrix} 0_{3\times 3} \\ I_{3\times 3} \end{bmatrix} \tag{2.26}$$

This includes three control terms (u_x, u_y, and u_z). Each represents the control in one of three principle directions that define the frame that the state vector and its dynamics are defined in. The state vector we use for estimation in these simulations includes cartesian position and velocity in the Earth Centered Inertial (ECI) frame with respect to the center of the Earth. That state vector is defined below.

$$\vec{x}^T = \begin{bmatrix} r_x & r_y & r_z & v_x & v_y & v_z \end{bmatrix} \tag{2.27}$$

2.3.1 State dynamics

The full natural state dynamical model is expressed in Eq. 2.28.

$$\vec{f}_n(t,\vec{x}) = -\frac{\mu}{r^3}\vec{r} + \vec{a}_{J2}(t,\vec{x}) + \vec{a}_{Drag}(t,\vec{x}) + \vec{a}_{SRP}(t,\vec{x}) + \vec{a}_{3B}(t,\vec{x}) + \vec{a}_{other}(t,\vec{x}) \tag{2.28}$$

In order from left to right these accelerations represent the effects of two-body gravity, Earth oblateness effects (J2), atmospheric drag, solar radiation pressure (SRP), third-body gravity effects, and other perturbations. By "other" we mean that any perturbation not mentioned here such as outgassing, known maneuvers, non-spherical gravity terms, etc. The individual perturbations are fully defined in the following subsections.

2.3.1.1 Non-Spherical Gravity (J_2)Acceleration

The J_2 acceleration is expressed in the ECI frame in Eqs. 2.29 and 2.30.

$$\vec{a}_{J2}(t,\vec{x}) = \frac{-3\mu Re^2 J_2}{2r^5}\begin{bmatrix} (1-5\sin\eta^2)r_x \\ (1-5\sin\eta^2)r_y \\ (3-5\sin\eta^2)r_z \end{bmatrix} \tag{2.29}$$

$$\sin\eta = \frac{r_z}{r} \tag{2.30}$$

The spacecraft position is parameterized into ECI components (r_x, r_y, and r_z) within this definition. Relevant parameters are defined in Table 2.1. The functional form comes from the spherical harmonics definitions, which uses Legendre polynomials to express the gravitational potential of an arbitrary mass distribution [84].

2.3.1.2 Atmospheric Drag

The atmospheric drag acceleration model used in this paper is defined in Eqs. 2.31-2.35.

$$\vec{a}_{Drag}(t,\vec{x}) = -\frac{1}{2}\rho(r)Bv_{rel}\vec{v}_{rel} \tag{2.31}$$

Table 2.1: Gravitational Dynamics Parameters

Parameter	Notation	Value	Units
Earth's Gravitational Parameter	μ	3.986x10^{14}	m^3/s^2
Earth's Mean Equatorial Radius	Re	6378136.3	m
Earth's Oblateness Parameter	J_2	1.0826x10^{-3}	–

$$B = \frac{C_D A}{m} \tag{2.32}$$

$$\rho(r) = \rho_0 \exp\left[\frac{r_0 - r}{H}\right] \tag{2.33}$$

$$\vec{v}_{rel} = \vec{v} - \vec{\omega}^{A/N} \times \vec{r} \tag{2.34}$$

$$\vec{\omega}^{A/N} = \dot{\theta}\hat{K} \tag{2.35}$$

The model uses a typical exponential decay law for atmospheric density as a function of orbital altitude. It also assumes that the atmosphere rotates with the Earth. Relevant parameters are defined in Table 2.2. $\hat{K}$ represents the unit vector along the spin axis of the Earth in the ECI frame.

Table 2.2: Atmospheric Drag Dynamics Parameters

Parameter	Notation	Value	Units
Exponential Cutoff Altitude	r_0	700	km
Atm. Scale Height	H	88.667	km
Density at Cutoff	ρ_0	$3.614x10^{-13}$	kg/m^3
Earth's Rotation Rate	$\dot{\theta}$	$7.2921x10^{-5}$	rad/s

This model is a simplified version of more complex dynamical models. We do not account for variation in atmospheric density except in the radial direction (i.e. it neglects solar interaction on the day side of Earth), and the atmosphere is forced to rotate with the Earth's surface. More complicated models account for these dynamic natural occurrences, but in general no drag model is perfect. Accounting for variation in the drag parameter due to attitude-coupling also offers more room for development of this theory, but this requires specific object models so the results would not be general to all objects in orbit as we aim for in this algorithm.

2.3.1.3 Solar Radiation Pressure

The Solar Radiation Pressure (SRP) model is defined in Eqs. 2.36-2.39.

$$\vec{a}_{SRP}(t,\vec{x}) = p_{SRP}P\left(\frac{{}^{S}\vec{r}}{{}^{S}r}\right) \tag{2.36}$$

$$P = \frac{SA}{m} \tag{2.37}$$

$$p_{SRP} = \frac{L_{sun}}{4c\pi({}^{S}r)^2} \tag{2.38}$$

$${}^{S}\vec{r} = \vec{r} - \vec{r}_{sun} \tag{2.39}$$

This simplified “cannonball” model simply applies an acceleration proportional to the SRP in the direction opposite the sun, and neglects effects such as shadowing. As the distance from the sun (${}^{S}r$) varies negligibly over the course of a typical geocentric orbit the acceleration associated with SRP is effectively constant. This also assumes a constant projected area (A). By definition, $\vec{r}_{sun}$ is the vector pointing from the Earth to the Sun with a magnitude equal to the distance between the two bodies. As such, ${}^{S}\vec{r}$ points from the Sun to the spacecraft, which means the SRP acceleration pushes the spacecraft away from the Sun. The cannonball model does not account for attitude coupling and non-axial forces and moments. More complicated models that rely on object geometry and attitude are available such as those that rely on quantizing an orbiting object into a finite number of facets and Fourier based models as discussed by McMahon [55], but these generally require knowing object geometry and parameters so they cannot be applied to an unknown object in orbit.

Table 2.3: Solar Radiation Pressure Constant Dynamics Parameters

Parameter	Notation	Value	Units
Solar Luminosity	L_S	3.8395x10^{26}	W
Earth-Sun Distance	d_S	1.4960x10^{11}	m
Speed of Light	c	299792458	m/s

2.3.1.4 Third Body Gravity

While the universal law of gravitation applies to all gravity forces, when considering the effects of a perturbing body on the two body solution we obtain a slightly different form as described in Eq. 2.40. In this definition, $\vec{r}_{3B}$ is position of the third body with respect to the primary (i.e. Earth), and $\Delta\vec{r}$ is the position of the third body with respect to the target (i.e. secondary body orbiting the Earth, $\Delta\vec{r} = \vec{r}_{3B} - \vec{r}$).

$$\vec{a}_{3B}(t,\vec{x}) = \mu_{3B}\left(\frac{\Delta\vec{r}}{|\Delta\vec{r}|^3} - \frac{\vec{r}_{3B}}{|\vec{r}_{3B}|^3}\right) \tag{2.40}$$

This equation requires an ephemeris of the third body, so that its position may be calculated as a function of time since this is not part of the state vector. Additionally, gravitational parameters for the perturbing bodies must be known. These values are summarized for the sun and moon (the chief perturbing bodies for Earth orbit) in Table 2.4.

Table 2.4: Third Body Gravitational Dynamics Parameters

Parameter	Notation	Value	Units
Sun's Gravitational Parameter	μ_{sun}	1.327x10^{20}	m^3/s^2
Moon's Gravitational Parameter	μ_{moon}	4.903x10^{12}	m^3/s^2

2.3.2 Adjoint Dynamics

Deriving the adjoint dynamics for this specific natural dynamical model requires one to apply Eq. 2.6 to the acceleration models. These dynamics are defined in Eq. 2.41 with simplified results provided in Eqs. 2.42-2.48.

$$\dot{\vec{p}} = \begin{bmatrix} -\left(\frac{\partial \vec{f}_n}{\partial \vec{r}}\right)^T \vec{p}_v \\ -\vec{p}_r - \left(\frac{\partial \vec{f}_n}{\partial \vec{v}}\right)^T \vec{p}_v \end{bmatrix} = \begin{bmatrix} -\left[\frac{\partial}{\partial \vec{r}}\left(-\frac{\mu}{r^3}\vec{r} + \vec{a}_{J2}(t,\vec{x}) + \vec{a}_{Drag}(t,\vec{x}) + \vec{a}_{SRP}(t,\vec{x}) + \vec{a}_{3B}(t,\vec{x})\right)\right]^T \vec{p}_v \\ -\vec{p}_r - \left[\frac{\partial}{\partial \vec{v}}\left(\vec{a}_{Drag}(t,\vec{x})\right)\right]^T \vec{p}_v \end{bmatrix} \tag{2.41}$$

$$\frac{\partial}{\partial \vec{r}}\left(-\frac{\mu}{r^3}\vec{r}\right) = -\frac{\mu}{r^3}\left(I_{3x3} - \frac{3}{r^2}\vec{r}\vec{r}^T\right) \tag{2.42}$$

$$\frac{\partial}{\partial \vec{r}}\left(\vec{a}_{J2}(t,\vec{x})\right) = \left(-\frac{3\mu Re^2 J_2}{2r^5}\right)\Bigg[-\frac{5}{r^2}\left(\left(1-5\sin^2\eta\right)\vec{r}\vec{r}^T + 2r_z\hat{K}\vec{r}^T\right) + \left(1-5\sin^2\eta\right)I_{3x3} - \frac{10r_z\vec{r}}{r^2}\left(\hat{K}^T - \frac{r_z\vec{r}^T}{r^2}\right) + 2\hat{K}\hat{K}^T\Bigg] \tag{2.43}$$

$$\frac{\partial}{\partial \vec{r}}\left(\vec{a}_{Drag}(t,\vec{x})\right) = -\frac{\vec{a}_{Drag}\vec{r}^T}{rH} + \frac{1}{2}B\rho(r)\left(v_{rel}I_{3x3} + \frac{\vec{v_{rel}}\vec{v_{rel}}^T}{v_{rel}}\right)[\widetilde{\omega}] \tag{2.44}$$

$$[\widetilde{\omega}] = \begin{bmatrix} 0 & -\omega_z & \omega_y \\ \omega_z & 0 & -\omega_x \\ -\omega_y & \omega_x & 0 \end{bmatrix} = \begin{bmatrix} 0 & -\dot{\theta} & 0 \\ \dot{\theta} & 0 & 0 \\ 0 & 0 & 0 \end{bmatrix} \tag{2.45}$$

$$\frac{\partial}{\partial \vec{r}}\left(\vec{a}_{SRP}(t,\vec{x})\right) = -\frac{3\vec{a}_{SRP}\left({}^S\vec{r}\right)^T}{\left({}^S r\right)^2} + \frac{p_{SRP}P}{\left({}^S r\right)}I_{3x3} \tag{2.46}$$

$$\frac{\partial}{\partial \vec{r}}\left(\vec{a}_{3B}(t,\vec{x})\right) = -\frac{\mu_{3B}}{\Delta r^3}\left[I_{3\times 3} - 3\frac{\Delta\vec{r}\Delta\vec{r}^T}{\Delta r^2}\right] \tag{2.47}$$

$$\frac{\partial}{\partial \vec{v}}\left(\vec{a}_{Drag}(t,\vec{x})\right) = -\frac{1}{2}B\rho(r)\left(v_{rel}I_{3x3} + \frac{\vec{v_{rel}}\vec{v_{rel}}^T}{v_{rel}}\right) \tag{2.48}$$

It is important to include all perturbations in the adjoint dynamics. Without the appropriate partials, the OCP will not replicate the mismodeled dynamics as accurately.

2.4 Measurement Models for Space Situational Awareness

In this section, we define the four types of measurements used throughout simulations in this paper. These include range and range-rate observations as well as optical (azimuth and elevation) measurements. In these expressions, $\vec{r}$ refers the vector position of the target with respect to the center of the Earth and $\vec{r}_{obs}$ is the position of the observer with respect to the center of the Earth. It assumed that the observer is fixed in the Earth Centered Fixed (ECF) frame - a frame that rotates with the Earth. As such these equations are valid for observers fixed to the Earth and space-based observatories in Geostationary orbit. These equations do not account for Earth tides. It assumes the Earth is a constantly rotating rigid body.

2.4.1 Range and Range-Rate Measurements

Range and range-rate observation are two types of common SSA measurements. To calculate them, we first define a range vector, which describes the position of the target with respect to the observer as shown below.

$$\vec{\rho} = \vec{r} - \vec{r}_{obs} \tag{2.49}$$

In this definition, it is important that both vectors are expressed in the same reference frame. Using this definition, we easily calculate range as the L2 norm of the vector (all norms are assumed L2 unless otherwise stated). Additionally, range-rate may be calculated by taking the time derivative of range as shown below.

$$\rho = ||\vec{\rho}|| \tag{2.50}$$

$$\dot{\rho} = \frac{\vec{\rho}^T \left(\vec{v} - \vec{\omega}_{\earth} \times \vec{r} \right)}{\rho} \tag{2.51}$$

In this calculation, we assume that the observer rotates with the Earth such that its position is constant in the ECF frame. $\vec{\omega}_{\earth}$ refers to the rotation of the Earth with respect to the inertial frame. Together these equations define an explicit mapping from target position and velocity ($\vec{v}$) to range and range-rate measurements.

2.4.2 Optical Measurements

Optical measurements are another typical type of observation for SSA applications. These can be attained for both LEO and GEO targets. They simply require a camera system capable of providing accurate pointing information (on the order of arcseconds) and the ability to detect transiting objects. These measurements consist of the azimuth and elevation angles of the target with respect to the observer in an East-North-Up (ENU) frame. We define the ENU frame as shown below where $\hat{K}$ is the inertially-fixed rotation pole of the Earth.

$$\hat{u} = \frac{\vec{r}_{obs}}{||\vec{r}_{obs}||} \tag{2.52}$$

$$\hat{e} = \frac{\hat{K} \times \hat{u}}{||\hat{K} \times \hat{u}||} \tag{2.53}$$

$$\hat{n} = \hat{u} \times \hat{e} \tag{2.54}$$

Using these definitions, we calculate azimuth (γ) and elevation (ψ) as defined below.

$$\psi = \sin^{-1}\left[\frac{\vec{\rho} \cdot \hat{u}}{\rho}\right] \tag{2.55}$$

$$\gamma = \gamma_0 + \cos^{-1}\left[\frac{\vec{\rho} \cdot \hat{n}}{||\vec{\rho} - \rho \sin(\psi)\hat{u}||}\right] \tag{2.56}$$

$$\gamma_0 = \begin{cases} 0; & \vec{\rho} \cdot \hat{e} \geq 0 \\ \pi; & \vec{\rho} \cdot \hat{e} < 0 \end{cases} \tag{2.57}$$

The definition of γ_0 ensures this is a continuous function with a range of $[0, 2\pi)$.

Having defined all necessary dynamics and measurements, reviewed control distance metrics, and reviewed functional optimization of Bolza-type cost functions, we now have the proper background covered to proceed with the definition and derivation of the central algorithm of this thesis - the Optimal Control Based Estimator.

Chapter 3

The Optimal Control Based Estimator

In this chapter, the core algorithm of this thesis is developed - the Optimal Control Based Estimator. The OCBE is an estimation algorithm that is robust to dynamic mismodeling, and it is capable of providing information on mismodeled dynamics through the control estimates it provides. In combining state and control trajectories that are continuous across the observation gap, the OCBE effectively preserves the continuous-time nature of the observed system, whereas other estimation algorithms reduce it to a discrete-time system. This provides far more information between measurements, which is especially useful in data-sparse applications. When incorporating the full smoothing algorithm that accompanies the OCBE, a continuous state trajectory (with no jump discontinuities) and control profile are obtained throughout the entire measurement arc, thus expanding the benefits of a continuous time solution to the entirety of the timespan of interest.

This chapter starts with a discussion of the cost function used to derive this estimator and the inputs into the estimator. From here, an implicit formulation for the nonlinear estimator is developed from the necessary conditions for optimal control, and a theorem is provided relating to the existence of the nonlinear estimator. Next, the nonlinear OCBE is linearized to develop the GL-OCBE. Following this, the BL-OCBE is developed as a simplification of the GL-OCBE. A discussion on the BL-OCBE is provided including its special properties and its relation to the Kalman Filter algorithm. The theory is concluded with a development of the accompanying full smoothing algorithm. Finally, a concluding discussion of the algorithm is provided to sum up the contributions of this chapter. This chapter will focus on how the estimator is developed and what the resulting equations mean. An extended derivation of these equations is provided in Appendix A (derivation of estimates) and Appendix B (derivation of uncertainties of estimates).

It should also be noted that deriving an estimator through an optimal control formulation has been addressed before by Athans and Tse [6], but with a completely different cost function, framework, and results as compared to this study. Their control variable was not used to mimic an acceleration in the system like ours is, so the approach and results differ greatly. Rao, Rawling, and Mayne's constrained state estimation process [61] is also an estimator obtained through an optimal control process, but they focus on discrete systems with a finite time moving horizon. They estimate dynamic uncertainties as discrete processes that are constant across observation gaps, so like others it is best aimed at systems that are data-rich (though their method does provide the ability to constrain dynamic disturbances unlike other methods). This method pursues optimization in a completely different manner. They use more of a batch approach over moving finite windows (rather than the sequential process used in this paper), and the dynamic mismodelings it estimates are different, thus our method provides a unique contribution not provided in the existing literature.

3.1 Cost Function of the OCBE

Like any sequential state estimator, the OCBE takes advantage of the two main pieces of information in the system: 1) the a priori state estimate ($\bar{x}_{k-1|k-1} \in \mathbb{R}^n$) and its associated covariance ($\bar{P}_{k-1|k-1} \in \mathbb{R}^{n\times n}$) at the a priori epoch ($t_{k-1} \in \mathbb{R}$) and 2) the measurement ($\vec{Y}_k \in \mathbb{R}^p$) and its covariance matrix ($R_k \in \mathbb{R}^{p\times p}$) at the measurement epoch ($t_k \in \mathbb{R}$). In this notation, the state estimate and state estimate covariance subscripts indicate both the epoch of the values as well as the epoch through which information is provided. For instance, $\bar{x}_{k|k-1}$ indicates the state estimate at t_k given information through t_{k-1}. Furthermore, the bar notation indicates pre-estimate values (i.e. values with information through t_{k-1}) whereas hats indicate optimal estimates using all available information (i.e. values with information through t_k).

The a priori state information is blended into the cost function via an initial least squares boundary cost as shown below.

$$K_{k-1}(\vec{x}_{k-1}) = \frac{1}{2}\left(\bar{x}_{k-1|k-1} - \vec{x}_{k-1}\right)^T \bar{P}^{-1}_{k-1|k-1}\left(\bar{x}_{k-1|k-1} - \vec{x}_{k-1}\right) \tag{3.1}$$

This cost attempts to select a state ($\vec{x}_{k-1}$) close to the a priori state estimate given the level of certainty in the estimate. It should be noted that this cost is entirely nonlinear (the states are absolute not relative to a reference trajectory), and unlike a Kalman Filter this a priori information is not propagated to the measurement epoch. This helps to decouple the uncertainties associated with the a priori estimate, and the mismodeling in the dynamical model.

Measurement information is included in a similar manner through a nonlinear least squares terminal boundary cost as shown below.

$$K_k(\vec{x}_k) = \frac{1}{2}\left(\vec{Y}_k - h(t_k, \vec{x}_k)\right)^T R_k^{-1}\left(\vec{Y}_k - h(t_k, \vec{x}_k)\right) \tag{3.2}$$

The nonlinearities in this cost are more apparent than they are in the a priori cost. In this cost the state-observation relationship ($h(t, \vec{x}) : \mathbb{R} \times \mathbb{R}^n \to \mathbb{R}^p$) is not linearized with respect to the state input. The cost just requires the selection of a state ($\vec{x}_k$) that when mapped to measurement space is close to the raw observation given the level of certainty in the observation.

As defined by these costs and the dynamically constrained cost function (Eq. 2.2 without the Lagrangian term), the assumed dynamical model would force the two state estimates to be connected in time. If the assumed dynamics are mismodeled this can lead to suboptimal estimation or even estimate divergence in extreme cases. To account for this we include the third piece of information available to the estimator: the dynamical model and its uncertainty. We include an estimated fictitious control policy ($\vec{u}(t) \in \mathbb{R}^m$), which acts along with the assumed dynamics to connect the state estimates at both epochs. This estimated control policy absorbs the errors associated with this mismodeling allowing for optimal state estimates. It physically represents the mismodeling in the system - providing a reconstruction of the event. The cost associated with this control is a weighted least squares Lagrangian where the control is differenced from our assumed control ($\bar{u}(t) \in \mathbb{R}^m$) as shown below.

$$\mathcal{L}\left(\vec{u}(t)\right) = \frac{1}{2}\left(\vec{u}(t) - \bar{u}(t)\right)^T \tilde{Q}(t)^{-1}\left(\vec{u}(t) - \bar{u}(t)\right) \tag{3.3}$$

In practice the assumed control has an expectation of zero for all time, meaning we assume no extra dynamics are needed on top of our assumed dynamical model (i.e. assume the dynamics are properly modeled). The weighting associated with this cost ($\tilde{Q}(t) \in \mathbb{R}^{m\times m}$) is defined in the following definition along with the statistical properties of the other inputs into the system.

Definition 3.1 (Stochastic Inputs): The values $\bar{x}_{k-1|k-1}$, $\vec{Y}_k$, and $\bar{u}(t)$ are inputs that are functions of the random variables $\vec{\eta}_{k-1|k-1}$, $\vec{\epsilon}_k$, and $\vec{w}(t)$ as shown in the following expressions. The asterisk superscript indicates values on the true trajectory.

$$\begin{aligned} \bar{x}_{k-1|k-1} &= \vec{x}^*_{k-1} + \vec{\eta}_{k-1|k-1} \\ \vec{Y}_k &= h(t_k, \vec{x}^*_k) + \vec{\epsilon}_k \\ \bar{u}(t) &= \vec{u}^*(t) + \vec{w}(t) \end{aligned} \tag{3.4}$$

These random variables are drawn from distributions defined with the following properties. Each is zero mean with the following defined covariances (we do not specify higher order moments at this point).

$$\begin{aligned} E[\vec{\eta}_{k-1|k-1}] &= \vec{0} \\ E[\vec{\epsilon}_k] &= \vec{0} \\ E[\vec{w}(t)] &= \vec{0};\ t \in [t_{k-1}, t_k] \end{aligned} \tag{3.5}$$

$$\begin{aligned} E\left[\vec{\eta}_{k-1|k-1}\vec{\eta}^T_{k-1|k-1}\right] &= \bar{P}_{k-1|k-1} \\ E\left[\vec{\epsilon}_k\vec{\epsilon}^T_k\right] &= R_k \\ E\left[\vec{w}(t)\vec{w}(\tau)^T\right] &= \tilde{Q}(t)\delta(t-\tau);\ t,\tau \in [t_{k-1}, t_k] \end{aligned} \tag{3.6}$$

■

As a note the assumed dynamic uncertainty ($\tilde{Q}(t)$) is not exactly a covariance in the dynamics. The presence of the Dirac delta function in its definition scales a quantity of units $\vec{w}(t)\vec{w}(t)^T$ by a time unit. This is very similar to a process noise term, and should be selected in a similar manner. Metrics that can be used to see if this value is set properly include measurement residuals and the distance metrics discussed in Chapter 5. The value is adjusted until the selected metric no longer is an outlier (according to the qualifications of the user). Care should be exercised when selecting this value such that it does not over compensate for the mismodeled dynamics. To accomplish this with measurement residuals, the user should select the value such that the residual is pushed just below the outlier threshold, and for the OCBE distance metrics an automated method is discussed in Chapter 6. By dividing the matrix by the observation gap time difference we can obtain an approximate average covariance in the dynamics (order of magnitude mismodeling in the dynamical model).

The cost function is designed as a weighted least squares where the weightings are the covariances of the stochastic inputs. This definition results in useful estimation properties as will be discussed in the BL-OCBE section. Through Definition 3.1 we are making the assumption that the inputs are unbiased - meaning we assume that the a priori state, measurement, and dynamics represent truth. These assumptions are validated or invalidated through the distance metric hypothesis testing. Details on this are provided in Chapter 5.

It should be noted that the a priori state estimate is the best estimate at time t_{k-1} given information through time t_{k-1}. As such the following notational equivalencies exist: $\hat{x}_{k-1|k-1} = \bar{x}_{k-1|k-1}$ and $\hat{P}_{k-1|k-1} = \bar{P}_{k-1|k-1}$. This equivalence is important to the smoothing discussion later on in section 3.5.

Having defined the inputs into the algorithm (t_{k-1}, $\bar{x}_{k-1|k-1}$, $\bar{P}_{k-1|k-1}$, t_k, $\vec{Y}_k$, R_k, $\bar{u}(t)$, and $\tilde{Q}(t)$), and the cost function they are involved with the next task is to apply the necessary conditions for optimality to obtain a solution for the outputs. In doing this we will create the nonlinear OCBE.

3.2 The Nonlinear OCBE

The nonlinear OCBE is defined as the nonlinear solution that minimizes the cost function defined in the previous subsection. Our outputs include: 1) $\hat{x}_{k-1|k}$ the best estimate of the state at the a priori epoch given information through the measurement epoch, $\hat{x}_{k|k}$ the best estimate of the state at the measurement epoch given information through the measurement epoch, and $\hat{u}(t)$ the best estimate of mismodeled dynamics in the form of an optimal control policy. In the next two subsections we will develop the equations defining this nonlinear estimator, and then provide a proof of existence of that solution.

3.2.1 Equations of the Nonlinear OCBE

Having defined the cost function of interest, we may now proceed with applications of the necessary conditions for optimality in order to obtain the equations of the OCBE. As discussed, the cost function is written to be nonlinear, thus the resulting estimator equations should be nonlinear as well.

Optimization is accomplished through application of the necessary conditions. Applying the transversality conditions (specifically Eqs. 2.8 and 2.10) to the cost function of interest we obtain the results of Eqs. 3.7 and 3.8, respectively.

$$\hat{p}_{k-1|k} = -\left.\frac{\partial K_{k-1}}{\partial \vec{x}_{k-1}}\right|^{T}_{(t_{k-1},\hat{x}_{k-1})} = \bar{P}^{-1}_{k-1|k-1}\left(\bar{x}_{k-1|k-1} - \hat{x}_{k-1|k}\right) \tag{3.7}$$

$$\hat{p}_{k|k} = \left.\frac{\partial K_{k}}{\partial \vec{x}_{k}}\right|^{T}_{(t_{k},\hat{x}_{k})} = -\left.\frac{\partial h}{\partial \vec{x}_{k}}\right|^{T}_{(t_{k},\hat{x}_{k|k})} R_k^{-1}\left(\vec{Y}_k - h(t_k, \hat{x}_{k|k})\right) \tag{3.8}$$

Next, applying the Pontryagin Minimum Principle (Eq. 2.4) we can obtain an expression for the optimal control policy in terms of the system's adjoint (Eq. 3.9).

$$\hat{u}(t) = -\tilde{Q}(t)B(t)^T\hat{p}(t) + \bar{u}(t) \tag{3.9}$$

It should be noted that if the system is affine in the control, then this equation is state independent and explicit. This is not a requirement for this method, but it simplifies the notation so we will assume this for now on. Finally, the solution flow equations (Eqs. 3.10 and 3.11) are simply obtained as defined previously.

$$\hat{x}_{k|k} = \phi_x(t_k; t_{k-1}, \hat{x}_{k-1|k}, \hat{p}_{k-1|k}) \tag{3.10}$$

$$\hat{p}_{k|k} = \phi_p(t_k; t_{k-1}, \hat{x}_{k-1|k}, \hat{p}_{k-1|k}) \tag{3.11}$$

As a consequence of the Pontryagin Minimum Principle, state and adjoint trajectories are merely functions of initial conditions in the state and adjoint, thus control is not considered an input parameter. However, the assumed control ($\bar{u}(t)$) is an input into these trajectory propagations. This is not a function of any outputs, though, so we do not need to explicitly address it other than addressing the uncertainty it propagates into the state and adjoint trajectories and possibly its deterministic effects (if it selected to be anything other then a zero mean process).

These results may be rearranged in a manner, such that the optimized variables $\hat{x}_{k-1|k}$, $\hat{x}_{k|k}$, and $\hat{p}_{k-1|k}$ must be selected to satisfy certain implicit functions. This result is summarized in the following definition.

Definition 3.2 (Necessary Conditions for Optimal Solution): Given inputs t_{k-1}, $\bar{x}_{k-1|k-1}$, $\bar{P}_{k-1|k-1}$, t_k, $\vec{Y}_k$, R_k, $h(t,\vec{x})$, $\bar{u}(t)$, and $\tilde{Q}(t)$ as defined in Definition 3.1, the OCBE is the estimator that minimizes the cost function defined below.

$$\begin{aligned}\mathcal{J}\left(\vec{x}_{k-1}, \vec{x}_k, \vec{u}(t)\right) =& \frac{1}{2}\left(\bar{x}_{k-1|k-1} - \vec{x}_{k-1}\right)^T \bar{P}_{k-1|k-1}^{-1}\left(\bar{x}_{k-1|k-1} - \vec{x}_{k-1}\right) \\ &+ \frac{1}{2}\left(\vec{Y}_k - h(t_k, \vec{x}_k)\right)^T R_k^{-1}\left(\vec{Y}_k - h(t_k, \vec{x}_k)\right) \\ &+ \int_{t_{k-1}}^{t_k} \frac{1}{2}\left(\vec{u}(\tau) - \bar{u}(\tau)\right)^T \tilde{Q}(\tau)^{-1}\left(\vec{u}(\tau) - \bar{u}(\tau)\right) d\tau\end{aligned} \tag{3.12}$$

Where the state dynamics are constrained to the form: $\dot{\vec{x}}(t) = f(t, \vec{x}(t), \vec{u}(t))$. A solution that minimizes this cost function has the following necessary conditions for optimality. In these definitions the control is not explicitly indicated as the optimal solution is a function of the adjoint via the results of the Pontryagin Minimum Principle (Eq. 3.9).

$$\vec{F}_1(\hat{x}_{k-1|k}, \hat{x}_{k|k}, \hat{p}_{k-1|k}) = \phi_p(t_k; t_{k-1}, \hat{x}_{k-1|k}, \hat{p}_{k-1|k}) + \left.\frac{\partial h}{\partial \vec{x}_k}\right|_{(t_k, \hat{x}_{k|k})}^T R_k^{-1}\left(\vec{Y}_k - h(t_k, \hat{x}_{k|k})\right) = \vec{0} \tag{3.13}$$

$$\vec{F}_2(\hat{x}_{k-1|k}, \hat{x}_{k|k}, \hat{p}_{k-1|k}) = \hat{p}_{k-1|k} - \bar{P}_{k-1|k-1}^{-1}\left(\bar{x}_{k-1|k-1} - \hat{x}_{k-1|k}\right) = \vec{0} \tag{3.14}$$

$$\vec{F}_3(\hat{x}_{k-1|k}, \hat{x}_{k|k}, \hat{p}_{k-1|k}) = \hat{x}_{k|k} - \phi_x(t_k; t_{k-1}, \hat{x}_{k-1|k}, \hat{p}_{k-1|k}) = \vec{0} \tag{3.15}$$

■

These three equations define the nonlinear OCBE. A comprehensive treatment of the uncertainty associated with the resulting estimates will not be provided here in order to preserve generality in the state dynamics and the state-observation relationship. Instead, uncertainties will be obtained via linearization of the estimator. First, however, an overview of solution existence is provided in following section.

3.2.2 Existence of a Solution

Having defined the necessary conditions on a solution of this optimization problem we now analyze the existence of such a solution in the following theorem and proof.

Theorem 3.1 (OCBE Solution Existence): The implicit functions defining the nonlinear solution to this optimization problem (Eqs. 3.13 - 3.15) are invertible, and a solution exists for a system with arbitrary inputs.

Proof: Equations 3.13-3.15 are a set of implicit functions with inputs t_{k-1}, $\bar{x}_{k-1|k-1}$, $\bar{P}_{k-1|k-1}$, t_k, $\vec{Y}_k$, R_k, $\bar{u}(t)$, and $Q(t)$ and outputs $\hat{p}_{k-1|k}$, $\hat{x}_{k-1|k}$, and $\hat{x}_{k|k}$. Through the Implicit Function Theorem we know that a solution to this nonlinear problem exists if we can solve for linear variations $\delta\hat{x}_{k-1|k}$, $\delta\hat{x}_{k|k}$, and $\delta\hat{p}_{k-1|k}$ about any arbitrary point. As such we will linearize these implicit relations about this arbitrary solution, and solve for the variations to determine requirements for existence.

Furthermore, it is obvious from Eqs. 3.14 and 3.15 that if a solution to $\hat{x}_{k-1|k}$ exists, then solutions to $\hat{x}_{k|k}$ and $\hat{p}_{k-1|k}$ also exist. As such we only need to worry about finding a solution for $\hat{x}_{k-1|k}$ about an arbitrary point. The other two outputs may also be set arbitrarily, but it is not required to demonstrate existence.

We start by linearizing these expressions about a nominal trajectory defined by the following arbitrary initial state and adjoint: $\tilde{x}_{k-1}$ and $\tilde{p}_{k-1}$. We will specify the nominal state and adjoint trajectories as such: $\tilde{x}(t) = E\left[\phi_x(t; t_{k-1}, \tilde{x}_{k-1}, \tilde{p}_{k-1})\right]$ and $\tilde{p}(t) = E\left[\phi_p(t; t_{k-1}, \tilde{x}_{k-1}, \tilde{p}_{k-1})\right]$. Furthermore, we specifically define the nominal state and adjoint at the final time as $\tilde{x}_k = \tilde{x}(t_k)$ and

$\tilde{p}_k = \tilde{p}(t_k)$, respectively. This linearization process is shown in Eqs. 3.16-3.18.

$$\begin{aligned}\vec{F}_1(\hat{x}_{k-1|k}, \hat{x}_{k|k}, \hat{p}_{k-1|k}) \approx{} & \vec{F}_1(\tilde{x}_{k-1}, \tilde{x}_k, \tilde{p}_{k-1}) + \left.\frac{\partial \vec{F}_1}{\partial \hat{x}_{k-1|k}}\right|_{(\tilde{x}_{k-1},\tilde{x}_k,\tilde{p}_{k-1})} \delta\hat{x}_{k-1|k} \\ & + \left.\frac{\partial \vec{F}_1}{\partial \hat{x}_{k|k}}\right|_{(\tilde{x}_{k-1},\tilde{x}_k,\tilde{p}_{k-1})} \delta\hat{x}_{k|k} + \left.\frac{\partial \vec{F}_1}{\partial \hat{p}_{k-1|k}}\right|_{(\tilde{x}_{k-1},\tilde{x}_k,\tilde{p}_{k-1})} \delta\hat{p}_{k-1|k} = \vec{0}\end{aligned} \tag{3.16}$$

$$\begin{aligned}\vec{F}_2(\hat{x}_{k-1|k}, \hat{x}_{k|k}, \hat{p}_{k-1|k}) \approx{} & \vec{F}_2(\tilde{x}_{k-1}, \tilde{x}_k, \tilde{p}_{k-1}) + \left.\frac{\partial \vec{F}_2}{\partial \hat{x}_{k-1|k}}\right|_{(\tilde{x}_{k-1},\tilde{x}_k,\tilde{p}_{k-1})} \delta\hat{x}_{k-1|k} \\ & + \left.\frac{\partial \vec{F}_2}{\partial \hat{x}_{k|k}}\right|_{(\tilde{x}_{k-1},\tilde{x}_k,\tilde{p}_{k-1})} \delta\hat{x}_{k|k} + \left.\frac{\partial \vec{F}_2}{\partial \hat{p}_{k-1|k}}\right|_{(\tilde{x}_{k-1},\tilde{x}_k,\tilde{p}_{k-1})} \delta\hat{p}_{k-1|k} = \vec{0}\end{aligned} \tag{3.17}$$

$$\begin{aligned}\vec{F}_3(\hat{x}_{k-1|k}, \hat{x}_{k|k}, \hat{p}_{k-1|k}) \approx{} & \vec{F}_3(\tilde{x}_{k-1}, \tilde{x}_k, \tilde{p}_{k-1}) + \left.\frac{\partial \vec{F}_3}{\partial \hat{x}_{k-1|k}}\right|_{(\tilde{x}_{k-1},\tilde{x}_k,\tilde{p}_{k-1})} \delta\hat{x}_{k-1|k} \\ & + \left.\frac{\partial \vec{F}_3}{\partial \hat{x}_{k|k}}\right|_{(\tilde{x}_{k-1},\tilde{x}_k,\tilde{p}_{k-1})} \delta\hat{x}_{k|k} + \left.\frac{\partial \vec{F}_3}{\partial \hat{p}_{k-1|k}}\right|_{(\tilde{x}_{k-1},\tilde{x}_k,\tilde{p}_{k-1})} \delta\hat{p}_{k-1|k} = \vec{0}\end{aligned} \tag{3.18}$$

Evaluating the partial derivatives in these linearizations we obtain the results of Eqs. 3.19-3.21 given the definitions in Eqs. 3.22-3.26.

$$\begin{aligned}\left(\tilde{p}_k + \vec{v}_p(t_k) + \tilde{H}_k^T R_k^{-1} \delta\vec{y}_k\right) + \Phi_{px}\delta\hat{x}_{k-1|k} - \tilde{H}_k^T R_k^{-1} \tilde{H}_k \delta\hat{x}_{k|k} \\ + \Phi_{pp}\delta\hat{p}_{k-1|k} = \vec{0}\end{aligned} \tag{3.19}$$

$$\left(\tilde{p}_{k-1} - \bar{P}^{-1}_{k-1|k-1}\delta\bar{x}_{k-1|k-1}\right) + \bar{P}^{-1}_{k-1|k-1}\delta\hat{x}_{k-1|k} + \delta\hat{p}_{k-1|k} = \vec{0} \tag{3.20}$$

$$-\vec{v}_x(t_k) - \Phi_{xx}\delta\hat{x}_{k-1|k} + \delta\hat{x}_{k|k} - \Phi_{xp}\delta\hat{p}_{k-1|k} = \vec{0} \tag{3.21}$$

$$\delta\vec{y}_k = \vec{Y}_k - h(t_k, \tilde{x}_k) \tag{3.22}$$

$$\delta\bar{x}_{k-1|k-1} = \bar{x}_{k-1|k-1} - \tilde{x}_{k-1} \tag{3.23}$$

$$\tilde{H}_k = \left.\frac{\partial h}{\partial \vec{x}}\right|_{(t_k,\tilde{x}_k)} \tag{3.24}$$

$$\vec{v}_x(t) = \phi_x(t; t_{k-1}, \tilde{x}_{k-1}, \tilde{p}_{k-1}) - E\left[\phi_x(t; t_{k-1}, \tilde{x}_{k-1}, \tilde{p}_{k-1})\right] \tag{3.25}$$

$$\vec{v}_p(t) = \phi_p(t; t_{k-1}, \tilde{x}_{k-1}, \tilde{p}_{k-1}) - E\left[\phi_p(t; t_{k-1}, \tilde{x}_{k-1}, \tilde{p}_{k-1})\right] \tag{3.26}$$

It should be noted that the term involving the second derivative of the observation state relationship ($\partial^2 h/\partial \vec{x}^2$) is not included in this linearization because it contains $\delta\tilde{y}_k \cdot \delta\hat{x}_{k|k}$, which is a second order term that we assume to be zero for this linearized system. It should also be noted that the time arguments for portions of the STM are excluded for convenience. When they are excluded it is implied that it is evaluated from t_{k-1} to t_k. The $\vec{v}_x$ and $\vec{v}_p$ terms account for the stochastic nature of the solution flow.

Rearranging these equations we solve for the optimal estimate of the state at the a priori epoch as shown in Eq. 3.27.

$$\begin{aligned} \delta\hat{x}_{k-1|k} = &\left[\left(\Phi_{px} - \tilde{H}_k^T R_k^{-1}\tilde{H}_k\Phi_{xx}\right) - \left(\Phi_{pp} - \tilde{H}_k^T R_k^{-1}\tilde{H}_k\Phi_{xp}\right)\bar{P}_{k-1|k-1}^{-1}\right]^{-1} \\ &\times\left[\left(\Phi_{pp} - \tilde{H}_k^T R_k^{-1}\tilde{H}_k\Phi_{xp}\right)\left(\tilde{p}_{k-1} - \bar{P}_{k-1|k-1}^{-1}\delta\bar{x}_{k-1|k-1}\right)\right. \\ &\left.-\left[\tilde{p}_k + \vec{v}_p(t_k) + \tilde{H}_k^T R_k^{-1}\left(\delta\tilde{y}_k - \tilde{H}_k\vec{v}_x(t_k)\right)\right]\right] \end{aligned} \tag{3.27}$$

Further rearranging this solution through application of the Schur Identity results in the solution defined in Eqs. 3.28 - 3.31

$$\begin{aligned} \delta\hat{x}_{k-1|k} = &\left[I + \bar{P}_{k-1|k-1}\left(\Phi_{pp} - \Phi_{px}\bar{P}_{k-1|k-1}\right)^{-1}\Phi_{px}\right]\delta\bar{x}_{k-1|k-1} + L_{k-1}\left[\delta\tilde{y}_k - \tilde{H}_k\left(\delta\bar{x}_{k|k-1} + \vec{v}_x(t_k)\right)\right] \\ &+\left[\bar{P}_{k-1|k-1}\left(\Phi_{xx}\bar{P}_{k-1|k-1} - \Phi_{xp}\right)^{-1} - L_{k-1}\tilde{H}_k\right]\mathcal{P}_{k|k-1}\left(\tilde{p}_k + \vec{v}_p(t_k)\right) \\ &-\left[I + \bar{P}_{k-1|k-1}\left(\Phi_{pp} - \Phi_{px}\bar{P}_{k-1|k-1}\right)^{-1}\Phi_{px} - L_{k-1}\tilde{H}_k\left(\Phi_{xx} + \mathcal{P}_{k|k-1}\Phi_{px}\right)\right]\bar{P}_{k-1|k-1}\tilde{p}_{k-1} \end{aligned} \tag{3.28}$$

$$L_{k-1} = \left(\Phi_{pp}\bar{P}_{k-1|k-1}^{-1} - \Phi_{px}\right)^{-1}\tilde{H}_k^T\left(R_k + \tilde{H}_k\mathcal{P}_{k|k-1}\tilde{H}_k^T\right)^{-1} \tag{3.29}$$

$$\delta\bar{x}_{k|k-1} = \left(\Phi_{xx} + \mathcal{P}_{k|k-1}\Phi_{px}\right)\delta\bar{x}_{k-1|k-1} \tag{3.30}$$

$$\mathcal{P}_{k|k-1} = \left(\Phi_{xx}\bar{P}_{k-1|k-1} - \Phi_{xp}\right)\left(\Phi_{pp} - \Phi_{px}\bar{P}_{k-1|k-1}\right)^{-1} \tag{3.31}$$

Existence of this solution requires that the three matrices shown below are nonsingular in addition to the matrices that are defined to be nonsingular in the problem statement (e.g. R_k,

$\bar{P}_{k-1|k-1}$, and $\tilde{Q}(t)$).

$$\left|R_k + \tilde{H}_k \mathcal{P}_{k|k-1} \tilde{H}_k^T\right| \neq 0$$

$$\left|\Phi_{pp} - \Phi_{px} \bar{P}_{k-1|k-1}\right| \neq 0$$

$$\left|\Phi_{xx} \bar{P}_{k-1|k-1} - \Phi_{xp}\right| \neq 0$$

The first matrix is invertible under the condition that $\mathcal{P}_{k|k-1}$ is symmetric positive definite. This is because the first term is symmetric positive definite by construction, and the second term is at least semi-positive definite with this condition, thus the sum may be easily shown to be symmetric positive definite. The next two matrices are used to calculate $\mathcal{P}_{k|k-1}$ in a way that they both are invertible if $\mathcal{P}_{k|k-1}$ is invertible. As such, proving arbitrary solution existence only requires demonstrating $\mathcal{P}_{k|k-1}$ is a symmetric positive definite matrix.

To demonstrate that this matrix is symmetric positive definite we express it as a function with the measurement time as the dependent variable t.

$$\mathcal{P}(t|t_{k-1}) = \left(\Phi_{xx}(t,t_{k-1})\bar{P}_{k-1|k-1} - \Phi_{xp}(t,t_{k-1})\right)\left(\Phi_{pp}(t,t_{k-1}) - \Phi_{px}(t,t_{k-1})\bar{P}_{k-1|k-1}\right)^{-1} \tag{3.32}$$

Taking the derivative of this expression, we obtain its dynamical equation as shown below.

$$\begin{aligned}\dot{\mathcal{P}}(t|t_{k-1}) =& A_{xx}(t)\mathcal{P}(t|t_{k-1}) + \mathcal{P}(t|t_{k-1})A_{xx}(t)^T \\ &+ B(t)\tilde{Q}(t)B(t)^T + \mathcal{P}(t|t_{k-1})A_{px}(t)\mathcal{P}(t|t_{k-1})\end{aligned} \tag{3.33}$$

This dynamical equation is identical to a matrix Ricatti differential equation. Futhermore, we know its initial condition via Eq. 3.32 ($\mathcal{P}(t|t_{k-1}) = \bar{P}_{k-1|k-1}$). As the solution to a matrix Riccati equation with a symmetric matrix for an initial condition, $\mathcal{P}(t|t_{k-1})$ is guaranteed to be symmetric for all time. Given the initial condition is positive definite, and $\tilde{Q}(t)$ also has this requirement, $\mathcal{P}(t|t_{k-1})$ is also guaranteed to be a positive definite matrix for all time beyond t_{k-1} [14]. Having proven this property, we have proven solution existence for arbitrary inputs. ■

To this point we have derived the Nonlinear OCBE, and demonstrated its existence given certain conditions. In its implicit formulation there is no analytical solution for the estimates or their uncertainties. To find an analytical solution, we will derive a linear version of the estimator in the following section.

3.3 The Generalized Linear OCBE

With no analytical solution to the Nonlinear OCBE, a linearized version of the estimator provides a means to solve the necessary equations and calculate the uncertainty on the estimates. The GL-OCBE is a version of the OCBE linearized about an arbitrary initial state and initial adjoint with nominal trajectories defined in Theorem 3.1. As such, this linear estimator may be iterated until converging on the nonlinear solution. In this section we summarize this estimator and analyze the terms within it. A derivation of the GL-OCBE is provided in Appendices A and B.

3.3.1 Equations of the GL-OCBE

In this section we formally define the equations of the GL-OCBE including the time update equations, measurement update equations, control estimates, and the estimate uncertainties. An analysis of what these equations mean and how they operate is provided in the following section.

Definition 3.3 (Generalized Linear Optimal Control Based Estimator): The linear estimator that satisfies the cost function of interest with arbitrary initial nominal state and adjoint (as defined in Theorem 3.1) satisfies the equations given in this definition.

First, Eqs. 3.34 - 3.36 define the time update step of the estimator. These defined values are referred to as the propagated a priori state, the propagated a priori state quasi-covariance, and the propagated a priori state covariance, respectively.

$$\delta\bar{x}_{k|k-1} = \left(\Phi_{xx} + \mathcal{P}_{k|k-1}\Phi_{px}\right)\delta\bar{x}_{k-1|k-1} \tag{3.34}$$

$$\mathcal{P}_{k|k-1} = \left(\Phi_{xx}\bar{P}_{k-1|k-1} - \Phi_{xp}\right)\left(\Phi_{pp} - \Phi_{px}\bar{P}_{k-1|k-1}\right)^{-1} \tag{3.35}$$

$$\dot{\bar{P}}(t|t_{k-1}) = \left[A_{xx}(t) + \mathcal{P}(t|t_{k-1})A_{px}(t)\right]\bar{P}(t|t_{k-1}) + \bar{P}(t|t_{k-1})\left[A_{xx}(t) + A_{px}(t)\mathcal{P}(t|t_{k-1})\right]^T + B(t)\tilde{Q}(t)B(t)^T \tag{3.36}$$

The latter of these equations is a dynamical equation that must be solved by integration from the a priori epoch to the measurement epoch with the a priori state covariance ($\bar{P}_{k-1|k-1}$) as the initial condition.

Next, we define the measurement update equations. These equations incorporate information from the given measurement and update the state and adjoint estimates as a result. The equations defining the state estimate at the a priori epoch ($\delta\hat{x}_{k-1|k}$) are defined in Eqs. 3.37 - 3.40. We will refer to $\mathcal{I}_{k-1}$ as the a priori OCBE state gain, L_{k-1} as the a priori OCBE innovations gain and $\tilde{b}_{k-1}$ as the a priori epoch state biasing term.

$$\delta\hat{x}_{k-1|k} = \mathcal{I}_{k-1}\left(\delta\bar{x}_{k-1|k-1} + \tilde{b}_{k-1}\right) + L_{k-1}\left[\delta\vec{y}_k - \tilde{H}_k\left(\delta\bar{x}_{k|k-1} + \tilde{b}_k + \vec{v}_x(t_k|t_{k-1})\right)\right] \tag{3.37}$$

$$\mathcal{I}_{k-1} = I_{n\times n} + \bar{P}_{k-1|k-1}\left(\Phi_{pp} - \Phi_{px}\bar{P}_{k-1|k-1}\right)^{-1}\Phi_{px} \tag{3.38}$$

$$L_{k-1} = \left(\Phi_{pp}\bar{P}^{-1}_{k-1|k-1} - \Phi_{px}\right)^{-1}\tilde{H}_k^T\left(R_k + \tilde{H}_k\mathcal{P}_{k|k-1}\tilde{H}_k^T\right)^{-1} \tag{3.39}$$

$$\tilde{b}_{k-1} = \bar{P}_{k-1|k-1}\left[\Phi_{pp}^{-1}\left(\tilde{p}_k + \vec{v}_p(t_k|t_{k-1})\right) - \tilde{p}_{k-1}\right] \tag{3.40}$$

Equations 3.41 - 3.43 define the state estimate at the measurement epoch ($\delta\hat{x}_{k|k}$). We will refer to L_k as the OCBE gain and $\tilde{b}_k$ as the measurement epoch state biasing term.

$$\delta\hat{x}_{k|k} = \left(\delta\bar{x}_{k|k-1} + \tilde{b}_k + \vec{v}_x(t_k|t_{k-1})\right) + L_k\left[\delta\vec{y}_k - \tilde{H}_k\left(\delta\bar{x}_{k|k-1} + \tilde{b}_k + \vec{v}_x(t_k|t_{k-1})\right)\right] \tag{3.41}$$

$$L_k = \mathcal{P}_{k|k-1}\tilde{H}_k^T\left(R_k + \tilde{H}_k\mathcal{P}_{k|k-1}\tilde{H}_k^T\right)^{-1} \tag{3.42}$$

$$\tilde{b}_k = \mathcal{P}_{k|k-1}\left(\tilde{p}_k + \vec{v}_p(t_k|t_{k-1})\right) - \left(\Phi_{xx} + \mathcal{P}_{k|k-1}\Phi_{px}\right)\bar{P}_{k-1|k-1}\tilde{p}_{k-1} \tag{3.43}$$

Equations 3.44 - 3.46 define the adjoint ($\delta\hat{p}_{k-1|k}$) and control estimates ($\delta\hat{u}(t)$). $\tilde{u}(t)$ is the nominal control trajectory that the control estimate is with respect to.

$$\delta\hat{p}_{k-1|k} = \bar{P}^{-1}_{k-1|k-1}\left(\delta\bar{x}_{k-1|k-1} - \delta\hat{x}_{k-1|k}\right) - \tilde{p}_{k-1|k} \tag{3.44}$$

$$\begin{aligned}\delta\hat{u}(t) = &\left[\vec{w}(t) - \tilde{Q}(t)B(t)^T\left(\vec{v}_p(t|t_{k-1}) - \Phi_{pp}(t,t_{k-1})\tilde{p}_{k-1}\right)\right] \\ &- \tilde{Q}(t)B(t)^T\left[\left(\Phi_{px}(t,t_{k-1}) - \Phi_{pp}(t,t_{k-1})\bar{P}^{-1}_{k-1|k-1}\right)\delta\hat{x}_{k-1|k} + \Phi_{pp}(t,t_{k-1})\bar{P}^{-1}_{k-1|k-1}\delta\bar{x}_{k-1|k-1}\right]\end{aligned} \tag{3.45}$$

$$\tilde{u}(t) = -\tilde{Q}(t)B(t)^T E\left[\phi_p(t;t_{k-1},\tilde{x}_{k-1},\tilde{p}_{k-1})\right] + E\left[\bar{u}(t)\right] \tag{3.46}$$

Finally, the covariances of the state estimates at the a priori and measurement epochs are defined in Eqs. 3.47 and 3.48, respectively.

$$\begin{aligned}\hat{P}_{k-1|k} =& \mathcal{I}_{k-1}\bar{P}_{k-1|k-1}\mathcal{I}^T_{k-1} + L_{k-1}\left(R_k + \tilde{H}_k\bar{P}_{k|k-1}\tilde{H}^T_k\right)L^T_{k-1} \\ &+ \mathcal{I}_{k-1}\bar{P}_{k-1|k-1}\Phi^{-1}_{pp}\left(\int_{t_{k-1}}^{t}\Phi_{px}(t,\tau)B(\tau)\tilde{Q}(\tau)B(\tau)^T\Phi_{px}(t,\tau)^T d\tau\right)\Phi^{-T}_{pp}\bar{P}_{k-1|k-1}\mathcal{I}^T_{k-1} \\ &- \mathcal{I}_{k-1}\bar{P}_{k-1|k-1}\left[\Phi_{xx} + \mathcal{P}_{k|k-1}\Phi_{px}\right]^T\tilde{H}^T_k L^T_{k-1} - L_{k-1}\tilde{H}_k\left[\Phi_{xx} + \mathcal{P}_{k|k-1}\Phi_{px}\right]\bar{P}_{k-1|k-1}\mathcal{I}^T_{k-1} \\ &- \mathcal{I}_{k-1}\bar{P}_{k-1|k-1}\Phi^{-1}_{pp}\left[\int_{t_{k-1}}^{t}\Phi_{px}(t,\tau)B(\tau)\tilde{Q}(\tau)B(\tau)^T\Phi_{px}(t,\tau)^T d\tau\mathcal{P}_{k|k-1}\right]\tilde{H}^T_k L^T_{k-1} \\ &- \mathcal{I}_{k-1}\bar{P}_{k-1|k-1}\Phi^{-1}_{pp}\left[\int_{t_{k-1}}^{t}\Phi_{px}(t,\tau)B(\tau)\tilde{Q}(\tau)B(\tau)^T\Phi_{xx}(t,\tau)^T d\tau\right]\tilde{H}^T_k L^T_{k-1} \\ &- L_{k-1}\tilde{H}_k\left[\mathcal{P}_{k|k-1}\int_{t_{k-1}}^{t}\Phi_{px}(t,\tau)B(\tau)\tilde{Q}(\tau)B(\tau)^T\Phi_{px}(t,\tau)^T d\tau\right]\Phi^{-T}_{pp}\bar{P}_{k-1|k-1}\mathcal{I}^T_{k-1} \\ &- L_{k-1}\tilde{H}_k\left[\int_{t_{k-1}}^{t}\Phi_{xx}(t,\tau)B(\tau)\tilde{Q}(\tau)B(\tau)^T\Phi_{px}(t,\tau)^T d\tau\right]\Phi^{-T}_{pp}\bar{P}_{k-1|k-1}\mathcal{I}^T_{k-1}\end{aligned} \tag{3.47}$$

$$\hat{P}_{k|k} = \left(I - L_k\tilde{H}_k\right)\bar{P}_{k|k-1}\left(I - L_k\tilde{H}_k\right)^T + L_k R_k L^T_k \tag{3.48}$$

The covariance of the control estimate is also defined in Appendix B (Eq. B.38). ∎

This fully defines the GL-OCBE. All linear estimates are taken with respect to the nominal state and adjoint trajectories as defined in Theorem 3.1. In the next section, an analysis and discussion of these equations is provided in order to promote a fuller understanding of how this estimator operators.

3.3.2 Analysis of GL-OCBE

As defined in Definition 3.3, the GL-OCBE has a somewhat similar form to a Kalman Filter, but it also has many additional terms. In this section we will focus on what these terms mean, and what their purposes are.

Starting with the time update, the form of the propagated a priori state is quite different than what is seen in a Kalman Filter. It includes an additional term to account for the non-zero adjoint term. The propagated a priori quasi-covariance is covered in detail in Appendix B. This matrix is symmetric positive definite and has a very similar dynamical equation to the true covariance, but the nonzero nominal adjoint introduces slight differences. These two matrices are actually identical for a ballistic nominal adjoint (as discussed in the BL-OCBE development).

In the calculation of the propagated a priori state covariance there are two random variables that have not been fully analyzed - $\vec{v}_x(t_k)$ and $\vec{v}_p(t_k)$. These were defined in Theorem 3.1, but this definition did not include a discussion of their stochastic properties. Both values are zero mean by definition, but their covariances are not easily determined due to the nonlinear nature of the solution flow equations. Given this is a linearization of the nonlinear OCBE, we also linearize these random variables. The linearization of the equations of motion are given below with the solution given in Eq. 3.50.

$$\begin{aligned}\delta\dot{\phi}_x(t) &= \dot{\phi}_x(t;t_{k-1},\vec{x}_{k-1},\vec{p}_{k-1}) - \dot{\vec{x}}(t) \approx A_{xx}(t)\delta\vec{x}(t) + A_{xp}(t)\delta\vec{p}(t) + B(t)\vec{w}(t) \\ \delta\dot{\phi}_p(t) &= \dot{\phi}_p(t;t_{k-1},\vec{x}_{k-1},\vec{p}_{k-1}) - \dot{\vec{p}}(t) \approx A_{px}(t)\delta\vec{x}(t) + A_{pp}(t)\delta\vec{p}(t)\end{aligned} \tag{3.49}$$

$$\begin{aligned}\delta\phi_x(t) &= \Phi_{xx}(t,t_{k-1})\delta\vec{x}_{k-1} + \Phi_{xp}(t,t_{k-1})\delta\vec{p}_{k-1} + \int_{t_{k-1}}^{t}\Phi_{xx}(t,\tau)B(\tau)\vec{w}(\tau)d\tau \\ \delta\phi_p(t) &= \Phi_{px}(t,t_{k-1})\delta\vec{x}_{k-1} + \Phi_{pp}(t,t_{k-1})\delta\vec{p}_{k-1} + \int_{t_{k-1}}^{t}\Phi_{px}(t,\tau)B(\tau)\vec{w}(\tau)d\tau\end{aligned} \tag{3.50}$$

Because the solution flow and the nominal trajectory have identical initial conditions the $\delta\vec{x}_{k-1}$ and $\delta\vec{p}_{k-1}$ are both zero, thus we define the random variables $\vec{v}_x(t)$ and $\vec{v}_p(t)$ solely in terms of the random acceleration as shown below.

$$\begin{aligned}\vec{v}_x(t|t_{k-1}) &= \int_{t_{k-1}}^{t}\Phi_{xx}(t,\tau)B(\tau)\vec{w}(\tau)d\tau \\ \vec{v}_p(t|t_{k-1}) &= \int_{t_{k-1}}^{t}\Phi_{px}(t,\tau)B(\tau)\vec{w}(\tau)d\tau\end{aligned} \tag{3.51}$$

When evaluated at t_k, these values are abbreviated as $\vec{v}_x(t_k)$ and $\vec{v}_p(t_k)$, respectively. Knowing these values we may calculate the propagated a priori state covariance. This calculation is done in Appendix B.

The measurement update equations all have similar forms to the Kalman Filter as well. The state estimate at the measurement epoch has the exact same form - the propagated a priori state added to the filter innovations that are weighted by a gain matrix. The differences include the terms added to the propagated a priori state and the form of the gain matrix. Unlike the Kalman filter the propagated a priori state is combined with a biasing term ($\tilde{b}_k$) and a state propagation error term ($\vec{v}_x(t_k)$). The biasing term represents assumed dynamic mismodeling due to a nonzero nominal adjoint. Making the assumption that the OCBE is an unbiased estimator means that this biasing term makes the adjustments to the propagated a priori state to ensure that it is not biased due to mismodeled dynamics (Eq. 3.52).

$$\begin{aligned} \delta\vec{x}_k^* =& E\left[\delta\hat{x}_{k|k}\right] \\ =& E\left[\delta\bar{x}_{k|k-1}\right] + E\left[\tilde{b}_k\right] \end{aligned} \tag{3.52}$$

The other term added to the propagated a priori state accounts for the dynamic uncertainty. It is effectively a term that accounts for process noise explicitly and automatically, rather than having to be enforced in a Kalman Filter. More details on this term are provided in the BL-OCBE discussion.

The OCBE gain is also slightly different than the Kalman Gain. It has an almost identical form, but instead of using the propagated a priori state covariance, the OCBE gain uses the propagated a priori state quasi-covariance. When these two matrices are equal the two gains are equal (assuming the Kalman gain has an equivalent amount of process noise included). This situation is discussed in the following BL-OCBE development.

Because the Kalman Filter has no state estimate at the a priori epoch it is necessary to compare the OCBE state estimate at the a priori epoch to a smoothed Kalman estimate. As with the measurement epoch estimate, if we make the assumption that the estimate is unbiased, then the biasing term is meant to account for assumed dynamic uncertainty.

$$\begin{aligned} \delta\vec{x}_{k-1}^* =& E\left[\delta\hat{x}_{k-1|k}\right] \\ =& \mathcal{I}_{k-1}\left(E\left[\delta\bar{x}_{k-1|k-1}\right] + E\left[\tilde{b}_{k-1}\right]\right) \end{aligned} \tag{3.53}$$

It should be noted that the assumption was that the a priori state estimate was also unbiased ($E\left[\delta\bar{x}_{k-1|k-1}\right] = \delta\vec{x}^*_{k-1}$). For both of these assumptions to be true we also require the following: $E\left[\tilde{b}_{k-1}\right] = \mathcal{I}^{-1}_{k-1}\left(I_{n\times n} - \mathcal{I}_{k-1}\right)\delta\vec{x}^*_{k-1}$. It is interesting to note that these combined assumptions and conditions lead to the following:

$$\delta\vec{x}^*_k = \Phi_{xx}\delta\vec{x}^*_{k-1} - \Phi_{xp}\tilde{p}_{k-1} \tag{3.54}$$

This important result tells us that our unbiased assumptions are valid. Essentially, the odd form of the propagated a priori state is effectively balanced against the biasing terms to ensure that the true states lie along the same ballistic trajectory. This is indicated by the fact that the adjoint term is equal and opposite the nominal adjoint, thus nullifying it in a linear sense. Hence the resulting truth trajectory is ballistic and continuous.

With this assumption defined, the smoothed Kalman estimate and the OCBE state estimate at the a priori epoch have similar forms. it involves the summation of the a priori state estimate and a weighted version of the innovations, which could be reformed into a more typical smoother formulation (see BL-OCBE results). Given that the Kalman Filter has nothing like a nominal adjoint trajectory, we cannot make direct claims of equivalence, but we can qualitatively say they act the same. Both estimates take information from one measurement in the future and output the state estimate that minimizes a meaningful cost - minimum variance for the Kalman Filter, and the OCBE cost function for the OCBE.

The final estimates associated with this estimator are the adjoint estimate at the a priori epoch and the control estimate. As might be expected from the result of Eq. 3.54 the true adjoint deviations according to this estimator should be equal and opposite the nominal adjoint, thus nullifying the nonlinear estimate. This is exactly what we find. The mean of the nonlinear adjoint estimate is zero leading to a zero mean control estimate, thus the estimator assumes the dynamics are properly modeled. When errors are present, though, the estimator estimates a nonzero control policy to account for dynamic mismodeling. This makes the estimator robust to these mismodelings.

Analysis of the GL-OCBE equations led to important insights. Most important is that the estimator is unbiased, the true states are assumed ballistically connected, and that the expected value of the adjoint is zero thus resulting in the ballistic trajectory. This makes sense given the form of the cost function. It penalizes deviation from a ballistic trajectory, thus it should favor this solution. In the next section we analyze a simplification of these equations known as the Ballistic Linear OCBE. This requires setting the nominal adjoint to be zero. The resulting estimator has many desirable properties that are far more explicit, since it is far more comparable to the Kalman Filter.

3.4 The Ballistic Linear OCBE

The BL-OCBE is a simplified version of the GL-OCBE that requires the nominal adjoint trajectory to be ballistic (i.e. zero for all time). Because of this, the estimator cannot be iterated to solve the nonlinear estimation problem. What is lost in nonlinearity is gained in ideal linear estimation properties, though. This section outlines this version of the OCBE and its special properties. It starts with a discussion of properties that result from linearization about a ballistic nominal trajectory. Next, the equations of the BL-OCBE are obtained by simplification of the GL-OCBE equations. Finally, we discuss the properties that make this an ideal estimator in many respects including its noise propagation properties, its smoothing properties, and its relation to the Kalman Filter.

3.4.1 Ballistic Properties

By specifying the nominal adjoint trajectory to be ballistic certain properties are obtained. The most obvious property is that the nominal adjoints are zero, thus the bias terms in the GL-OCBE are both zero and the stochastic terms within them will also be shown to be deterministically zero for this estimator. Beyond this there are some ballistic properties associated with the linearized system's STM. These properties are developed in the following Lemma and proof.

Lemma 3.1 (State Transition Matrix Quadrant Relations): When modeled about a ballistic nominal trajectory (Eq. 3.55), the four quadrants of the full state transition matrix (state and adjoint) are related as shown in Eq. 3.56 where $t, \tau \in \mathbb{R}$.

$$\begin{aligned} \tilde{x}(t) &= E\left[\phi_x(t; t_{k-1}, \tilde{x}_{k-1}, \tilde{p}_{k-1} = \vec{0})\right] \\ \tilde{p}(t) &= E\left[\phi_p(t; t_{k-1}, \tilde{x}_{k-1}, \tilde{p}_{k-1} = \vec{0})\right] = \vec{0} \end{aligned} \tag{3.55}$$

$$\begin{gathered} \Phi_{px}(t,\tau) = 0_{n\times n} \\ \Phi_{pp}(t,\tau)\Phi_{xx}(t,\tau)^T = I_{n\times n} \\ \Phi_{xp}(t,\tau)\Phi_{xx}(t,\tau)^T = \left(\Phi_{xp}(t,\tau)\Phi_{xx}(t,\tau)^T\right)^T \end{gathered} \tag{3.56}$$

Proof: Recalling Eqs. 2.14 and 2.15, we will probe the dynamics of the STM quadrants on a ballistic nominal trajectory in order to demonstrate these properties. The specific $A(t)$ matrix for the system we have defined so far is given in Eq. 3.57.

$$A(t) = \left.\begin{bmatrix} \frac{\partial \vec{f}}{\partial \vec{x}} & -B(t)\tilde{Q}(t)B(t)^T \\ -\frac{\partial^2}{\partial \vec{x}^2}\left(\vec{f}^T\vec{p}\right) & -\frac{\partial \vec{f}}{\partial \vec{x}}^T \end{bmatrix}\right|_{(t,\tilde{x}(t),\tilde{p}(t))} \tag{3.57}$$

Using these equations we can solve for $\dot{\Phi}_{px}$, which allows us to solve for the matrix for all time:

$$\dot{\Phi}_{px}(t,\tau) = -\frac{\partial^2}{\partial \vec{x}^2}\left(\vec{f}^T\vec{p}\right)\bigg|_{(t,\tilde{x}(t),\tilde{p}(t))}\Phi_{xx}(t,\tau) - \frac{\partial \vec{f}}{\partial \vec{x}}\bigg|_{(t,\tilde{x}(t))}^T\Phi_{px}(t,\tau) \tag{3.58}$$

The first term in this dynamical equation is zero for all time because the nominal adjoint is equal to zero on a ballistic trajectory, which yields Eq. 3.59. The solution to this type of ODE is given by Eq. 3.60, where the dynamics of the matrix $\Omega(t,\tau)$ are given by Eq. 3.61.

$$\dot{\Phi}_{px}(t,\tau) + \frac{\partial \vec{f}}{\partial \vec{x}}\bigg|_{(t,\tilde{x}(t))}^T\Phi_{px}(t,\tau) = 0_{n\times n} \tag{3.59}$$

$$\Phi_{px}(t,\tau) = \Omega(t,\tau)\Phi_{px}(\tau,\tau) \tag{3.60}$$

$$\dot{\Omega}(t,\tau) = -\frac{\partial \vec{f}}{\partial \vec{x}}\bigg|_{(t,\tilde{x}(t))}^T\Omega(t,\tau) \tag{3.61}$$

The initial conditions for Φ_{px} are zero since it is an off-diagonal portion of the STM ($\Phi_{px}(\tau,\tau) = 0_{n\times n}$). Thus, from Eq. 3.60 we conclude $\Phi_{px}(t,\tau) = 0_{n\times n}$, $\forall t,\tau \in \mathbb{R}$. Subbing this result into Eq.

2.16 yields the required quadrant relations. The first two of the expressions are obtained simply. The third expression in Eq. 3.56 is obtained by observing that $\Phi_{pp}(t,\tau)^T = \Phi_{xx}(t,\tau)^{-1}$. Making this substitution and rearranging yields the final desired result. ■

These STM properties lead to many simplifications in the GL-OCBE equations. The next section will present these simplified equations, which define the BL-OCBE.

3.4.2 Equations of the BL-OCBE

The equations of the BL-OCBE are obtained by applying the ballistic simplifications to the GL-OCBE equations. We also specifically specify that the inputs are Gaussian, thus fixing their higher order moments. This provides more room for comparison with the Kalman Filter.

Having defined all of the inputs into the BL-OCBE and the STM properties for ballistic nominal trajectory, we can proceed with defining the equations of the BL-OCBE. This definition is given below.

Definition 3.4 (Ballistic Linear Optimal Control Based Estimator): The linear estimator that satisfies the cost function of interest with a ballistic nominal trajectory satisfies the equations in this definition.

Equations 3.62 and 3.63 define the time update step of the estimator. The propagated the a priori state estimate and its covariance to the measurement epoch along a ballistic nominal trajectory.

$$\delta\bar{x}_{k|k-1} = \Phi_{xx}\delta\bar{x}_{k-1|k-1} \tag{3.62}$$

$$\bar{P}_{k|k-1} = \Phi_{xx}\bar{P}_{k-1|k-1}\Phi_{xx}^T - \Phi_{xp}\Phi_{xx}^T \tag{3.63}$$

Equations 3.64 and 3.65 define the state estimate at the a priori epoch.

$$\delta\hat{x}_{k-1|k} = \delta\bar{x}_{k-1|k-1} + L_{k-1}\left[\delta\vec{y}_k - \tilde{H}_k\left(\delta\bar{x}_{k|k-1} + \vec{v}_x(t_k)\right)\right] \tag{3.64}$$

$$L_{k-1} = \bar{P}_{k-1|k-1}\Phi_{xx}^T\tilde{H}_k^T\left(R_k + \tilde{H}_k\bar{P}_{k|k-1}\tilde{H}_k^T\right)^{-1} \tag{3.65}$$

Equations 3.66 and 3.67 define the state estimate at the measurement epoch.

$$\delta\hat{x}_{k|k} = \left(\delta\bar{x}_{k|k-1} + \vec{v}_x(t_k)\right) + L_k\left[\delta\vec{y}_k - \tilde{H}_k\left(\delta\bar{x}_{k|k-1} + \vec{v}_x(t_k)\right)\right] \tag{3.66}$$

$$L_k = \bar{P}_{k|k-1}\tilde{H}_k^T\left(R_k + \tilde{H}_k\bar{P}_{k|k-1}\tilde{H}_k^T\right)^{-1} \tag{3.67}$$

Equations 3.68 - 3.70 define the adjoint estimate at the a priori epoch, the control estimate, and the nominal control policy, respectively.

$$\delta\hat{p}_{k-1|k} = -\bar{P}_{k-1|k-1}^{-1}L_{k-1}\left[\delta\vec{y}_k - \tilde{H}_k\left(\delta\bar{x}_{k|k-1} + \vec{v}_x(t_k)\right)\right] \tag{3.68}$$

$$\delta\vec{u}(t) = -\tilde{Q}(t)\frac{\partial\vec{f}}{\partial u}^T\Phi_{pp}(t, t_{k-1})\delta\hat{p}_{k-1|k} + \vec{w}(t) \tag{3.69}$$

$$\tilde{u}(t) = E\left[\bar{u}(t)\right] \tag{3.70}$$

Both of these state estimates are unbiased with known covariances as shown below.

$$E(\delta\hat{x}_{k-1|k}) = E(\delta\bar{x}_{k-1|k-1}) + L_{k-1}\left(E(\delta\vec{y}_k - \tilde{H}_k\delta\bar{x}_{k|k-1})\right) = \delta\vec{x}_{k-1}^* \tag{3.71}$$

$$E(\delta\hat{x}_{k|k}) = E(\delta\bar{x}_{k|k-1}) + L_k\left(E(\delta\vec{y}_k - \tilde{H}_k\delta\bar{x}_{k|k-1})\right) = \delta\vec{x}_k^* \tag{3.72}$$

$$\hat{P}_{k-1|k} = \bar{P}_{k-1|k-1} - L_{k-1}\left(R_k + \tilde{H}_k\bar{P}_{k|k-1}\tilde{H}_k^T\right)L_{k-1}^T \tag{3.73}$$

$$\hat{P}_{k|k} = \left(I - L_k\tilde{H}_k\right)\bar{P}_{k|k-1}\left(I - L_k\tilde{H}_k\right)^T + L_kR_kL_k^T \tag{3.74}$$

Having defined the estimates and estimate uncertainties, we have fully defined the Ballistic Linear Optimal Control Based Estimator. ■

In this definition there is no $\mathcal{P}_{k|k-1}$ matrix. This is because for the BL-OCBE, this matrix is equivalent to the covariance of the propagated a priori state ($\bar{P}_{k|k-1}$). A proof of this is provided in following section along with discussions of other properties of the estimator.

3.4.3 Special Properties of the BL-OCBE

The BL-OCBE has special properties that are significant with regards to estimation theory. In this section we analyze three of those important properties. First, we discuss the propagation a priori state uncertainty in the BL-OCBE. Next, a proof relating to the smoothing properties of the estimator is provided. Finally, we draw important comparisons between the BL-OCBE and the Kalman Filter.

3.4.3.1 Noise Propagation

Without proof, in Eq. 3.63 we quantified the uncertainty of the propagated a priori state deviation effectively equating $\mathcal{P}_{k|k-1}$ and $\bar{P}_{k|k-1}$. In this section we provide proof for this statement, and demonstrate that this propagated uncertainty is identical to the inclusion of continuous process noise. This proof and discussion is given in the following Lemma.

Lemma 3.2 (Noise Propagation in the BL-OCBE):

In the BL-OCBE the matrix $\mathcal{P}_{k|k-1}$ is equivalent to the covariance of the propagated a priori state ($\bar{P}_{k|k-1}$). Additionally, the assumed dynamic uncertainty ($\tilde{Q}(t)$) is propagated within this covariance in a manner that is identical to continuous process noise.

Proof: First we must demonstrate that the matrix $\mathcal{P}_{k|k-1}$ is equivalent to the covariance of $\delta\bar{x}_{k|k-1}$. In the BL-OCBE the equations for these two properties are given below as functions of time to preserve the continuous nature of the system.

$$\begin{aligned} \delta\bar{x}(t|t_{k-1}) + \vec{v}_x(t|t_{k-1}) =& \Phi_{xx}(t,t_{k-1})\delta\bar{x}_{k-1|k-1} + \int_{t_{k-1}}^{t} \Phi_{xx}(t,\tau)B(\tau)\vec{w}(\tau)d\tau \\ \mathcal{P}(t|t_{k-1}) =& \Phi_{xx}(t,t_{k-1})\bar{P}_{k-1|k-1}\Phi_{xx}(t,t_{k-1})^T - \Phi_{xp}(t,t_{k-1})\Phi_{xx}(t,t_{k-1})^T \end{aligned} \tag{3.75}$$

Differentiating these expressions with respect to time, and making the proper STM dynamics substitutions we obtain the following dynamics of these two values as shown below.

$$\delta\dot{\bar{x}}(t|t_{k-1})\dot{\vec{v}}_x(t|t_{k-1}) = \left.\frac{\partial\vec{f}}{\partial\vec{x}}\right|_{(t,\tilde{x}(t))} \delta\bar{x}(t|t_{k-1}) + B(t)\vec{w}(t) \tag{3.76}$$

$$\dot{\mathcal{P}}(t|t_{k-1}) = \left.\frac{\partial\vec{f}}{\partial\vec{x}}\right|_{(t,\tilde{x}(t),\tilde{p}(t))} \mathcal{P}(t|t_{k-1}) + \mathcal{P}(t|t_{k-1}) \left.\frac{\partial\vec{f}}{\partial\vec{x}}\right|^{T}_{(t,\tilde{x}(t),\tilde{p}(t))} + B(t)\tilde{Q}(t)B(t)^{T} \tag{3.77}$$

The covariance of the propagated a priori state, and its dynamical equation are defined below.

$$\bar{P}(t|t_{k-1}) = E\left[\left(\delta\bar{x}(t|t_{k-1}) - E[\delta\bar{x}(t|t_{k-1})]\right)\left(\delta\bar{x}(t|t_{k-1}) - E[\delta\bar{x}(t|t_{k-1})]\right)^{T}\right] \tag{3.78}$$

$$\begin{aligned}\dot{\bar{P}}(t|t_{k-1}) =& E\Big[\left(\delta\dot{\bar{x}}(t|t_{k-1}) - E[\delta\dot{\bar{x}}(t|t_{k-1})]\right)\left(\delta\bar{x}(t|t_{k-1}) - E[\delta\bar{x}(t|t_{k-1})]\right)^{T} \\ &+ \left(\delta\bar{x}(t|t_{k-1}) - E[\delta\bar{x}(t|t_{k-1})]\right)\left(\delta\dot{\bar{x}}(t|t_{k-1}) - E[\delta\dot{\bar{x}}(t|t_{k-1})]\right)^{T}\Big] \\ =& \left.\frac{\partial\vec{f}}{\partial\vec{x}}\right|_{(t,\tilde{x}(t),\tilde{p}(t))} \bar{P}(t|t_{k-1}) + \bar{P}(t|t_{k-1}) \left.\frac{\partial\vec{f}}{\partial\vec{x}}\right|^{T}_{(t,\tilde{x}(t),\tilde{p}(t))} \\ &+ B(t)E\left[\vec{w}(t)\delta\bar{x}(t|t_{k-1})^{T}\right] + E\left[\delta\bar{x}(t|t_{k-1})\vec{w}(t)^{T}\right]B(t)^{T}\end{aligned} \tag{3.79}$$

Following the development in Ref. [83], this covariance equation of motion may reduced to form shown below.

$$\dot{\bar{P}}(t|t_{k-1}) = \left.\frac{\partial\vec{f}}{\partial\vec{x}}\right|_{(t,\tilde{x}(t),\tilde{p}(t))} \bar{P}(t|t_{k-1}) + \bar{P}(t|t_{k-1}) \left.\frac{\partial\vec{f}}{\partial\vec{x}}\right|^{T}_{(t,\tilde{x}(t),\tilde{p}(t))} + B(t)\tilde{Q}(t)B(t)^{T} \tag{3.80}$$

This dynamical equation (with solution given in Eq. 3.81) is identical to the matrix equation of motion in Eq. 3.77. Given the equivalency in dynamics and that the initial conditions for the matrices are equivalent ($\mathcal{P}(t_{k-1}|t_{k-1}) = \bar{P}(t_{k-1}|t_{k-1}) = \bar{P}_{k-1|k-1}$), the result is that the matrices are equal to one another. Thus $\mathcal{P}_{k|k-1}$ is the covariance of the propagated a priori state: $\mathcal{P}_{k|k-1} = \bar{P}_{k|k-1}$.

Beyond this equivalence, we also conclude that the equation of motion for the BL-OCBE propogated a priori state is fully equivalent to the covariance dynamical equation for a Kalman Filter with continuous process noise [83]. Given that these equations have identical initial conditions ($\bar{P}(t_{k-1}|t_{k-1}) = \bar{P}_{k-1|k-1}$), it means that the covariances are equivalent for all time. Thus, the propagated state covariance for the BL-OCBE is identical to propagated state covariance for a Kalman Filter with process noise defined by the same dynamic uncertainty ($\tilde{Q}(t)$). The solution to this covariance equation of motion is given below, which is fully equivalent to the BL-OCBE covariance equation in Eq. 3.63.

$$\bar{P}_{k|k-1} = \Phi_{xx}(t_k,t_{k-1})\bar{P}_{k-1|k-1}\Phi_{xx}(t_k,t_{k-1})^{T} + \int_{t_{k-1}}^{t_k} \Phi_{xx}(t,\tau)\frac{\partial\vec{f}}{\partial\vec{u}}\tilde{Q}(\tau)\frac{\partial\vec{f}}{\partial\vec{u}}^{T}\Phi^{T}_{xx}(t,\tau)d\tau \tag{3.81}$$

■

As shown, this algorithm automatically generates continuous dynamic noise via the form of its cost function. This noise is guaranteed to be positive semi-definte due to restrictions on $\tilde{Q}(t)$ (which is symmetric positive definite), and the symmetric form of Eq. 3.81.

It should be noted that the BL-OCBE achieves this continuous process-noise equivalent dynamic uncertainty via solution of a simple linear dynamical equation in the STM. Often Kalman Filter algorithms will make a discrete process noise assumption to simplify propagation of state uncertainty, but the results are not equivalent ([9],[81],[82]). The BL-OCBE automatically computes continuous process noise as part of the system. The user only needs to select the assumed dynamic uncertainty matrix ($\tilde{Q}(t)$), then the system automatically accounts for the effect on state propagation via the STM equations of motion.

Having established the noise propagation properties of this estimator, the next property to discuss is the special property associated with the state estimate at the a priori epoch. These are discussed in the next subsection.

3.4.3.2 Smoothing

The a priori state estimate that comes out of the BL-OCBE is extra information that is not provided by the standard Kalman Filter. However, a complimentary algorithm to the Kalman Filter offers a basis for comparison. Smoothing algorithms take information from later time epochs and propagate it backward to obtain a trajectory with full information content at every epoch. In terms of optimality, a smoothed state estimate maximizes the probability density function at the a priori epoch conditioned on measurements through the final time. In this section we will establish an equivalence between the BL-OCBE a priori state estimates and the equivalent smoothed Kalman estimate. This will lead to an additional algorithm that fully smooths the state estimates across multiple epochs for the BL-OCBE as discussed later in this chapter.

Lemma 3.3 (One-step Smoother Equivalence): The update to the state estimate at the a priori epoch for the BL-OCBE ($\delta\hat{x}_{k-1|k}$) is equivalent to the state estimate update for a Kalman algorithm when applying a smoothing algorithm given the same inputs. This is equivalent to stating that the state estimate at the a priori epoch for the BL-OCBE is the state estimate that maximizes the state probability density function at t_{k-1} conditioned on measurements through time t_k.

Proof: To start, we define the smoothed estimate that results from the smoothing algorithm applied to the Kalman filter in Eqs. 3.82 - 3.84.

$$\delta\hat{x}_{k-1|k} = \delta\hat{x}_{k-1|k-1} + S_{k-1}\left[\delta\hat{x}_{k|k} - \Phi_{xx}\delta\hat{x}_{k-1|k-1}\right] \tag{3.82}$$

$$S_{k-1} = P_{k-1|k-1}\Phi_{xx}^T P_{k|k-1}^{-1} \tag{3.83}$$

$$\hat{P}_{k-1|k} = \hat{P}_{k-1|k-1} + S_{k-1}\left(\hat{P}_{k|k} - \bar{P}_{k|k-1}\right)S_{k-1}^T \tag{3.84}$$

Restating Eq. 3.64, with some slight modifications we obtain the result in Eq. 3.85.

$$\delta\hat{x}_{k-1|k} = \delta\bar{x}_{k-1|k-1} + \bar{P}_{k-1|k-1}\Phi_{xx}^T\bar{P}_{k|k-1}^{-1}\left[L_k\left(\delta\vec{y}_k - \tilde{H}_k\left(\delta\bar{x}_{k|k-1} + \vec{v}_x(t_k)\right)\right)\right] \tag{3.85}$$

The portion of this equation in brackets may be substituted for a rearranged form of Eq. 3.66 as shown in Eq. 3.86.

$$\delta\hat{x}_{k-1|k} = \delta\bar{x}_{k-1|k-1} + \bar{P}_{k-1|k-1}\Phi_{xx}^T\bar{P}_{k|k-1}^{-1}\left[\delta\hat{x}_{k|k} - \delta\bar{x}_{k|k-1} - \vec{v}_x(t_k)\right] \tag{3.86}$$

Equation 3.86 is identical to Eqs. 3.82 and 3.83 a side from the fact that the OCBE process noise term is explicit - the Kalman filter term is built into the terms so they are still equivalent. This demonstrates equivalence in the state estimates at the a priori epoch. Next, we show equivalence in the covariance for completeness. Rearranging both Eqs. 3.73 and 3.74 we obtain the results shown below.

$$\hat{P}_{k-1|k} = \bar{P}_{k-1|k-1} - S_{k-1}L_k\left(R_k + \tilde{H}_k\bar{P}_{k|k-1}\tilde{H}_k^T\right)L_k^T S_{k-1}^T \tag{3.87}$$

$$\hat{P}_{k|k} = \bar{P}_{k|k-1} - L_k\left(R_k + \tilde{H}_k\bar{P}_{k|k-1}\tilde{H}_k^T\right)L_k^T \tag{3.88}$$

Rearranging Eq. 3.88 and plugging it into Eq. 3.87, we obtain the result shown in Eq. 3.89. This is identical to the stated uncertainty from the smoothed Kalman estimate (Eq. 3.84), which demonstrates their equivalency.

$$\hat{P}_{k-1|k} = \bar{P}_{k-1|k-1} + S_{k-1}\left(\hat{P}_{k|k} - \bar{P}_{k|k-1}\right)S_{k-1}^{T} \tag{3.89}$$

■

To this point we have identified several similarities between the BL-OCBE and the Kalman Filter. In the next section we will formalize this by officially stating the relation between these two algorithms.

3.4.3.3 Generalization of the Kalman Filter

The Kalman Filter is the standard linear sequential estimator for a dynamical system that optimizes a number of cost functions including minimum variance and weighted least squares. The optimality of its solution is summarized as the best (minimum variance), linear, unbiased (mean of estimate distribution is truth) state estimate. While we have demonstrated the the BL-OCBE optimizes our cost function of interest and this cost function has strong physical and mathematical significance, it would be valuable to compare this optimality to more standard estimation techniques (i.e. the Kalman Filter) or even demonstrate equivalence. In this section we will demonstrate an equivalence between the BL-OCBE and the Kalman Filter with process noise.

Theorem 3.2 (BL-OCBE Equivalence to Kalman Filter): The state estimate at the measurement epoch and its associated uncertainty from the BL-OCBE are equivalent to the Kalman Filter solutions when provided identical inputs. This is equivalent to saying the BL-OCBE outputs the minimum variance, unbiased state estimate at the measurement epoch.

Proof: To start we define the Kalman filter estimate with process noise in the notation of this paper through Eqs. 3.90-3.94.

$$\delta\hat{x}_{k|k} = \delta\bar{x}_{k|k-1} + K_k\left(\delta\vec{y}_k - \tilde{H}_k\delta\bar{x}_{k|k-1}\right) \tag{3.90}$$

$$\hat{P}_{k|k} = \left(I - K_k\tilde{H}_k\right)\bar{P}_{k|k-1}\left(I - K_k\tilde{H}_k\right)^{T} + K_kR_kK_k^{T} \tag{3.91}$$

$$K_k = \bar{P}_{k|k-1}\tilde{H}_k^T\left(R_k + \tilde{H}_k\bar{P}_{k|k-1}\tilde{H}_k^T\right)^{-1} \tag{3.92}$$

$$\delta\bar{x}_{k|k-1} = \Phi_{xx}\delta\bar{x}_{k-1|k-1} \tag{3.93}$$

$$\bar{P}_{k|k-1} = \Phi_{xx}\bar{P}_{k-1|k-1}\Phi_{xx}^T + \int_{t_{k-1}}^{t_k}\Phi_{xx}(t_k,\tau)\frac{\partial\vec{f}}{\partial\vec{u}}\tilde{Q}(\tau)\frac{\partial\vec{f}}{\partial\vec{u}}^T\Phi_{xx}^T(t_k,\tau)d\tau \tag{3.94}$$

Having proven that the Kalman propagated covariance is equivalent to the BL-OCBE propagated covariance given the same inputs, it becomes apparent that the Kalman Gain (K_k) is identical to the BL-OCBE Gain at the measurement epoch (L_k). Additionally because the state-state portions of the STMs (Φ_{xx}) are equivalent between the two estimators (because $\Phi_{px}(t,\tau) = 0$ from Lemma 3.1), the propagated state deviations are also equal to one another ($\delta\bar{x}_{k|k-1}$). Given these equivalencies, the state estimate and uncertainty at the measurement epoch are equivalent between both estimators. ■

While these estimators are equivalent in their measurement epoch state estimates and have the same optimality claims, the linear OCBE provides far more information. The estimator automatically accounts for dynamic uncertainty, estimates dynamic mismodeling, and estimates the state at the a priori epoch automatically. As such we may define the BL-OCBE as a generalization of the Kalman algorithm.

3.5 The OCBE Smoother

Given that the estimated control profiles are a highlight of this estimator, we aim to provide optimal control estimates based on all available information over the entire trajectory. Additionally, another goal for this estimator is to describe how optimal state estimates are connected in time. While we accomplish this over a single observation gap, the algorithm as presented to this point includes jump discontinuities at each measurement epoch due to the updated a priori state estimate. This problem is erased by application of a full-smoothing algorithm as developed in this section. The development starts with the definition of the smoother for the nonlinear OCBE. After this, separate treatments of this smoother applied to the GL-OCBE and BL-OCBE are provided.

3.5.1 Nonlinear OCBE Full Smoother

A smoother takes the latest measurement and applies that information to all previous estimation epochs in order to obtain trajectories that have the highest information content. In order to form a proper smoothing algorithm a cost function must be designed to take advantage of the available pieces of information: (1) the previous estimate at the time of interest and its associated covariance $(t_{k-1}, \hat{x}_{k-1|k-1}, \hat{P}_{k-1|k-1})$ and (2) knowledge of the dynamics and the level of mismodeling. As with the OCBE the OCBE smoother estimates a fictitious control policy to account for mismodeling using the same a priori values as the original estimator $(\bar{u}(t), \tilde{Q}(t))$.

In order to ensure a continuous state trajectory, the smoother should also be designed such that the smoothed states are required to be connected. This requirement results in a recursive algorithm that starts at the final measurement epoch, smooths to the previous measurement epoch, and continues until reaching the beginning of the estimation arc. At each step the following constraint is enforced:

$$\hat{x}_{k|l} = \phi_x(t; t_{k-1}, \hat{x}_{k-1|l}, \hat{p}_{k-1|l}) \tag{3.95}$$

This constraint enforces the continuous state trajectory constraint for a measurement arc with l measurements. It should be noted that the smoothed state at t_k has the associated covariance matrix $\hat{P}_{k|l}$. In the following definition we formally define a smoother cost function with the desired properties we have discussed here, and we define the necessary conditions for smoother optimality.

Definition 3.5 (Nonlinear OCBE Full Smoothing Algorithm): Given inputs t_{k-1}, $\hat{x}_{k-1|k-1}$, $\hat{P}_{k-1|k-1}$, t_k, $\hat{x}_{k|l}$, $\hat{P}_{k|l}$, $\bar{u}(t)$, and $\tilde{Q}(t)$ as previously defined the Nonlinear OCBE Full Smoothing Algorithm is defined as the state and controls that minimize the cost function defined below.

$$\begin{aligned}\mathcal{J}_{smooth}(\vec{x}_{k-1}, \vec{u}(t)) = &\frac{1}{2}\int_{t_{k-1}}^{t_k} (\vec{u}(\tau) - \bar{u}(\tau))^T \tilde{Q}(\tau)^{-1} (\vec{u}(\tau) - \bar{u}(\tau)) d\tau \\ &+ \frac{1}{2}\left(\hat{x}_{k-1|k-1} - \vec{x}_{k-1}\right)^T \hat{P}_{k-1|k-1}^{-1} \left(\hat{x}_{k-1|k-1} - \vec{x}_{k-1}\right)\end{aligned} \tag{3.96}$$

This cost function is constrained by state dynamics as defined for the OCBE, and that the state at t_{k-1} $(\vec{x}_{k-1})$ and the control policy $(\vec{u}(t))$ should be chosen such that when propagated they result in the smoothed state at t_k for a state with l observation epochs ($\hat{x}_{k|l}$).

The optimal solutions to this cost function ($\hat{x}_{k-1|l}$ and $\hat{p}_{k-1|l}$) are defined as solutions that satisfy the following two necessary conditions for smoother optimality.

$$F_1(\hat{x}_{k-1|l}, \hat{p}_{k-1|l}) = \hat{p}_{k-1|l} - \hat{P}^{-1}_{k-1|k-1}\left(\hat{x}_{k-1|k-1} - \hat{x}_{k-1|l}\right) = \vec{0} \tag{3.97}$$

$$F_2(\hat{x}_{k-1|l}, \hat{p}_{k-1|l}) = \hat{x}_{k|l} - \phi_x(t; t_{k-1}, \hat{x}_{k-1|l}, \hat{p}_{k-1|l}) = \vec{0} \tag{3.98}$$

Once solved, the optimal control policy may be obtained from the state and adjoint trajectories via the results of the Pontryagin Minimum Principle (Eq. 3.9). ■

Just like the nonlinear OCBE, there is no analytical solution to this optimization problem, and no means to quantify uncertainty in the estimates. As such, we will pursue linear solutions to this problem.

3.5.2 GL-OCBE Full Smoother

As was the case with the GL-OCBE, the GL-OCBE full smoother is a linearization of the nonlinear algorithm about arbitrary state and adjoint trajectories. Defining the linearization the same as we did for the GL-OCBE, the linearized necessary conditions are defined below.

$$\vec{F}_1(\hat{x}_{k-1|l}, \hat{p}_{k-1|l}) \approx \vec{F}_1(\tilde{x}_{k-1}, \tilde{p}_{k-1}) + \left.\frac{\partial \vec{F}_1}{\partial \hat{x}_{k-1|l}}\right|_{(\tilde{x}_{k-1}, \tilde{p}_{k-1})} \delta\hat{x}_{k-1|l} + \left.\frac{\partial \vec{F}_1}{\partial \hat{p}_{k-1|l}}\right|_{(\tilde{x}_{k-1}, \tilde{p}_{k-1})} \delta\hat{p}_{k-1|l} = \vec{0} \tag{3.99}$$

$$\vec{F}_2(\hat{x}_{k-1|l}, \hat{p}_{k-1|l}) \approx \vec{F}_2(\tilde{x}_{k-1}, \tilde{p}_{k-1}) + \left.\frac{\partial \vec{F}_2}{\partial \hat{x}_{k-1|l}}\right|_{(\tilde{x}_{k-1}, \tilde{p}_{k-1})} \delta\hat{x}_{k-1|l} + \left.\frac{\partial \vec{F}_2}{\partial \hat{p}_{k-1|l}}\right|_{(\tilde{x}_{k-1}, \tilde{p}_{k-1})} \delta\hat{p}_{k-1|l} = \vec{0} \tag{3.100}$$

Subbing in all necessary values, the following linear necessary conditions are obtained. In these equations all values with a δ are relative to the nominal trajectory.

$$\left[\tilde{p}_{k-1} - \hat{P}^{-1}_{k-1|k-1}\delta\hat{x}_{k-1|k-1}\right] + \hat{P}^{-1}_{k-1|k-1}\delta\hat{x}_{k-1|l} + \delta\hat{p}_{k-1|l} = \vec{0} \tag{3.101}$$

$$\left[\delta\hat{x}_{k|l} - \vec{v}_x(t_k)\right] - \Phi_{xx}\delta\hat{x}_{k-1|l} - \Phi_{xp}\delta\hat{p}_{k-1|l} = \vec{0} \tag{3.102}$$

Definition 3.6 (GL-OCBE Full Smoother Algorithm): The linear algorithm with arbitrary initial state and adjoint (nominal trajectories defined by $\tilde{x}(t) = E\left[\phi_x(t; t_{k-1}, \tilde{x}_{k-1}, \tilde{p}_{k-1})\right]$ and $\tilde{p}(t) = E\left[\phi_p(t; t_{k-1}, \tilde{x}_{k-1}, \tilde{p}_{k-1})\right]$, respectively) that minimizes the cost function defined in Definition 3.5 is called the GL-OCBE Full Smoother Algorithm. It is defined by the state, adjoint, and control estimates given below.

$$\delta\hat{x}_{k-1|l} = \delta\hat{x}_{k-1|k-1} + S_{k-1}\left[\delta\hat{x}_{k|l} - \left(\Phi_{xx}\delta\hat{x}_{k-1|k-1} - \Phi_{xp}\tilde{p}_{k-1} + \vec{v}_x(t_k)\right)\right] \tag{3.103}$$

$$S_{k-1} = \hat{P}_{k-1|k-1}\left(\Phi_{xx}\hat{P}_{k-1|k-1} - \Phi_{xp}\right)^{-1} \tag{3.104}$$

$$\delta\hat{p}_{k-1|l} = -\hat{P}^{-1}_{k-1|k-1}S_{k-1}\left[\delta\hat{x}_{k|l} - \left(\Phi_{xx}\delta\hat{x}_{k-1|k-1} - \Phi_{xp}\tilde{p}_{k-1} + \vec{v}_x(t_k)\right)\right] - \tilde{p}_{k-1} \tag{3.105}$$

$$\begin{aligned}\delta\hat{u}(t|t_l) = &\left[\vec{w}(t) - \tilde{Q}(t)B(t)^T\left(\vec{v}_p(t|t_{k-1}) - \Phi_{pp}(t, t_{k-1})\tilde{p}_{k-1}\right)\right] \\ &- \tilde{Q}(t)B(t)^T\left[\left(\Phi_{px}(t, t_{k-1}) - \Phi_{pp}(t, t_{k-1})\hat{P}^{-1}_{k-1|k-1}\right)\delta\hat{x}_{k-1|l} + \Phi_{pp}(t, t_{k-1})\hat{P}^{-1}_{k-1|k-1}\delta\bar{x}_{k-1|k-1}\right]\end{aligned} \tag{3.106}$$

$$\tilde{u}(t) = -\tilde{Q}(t)B(t)^T E\left[\phi_p(t; t_{k-1}, \tilde{x}_{k-1}, \tilde{p}_{k-1})\right] + E\left[\bar{u}(t)\right] \tag{3.107}$$

The covariance associated with this smoothed state estimate ($\delta\hat{x}_{k-1|l}$) is defined below.

$$\hat{P}_{k-1|l} = \hat{P}_{k-1|k-1} + S_{k-1}\left[\hat{P}_{k|l} + \bar{P}_{k|k-1}\right]S^T_{k-1} - \left[S_{k-1}\Phi_{xx}\hat{P}_{k-1|k-1} + \hat{P}_{k-1|k-1}\Phi^T_{xx}S^T_{k-1}\right] \tag{3.108}$$

■

The GL-OCBE smoother may be iterated to solve the nonlinear smoothing problem. As such the linearization about the solution may be used to provide uncertainty estimates for the nonlinear estimates. In the next section we will simplify this smoother by specifying the nominal adjoint to be zero for all time (i.e. ballistic), thus creating the BL-OCBE Full Smoother Algorithm.

3.5.3 BL-OCBE Smoother

By applying the same ballistic simplifications that were defined for the BL-OCBE, we can simplify the GL-OCBE Full Smoother into the BL-OCBE Full Smoother. This smoother is formally defined in Definition 3.7.

Definition 3.7 (BL-OCBE Full Smoother Algorithm): The linear algorithm with arbitrary initial state (nominal state and adjoint trajectories defined by $\tilde{x}(t) = E\left[\phi_x(t;t_{k-1},\tilde{x}_{k-1},\tilde{p}_{k-1} = \vec{0})\right]$ and $\tilde{p}(t) = E\left[\phi_p(t;t_{k-1},\tilde{x}_{k-1},\tilde{p}_{k-1} = \vec{0})\right] = \vec{0}$, respectively) and ballistic nominal adjoint (i.e. zero for all time) that minimizes the cost function defined in Definition 3.5 is called the BL-OCBE Full Smoother Algorithm. It is defined by the state, adjoint, and control estimates given below (where $\bar{P}_{k|k-1}$ is defined by Eq. 3.63).

$$\delta\hat{x}_{k-1|l} = \delta\hat{x}_{k-1|k-1} + S_{k-1}\left[\delta\hat{x}_{k|l} - \left(\Phi_{xx}\delta\hat{x}_{k-1|k-1} + \vec{v}_x(t_k)\right)\right] \tag{3.109}$$

$$S_{k-1} = \hat{P}_{k-1|k-1}\Phi_{xx}^T\bar{P}_{k|k-1}^{-1} \tag{3.110}$$

$$\delta\hat{p}_{k-1|l} = -\hat{P}_{k-1|k-1}^{-1}S_{k-1}\left[\delta\hat{x}_{k|l} - \left(\Phi_{xx}\delta\hat{x}_{k-1|k-1} + \vec{v}_x(t_k)\right)\right] \tag{3.111}$$

$$\delta\hat{u}(t|t_l) = -\tilde{Q}(t)B(t)^T\Phi_{pp}(t,t_{k-1})\hat{P}_{k-1|k-1}^{-1}\left[\delta\bar{x}_{k-1|k-1} - \delta\hat{x}_{k-1|l}\right] + \vec{w}(t) \tag{3.112}$$

$$\tilde{u}(t) = E\left[\bar{u}(t)\right] \tag{3.113}$$

The covariance associated with this smoothed state estimate ($\delta\hat{x}_{k-1|l}$) is defined below.

$$\hat{P}_{k-1|l} = \hat{P}_{k-1|k-1} + S_{k-1}\left[\hat{P}_{k|l} - \bar{P}_{k|k-1}\right]S_{k-1}^T \tag{3.114}$$

■

These equations are incredibly similar to the state estimate at the a priori epoch that comes out of the BL-OCBE. As with that estimate, we can demonstrate an equivalence between this smoother and the Kalman smoother, except now it extends to all measurement epochs - not just a one step operation. This proof follows the exact form of Lemma 3.3, thus it is unnecessary to repeat here. The only difference is the estimates contain information through t_l rather than t_k.

With this property it is clear that Eq. 3.96 was aptly chosen to be the cost function for the OCBE Full Smoothing Algorithm. Not only does this algorithm output a continuous state trajectory with associated controls that use information from the entire measurement arc, but it also preserves the optimality conditions of the Kalman Smoother. These include a minimum variance criterion and optimality in a Bayesian sense.

3.6 Conclusions

This chapter presented a full treatment of the OCBE. This included the definition of the OCBE cost function and all relevant inputs, the definition of the necessary conditions for a solution to the estimate, and a proof of existence. Furthermore, we found that the equations were not analytically solvable for an arbitrary nonlinear system, thus we linearized the system to create the GL-OCBE. The GL-OCBE provides a linearized algorithm to better understand the manner in which the algorithm works, and a means to solve the nonlinear estimation problem via iteration on the linear solutions. Through this linearization we were able to determine that the algorithm is unbiased, and that it assumes the system is properly modeled, though it will add dynamic mismodeling when errors dictate that it should.

After completing analysis of the GL-OCBE, we simplified the equations by assuming a ballistic nominal trajectory, which resulted in the BL-OCBE. This linear estimator has a much simpler form, but it cannot be iterated to solve the nonlinear estimation problem. What it loses in nonlinearity it gains in ideal properties for a linear estimator. We demonstrated that the BL-OCBE is a generalization of the Kalman Filter with an equivalent state estimate at the measurement epoch and associated covariance, a propagated a priori covariance that is equivalent to the Kalman filter with continuous process noise, and the state estimate at the a priori epoch and its covariance are equal to a smoothed Kalman estimate. Being a generalization of the Kalman Filter, we can make the same optimality claims which include the fact that the BL-OCBE is a minimum variance estimator, Bayesian Estimator, and a Maximum Likelihood Estimator.

We concluded the discussion of this algorithm by developing a complementary algorithm that smoothed all state estimates and the control estimates. This algorithm outputs a continuous state trajectory across all measurement epoch with a corresponding control trajectory, so that in the end we have a continuous state solution based on all measurements that has no jump discontinuities. We developed GL-OCBE and BL-OCBE versions of this algorithm, with the latter being shown to be completely equivalent to a Kalman smoother with the addition of control estimates.

Having fully developed this algorithm, the remaining chapters of this thesis will focus on demonstrating the algorithm and making an even more sophisticated algorithm with the development of complementary algorithms that detect maneuvers using the state and control estimates from the OCBE along with a method to automate the estimator.

Chapter 4

Applications of the Optimal Control Based Estimator

In this Chapter we demonstrate the properties of the OCBE through numerical simulation. This includes three separate systems: (1) a mass-spring-damper system with mismodeled dynamics, (2) a Low Earth Orbit (LEO) satellite with mismodeled atmospheric drag dynamics and an unknown actuated maneuver, and (3) a spacecraft in Geosynchronous Earth Orbit (GEO) that is undergoing unknown stationkeeping maneuvers. For the first simulation we only apply the BL-OCBE since it is a linear system that does not require iteration. For the latter two simulations an analysis using both the BL-OCBE and the Nonlinear OCBE (iterated GL-OCBE) is provided. In each application a discussion is provided detailing the results of the simulation, while highlighting the performance of the OCBE.

4.1 Mass-Spring-Damper System with Dynamical Mismodeling

In these simulations we apply the BL-OCBE to a simple Mass-Spring Damper system in order to show its abilities with a simple linear system. There are two different applications. The first includes an unknown perturbing acceleration, and the second includes spring and damper mismodeling. Together these simulations demonstrate the BL-OCBE applied to problems with unknown maneuvers and natural dynamical mismodeling. Because this is a linear system, application of the iterated GL-OCBE would yield the same results so we will limit analysis to the BL-OCBE. For both of these simulations the parameters in Table 4.1 are used.

Table 4.1: True System Parameters and Initial Conditions for Mass-Spring-Damper Simulation

Parameter	Symbol	Value	Units
Mass	m	100	kg
Spring Constant	K	10	N/m
Damping Constant	C	1	Ns/m
Acceleration Offset	a_{off}	0.5	m/s^2
Acceleration Magnitude	a_{mag}	0.1	m/s^2
Acceleration Sinusoid Rate	ω	$2\pi/5$	rad/s
Initial Position	x_0	0	m
Initial Velocity	$\dot{x}_0$	0	m/s

4.1.1 Example I: Mass-Spring-Damper with Unmodeled Perturbation

This first simulation applies the BL-OCBE algorithm to a simple linear system - a forced mass-spring-damper system with an unknown forcing function. Without knowledge of the forcing function the problem becomes an issue of estimation in a dynamically mismodeled system. The input force is an offset sinusoidal defined by Eq. 4.1 and the parameters in Table 4.1.

$$a(t) = a_{off} + a_{mag} \sin(\omega t) \tag{4.1}$$

Observations of the position state are taken once every second for 100 continuous seconds. These observations include 0.01 m Gaussian uncertainty. We will limit the estimated input as a single dimension acceleration with constant uncertainty ($B(t)^T = [0,1]$ and $Q(t) = \sigma_Q^2$).

Tracking results with varied assumed dynamic uncertainty (σ_Q^2) for this simulation are shown in Fig. 4.1. These deviations are taken with respect to the true trajectory (integrated using the initial conditions in Table 4.1). The three assumed dynamic uncertainties represent underestimating the perturbing force (blue), overestimating the perturbing force (black), and using the true level of dynamic uncertainty (red). We see in these results that underestimating the dynamic mismodeling leads to poor tracking since the system has a biased force for which it cannot account. Overestimating the mismodeling leads to similar tracking results as properly accounting for the mismodeling, though the latter does perform slightly better especially in the first several measurements.

Though overestimating the mismodeling yields similar tracking results not all things are equal.

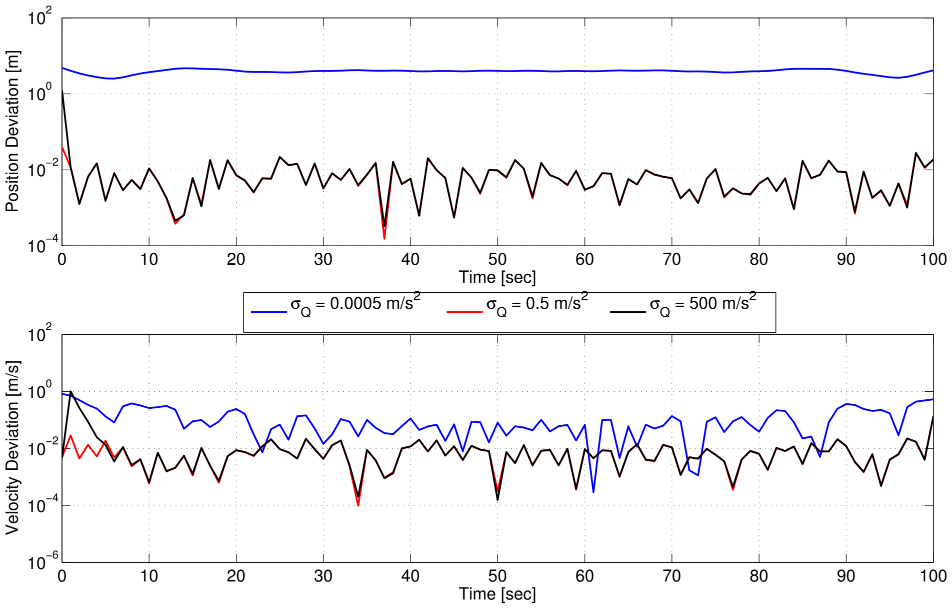

Figure 4.1: Smoothed state tracking results (deviations relative to truth) with varied assumed dynamic uncertainty (σ_Q).

The uncertainty results (Fig. 4.2) show that the velocity should only be tracking at an accuracy of 200 m/s rather than the 0.01 m/s that it is actually achieving. This discontinuity indicates that the tracking with too high of an assumed dynamic uncertainty is not ideal. In systems where the measurement model is highly nonlinear we also find that using too high of an assumed dynamic uncertainty leads to degraded tracking as well.

The control results from this simulation are summarized in Fig. 4.3. Plotted are the results from all three assumed dynamic uncertainties against truth (using the model in Eq. 4.1). As is expected, the results from the under estimation case are poor considering the associated state estimates were also poor. Both of the other other cases accurately replicate the offset sinusoidal nature of the true perturbation. A detailed look at the control estimates for the case with the true level of dynamic uncertainty is provided in Fig. 4.4. In these results we can see the accurate reconstruction of the unknown input force. The uncertainty in the control accurately bounds the deviations indicating that we have accurately tuned the estimator. This demonstrates the

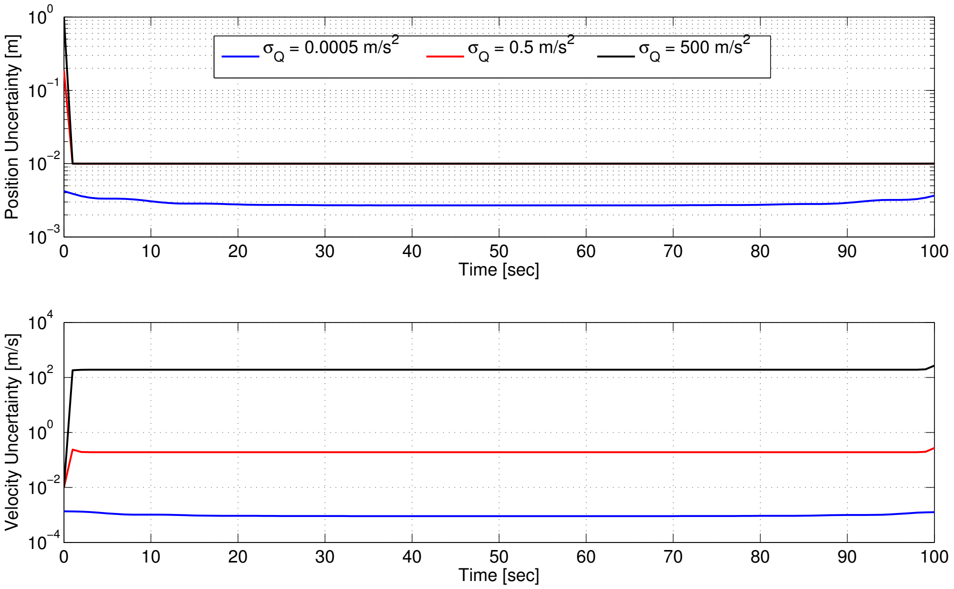

Figure 4.2: Smoothed uncertainty in state estimates with varied assumed dynamic uncertainty (σ_Q).

estimator's ability to recover unknown dynamics through independent observation.

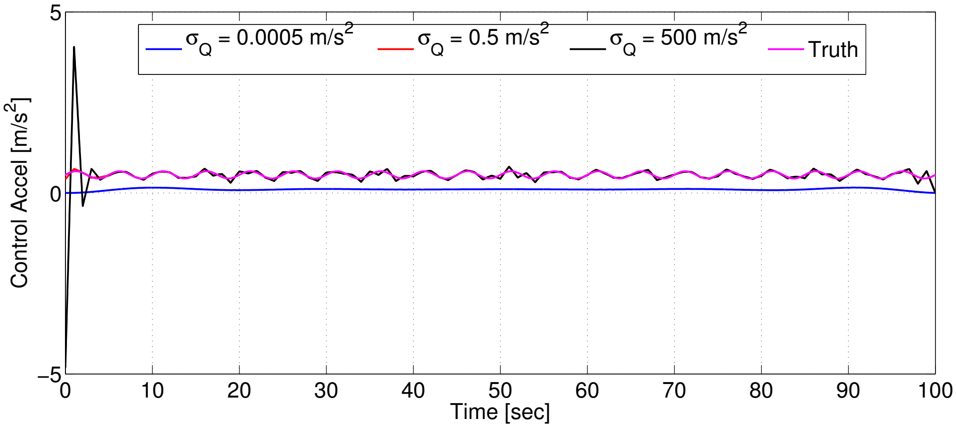

Figure 4.3: Smoothed control estimates against true input acceleration with varied assumed dynamic uncertainty (σ_Q).

True state deviations are not an achievable metric for real system application. Tuning the assumed dynamic uncertainty does not rely on this though. We use a separate maneuver detection process as described in Chapter 5. This method involves the user determining the statistical sig-

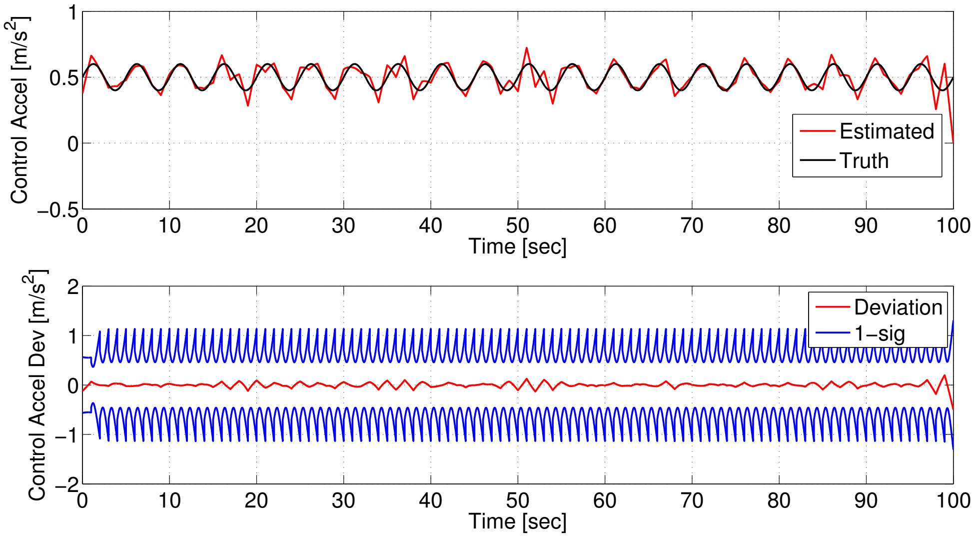

Figure 4.4: (Top) Control Estimate using correct dynamic uncertainty and the true mismodeling. (Bottom) Deviation between these control estimates and the true mismodeling with a 1-σ envelope.

nificance of the estimated control properties, and then adjusting the assumed dynamic uncertainty such that the unknown dynamics properly accounted for and dealt with.

4.1.2 Example II: Spring-Mass-Damper with Mismodeled Natural Dynamics

Through the previous example we demonstrated this algorithm's ability to recognize and replicate unmodeled input forces. In this next example we will test the algorithm's effectiveness against mismodeled natural dynamics. We use the same setup as the previous example (without the input force) except that the estimator is given a flawed natural dynamical model - a twenty percent overestimate in the spring constant, and a fifty percent underestimate in the damping constant.. This corresponds to around +/- 0.02 m/s^2 in the acceleration.

Tracking results for this setup with varied assumed dynamic uncertainty are given in Fig. 4.5. As with the previous example the assumed dynamic uncertainty is set to three levels: too low (under representing the true dynamic uncertainty), too high (over-compensating for the dynamic uncertainty), and the correct level (on the order of magnitude of the true mismodeling). Using both too high and too low of an assumed dynamic uncertainty results in degraded tracking performance because in the former case more uncertainty is injected into the system than needs to be, and in the latter case the injected uncertainty does not fully account for the dynamic mismodeling.

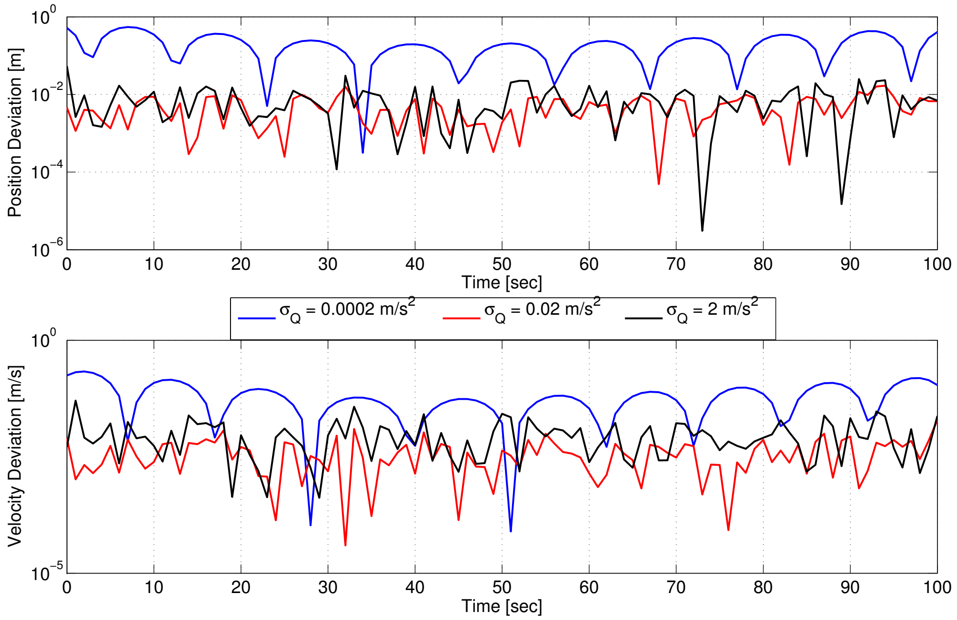

Figure 4.5: Smoothed state tracking results (deviations relative to truth) with varied assumed dynamic uncertainty (σ_Q).

This degraded performance is further highlighted by comparing the tracking results with the uncertainty results (Fig. 4.6). When using too high or too low of an assumed dynamic uncertainty the state deviations are either too large or too small relative to the accompanying uncertainty. In the estimation process it is important for uncertainty to reflect that actual deviations in the estimates in order to assign a proper level of confidence in the solution. For the case where we use the correct dynamic uncertainty we achieve the complementary behavior between the tracking and uncertainty results.

The control results with varied assumed dynamic uncertainty are provided in Fig. 4.7. When too high of an assumed dynamic uncertainty is used the resulting control profiles are too large and noisy. Using too low of an assumed dynamic uncertainty results in less noise, but the estimates are far too small.

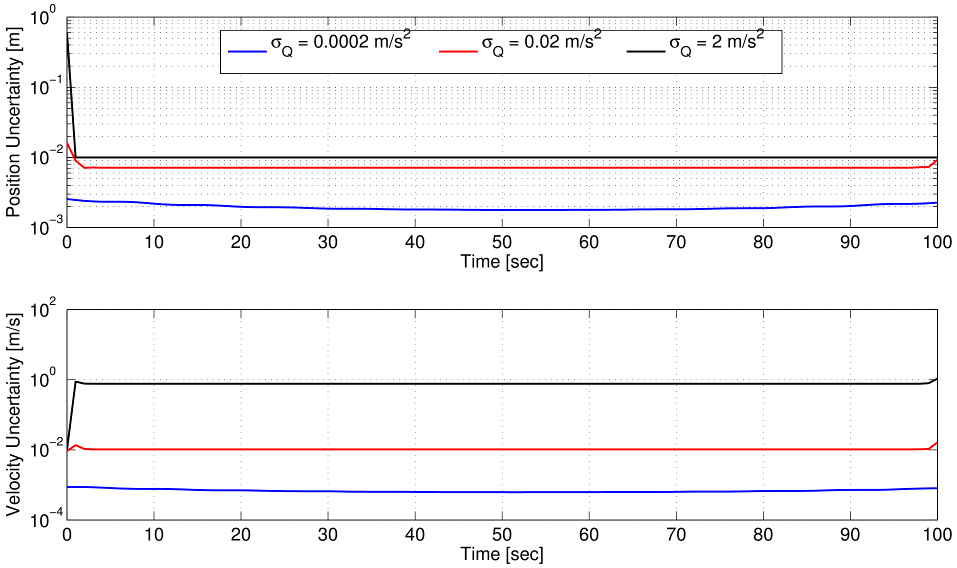

Figure 4.6: Smoothed uncertainty in state estimates with varied assumed dynamic uncertainty (σ_Q).

Detailed looks at the case where we use the correct dynamic uncertainty are provided in Fig. 4.8. It is clear in these results that the estimated control models the behavior of the true mismodeling with noise introduced from measurement and a priori state uncertainty. We also find that the uncertainty in these estimates accurately captures the deviation of the estimates from truth - the uncertainty is calculated by taking the expectation of the smoothed adjoint equation, and then propagating that through to a control uncertainty. These results are important because it clearly indicates there is a biasing in the dynamical model. Making the hypothesis that this is a natural dynamics mismodeling, one can estimate the spring and damping coefficients from these control estimates using the natural dynamics estimation algorithm developed in Chapter 5.

Through these two examples we have shown the abilities of this algorithm when applied to dynamically mismodeled systems regardless of whether that mismodeling is natural or forced. The power of the OCBE lies in the control estimates it outputs. These accurately reconstruct completely unknown dynamics as optimal control policies, which are quite similar to the true dynamics they are replicating.

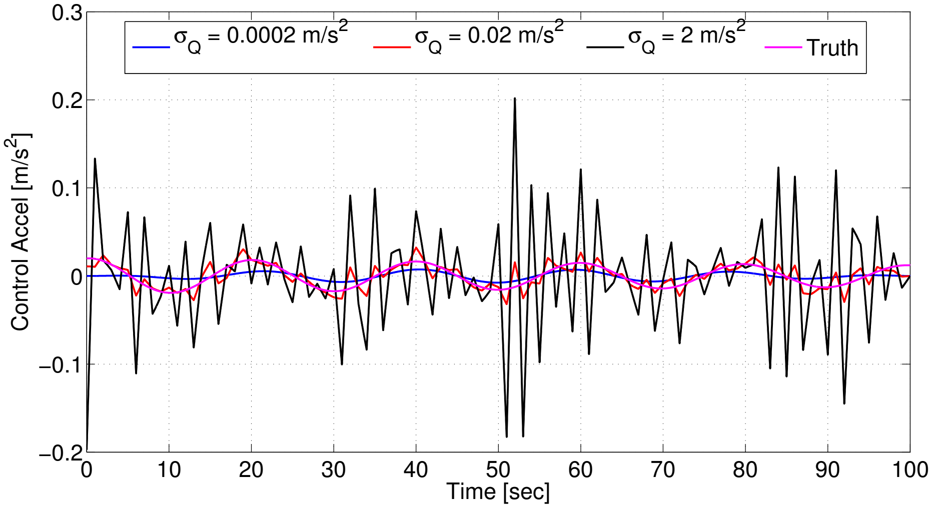

Figure 4.7: Smoothed control estimates against true natural mismodeling with varied assumed dynamic uncertainty (σ_Q).

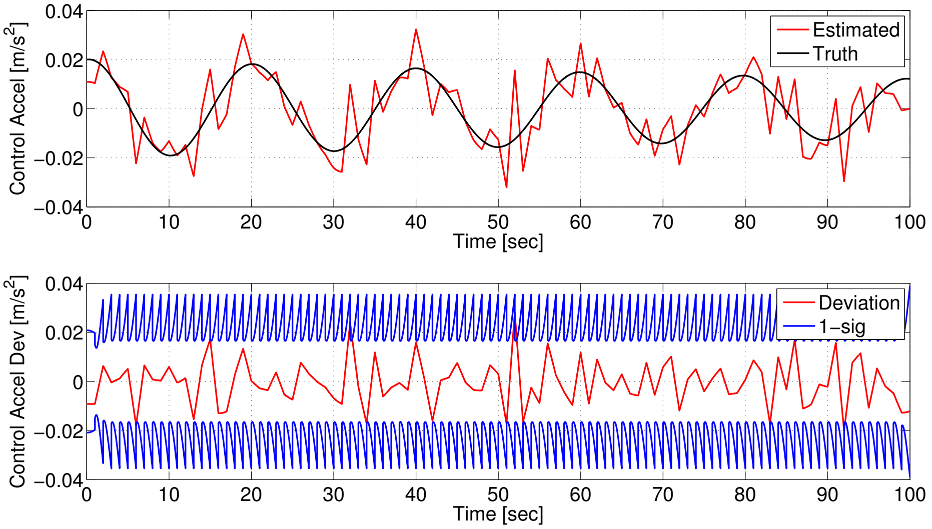

Figure 4.8: (Top) Control Estimate with correct dynamic uncertainty and the true mismodeling. (Bottom) Deviation between these control estimates and the true mismodeling with a 1-σ envelope.

4.2 Tracking a Spacecraft in LEO with Mismodeled Drag and an Unknown Maneuver

As a first application of this algorithm to an astrodynamics tracking scenario we apply this problem to a Low Earth Orbit (LEO) target that has an atmospheric drag mismodeling of 50%

and an unknown cross track maneuver at some point during the observation arc. In terms of observations, the target is observed with range and range-rate observations (1 m and 0.01 m/s Gaussian error, respectively) once every hour for a total of 150 consecutive hours by one of three space-based observers. In this simulation we set the assumed dynamic uncertainty in the form of $\tilde{Q}(t) = (t_k - t_{k-1})\sigma_Q^2 I_{m\times m}$. Specific simulation parameters are defined in Table 4.2. We will independently address the problem through application of the BL-OCBE and the Nonlinear OCBE to demonstrate the performance of each version of the OCBE.

Table 4.2: True System Parameters and Initial Conditions for LEO Simulation

Parameter	Symbol	Value	Units
Mass	m	970	kg
Projected Area	A_{proj}	3.0	m^2
Drag Coefficient	C_D	2	-
Reflectivity Coefficient	S_{SRP}	1.5	-
Initial Position Error	σ_R	10	m
Initial Velocity Error	σ_V	0.01	m/s
Initial True ECI Position	$\vec{x}_0$	$757.7\hat{I} + 5,222.607\hat{J} + 4,851.5\hat{K}$	km
Initial True ECI Velocity	$\vec{v}_0$	$2.21321\hat{I} + 4.67834\hat{J} - 5.37130\hat{K}$	km/s

4.2.1 Tracking with the BL-OCBE

To begin this simulation, we first pass the observations through the OCBE at a low assumed dynamic uncertainty ($\sigma_Q = 10^{-12}$ m/s^2) to assess what is happening. The resulting postfit residuals are shown in Fig. 4.9. These results clearly indicate the presence of some unknown dynamic mismodeling as evidenced by the large deviations from zero. The deviations are slight initially, and then they deviate rapidly around the 40th measurement. This is likely indicative of some slight continuous mismodeling (i.e. natural dynamics) followed by a large sudden mismodeling (i.e. an actuated maneuver). These mismodelings are most likely uncorrelated, thus we will approach them differently.

To address the slight mismodeling seen in the first 40 measurements, we adjust the assumed dynamic uncertainty until the resulting postfit residuals are within the expected range - in future chapters we will adjust this approach to focus on distance metrics rather than measurement residuals. The resulting postfit residuals obtained with an assumed dynamic uncertainty of $\sigma_Q = 2 \times 10^{-8}$ m/s^2 are shown in Fig. 4.10.

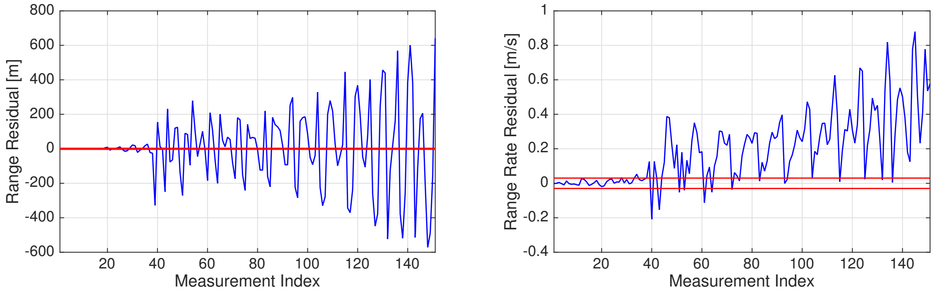

Figure 4.9: Postfit measurement residuals with 3-σ bounds after running BL-OCBE ($\sigma_Q = 10^{-12}$ m/s^2).

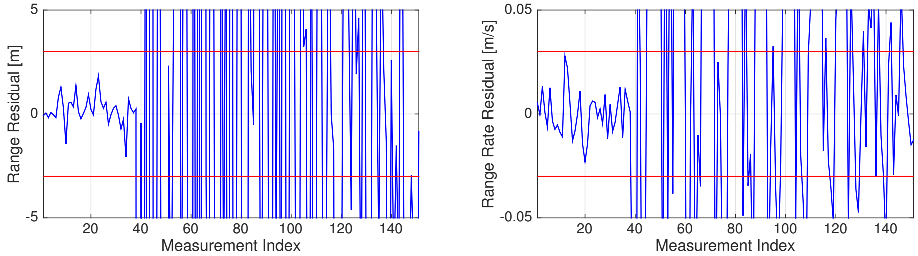

Figure 4.10: Zoomed-in postfit measurement residuals after accounting for drag mismodeling ($\sigma_Q = 2 \times 10^{-8}$ m/s^2)

These results show an expected distribution of postfit residuals within the first 38 measurements, thus indicating we have properly compensated for the presence of the slight constant mismodeling. However, the sudden mismodeling is still present at the 39th measurement and it is clouding our ability to assess the presence of dynamic mismodeling beyond it.

That sudden dynamic mismodeling is accounted for by adjusting the assumed dynamic uncertainty for that specific measurement epoch ($\sigma_Q = 7.3 \times 10^{-5}$ m/s^2). The resulting postfit measurement residuals are shown in Fig. 4.11. These residuals fall well within the 3-σ bounds without being too small (which would indicate over-reliance on measurements). This indicates successful tracking over the entire data arc, thus we can move on to analyze the other outputs of the estimation process.

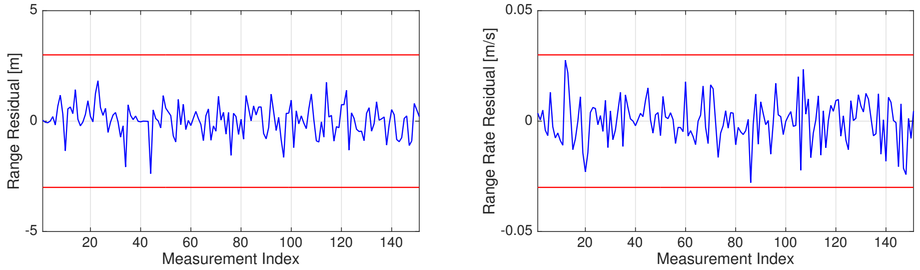

Figure 4.11: Postfit measurement residuals after accounting for drag mismodeling and maneuver

Though the true states are unattainable in practice, we may use them as a means to demonstrate the successful tracking obtained via application of the OCBE to this problem with mismodeled dynamics. Figure 4.12 depicts the state deviations (measurement epoch estimates minus truth) with a 3-σ envelope as a function of the measurement index. These show tracking on a meter level in position, with a max just under 1 kilometer following the maneuver. Removing the drag mismodeling would yield even more accurate results. For all measurements the state deviations remained bounded by the uncertainty envelope, thus indicating we never lose track of the spacecraft even following the maneuver. This demonstrates the OCBE's robustness to dynamic mismodeling whether it is continuous or discontinuous.

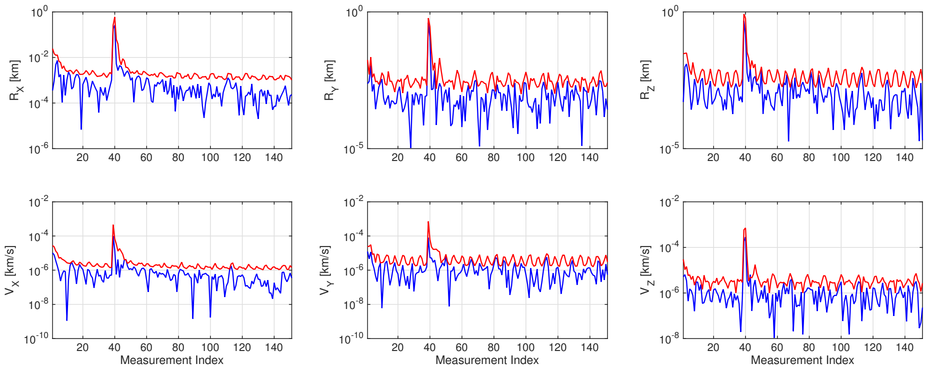

Figure 4.12: ECI state estimate deviations relative to truth with a 3-σ envelope after accounting for drag mismodeling and maneuver

One of the most important outputs from the OCBE is the control estimate. These estimates as a function of time in the Hill frame for this simulation are shown in Fig. 4.13. In these estimates the maneuver clearly stands out among the rest. In truth the maneuver is a 0.5 m/s cross track maneuver. Our estimates equate it as a 0.34 m/s maneuver with a strong cross-track component, but the drag mismodeling induces in-plane components as well. Removing the drag mismodeling would help to refine this maneuver estimate (size and directionality). The other, smaller control estimates are clearly dominated by along-track dynamics. Combined with the fact that the controls are of order 10^{-8} m/s^2, these estimates correspond well with the 50% overestimate in drag. This mismodeling may be removed by appending the parameter to the state vector or using the natural dynamics estimation method in Chapter 5. This combined with the OCBE smoother algorithm would result in more accurate control estimate.

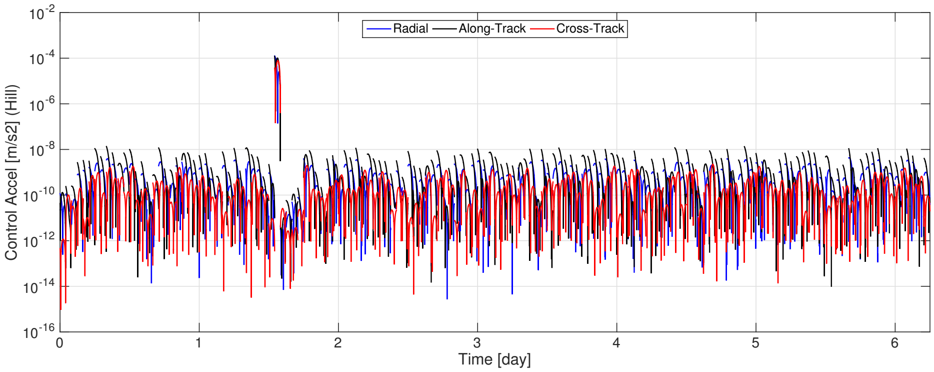

Figure 4.13: Hill frame control estimate magnitudes after accounting for drag mismodeling and maneuver

Application of the BL-OCBE smoother, yields the true state deviations shown in Fig. 4.14. The influence of the cross track maneuver is almost nonexistent in these results, meaning we have full compensated for it and reconstructed it. That reconstruction is obtained via the smoothed control estimates (Fig. 4.15). In these reconstructions, we see that the maneuver is estimated as a cross-track event with a magnitude of approximately 0.658 m/s (compared to the true value of 0.5 m/s). Beyond this maneuver, the drag mismodeling is accurately reconstructed as a bias in the negative along-track direction the order of 10^{-8} m/s^2 with a periodicity equal to the orbit period.

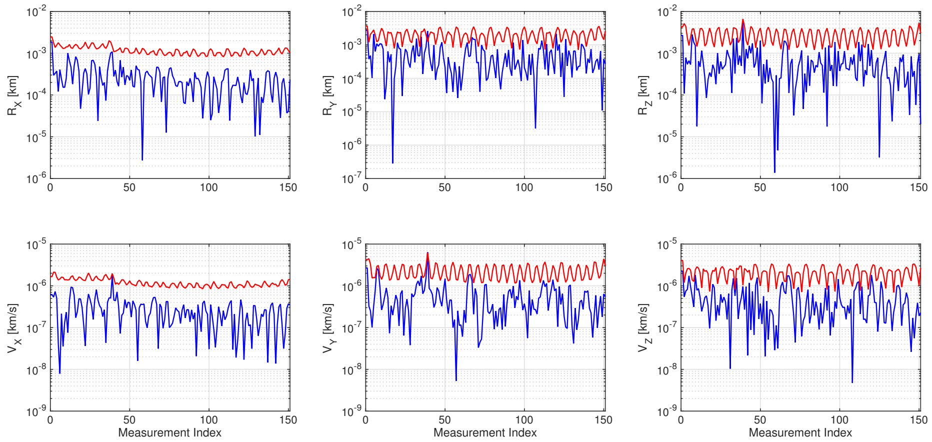

Figure 4.14: ECI smoothed state estimate deviations relative to truth with a 3-σ envelope after accounting for drag mismodeling and maneuver

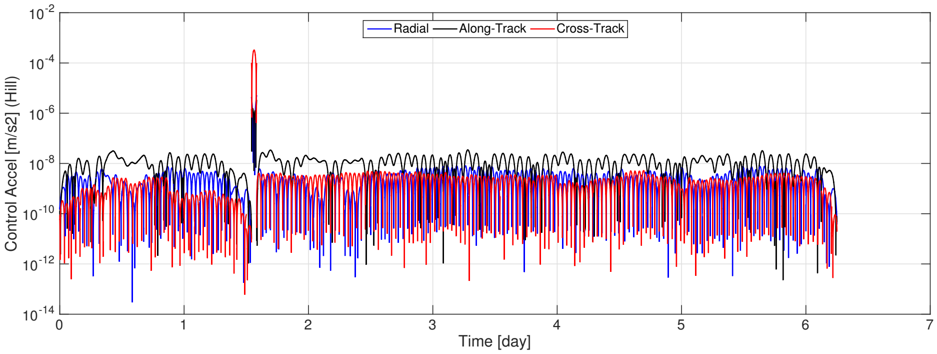

Figure 4.15: Hill frame smoothed control estimate magnitudes after accounting for drag mismodeling and maneuver

Table 4.3: LEO Tracking RMS Values with the BL-OCBE

ECI State	a priori Epoch Estimate	Measurement Epoch Measurement	Smoothed Estimate
R_X(m)	8.411	25.643	0.388
R_Y(m)	19.548	33.964	0.759
R_Z(m)	7.755	40.175	0.991
V_X(mm/s)	10.228	8.329	0.358
V_Y(mm/s)	16.217	6.821	0.925
V_Z(mm/s)	18.204	27.498	0.717

The improved tracking with the smoother is illustrated through RMS values shown in Table

4.3. The smoothed RMS values are almost 50 times smaller in certain categories, indicating on average far better tracking with the smoother. These are representative of the fact that the smoother deals with the maneuver much better, and has better tracking in general since its trajectory is based on all available information.

This example has shown the BL-OCBE may be applied to a LEO target with both natural dynamic mismodeling and unmodeled actuated maneuvers. The results provide a lot of information about the system including indications of how the dynamics are mismodeled. While this method is involved as presented, the automated version of the algorithm will remove the manual iteration that was required for this problem.

4.2.2 Tracking with the Nonlinear OCBE

To obtain the nonlinear OCBE solution to this tracking problem we need only apply the iterative GL-OCBE algorithm until the necessary conditions converge to zero. Applying the same method described in the BL-OCBE section, we are able to see the consistent mismodeling due to error in the atmospheric drag model as well as the effects of a one-time maneuver. After compensating for these mismodelings by adjusting the assumed dynamic uncertainty in the same manner as with the BL-OCBE, we obtain the postfit measurement residuals shown in 4.16. As can be seen, these residuals are incredibly similar to analysis with the BL-OCBE.

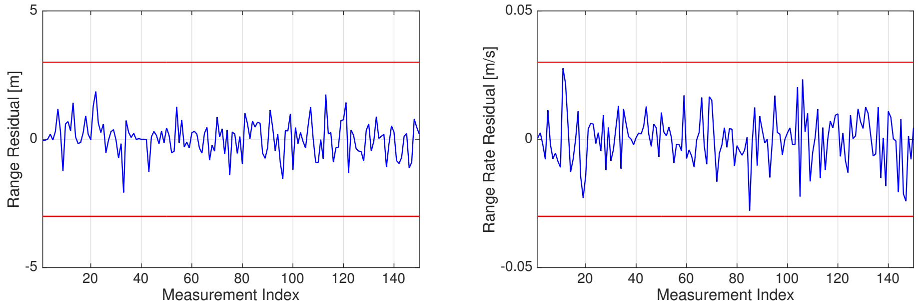

Figure 4.16: Nonlinear OCBE postfit measurement residuals after accounting for drag mismodeling and the cross-track maneuver

The level of tracking may also be assessed via the state estimate deviations (Fig. 4.17).

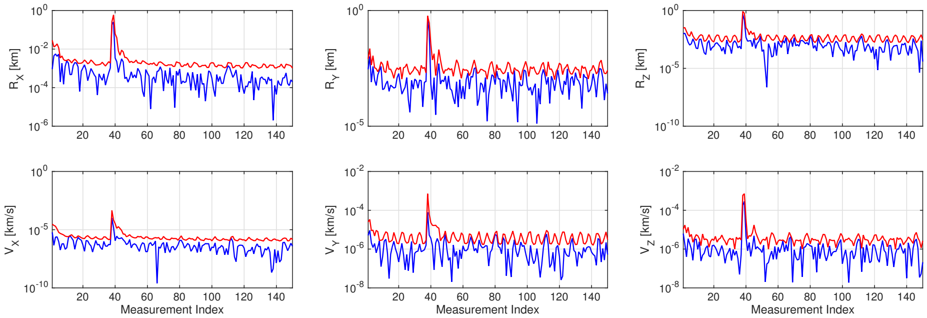

Figure 4.17: Nonlinear OCBE ECI state estimate deviations relative to truth with a 3-σ envelope after accounting for drag mismodeling and the cross-track maneuver

These results show similarity to the BL-OCBE results as well. This is indicative of the fact that mismodelings are small on the scale of the problem and measurements are taken frequently enough to maintain linearity assumptions such that the BL-OCBE tracks accurately.

Finally, the control estimates from tracking with the Nonlinear OCBE are shown in Fig. 4.18. These results clearly show the along-track biasing due to the drag mismodeling. The cross-track maneuver also clearly sticks, out though the drag mismodeling makes it difficult to determine directionality. Applying the smoother or removing the drag mismodeling would increase these reconstructions.

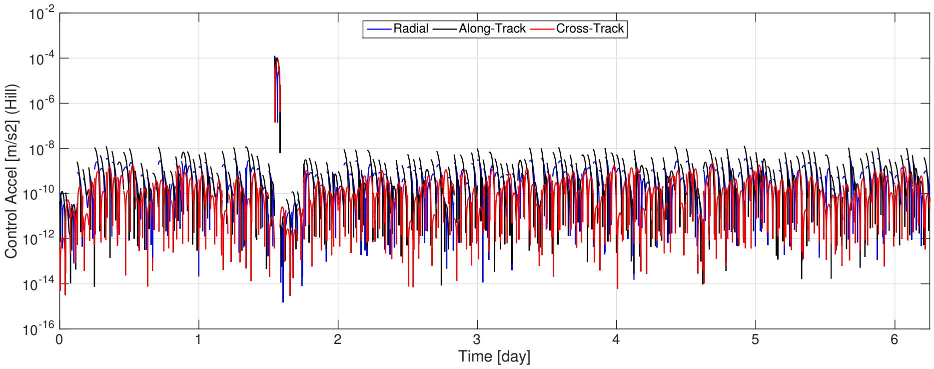

Figure 4.18: Nonlinear OCBE Hill frame control estimate magnitudes after accounting for drag mismodeling and the cross-track maneuver

After applying the OCBE smoother, we obtain state estimate deviations in Fig. 4.19. The state deviations are much less than the unsmoothed results and the effects of the maneuver have been almost completely removed. This maneuver is accurately reconstructed via the smoothed control estimates (Fig. 4.20). The cross-track directionality is apparent in the reconstruction, and we estimate it as a 0.659 m/s maneuver. Additionally, the drag mismodeling is evident via the consistent biasing in the along-track direction, which has a periodicity equal to the spacecraft's orbital period and the magnitude is consistent with a 50% underestimate in atmospheric drag.

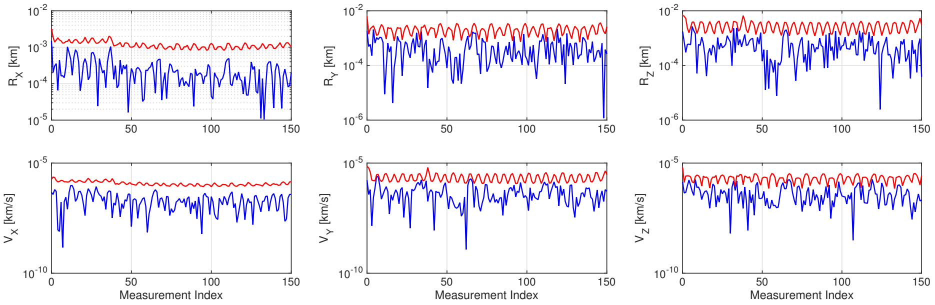

Figure 4.19: Nonlinear OCBE ECI state estimate deviations relative to truth with a 3-σ envelope after accounting for drag mismodeling and the cross-track maneuver

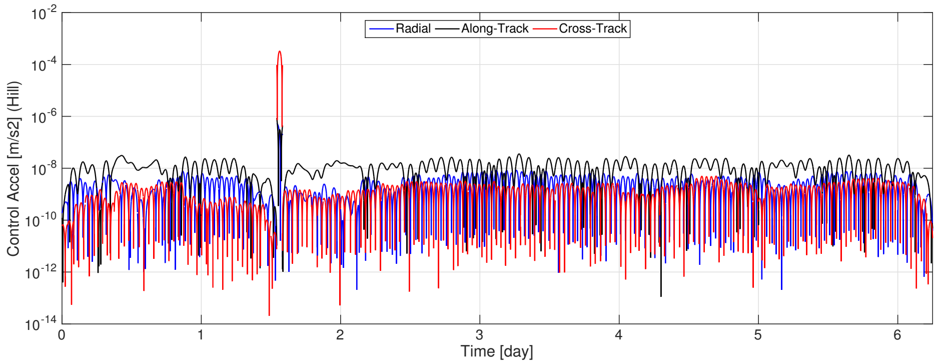

Figure 4.20: Nonlinear OCBE Hill frame control estimate magnitudes after accounting for drag mismodeling and the cross-track maneuver

As with the BL-OCBE results, we can show the vast improvements in tracking obtained via application of the OCBE smoother through the state deviation RMS values (Table 4.4). We can also compare these results to the BL-OCBE results (Table 4.3) and see modest improvements with the Nonlinear OCBE. These improvements are only modest because the actual dynamical mismodeling are not large enough to push the linear assumptions on the BL-OCBE given the level of information in the problem. However, another metric clearly indicates the Nonlinear OCBE's improved performance with respect to the BL-OCBE. That metric is a squared weighted RMS, where the state deviations are weighted by the inverse of the state estimate covariance. This forms a χ^2-like statistic assuming the estimates are not strongly correlated, with a mean of 6 (the number of estimated states). These values are summarized in Table 4.5. The Nonlinear OCBE results are far closer to the mean, which indicates better correspondence between tracking and estimated uncertainty. This is representative of the fact the Nonlinear OCBE deals better with maneuvers and other mismodeled dynamics, thus the uncertainties it outputs better represent the actual tracking level. The smoothed values are much lower due to the fact the estimates are much more correlated between epochs in a smoother.

Table 4.4: LEO Tracking RMS Values with the Nonlinear OCBE

ECI State	a priori Epoch Estimate	Measurement Epoch Measurement	Smoothed Estimate
R_X(m)	8.417	25.686	0.327
R_Y(m)	19.591	34.068	0.671
R_Z(m)	7.683	40.306	0.802
V_X(mm/s)	10.122	8.295	0.303
V_Y(mm/s)	16.131	6.731	0.703
V_Z(mm/s)	18.232	27.512	0.660

Table 4.5: LEO Tracking squared weighted RMS values with the BL-OCBE and the Nonlinear OCBE

Estimate Type	Nonlinear OCBE	BL-OCBE
a priori epoch estimates	5.546	7.183
Measurement epoch state estimates	5.604	7.354
Smoothed state estimates	3.662	4.707

This example shows that the BL-OCBE may obtain very comparable results to the full nonlinear estimator when dynamic mismodeling is not too large and the observations are not too sparse. When this is not the case though, the nonlinear algorithm will display noticebly better performance.

4.3 Tracking a Spacecraft in GEO with Unknown Stationkeeping Maneuvers

In this sample tracking scenario, a spacecraft in GEO is being observed via a ground station with non-cooperative range (10 m Gaussian uncertainty) and azimuth and elevation angle (1 arc-second Gaussian uncertainty) observations. The spacecraft is observed for two hours each night (observations taken every 100 seconds) over the course of fifteen days. Unknown to the estimator, the spacecraft executes stationkeeping maneuvers periodically to account for latitude (North-South [NS] maneuver) and longitude (East-West [EW] maneuver) deviations from the nominal geosynchronous orbit at a longitude of 60 degrees. The true dynamical model includes two body gravity, oblateness effects, solar radiation pressure (with area-to-mass ratio of 0.024), third body effects (sun and moon), and the actuated maneuvers. More perturbations may be included, but they do not tend to effect the significantly results unless they are mismodeled.

The actuated maneuvers are designed as low thrust events that last 4 hours. They initiate when a latitude or longitude nominal deviation barrier is crossed (0.05 degrees latitude and 0.1 degrees longitude), and conclude 4 hours later when the latitude or longitude has been reset to the nominal value. The maneuvers are decoupled such that latitude maneuvers do not influence longitude and vice versa. The spacecraft starts with an initial 0.25 degree deviation from nominal in latitude, a 0.2 degree deviation from nominal in longitude, and no deviation from nominal in radius. To start the simulation the true trajectory is mismodeled on the order of 1 km in position and 1 m/s in velocity. In the following two sections we track this spacecraft with the given measurements using the BL-OCBE and the Nonlinear OCBE, respectively.

4.3.1 Tracking with the BL-OCBE

Tracking this spacecraft with the BL-OCBE, we initially pass the data through the estimator with $\sigma_{Q,NF} = 10^{-10}$ m/s^2 in order to assess the presence of any mismodeling beyond this level. The resulting postfit measurement residuals for this pass through the data are shown in Fig. 4.21. It is clear from these results that the first batch of measurements are processed properly, however just past the 200^{th} measurement there is a large event.

To account for this event we adjust the assumed dynamic uncertainty for this specific measurement epoch until linear postfit measurement residuals are within an acceptable level (+/- 3σ). The resulting nonlinear postfit measurement residuals (i.e. using) after accounting for this first maneuver are shown in Fig. 4.21. These results confirm that the observed event was a one time maneuver, since the residuals immediately following the event are within the nominal range without additional compensation. However, a second event occurs much later in the data set.

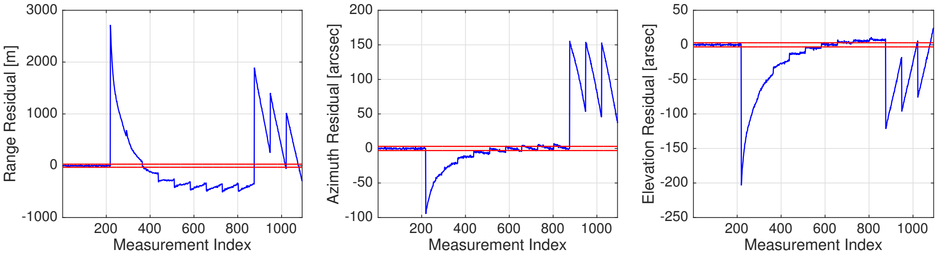

Figure 4.21: BL-OCBE postfit measurement residuals with a 3-σ envelope when processing GEO observations with $\sigma_{Q,NF} = 10^{-10}$ m/s^2.

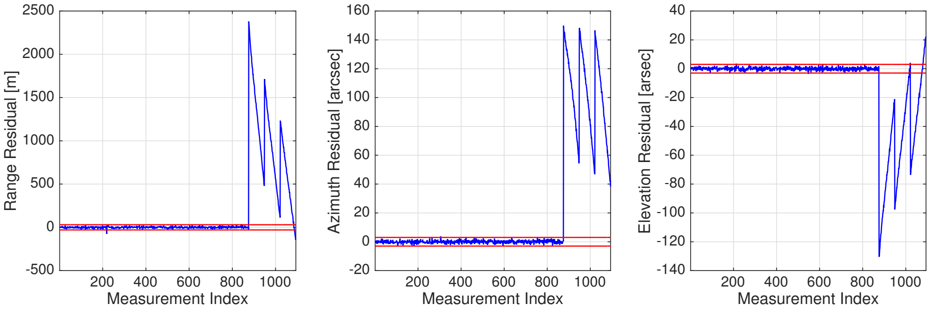

Figure 4.22: BL-OCBE postfit measurement residuals with a 3-σ envelope after accounting for first observed maneuver.

We account for this observed event in the same manner as the previous event. The resulting postfit measurement results are plotted in Fig. 4.23. These results clearly indicate that all statistically significant dynamic mismodelings have been addressed, but there is a strong outlier that corresponds to the first maneuver. There is a similar outlier for the second maneuver as well, but this one is much less statistically significant than the first. The reason these remain is due to limitations in the linear assumptions of the estimator. The maneuvers are large enough to push the tracking outside of this regime, which results in the linear residuals being appropriately distributed, but the nonlinear residuals do not reflect this. As we will see, the Nonlinear OCBE avoids these issues.

The state estimate deviations for this scenario are shown in Fig. 4.24. These results clearly indicate that the BL-OCBE never loses track of the objects even with the linear issues identified in the measurement residuals. We achieve tracking on the order of 10 m in position and sub 1 mm/s in velocity, which corresponds with expected values given these type of observations for this orbit. Even following the maneuvers, the tracking never exceeds 1 km for all time in any of the 3 ECI dimensions.

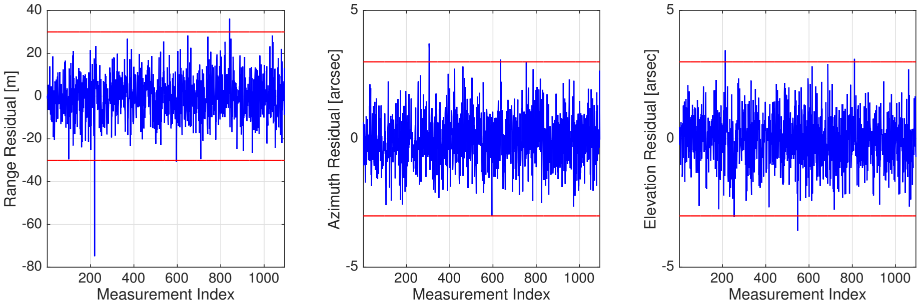

Figure 4.23: BL-OCBE postfit measurement residuals with a 3-σ envelope after accounting for both observed maneuvers.

The control estimates that come out of the BL-OCBE for this scenario are plotted as magnitudes in the Hill frame in Fig. 4.25. The maneuvers are evident in these results, and we may also characterize them. The first maneuver is clearly in-plane dominated, thus it represents an EW maneuver. We can quantify the maneuver with a ΔV estimate of 0.5262 m/s. This assumes optimality in the true maneuver, which is not the case here so this estimate is a lower bound on the true value of 16.8652 m/s. Similarly, the second maneuver is cross-track dominated, thus we can characterize it as a NS maneuver with a ΔV of 2.5350 m/s (compared to the true value of 7.6552 m/s). These are the only two true dynamic mismodelings within the data set, and the BL-OCBE

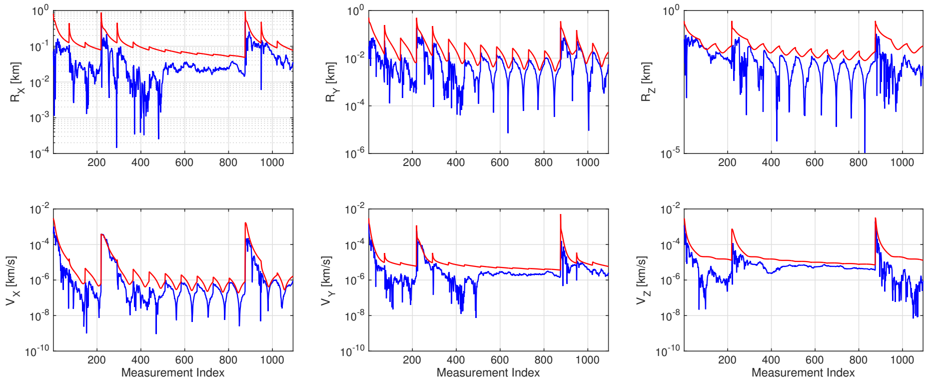

Figure 4.24: BL-OCBE state estimate deviations relative to truth with a 3-σ envelope after accounting for both observed maneuvers.

is able to identify both, characterize them, and reconstruct them through the control estimates.

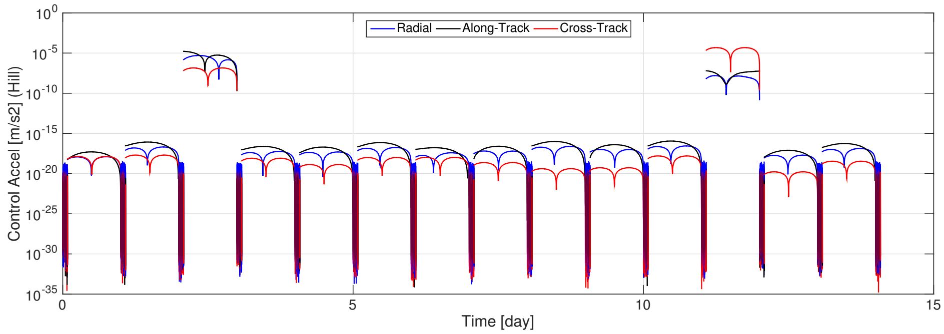

Figure 4.25: BL-OCBE control estimates magnitude in a Hill frame after accounting for both observed maneuvers.

After applying the BL-OCBE smoother, we obtain the state deviations in Fig. 4.26. The effects of the maneuvers are still seen in these residuals however they are greatly diminished. The results indicate a good level of tracking for the situation even in the presence of two maneuvers. These maneuvers are reconstructed through the smoothed control estimates (Fig. 4.27). The maneuvers clearly stand out from the noise. The first maneuver is obviously biased toward in-plane accelerations, thus it represents an EW maneuver with an estimated magnitude of 1.007 m/s. The second maneuver clearly stands out as a NS maneuver with an estimated magnitude of 3.551 m/s.

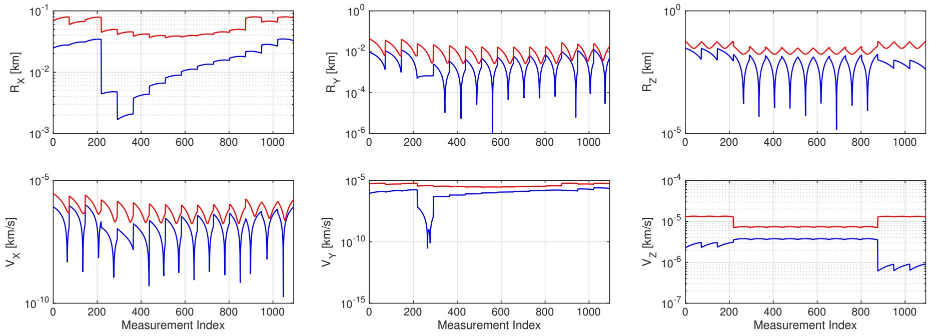

Figure 4.26: BL-OCBE smoothed state estimate deviations relative to truth with a 3-σ envelope after accounting for both observed maneuvers.

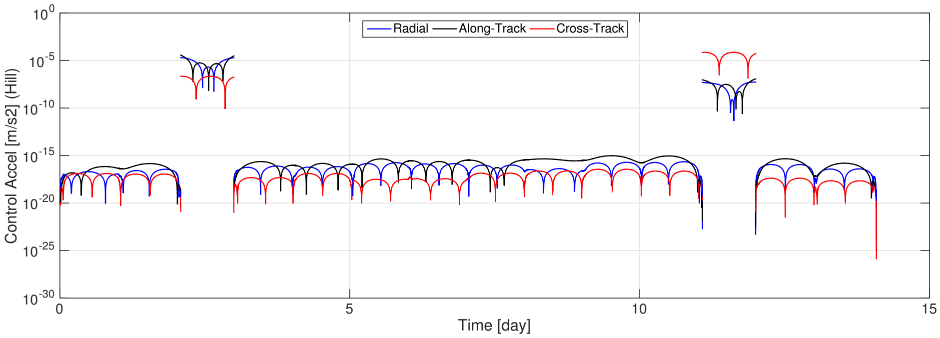

Figure 4.27: BL-OCBE smoothed control estimates magnitude in a Hill frame after accounting for both observed maneuvers.

Table 4.6: GEO Tracking RMS Values with the BL-OCBE

ECI State	a priori Epoch Estimate	Measurement Epoch Measurement	Smoothed Estimate
R_X(m)	56.119	61.665	20.336
R_Y(m)	17.685	20.017	4.511
R_Z(m)	31.989	33.431	11.834
V_X(mm/s)	72.631	73.515	0.312
V_Y(mm/s)	58.340	60.802	3.156
V_Z(mm/s)	75.303	95.699	0.717

Finally, we can compare real-time tracking results and the smoother algorithm using RMS values for state deviations (Table 4.6). It is clear in these results that the smoother provides orders of magnitude more accuracy in tracking. This demonstrates the effectiveness of the algorithm even in the presence of two large maneuvers, though it is limited to a post-processing tool.

This example has shown the BL-OCBE's ability to track a GEO spacecraft through two unknown maneuvers while obtaining some information about those maneuvers. While there were some issues associated with the linearization, the algorithm never diverges, and successfully tracks the spacecraft for all time.

4.3.2 Tracking with the Nonlinear OCBE

We now apply the Nonlinear OCBE algorithm to this tracking problem. Following the same process outlined in the BL-OCBE application, we are able to detect and compensate for two events within the observation set. The resulting postfit measurement residuals after compensating for these two maneuvers are shown in Fig 4.28. These residuals show no outliers, like we saw with the BL-OCBE, thus demonstrating a key difference between the algorithms.

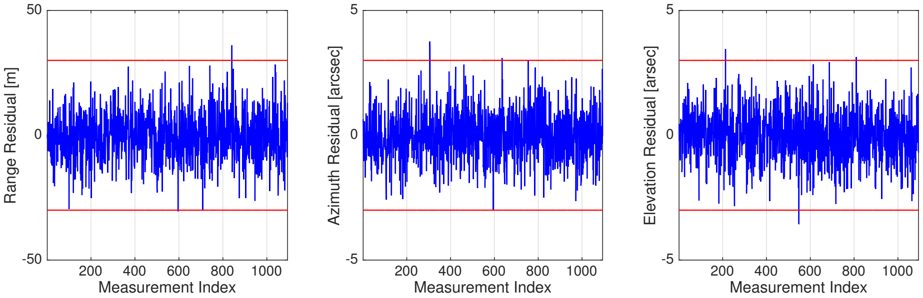

Figure 4.28: Nonlinear OCBE postfit measurement residuals with a 3-σ envelope after accounting for both observed maneuvers.

The resulting state deviations are shown in Fig. 4.29. The tracking levels are very similar to the BL-OCBE results, however there are fewer instances where the deviations approach the 3-σ envelopes following the maneuvers, especially in the velocity. This shows that the nonlinear estimator is far more robust to large maneuvers as compared to the BL-OCBE, which is what we should expect.

The control estimate magnitudes in a Hill frame are depicted in Fig. 4.30. We are able to characterize the first maneuver as a 0.5254 m/s EW maneuvers, and the second maneuver as a 2.5350 m/s NS maneuver. This reflects the true mismodeling (though the size estimates are biased by the optimality assumption). Application of the OCBE smoother would inform these estimates even further.

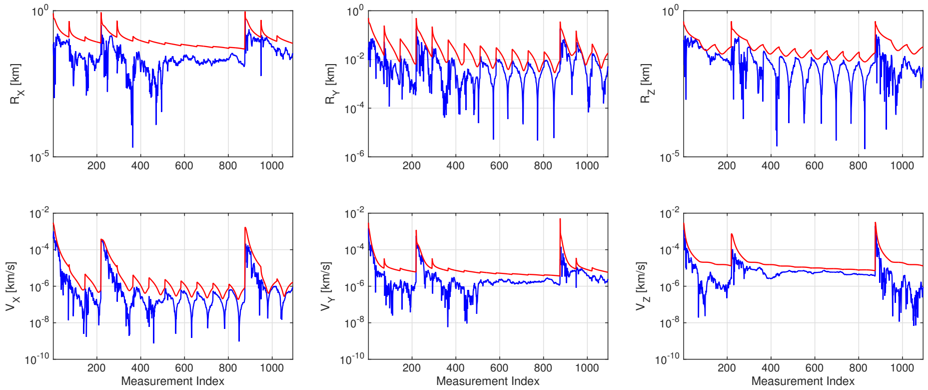

Figure 4.29: Nonlinear OCBE state estimate deviations relative to truth with a 3-σ envelope after accounting for both observed maneuvers.

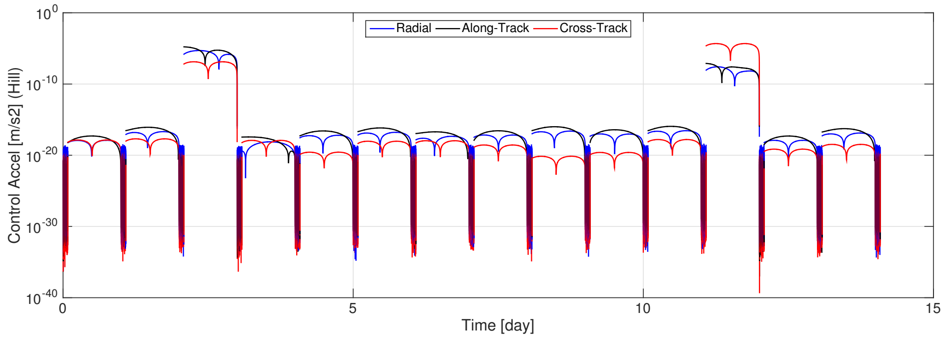

Figure 4.30: Nonlinear OCBE control estimates magnitude in a Hill frame after accounting for both observed maneuvers.

After applying the OCBE smoother, we obtain the state deviations in Fig. 4.31. The effects of the maneuvers are still seen in these residuals however they are greatly diminished. The results indicate a good level of tracking for the situation even in the presence of two maneuvers. These maneuvers are reconstructed through the smoothed control estimates (Fig. 4.32). The maneuvers clearly stand out from the noise. The first maneuver is obviously biased toward in-plane accelerations, thus it represents an EW maneuver with an estimated magnitude of 0.994 m/s. The second maneuver clearly stands out as a NS maneuver with an estimated magnitude of 3.551 m/s.

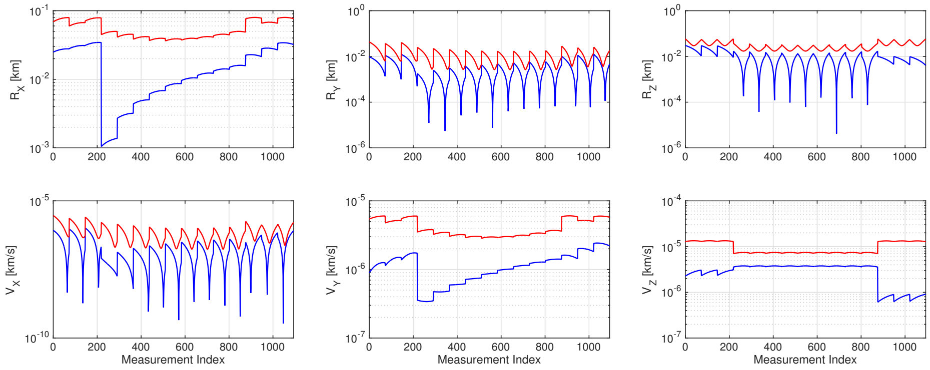

Figure 4.31: Nonlinear OCBE smoothed state estimate deviations relative to truth with a 3-σ envelope after accounting for both observed maneuvers.

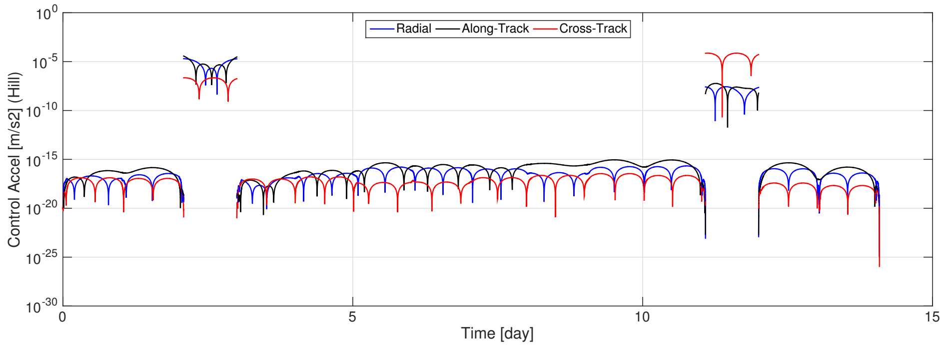

Figure 4.32: Nonlinear OCBE smoothed control estimates magnitude in a Hill frame after accounting for both observed maneuvers.

Table 4.7: GEO Tracking RMS Values with the Nonlinear OCBE

ECI State	a priori Epoch Estimate	Measurement Epoch Measurement	Smoothed Estimate
R_X(m)	51.921	55.896	20.055
R_Y(m)	15.933	17.311	4.389
R_Z(m)	32.825	34.315	11.845
V_X(mm/s)	63.238	64.260	0.308
V_Y(mm/s)	54.797	57.502	1.310
V_Z(mm/s)	75.809	96.098	3.166

Finally, we can compare real-time tracking results and the smoother algorithm using RMS values for state deviations (Table 4.7). It is clear in these results that the smoother provides orders of magnitude more accuracy in tracking. This demonstrates the effectiveness of the algorithm even in the presence of two large maneuvers, though it is limited to a post-processing tool. Comparing the Nonlinear results to the BL-OCBE results, it is evident that the Nonlinear algorithm has a slight edge. Its RMS values are generally lower on the order of meters in position and 1-10 mm/s in velocity. This is because the nonlinear algorithm handles large maneuvers far better than the linearized algorithm. Additionally, the weighted RMS values (Table 4.8) in general show that the nonlinear state estimate uncertainties more accurately reflect the true level of tracking fas compared to the BL-OCBE values. This is also representative of the nonlinear algorithm's increased ability to deal with large maneuvers as compared to the linear algorithm.

Table 4.8: GEO Tracking squared weighted RMS values with the BL-OCBE and the Nonlinear OCBE

Estimate Type	Nonlinear OCBE	BL-OCBE
a priori epoch estimates	8.086	8.980
Measurement epoch state estimates	8.089	9.037
Smoothed state estimates	5.678	6.717

This example shows that the Nonlinear OCBE algorithm may be used in systems with large dynamic mismodeling without having the same linearization issues as the BL-OCBE. The BL-OCBE has a much simpler and computationally efficient form, thus this method is generally preferred unless more accurate and robust results are desired.

4.4 Conclusions

In this chapter, we have focused on demonstrating the OCBE through application to three different tracking problems. These include a simple linear system with both natural mismodeling and an unknown perturbation, a LEO-based tracking scenario with mismodeled atmospheric drag and an unknown cross-track maneuver, and a GEO-based simulation where the observed target undergoes two unknown stationkeeping maneuvers.

The first simulation demonstrated the BL-OCBE as applied to a linear system. In this scenario the results are equivalent to a full nonlinear treatment due to the linear nature of the system.

This example demonstrated the algorithm's ability to successfully track a dynamically mismodeled system as well as reconstruct that mismodeling especially when the results are smoothed. In the case where an unknown perturbation was present, the algorithm was able to lock on to that perturbation and successfully reconstruct it even though it was biased from zero. The natural mismodeling was also successfully identified and reconstructed, though a separate parameter estimation scheme (such as the one discussed in Chapter 5) would be needed to permanently remove the mismodeling from the system.

The LEO and GEO simulations demonstrated this algorithm in an astrodynamics context. In both scenarios the OCBE was able to keep track of the target even in the presence of large maneuvers. These maneuvers were clearly observed in the process along with natural mismodeling. We were able to compensate for these by adjusting the assumed dynamic uncertainty. The resulting control estimates gave us information on these mismodelings including size, directionality, and a time-series representation of them. There were slight errors with the BL-OCBE due to pushing the bounds of the linearization assumption, but the algorithm never loses the track of the target. The Nonlinear OCBE generally has better tracking performance, but the differences are not always large unless a large maneuver has taken place. Given the BL-OCBE is much more efficient computationally this algorithm may generally be defaulted too unless long observation gaps and large maneuvers necessitate a nonlinear estimator.

While the algorithm successfully tracks the target in the presence of dynamic mismodeling, the process is very manual at this point and there is no formal method for identifying the presence of mismodeling other than analysis of measurement residuals. In the next two chapters we will alleviate these concerns by introducing a method to detect the presence of dynamic mismodeling and automatically compensate for it so that the user does not have to be in the loop while observations are being processed.

Chapter 5

Maneuver Detection and Reconstruction with the OCBE

The OCBE is an optimal state estimator that is robust to dynamic mismodeling, but its most advantageous properties relate to its control estimates. These control estimates are unique to the OCBE. On their own, they are reconstructions of mismodeled dyamics, thus they can indicate important aspects of mismodeling including: directionality, magnitude, intent (for active dynamics), and possibly even the source. Additionally, the controls can be used in a maneuver detection algorithm based on the control distance metric formulation of Holzinger, Scheeres, and Alfried [28].

In this chapter we will develop the maneuver detection abilities of the OCBE in a control distance metric framework. This will include an overview of the nonlinear metrics, the metrics in a GL-OCBE context, and the metrics in a BL-OCBE context. In each discussion we will treat the functional form of the metrics and the statistical properties of the metrics. There is also a discussion of how these statistics may be used to determine whether the calculated metric is statistically significant enough to indicate the presence of deterministic mismodeling in the system.

5.1 Nonlinear OCBE Distance Metrics

The estimates that come out of the OCBE may not be valid if there exists mismodeling in the system that was not compensated for. To ascertain the validity of our estimate we employ certain metrics to measure the validity of the fit. These metrics are specifically called the OCBE distance metrics, and they effectively measure the "distance" between the information put into the filter and the estimates coming out of the filter. Given both the inputs and estimates are stochastic values, the resulting distance metrics are stochastic as well. Using the stochastic properties of the distance metrics, we can determine whether the calculated distance metrics are statistically significant enough to indicate the presence of uncompensated mismodeling in the system.

These metrics measure distance in between members of a set defined by the inputs into the process. We define this set as shown below:

$$\mathcal{A} : \mathbb{R} \times \mathbb{R}^n \times \mathbb{R} \times \mathbb{R}^p \times \mathcal{U} \tag{5.1}$$

This set is defined by five quantities: initial time, initial state, final time, measurement, and control process. We define the the input information (a) and estimates (b) as members of this set as shown below.

$$\begin{aligned} a &= \left\{t_{k-1}, \bar{x}_{k-1|k-1}, t_k, \vec{Y}_k, \bar{u}(t)\right\} \in \mathcal{A} \\ b &= \left\{t_{k-1}, \hat{x}_{k-1|k}, t_k, h(t_k, \hat{x}_{k|k}), \hat{u}(t)\right\} \in \mathcal{A} \end{aligned} \tag{5.2}$$

The goal is to measure the distance between a and b, and determine if this distance is statistically significant to indicate the presence of uncompensated mismodeling.

In keeping with the nonlinear nature of the OCBE, the metrics designed for maneuver detection are fully nonlinear. Because of this statistics cannot be generated for them without losing generality in the state dynamics and the state-observation relationship. As such, this discussion will only define the metrics to be used. All statistical analysis will be reserved for the linearizations to follow. Once the nonlinear estimator is solved through iteration of the GL-OCBE, linear statistics may be used to perform maneuver detection for the nonlinear OCBE.

Following the control distance metric framework, we desire a metric that may be used to tell us whether an estimated control is statistically significant. A metric that captures this is the integrated Lagrangian portion of the OCBE cost function. Defined in Eq. 5.3, this metric will be referred to as the OCBE control distance metric.

$$D_C(a, b) = \int_{t_{k-1}}^{t_k} \frac{1}{2} \left(\vec{u}(\tau) - \bar{u}(\tau)\right)^T \tilde{Q}(\tau)^{-1} \left(\vec{u}(\tau) - \bar{u}(\tau)\right) d\tau \tag{5.3}$$

This metric balances the estimated control against the expected level of mismodeling weighted by the covariance in the dynamics. The larger the metric, the more significant the mismodeling. The metric is positive definite, and for Gaussian errors the resulting metric would have a χ^2-like form. In the GL-OCBE and BL-OCBE implementations these statistics will be derived along with a χ^2-based statistical test to determine if the control estimate represents actual mismodeling in the system.

This nonlinear metric is clearly a portion of the OCBE cost function. Following that logic one may develop distance metrics based on the other portions of the cost function. By creating separate metrics we are able to understand how the optimization is balancing the error in the system. It tells us whether the error is control dominated, measurement dominated, or a priori state dominated. This information provides more thorough overview of what is happening in the system, and allows us to address mismodeling when present even if the control metric does not indicate its presence.

The first of these metrics is called the OCBE measurement distance metric (Eq. 5.4). Like the control distance metric, it satisfies all of the properties of a distance metric [28], and it has a more historically significant form. Measurement residuals have long been used to determine if a filter is estimating properly. Because true state trajectories are unavailable in practice for filter analysis, the distribution of residuals may be used to assess the accuracy of the fit. The distribution should be mean zero with a covariance equal to the measurement covariance. For data sparse applications, though, this type of analysis is not necessarily possible. Instead a metric analysis may be done on a measurement-by-measurement basis (as is suggested here) to determine whether the residual is a function of error in the system or representative of some deterministic mismodeling.

$$D_M(a,b) = \frac{1}{2}\left(\vec{Y}_k - h(t_k,\vec{x}_k)\right)^T R_k^{-1}\left(\vec{Y}_k - h(t_k,\vec{x}_k)\right) \tag{5.4}$$

Similarly, the OCBE a priori state distance metric (Eq. 5.5), may be used to asses the appropriateness of the fit in terms of the state estimate at the a priori epoch. This method does not have as strong of a historical significance as the measurement metric because Kalman filters propagate a priori information to the measurement epoch. Thus, this metric is unique to the OCBE as well.

$$D_A(a,b) = \frac{1}{2}\left(\bar{x}_{k-1|k-1} - \vec{x}_{k-1}\right)^T \bar{P}_{k-1|k-1}^{-1}\left(\bar{x}_{k-1|k-1} - \vec{x}_{k-1}\right) \tag{5.5}$$

These three metrics allow us to independently assess the fit in terms of a priori state, measurement, and control errors. While there is coupling between the metrics because the optimal estimates are coupled. However, there may be situations where one metric detects an anomaly where another does not, so employing all three independently results in a more robust anomaly detection procedure. The anomalies detected will generally be in one of three categories: (1) mismodeled dynamics, (2) measurement outlier, and (3) a priori state outlier. The first anomaly is the focus of this estimator, but the others often occur in state estimation. As such, these three metrics may be employed to help inform what type of error is most likely to have occurred.

5.2 Maneuver Detection with OCBE Distance Metrics

The distance metrics as defined are all quadratic measures. For the linear estimators the inputs were defined as Gaussian, thus the outputs of the linear system are Gaussian as well. As will be shown each of the Gaussian random variables defining the metrics are zero-mean. As weighted quadratic-Gaussian measures these random variables are quite similar to χ^2 random variables. In this section we will detail a method for testing how statistically significant a metric is against a χ^2 distribution. As this method is numerical, we also provide an analytical method based on Gaussian properties. We will develop these methods for an arbitrary metric of the form defined below.

$$\begin{aligned} D_Z &= \vec{z}^T M_z \vec{z} \qquad (5.6) \\ E\left[\vec{z}\right] &= \vec{0} \\ E\left[\vec{z}\vec{z}^T\right] &= P_z \end{aligned}$$

As will be shown, each of the three metrics on a linear level conforms to the definition defined here.

The χ^2method for maneuver detection with these metrics relies upon a more accurate assumption than the Gaussian method we will discuss at the end of this section, but it is numerical as a result. The method follows Holzinger, Scheeres, and Alfriend's [28], original use of Pearson's approximation [54]. This approximates the distribution as a weighted chi-squared distribution, which is quite accurate given its quadratic-Gaussian functional form. The approximation begins by rearranging the distance metric into the form of Eq. 5.7.

$$\begin{aligned} D_z &= \sum_{i=1}^{r} \lambda_i U_i^2 \\ \vec{U} &= T^T P_z^{-1/2} \vec{z} \\ &= \begin{bmatrix} U_1 & \dots & U_r \end{bmatrix}^T \end{aligned} \tag{5.7}$$

This is an exact relation with no approximation made yet. In this notation the T matrix consists of the normalized eigenvectors of the matrix: $P_z^{-1/2} M_z P_z^{-1/2}$. λ_i are the accompanying eigenvalues. This method requires the set of eigenvectors to be orthonormal such that $T^{-1} = T^T$.

In this form we may apply Pearson's Approximation [54] such that the distance metric becomes a function of a chi-squared random variable with ν degrees of freedom (χ_ν^2) as shown below.

$$\begin{aligned} D_z &\approx \frac{\theta_3}{\theta_2} \chi_\nu^2 + \left(\theta_1 - \frac{\theta_2^2}{\theta_3} \right) \\ \theta_s &= \sum_{j=1}^{r} \lambda_j^s \\ \nu &= \frac{\theta_2^3}{\theta_3^2} \end{aligned} \tag{5.8}$$

The degrees of freedom associated with this chi-squared may be fractional. As such an interpolation method would need to be employed between integer degrees of freedom in order to obtain a continuous result.

Using this form of the distance metric we may perform a hypothesis test to determine whether the system is subject to deterministic mismodeling. We define our hypothesis as: the system is properly modeled and not subject to a deterministic errors. A threshold probability should be selected in order to run a one-tail χ^2 test. In general we select thresholds in the neighborhood of 95-99%, but this value should be selected based on the problem. Too large of a threshold promotes missed detections while too large promotes false detections. The χ_ν^2 value associated with this threshold percentile may be obtained numerically, then the result may be mapped into the distance metric of interest via Eq. 5.8. This threshold metric is then compared against the calculated metric. If the calculated metric is less than the threshold, then we confirm our null hypothesis that the system is properly modeled. However, if the metric exceeds the threshold we reject the null hypothesis and accept the alternative hypothesis that some deterministic mismodeling is present within the system.

While the χ^2 method is accurate, the Gaussian method is analytic. It assumes that the metric is actually Gaussian distributed according to the analytical mean and variance of distribution. This assumption will cause errors because the metric is positive definite thus it cannot be Gaussian, but it can provide reliable statistical threshold to test metrics against. This method follows the same procedure as the χ^2 method, but the threshold metric is obtained analytically through the definition of a z-score at the threshold percentile (Eq. 5.9).

$$D_{z,thresh} = \mu_z + \sigma_z z^* \tag{5.9}$$

As with the other method, the calculated metric is compared to this threshold to determine if the null hypothesis is accepted or rejected.

Once the null hypothesis has been rejected, the next step is compensating for the detected mismodeling. This is accomplished by increasing the assumed dynamic uncertainty ($\tilde{Q}(t)$). This process should be iterated until a maneuver is no longer detected. In practice, the aim is to select the assumed dynamic uncertainty that results in the metric and mean being equal. Details on this will be discussed in the development of the Adaptive OCBE (Chapter 6).

5.3 GL-OCBE Distance Metrics

Having defined the nonlinear metrics and the method for testing whether they are statistically significant, we now desire a linear version of the metrics so that we can incorporate them into our linear estimators. The version of the metrics linearized about an arbitrary initial state and adjoint will be called the GL-OCBE metrics. In this section we will derive these linearized metrics and their statistics. Using these values we may implement the χ^2 and Gaussian hypothesis testing methods to perform maneuver detection with each new measurement epoch.

Starting with the OCBE control distance metric, our goal is to linearize the control estimates, and obtain a form similar to Eq. 5.6. Using the GL-OCBE definition of the control estimate we define the difference from the a priori control as defined below.

$$\begin{aligned}\hat{u}(t) - \bar{u}(t) \approx &-\tilde{Q}(t)B(t)^T\Big[\left(\tilde{p}(t) + \vec{v}_p(t|t_{k-1})\right) + \Big(\Phi_{px}(t,t_{k-1}) - \Phi_{pp}(t,t_{k-1})\bar{P}^{-1}_{k-1|k-1}\Big)\delta\hat{x}_{k-1|k} \\ &+\Phi_{pp}(t,t_{k-1})\left(\bar{P}^{-1}_{k-1|k-1}\delta\bar{x}_{k-1|k-1} - \tilde{p}_{k-1}\right)\Big] \\ =&-\tilde{Q}(t)B(t)^T\Big[\vec{v}_p(t|t_{k-1}) + \Big(\Phi_{px}(t,t_{k-1}) - \Phi_{pp}(t,t_{k-1})\bar{P}^{-1}_{k-1|k-1}\Big)\hat{\eta}_{k-1|k} \\ &+\Phi_{pp}(t,t_{k-1})\bar{P}^{-1}_{k-1|k-1}\bar{\eta}_{k-1|k-1}\Big]\end{aligned}\tag{5.10}$$

As previously discussed, this difference is zero mean, which corresponds to the properties we desire for the Gaussian quadratic form of the metric. Defining a portion of this difference as $\Delta\vec{c}(t)$, we obtain its associated covariance as a function of time as described in Eq. 5.12.

$$\begin{aligned}\Delta\vec{c}(t) =&\Phi_{pp}(t,t_{k-1})\bar{P}^{-1}_{k-1|k-1}\left(\delta\bar{x}_{k-1|k-1} - \delta\hat{x}_{k-1|k}\right) + \Phi_{px}(t,t_{k-1})\delta\hat{x}_{k-1|k} \\ &+\left(\tilde{p}(t) + \vec{v}_p(t|t_{k-1})\right) - \Phi_{pp}(t,t_{k-1})\tilde{p}_{k-1} \\ =&\Phi_{pp}(t,t_{k-1})\bar{P}^{-1}_{k-1|k-1}\left(\bar{\eta}_{k-1|k-1} - \hat{\eta}_{k-1|k}\right) + \Phi_{px}(t,t_{k-1})\hat{\eta}_{k-1|k} + \vec{v}_p(t|t_{k-1})\end{aligned}\tag{5.11}$$

$$\begin{aligned}P_{\Delta c}(t) =&E\left[\Delta\vec{c}(t)\Delta\vec{c}(t)^T\right] \\ =&\Phi_{pp}(t,t_{k-1})\bar{P}^{-1}_{k-1|k-1}\Big[\hat{P}_{k-1|k} + \bar{P}_{k-1|k-1} - \bar{P}_{k-1|k-1}\left[\mathcal{I}_{k-1} - L_{k-1}\tilde{H}_k\left(\Phi_{xx} + \mathcal{P}_{k|k-1}\Phi_{px}\right)\right]^T \\ &-\left[\mathcal{I}_{k-1} - L_{k-1}\tilde{H}_k\left(\Phi_{xx} + \mathcal{P}_{k|k-1}\Phi_{px}\right)\right]\bar{P}_{k-1|k-1}\Big]\bar{P}^{-1}_{k-1|k-1}\Phi_{pp}(t,t_{k-1})^T + E\left[\vec{v}_p(t|t_{k-1})\vec{v}_p(t|t_{k-1})^T\right] \\ &+\Phi_{px}(t,t_{k-1})\hat{P}_{k-1|k}\Phi_{px}(t,t_{k-1})^T + \Big(\Phi_{px}(t,t_{k-1}) - \Phi_{pp}(t,t_{k-1})\bar{P}^{-1}_{k-1|k-1}\Big)E\left[\hat{\eta}_{k-1|k}\vec{v}_p(t|t_{k-1})^T\right] \\ &+E\left[\vec{v}_p(t|t_{k-1})\hat{\eta}^T_{k-1|k}\right]\Big(\Phi_{px}(t,t_{k-1}) - \Phi_{pp}(t,t_{k-1})\bar{P}^{-1}_{k-1|k-1}\Big)^T\end{aligned}\tag{5.12}$$

Having defined these values, we define the GL-OCBE control distance metric in terms of $\Delta\vec{c}(t)$ and its covariance as defined below.

$$D_C = \int_{t_{k-1}}^{t_k}\Delta\vec{c}(\tau)^T M_c(\tau)\Delta\vec{c}(\tau)d\tau\tag{5.13}$$

$$M_C(t) = \frac{1}{2}B(t)\tilde{Q}(t)B(t)^T \tag{5.14}$$

The result is slightly different than the form of Eq. 5.6 due to the presence of the integral. Because expectation operators and integrals are commutable we can still compute the statistics of this random variable in the same manner. The results of this calculation are summarized below.

$$\mu_C = \int_{t_{k-1}}^{t_k} \mathrm{Tr}\left[M_C(\tau)P_{\Delta c}(\tau)\right] d\tau \tag{5.15}$$

$$\sigma_C^2 = \int_{t_{k-1}}^{t_k} 2\mathrm{Tr}\left[M_C(\tau)P_{\Delta c}(\tau)M_C(\tau)P_{\Delta c}(\tau)\right] d\tau \tag{5.16}$$

The χ^2 approximation must be placed within the integral, thus the threshold like the mean and variance must be computed as a integral. Once this is computed, the hypothesis test may be run to test whether the control metric is statistically significant or not.

For the measurement metric, the linearization and simplification are straightforward due to the form of the equations. This linearization and simplification are shown below.

$$\begin{aligned} \vec{Y}_k - h(t_k, \hat{x}_{k|k}) &\approx \left[\vec{Y}_k - h(t_k, \tilde{x}_k)\right] - \tilde{H}_k \delta\hat{x}_{k|k} \\ &= \left(I_{p\times p} - \tilde{H}_k L_k\right)\left[\delta\vec{y}_k - \tilde{H}_k\left(\delta\bar{x}_{k|k-1} + \tilde{b}_k + \vec{v}_x(t_k)\right)\right] \\ &= \left(I_{p\times p} - \tilde{H}_k L_k\right)\left[\vec{\epsilon}_k - \tilde{H}_k \bar{\eta}_{k|k-1}\right] \end{aligned} \tag{5.17}$$

From this development it is clear that residual is zero mean with a known covariance. Subbing this simplification into the nonlinear OCBE measurement distance metric definition (Eq. 5.4), we obtain the GL-OCBE in terms of the measurement and the propagated a priori state(Eqs. 5.18 and 5.19).

$$D_M = \left[\delta\vec{y}_k - \tilde{H}_k\left(\delta\bar{x}_{k|k-1} + \tilde{b}_k + \vec{v}_x(t_k)\right)\right]^T M_M \left[\delta\vec{y}_k - \tilde{H}_k\left(\delta\bar{x}_{k|k-1} + \tilde{b}_k + \vec{v}_x(t_k)\right)\right] \tag{5.18}$$

$$M_M = \frac{1}{2}\left(I_{p\times p} - \tilde{H}_k L_k\right)^T R_k^{-1}\left(I_{p\times p} - \tilde{H}_k L_k\right) \tag{5.19}$$

Following the control distance metric development, the analytical mean and variance of this metric's distribution calculated as shown below.

$$\mu_M = \mathrm{Tr}\left[M_M\left(R_k + \tilde{H}_k \bar{P}_{k|k-1}\tilde{H}_k^T\right)\right] \tag{5.20}$$

$$\sigma_M^2 = 2\mathrm{Tr}\left[M_M\left(R_k + \tilde{H}_k\bar{P}_{k|k-1}\tilde{H}_k^T\right)M_M\left(R_k + \tilde{H}_k\bar{P}_{k|k-1}\tilde{H}_k^T\right)\right] \tag{5.21}$$

This metric is easily implementable because it requires no extra calculations beyond the matrices already developed in the OCBE. Its form is much simpler than the control metric in a GL-OCBE context. As we will see, it is also a far simpler model than the GL-OCBE a priori state distance metric.

While the nonlinear form of the OCBE a priori state distance metric is quite simple, the GL-OCBE has some complexities due to the more complex form of the state estimate at the a priori epoch. The development of the linear a priori state difference and its associated covariance are given below. The development of this covariance follows the derivation in Appendix B.3.

$$\begin{aligned}
\Delta\vec{a} =& \bar{x}_{k-1|k-1} - \hat{x}_{k-1|k} \\
\approx& \delta\bar{x}_{k-1|k-1} - \delta\hat{x}_{k-1|k} \\
=& \left(I_{n\times n} - \mathcal{I}_{k-1}\right)\delta\bar{x}_{k-1|k-1} - \mathcal{I}_{k-1}\tilde{b}_{k-1} - L_{k-1}\left[\delta\vec{y}_k - \tilde{H}_k\left(\delta\bar{x}_{k|k-1} + \tilde{b}_k + \vec{v}_x(t_k)\right)\right] \\
=& \left(I_{n\times n} - \mathcal{I}_{k-1}\right)\bar{\eta}_{k-1|k-1} - \mathcal{I}_{k-1}\bar{P}_{k-1|k-1}\Phi_{pp}^{-1}\vec{v}_p(t_k) - L_{k-1}\left[\vec{\epsilon} - \tilde{H}_k\bar{\eta}_{k|k-1}\right]
\end{aligned} \tag{5.22}$$

$$\begin{aligned}
P_a =& E\left[\Delta\vec{a}\Delta\vec{a}^T\right] \\
=& \left(I_{n\times n} - \mathcal{I}_{k-1}\right)\bar{P}_{k-1|k-1}\left(I_{n\times n} - \mathcal{I}_{k-1}\right)^T + L_{k-1}\left(R_k + \tilde{H}_k\bar{P}_{k|k-1}\tilde{H}_k^T\right)L_{k-1}^T \\
&+ \left(\mathcal{I}_{k-1}\bar{P}_{k-1|k-1}\Phi_{pp}^{-1}\right)E\left[\vec{v}_p(t_k)\vec{v}_p(t_k)^T\right]\left(\mathcal{I}_{k-1}\bar{P}_{k-1|k-1}\Phi_{pp}^{-1}\right)^T \\
&+ \left(I_{n\times n} - \mathcal{I}_{k-1}\right)\bar{P}_{k-1|k-1}\left[\Phi_{xx} + \mathcal{P}_{k|k-1}\Phi_{px}\right]^T\tilde{H}_k^T L_{k-1}^T \\
&+ L_{k-1}\tilde{H}_k\left[\Phi_{xx} + \mathcal{P}_{k|k-1}\Phi_{px}\right]\bar{P}_{k-1|k-1}\left(I_{n\times n} - \mathcal{I}_{k-1}\right)^T \\
&- \left(\mathcal{I}_{k-1}\bar{P}_{k-1|k-1}\Phi_{pp}^{-1}\right)\left(E\left[v_p(t_k)\vec{v}_p(t_k)^T\right]\mathcal{P}_{k|k-1}^T + E\left[\vec{v}_p(t_k)\vec{v}_x(t_k)^T\right]\right)^T\tilde{H}_k^T L_{k-1}^T \\
&- L_{k-1}\tilde{H}_k\left(\mathcal{P}_{k|k-1}E\left[\vec{v}_p(t_k)\vec{v}_p(t_k)^T\right] + E\left[\vec{v}_x(t_k)\vec{v}_p(t_k)^T\right]\right)\left(\mathcal{I}_{k-1}\bar{P}_{k-1|k-1}\Phi_{pp}^{-1}\right)^T
\end{aligned} \tag{5.23}$$

With these definitions, we may define the GL-OCBE a priori state distance metric and its statistics as shown below.

$$D_A = \Delta\vec{a}^T M_A \Delta\vec{a} \tag{5.24}$$

$$M_A = \frac{1}{2}\bar{P}_{k-1|k-1}^{-1} \tag{5.25}$$

$$\mu_A = \mathrm{Tr}\left[M_A P_a\right] \tag{5.26}$$

$$\sigma_A^2 = 2\mathrm{Tr}\left[M_A P_a M_A P_a\right] \tag{5.27}$$

This fully defines all three metrics and their statistics in a GL-OCBE context. In the next section we will simplify these expressions for implementation with the BL-OCBE. Additionally, a new combined metric will be defined that has a specific property specific to the BL-OCBE.

5.4 BL-OCBE Distance Metrics

The BL-OCBE metrics are obtained via simplification of the GL-OCBE metrics in a similar process to the BL-OCBE derivation. In this section we define all three OCBE metrics in a BL-OCBE context as well as define a new combined metric.

Starting with the control metric, the control estimate deviation for the BL-OCBE estimate is defined in Eq. 5.28.

$$\begin{aligned}\hat{u}(t) - \bar{u}(t) \approx& -\tilde{Q}(t)B(t)^T\Phi_{pp}(t,t_{k-1})\bar{P}_{k-1|k-1}^{-1}\left[\delta\bar{x}_{k-1|k-1} - \delta\hat{x}_{k-1|k}\right]\\ =&\tilde{Q}(t)B(t)^T\Phi_{pp}(t,t_{k-1})\bar{P}_{k-1|k-1}^{-1}L_{k-1}\left[\delta\vec{y}_k - \tilde{H}_k\left(\delta\bar{x}_{k|k-1} + \vec{v}_x(t_k|t_{k-1})\right)\right]\\ =&\tilde{Q}(t)B(t)^T\Phi_{pp}(t,t_{k-1})\bar{P}_{k-1|k-1}^{-1}L_{k-1}\left[\vec{\epsilon}_k - \tilde{H}_k\bar{\eta}_{k|k-1}\right]\end{aligned} \tag{5.28}$$

Subbing this into the definition of the metric we obtain the BL-OCBE control distance metric as shown in Eqs. 5.30 and 5.30.

$$D_C = \left[\delta\vec{y}_k - \tilde{H}_k\left(\delta\bar{x}_{k|k-1} + \vec{v}_x(t_k)\right)\right]^T M_C\left[\delta\vec{y}_k - \tilde{H}_k\left(\delta\bar{x}_{k|k-1} + \vec{v}_x(t_k)\right)\right] \tag{5.29}$$

$$\begin{aligned}M_C =&\frac{1}{2}L_{k-1}^T\bar{P}_{k-1|k-1}^{-1}\left[\int_{t_{k-1}}^{t_k}\Phi_{pp}(\tau,t_{k-1})^T B(\tau)\tilde{Q}(\tau)B(\tau)^T\Phi_{pp}(\tau,t_{k-1})d\tau\right]\bar{P}_{k-1|k-1}^{-1}L_{k-1}\\ =&-\frac{1}{2}L_{k-1}^T\bar{P}_{k-1|k-1}^{-1}\Phi_{pp}^T\left(\Phi_{xp}\Phi_{xx}^T\right)\Phi_{pp}\bar{P}_{k-1|k-1}^{-1}L_{k-1}\end{aligned} \tag{5.30}$$

An important result is that the metric gain matrix is equivalent to a product of already calculated portions of the STM, thus the BL-OCBE version of the metric does not require any additional integration. This makes it far more implementable into already existing systems. The resulting mean and variance statistics for this metric are defined below.

$$\mu_C = \mathrm{Tr}\left[M_C\left(R_k + \tilde{H}_k\bar{P}_{k|k-1}\tilde{H}_k^T\right)\right] \tag{5.31}$$

$$\sigma_C^2 = 2\mathrm{Tr}\left[M_C\left(R_k + \tilde{H}_k\bar{P}_{k|k-1}\tilde{H}_k^T\right)M_C\left(R_k + \tilde{H}_k\bar{P}_{k|k-1}\tilde{H}_k^T\right)\right] \tag{5.32}$$

Moving to the measurement metric, the postfit measurement residual for the BL-OCBE is defined in Eq. 5.33.

$$\begin{aligned}\vec{Y}_k - h(t_k, \hat{x}_{k|k}) &\approx \left[\vec{Y}_k - h(t_k, \tilde{x}_k)\right] - \tilde{H}_k\delta\hat{x}_{k|k} \\ &= \left(I_{p\times p} - \tilde{H}_kL_k\right)\left[\delta\vec{y}_k - \tilde{H}_k\left(\delta\bar{x}_{k|k-1} + \vec{v}_x(t_k)\right)\right] \\ &= \left(I_{p\times p} - \tilde{H}_kL_k\right)\left[\vec{\epsilon}_k - \tilde{H}_k\bar{\eta}_{k|k-1}\right]\end{aligned} \tag{5.33}$$

Plugging this result into the nonlinear definition of the OCBE measurement metric, we obtain the BL-OCBE measurement metric as defined in Eqs. 5.34 and 5.35.

$$D_M = \left[\delta\vec{y}_k - \tilde{H}_k\left(\delta\bar{x}_{k|k-1} + \vec{v}_x(t_k)\right)\right]^T M_M\left[\delta\vec{y}_k - \tilde{H}_k\left(\delta\bar{x}_{k|k-1} + \vec{v}_x(t_k)\right)\right] \tag{5.34}$$

$$M_M = \frac{1}{2}\left(I_{p\times p} - \tilde{H}_kL_k\right)^T R_k^{-1}\left(I_{p\times p} - \tilde{H}_kL_k\right) \tag{5.35}$$

The form is very similar to the GL-OCBE measurement metric other than the missing bias terms. Its also important to note that the BL-OCBE control and measurement metrics are both solely functions of the filter innovations with different gain matrices. This means the metrics will display the exact same behavior (i.e. both will detect or not detect simultaneously) when scalar measurements are used. This generally means there is no use in using both metrics simultaneously in these situations. The associated mean and variance for this metric are calculated below.

$$\mu_M = \mathrm{Tr}\left[M_M\left(R_k + \tilde{H}_k\bar{P}_{k|k-1}\tilde{H}_k^T\right)\right] \tag{5.36}$$

$$\sigma_M^2 = 2\mathrm{Tr}\left[M_M\left(R_k + \tilde{H}_k\bar{P}_{k|k-1}\tilde{H}_k^T\right)M_M\left(R_k + \tilde{H}_k\bar{P}_{k|k-1}\tilde{H}_k^T\right)\right] \tag{5.37}$$

To obtain the BL-OCBE a priori state distance metric, we first define the a priori state estimate deviation as shown below.

$$\begin{aligned}\bar{x}_{k-1|k-1} - \hat{x}_{k-1|k} &= -L_{k-1}\left[\delta\vec{y}_k - \tilde{H}_k\left(\delta\bar{x}_{k|k-1} + \vec{v}_x(t_k)\right)\right] \\ &= -L_{k-1}\left[\vec{\epsilon} - \tilde{H}_k\bar{\eta}_{k|k-1}\right]\end{aligned} \tag{5.38}$$

Plugging this result into the nonlinear OCBE a priori state distance metric, we obtain the BL-OCBE a priori state distance metric as shown in Eqs. 5.39 and 5.40. The associated mean and variance are defined in Eqs. 5.41 and 5.42.

$$D_A = \left[\delta\vec{y}_k - \tilde{H}_k\left(\delta\bar{x}_{k|k-1} + \vec{v}_x(t_k)\right)\right]^T M_A\left[\delta\vec{y}_k - \tilde{H}_k\left(\delta\bar{x}_{k|k-1} + \vec{v}_x(t_k)\right)\right] \tag{5.39}$$

$$M_A = \frac{1}{2}L_{k-1}^T\bar{P}_{k-1|k-1}^{-1}L_{k-1} \tag{5.40}$$

$$\mu_A = \mathrm{Tr}\left[M_A\left(R_k + \tilde{H}_k\bar{P}_{k|k-1}\tilde{H}_k^T\right)\right] \tag{5.41}$$

$$\sigma_A^2 = 2\mathrm{Tr}\left[M_A\left(R_k + \tilde{H}_k\bar{P}_{k|k-1}\tilde{H}_k^T\right)M_A\left(R_k + \tilde{H}_k\bar{P}_{k|k-1}\tilde{H}_k^T\right)\right] \tag{5.42}$$

Just like the previous two BL-OCBE metrics, this metric is a function of the filter innovations weighted by a gain matrix. This means that all three metrics are completely coupled for scalar measurement. If one detects a measurement the other two will as well. This means that only one metric is necessary to implement for maneuver detection purposes. Instead of selecting one of the metrics defined here, we define a combined metric, which is equal to the cost function of the OCBE. Summing the three BL-OCBE metrics we obtain the BL-OCBE distance metric as defined in Eqs. 5.43 and 5.44.

$$\begin{aligned}D_J &= D_A + D_M + D_C \\ &= \left[\delta\vec{y}_k - \tilde{H}_k\left(\delta\bar{x}_{k|k-1} + \vec{v}_x(t_k)\right)\right]^T M_J\left[\delta\vec{y}_k - \tilde{H}_k\left(\delta\bar{x}_{k|k-1} + \vec{v}_x(t_k)\right)\right]\end{aligned} \tag{5.43}$$

$$M_J = \frac{1}{2}\left(R_k + \tilde{H}_k \bar{P}_{k|k-1} \tilde{H}_k^T\right)^{-1} \tag{5.44}$$

Other than having the significance that this metric defines the OCBE, it also has a special property. Because its gain matrix is a scalar multiple of the inverse of the covariance of the metric's random vector, the metric may be reformulated as the sum of p (the number of measurements at t_k) independent-identically distributed zero-mean Gaussian random variables with unit variance. A metric of this form is identical to a χ^2 random variable with p degrees of freedom (Eq. 5.45).

$$D_J = \frac{1}{2}\chi_p^2 \tag{5.45}$$

Thus, for this metric Pearson's approximation is unnecessary - an exact relation to a χ^2 statistic is known. The χ^2-based maneuver detection method may be employed using this mapping as opposed to Pearson's Approximation (Eq. 5.8). To complete our definition of this metric we calculate its mean and variance as defined below.

$$\mu_J = p/2 \tag{5.46}$$

$$\sigma_J^2 = p/2 \tag{5.47}$$

It is interesting to note that the mean, variance, and threshold associated with this metric are independent of the assumed dynamic uncertainty - the one tuneable parameter the user may adjust to improve tracking. This result will be discussed in greater depth during the development of the Adaptive BL-OCBE in Chapter 6.

The BL-OCBE distance metric encompasses all three forms of error: a priori state error, measurement error, and dynamics mismodeling. We obtained an analytical result that tells us this metric has an exact relation to a known χ^2 statistic, which allows for more precise maneuver detection. After a maneuver is detected the maneuver reconstruction process commences. The control estimates are a reconstruction in themselves, but it is possible to extract more information. In the next section we will discuss a method for estimating natural dynamics using the estimated control profiles.

5.5 Natural Dynamics Estimation with Optimal Control Policies

The estimated controls that come out of the OCBE model the mismodeled dynamics within the system. As such they can be used to understand the source of the mismodeling. If that source is mismodeled natural dynamics we can estimate the parameters of those dynamics via a method discussed in this section. In this section we develop a cost function meant to estimate solar radiation pressure and atmospheric drag parameters (the main object-dependent perturbations in Earth orbit) by projecting the estimated controls on to a basis of these perturbations. For the purposes of this discussion the term "missing dynamics" refers to the difference (at each time) in acceleration between the true trajectory and the mismodeled trajectory (without the optimal control input). This difference identifies approximately how much control effort would be needed to stay on the true trajectory, which is what we are attempting to estimate via the optimal control policy. First we identify the similarities between optimal and natural dynamics, and follow this with a discussion of how these similarities may be used in this estimation method.

5.5.1 Comparison of Optimal and Natural Dynamics

The Optimal Control Policies (OCPs) resulting from the quadratic cost, as defined, may be used to assess the optimality of natural forces because (like natural forces) they are continuous and smooth. Figure 5.1 depicts the similarities between natural dynamics and OCPs for a case where drag and SRP are both mismodeled by 100%. These are evaluated on a nearly circular LEO trajectory (see LEO parameters in Table 5.2). The acceleration profiles agree almost exactly. There are only slight misalignments with the acceleration vector (less than 0.5 degrees for all time). Other than this the magnitude and periodicity of the dynamics are also well preserved. We can use this property to obtain information about these unknown natural dynamics.

When the boundary time and states are fixed we find that OCPs and the natural dynamics they replace are almost identical. This demonstrates that natural dynamics tend to minimize the quadratic control policy. This is likely due to the constraints in the system that limit the optimality

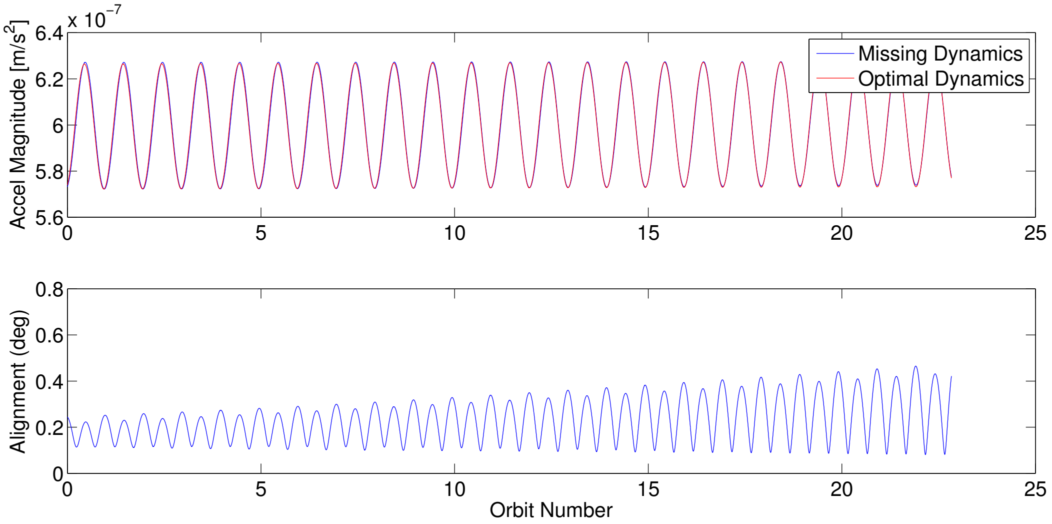

Figure 5.1: Optimal control policy with mismodeled atmospheric drag and SRP for true boundary states. (Top) Missing dynamics and OCP magnitudes. (Bottom) Alignment of OCP with missing dynamics

of the solution. In a typical tracking scenario there will be uncertainty in the boundary estimates, so it is important to see what occurs when boundary state uncertainty is introduced. In Fig. 5.2 we see a comparison between natural dynamics and OCPs when 100 m and 0.1 m/s Gaussian uncertainties are added to the initial and final states and there is a 100% error in both drag and SRP (as in the previous example). In this dispersed analysis we find that the similarities between the the OCPs and natural dynamics are not as strong (as is expected), but they still exist. Alignment can differ a lot at times, but generally stays in the lower range (acute angles). The periodicity is also largely maintained. The magnitude agreement is not as strong as the nominal case, but differences do tend to be an order of magnitude less than the true magnitude. For smaller boundary uncertainties we see better agreement (as would be expected). Reducing the boundary uncertainty we find dispersed trajectories that agree more with truth, and as we iterate and converge toward truth we find behavior closer to truth as well. While this dispersed analysis shows deviation from the true trajectory we still see signatures of the underlying true dynamics.

Through the nominal analysis we have identified a relation between OCPs and the natural dynamics it is replacing. For the nominal (true boundary state case) the accelerations are nearly

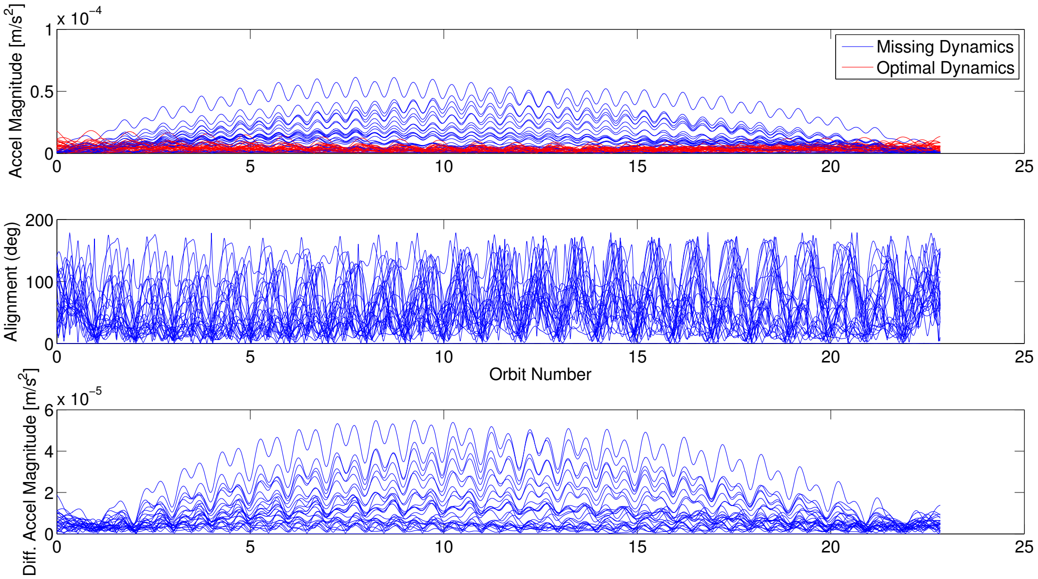

Figure 5.2: Optimal control policy with mismodeled atmospheric drag and SRP for dispersed boundary states. (Top) Missing dynamics and OCP magnitudes (Middle) Alignment of OCP with missing dynamics. (Bottom) Magnitude of differenced OCP and missing natural dynamic accelerations.

identical. Deviating from the boundary states we find larger differences in the accelerations, but similarities still remain. From these results we hypothesize that OCPs may be used to estimate the natural dynamics they are replacing.

5.5.2 Estimating Natural Dynamics Using OCPs

Following the hypothesis of the previous subsection, we develop a cost function that includes linearly mismodeled atmospheric drag and SRP (i.e. limited to coefficient errors) that act in place of the OCP. Essentially, when this cost function is minimized with respect to the mismodeleing parameters the degree to which each force is mismodeled may be quantified, and in an iterative process the OCP can be removed in place of updated natural dynamics. This cost function (with a quadratic form similar to the OCP cost function) is shown in Eqn. 5.48 with additional definitions in Eqns. 5.49 and 5.50.

$$\mathcal{J}(\Delta\vec{C}) = \int_{t_a}^{t_b} \frac{1}{2}\left(\hat{u}(\tau) - A(\vec{x}^*(\tau),\tau)\Delta\vec{C}\right)^T\left(\hat{u}(\tau) - A(\vec{x}^*(\tau),\tau)\Delta\vec{C}\right)d\tau \tag{5.48}$$

$$A(\vec{x}(t),t) = \begin{bmatrix} \tilde{a}_{Drag}(t,\vec{x}(t)) & \tilde{a}_{SRP}(t,\vec{x}(t)) \end{bmatrix} = \begin{bmatrix} -\frac{1}{2}\rho(r)v_{rel}\vec{v}_{rel} & p_{SRP}\left(\frac{S_{\vec{r}}}{S_r}\right) \end{bmatrix} \tag{5.49}$$

$$\Delta\vec{C} = \begin{bmatrix} \Delta B \\ \Delta P \end{bmatrix} \tag{5.50}$$

We seek the adjustments to the perturbation parameters ($\Delta\vec{C}$) that minimize the cost. This seeks to pull natural dynamics out of the optimal control, thus driving the control toward zero so that a natural (ballistic) trajectory may be obtained. Assuming the movements are ballistic this would drive the system toward the true dynamical model. The minimization and associated optimal solution are given in Eqns. 5.51 and 5.52, respectively.

$$\frac{\partial\mathcal{J}}{\partial\Delta\vec{C}} = -\int_{t_a}^{t_b}\left(\vec{u}^*(\tau) - A(\vec{x}^*(\tau),\tau)\Delta\vec{C}\right)^T A(\vec{x}^*(\tau),\tau)d\tau = 0 \tag{5.51}$$

$$\Delta\vec{C} = \left(\int_{t_a}^{t_b} A(\vec{x}^*(\tau),\tau)^T A(\vec{x}^*(\tau),\tau)d\tau\right)^{-1}\left(\int_{t_a}^{t_b} A(\vec{x}^*(\tau),\tau)^T\vec{u}^*(\tau)d\tau\right) \tag{5.52}$$

Investigating these equations, we find that the process indicates that no update to the dynamics is needed ($\Delta\vec{C} = \vec{0}$) when one of two situations occurs: (1) the optimal control policy is identically zero for all time or (2) the optimal control policy is orthogonal to the plane in which the drag and SRP perturbations lie. The first case occurs when the iterative estimation procedure is able to fully account for the OCP with drag and SRP mismodeling (a ballistic trajectory is found). The second case is more common. This occurs when additional error ensures that a ballistic trajectory cannot be established between the boundary states in the given time. This additional error typically comes from inaccurate boundary states or unmodeled dynamics such as a maneuver. These errors cause the parameter estimates to deviate from the truth, but in the case of inaccurate boundary conditions we can quantify the expected uncertainty in the parameter estimates.

To account for parameter uncertainty as a function of known error we expand the cost function in terms of uncertainty in the boundary states as shown in Eqn. 5.55 using the results from Eqn. 5.54.

$$\Lambda(t,t_0) = \begin{bmatrix} \Phi_{px}(t,t_0) - \Phi_{pp}(t,t_0)\Phi_{xp}(t_f,t_0)^\dagger\Phi_{xx}(t_f,t_0) & \Phi_{pp}(t,t_0)\Phi_{xp}(t_f,t_0)^\dagger \end{bmatrix} \tag{5.53}$$

$$\delta\vec{u}(t) = -\tilde{Q}\frac{\partial\vec{f}}{\partial\vec{u}}^T\Lambda(t,t_0)\delta\vec{z} \tag{5.54}$$

$$\begin{aligned}\mathcal{J}+\Delta\mathcal{J} &= \int_{t_a}^{t_b}\frac{1}{2}\left(\hat{u}(\tau)-\tilde{Q}\frac{\partial\vec{f}}{\partial\vec{u}}^T\Lambda(t,t_0)\delta\vec{z}-A(\hat{x}(\tau),\tau)\Delta\vec{C}\right)^T(\hat{u}(\tau) \\ &\quad -\tilde{Q}\frac{\partial\vec{f}}{\partial\vec{u}}^T\Lambda(t,t_0)\delta\vec{z}-A(\hat{x}(\tau),\tau)\Delta\vec{C}\Bigg)d\tau\end{aligned} \tag{5.55}$$

$$\begin{aligned}\Delta\vec{C} &= \left(\int_{t_a}^{t_b}A(\hat{x}(\tau),\tau)^TA(\hat{x}(\tau),\tau)d\tau\right)^{-1}\Bigg[\int_{t_a}^{t_b}A(\hat{x}(\tau),\tau)^T\hat{u}(\tau)d\tau \\ &\quad -\left(\int_{t_a}^{t_b}A(\hat{x}(\tau),\tau)^T\tilde{Q}\frac{\partial\vec{f}}{\partial\vec{u}}^T\Lambda(t,t_0)d\tau\right)\delta\vec{z}\Bigg]\end{aligned} \tag{5.56}$$

In this expansion we do not consider deviations in the natural dynamics due to boundary state uncertainty - a separate analysis indicated this effect to be negligible.

Using expectation operators we find that the expected value for the parameter deviation estimates is the same as that for the given by Eqn. 5.52, assuming unbiased boundary state deviaitons. We also obtain the associated variance-covariance matrix as shown in Eqn. 5.57.

$$\begin{aligned}P_{\Delta C} &= \left(\int_{t_a}^{t_b}A(\hat{x}(\tau),\tau)^TA(\hat{x}(\tau),\tau)d\tau\right)^{-1}\left(\int_{t_a}^{t_b}A(\hat{x}(\tau),\tau)^T\tilde{Q}\frac{\partial\vec{f}}{\partial\vec{u}}^T\Lambda(t,t_0)d\tau\right)P_z \\ &\quad \times\left(\int_{t_a}^{t_b}\Lambda(t,t_0)^T\frac{\partial\vec{f}}{\partial\vec{u}}\tilde{Q}A(\hat{x}(\tau),\tau)d\tau\right)\left(\int_{t_a}^{t_b}A(\hat{x}(\tau),\tau)^TA(\hat{x}(\tau),\tau)d\tau\right)^{-1}\end{aligned} \tag{5.57}$$

To verify this analytical model, a Monte Carlo analysis was performed to determine the nonlinear effect of boundary state uncertainty (Fig. 3). This analysis includes 100 m and 1 m?s error on the boundary states at an orbital altitude of 1000 km (a region where SRP and atmospheric drag have a similar magnitude). The simulation includes 3,873 nonlinear perturbation parameter estimates plotted as points with 1-3 sigma envelopes from the linear covariance approximation plotted for comparison. There are definite similarities between the numerical and analytical results. The covariance envelopes appropriately cover the spread of the nonlinear estimates, with the densest region around truth. The nonlinear results do not have the characteristic elliptical shape that linear theory predicts. They are more tightly packed along the minor axis of the covariance ellipse, and they extend too far along the major axis. Additionally, there is a slight rotation between the nonlinear and linear spreads, but it is hardly perceptible. These deviations from the analytical model are due to the linearizations made during the analytical formulation that discount perturbation coupling. In general though, this analytical covariance adequately represents the expected deviation in parameter estimates due to boundary state error.

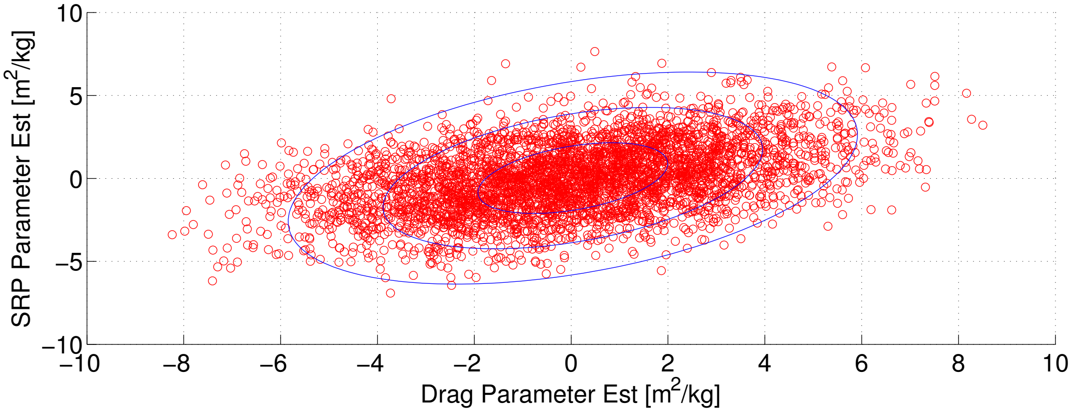

Figure 5.3: Nonlinear dispersed boundary state analysis with comparison to analytical covariance envelopes (1-3 σ).

Typically, this estimation procedure must be performed iteratively because the original OCP trajectory does not exactly correspond to the true trajectory due to the slight differences between the OCP and true perturbations as mentioned earlier. The complete iterative method is described below:

(1) Obtain initial/final states, time of flight, uncertainties, and nominal dynamical model ($i = 1$)

(2) Generate OCP for the given boundary states/times using the i^{th} nominal dynamical model

(3) With the generated OCP trajectory minimize the estimation cost function (Eqn. 5.48) using Eqn. 5.52

(4) Update the nominal atmospheric drag and SRP parameters as indicated in Eqn. 5.58.

$$\widetilde{C}^{i+1} = \widetilde{C}^{i} + \Delta\vec{C}^{i} \tag{5.58}$$

(5) Evaluate convergence using one of the following criteria:

   (a) Option 1 - Compare the distance metrics between two successive iterations to check for convergence: $\left|\frac{d_C^{i+1}(a,b) - d_C^{i}(a,b)}{d_C^{i+1}(a,b)}\right| < \delta$

   (b) Option 2 - Compare the dynamics parameter update magnitude compared to magnitude of nominal values to check for convergence: $\sqrt{\frac{(\Delta\vec{C}^i)^T W(\Delta\vec{C}^i)}{(\tilde{C}^i)^T W(\tilde{C}^i)}} < \delta$. If the nominal values are zero, then the denominator may be excluded.

(6) If convergence fails, then let $i = i+1$ and iterate by returning to step 2. Otherwise continue.

(7) Having converged set the final estimates: $\widetilde{C}_{est} = \widetilde{C}^{i+1}$

This iterative method has two options for convergence evaluation. These are related, but each expresses the convergence with a different physical significance. If tolerances are given in terms of distance metrics Option 1 is preferred, but if tolerances are geared more toward dynamics parameters Option 2 is preferred. The number of iterations needed to obtain convergence is generally a function of the boundary state uncertainty and the tolerances set. For the simulations in this paper we found about five iterations was enough to obtain convergence. In practice, we have not seen the process diverge, so convergence failures generally only occur when convergence is not deemed fast enough. These failures are detected by placing a maximum number of iterations on the process, so that when the process exceeds this iteration limit the estimation is stopped and the results are flagged with a failure indication.

The distance metric itself generally cannot be used as a convergence metric. Even though each iteration decreases the distance metric by turning control into natural dynamics, all of the control policy cannot be attributed perturbation mismodeling. The remaining control is usually the result of boundary state uncertainty or the presence of some other mismodeled acceleration. The distance metric remaining after estimating drag and SRP may be used to detect maneuvers in the same manner as discussed in the previous section. After drag and SRP mismodeling is removed through estimation, the distance metrics should conform to the probability distribution established by the boundary state uncertainty. If the remaining value still exceeds the calculated threshold we can conclude that some other dynamics mismodeling (maneuver) is present. An example of detecting a maneuver after estimation is provided in the following section.

This process may also be expanded to a batch process where the estimation procedure is run for each pair of states, and the estimates are combined in a weighted least-squares batch process. The estimate and covariance for this batch estimate are given in Eqns. 5.59 and 5.60, respectively.

$$\Delta\vec{C} = \left(\sum_{i=1}^{N} P_{\Delta C_i}^{-1}\right)^{-1} \left(\sum_{i=1}^{N} P_{\Delta C_i}^{-1} \Delta\vec{C}_i\right) \tag{5.59}$$

$$P_{\Delta C} = \left(\sum_{i=1}^{N} P_{\Delta C_i}^{-1}\right)^{-1} \tag{5.60}$$

In these expressions $\Delta\vec{C}_i$ and $P_{\Delta C_i}$ are the estimate and covariance of the dynamics parameter deviation for the ith measurement epoch, respectively. This is the recommended implementation of this algorithm, as it greatly increases the accuracy of the algorithm, and it is easily implementable in a tracking algorithm. This implementation also allows the user to identify outliers, which can signify the presence of maneuvers.

5.6 Sample Natural Dynamics Estimation Applications

In this section, we demonstrate the effectiveness of this algorithm through sample tracking scenarios. In the first simulation we demonstrate the use of this algorithm for LEO and GEO tracking with mismodeled drag and SRP parameters. In the second simulation, we also estimate mismodeled drag and SRP, but there is an additional unmodeled maneuver in the data. The true vehicle dynamics parameters used in these simulations are shown in Table 5.1.

The parameters were chosen to represent realistic objects in orbit. Specifically, the LEO case uses values consistent with a complete satellite and the GEO example is more representative of debris (hence the higher area to mass ratio). The LEO values are a combination of a reflectivity obtained from the TOPEX/POSEIDON spacecraft [62], area to mass ratio calculated from the dimensions and mass of ESA's Envisat [3], and a generic drag coefficient given by Vallado [84]. The GEO area to mass ratio was selected to be a low level for debris, but still higher than most complete spacecraft based on values given by Herzog and Schildknecht [26]. The higher reflectivity relative to the LEO example is representative of the fact that SRP-dominated debris generally consists of the most reflective portions of a spacecraft such as Multi-Layer Insulation (MLI) [17].

Table 5.1: True Object Parameters for LEO and GEO Simulations

Parameter	Notation	LEO Value	GEO Value	Units
Area to Mass Ratio	A/m	0.016	0.500	m^2/kg
Drag Coefficient	C_D	2.20	n/a	n/a
Refelctivity Coefficient	S	1.25	1.50	n/a

5.6.1 Simulation I: Biased Dynamics

This simulation includes two separate cases. One focuses on LEO tracking (drag-dominated) and the other focuses on GEO tracking (SRP-dominated). Drag is nonexistent at GEO, so estimating it can cause numerical issues. Similarily, drag is far stronger in LEO orbits than SRP for typical satellite geometries, which leads to issues estimating SRP as accurately. For this reason we only focus on the dominant perturbation in each regime (though SRP estimates are still reported for LEO tracking scenarios). Initial Keplerian elements are provided for each of these cases in Table 5.2.

Table 5.2: Initial Keplerian orbital elements for LEO and GEO cases in Simulation I

Parameter	Notation	LEO Value	GEO Value	Units
Semimajor Axis	a	6878.1363	$4.2164E+07$	km
Eccentricity	e	0.05	0.01	n/a
Inclination	i	50	0.05	deg
Right Asc. of the Asc. Node	Ω	0	0	deg
Argument of Perigee	ω	0	0	deg
Initial Mean Anomaly	M_0	0	0	deg

For all propagations two body gravity, J2 perturbations, atmospheric drag, and SRP are used. Consistent with the motivation of this work, we initially model drag and SRP as zero magnitude perturbations since we assume that we do not have accurate a priori measures of the associated dynamics parameters. The states at each observation epoch are infused with 100 m and 0.1 m/s Gaussian error. These states are assumed to be the state estimates from an arbitrary orbit determination process - obtained via any set of traditional observations (angle, angle rate, range, Doppler, etc.).

5.6.1.1 LEO Estimation

In this LEO simulation, state estimates are taken over a period of 360 hours. Long arc state estimates are reported every 12 hours and short arc estimates are reported every 6 hours (the estimates were generated separately), thus the long arc estimation uses half as many estimates in the batch process. Perturbation estimates for each pair of observation epochs and the batch estimate from this example are shown in Fig. 5.4. It is clear from these results that drag is much more accurately estimated than SRP, since the in SRP is much larger. This is because drag is the dominant perturbation having far more effect on the boundary state deviation than SRP does. It is also clear from these results that the longer arc parameter estimates have a much smaller spread than the short arc estimates given equal state estimate uncertainties. In practice we will generally see larger uncertainties for long arcs compared to short arcs, but this example only seeks to show the reduction in parameter estimate spread as the observation gap is increased. The physical reasoning behind this is that the boundary uncertainties have more time to average out in a longer observation gap. Additionally, drag and SRP have more time to perturb the trajectory so their mismodeling becomes more detectable as the time gap increases.

The evolution of error with increasing number of observation epochs for these different sized observation gaps is also considered as shown in Fig. 5.5. The x-axis is formatted in terms of time so that the long arc and short arc can have a side-by-side comparison. We see several important characteristics in these results. First and foremost, we see that for both long and short arc observation the percent error in the drag parameter quickly converges to unity magnitude at the 3-σ level, and sub-unity levels are attained by further observation. This demonstrates the accuracy of this estimation algorithm. Also, even with just one or two observations from the long arc we obtain an estimate that is within 20% of truth (3-σ level). This shows the quick convergence of this algorithm. At this level of convergence we could update the drag dynamical model with each new observation to improve propagation accuracy and identification at the next observation epoch. Beyond the accuracy of this estimation method, in these results one can see that even though the

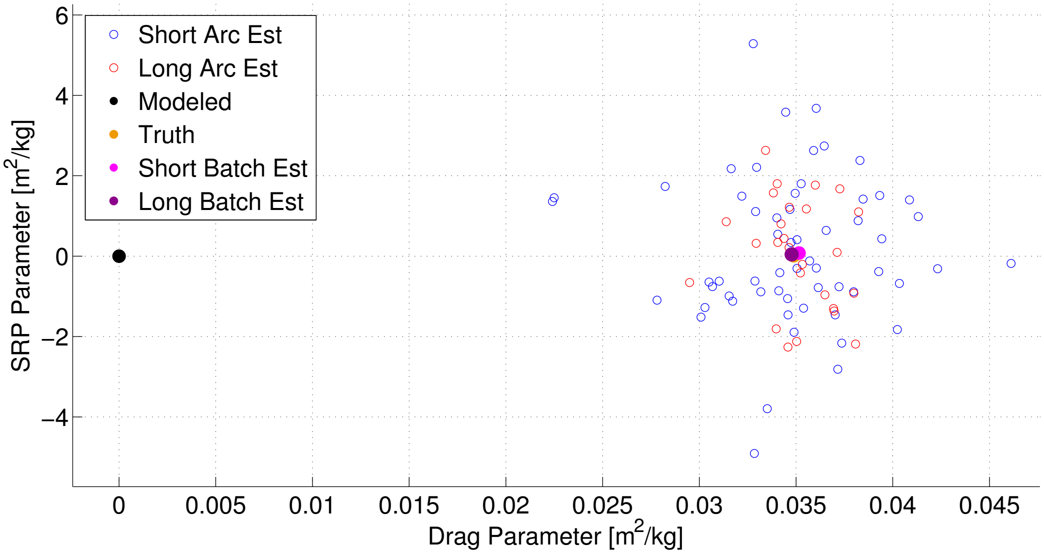

Figure 5.4: Long and short arc Drag and SRP parameter estimates from each pair of observation epochs for a tracked LEO object with mismodeled drag and SRP perturbations. The true parameters, initial modeled values, and batch estimates are indicated.

short arc uses double the amount of observations it yields virtually identical results (in uncertainty metrics) as compared to the long arc.

Along with the results from the previous figure, the long arc performance demonstrates how this algorithm is well-suited for data-sparse applications. Data sparse in this context is defined as observations taken very infrequently (generally less than once per orbit or less). At equal levels of uncertainty in the boundary states a longer observation gap is preferable since it averages out that uncertainty over the entire trajectory, which yields parameter estimates with smaller uncertainty. In practice longer observation gaps generally include larger boundary uncertainty, which would decrease performance to a degree but this is mitigated by this algorithm's preference for long observation gaps.

5.6.1.2 GEO Estimation

When SRP is not completely dominated by drag and it is given time to affect the trajectory, then its estimates become far more accurate. We demonstrate this with a GEO tracking example,

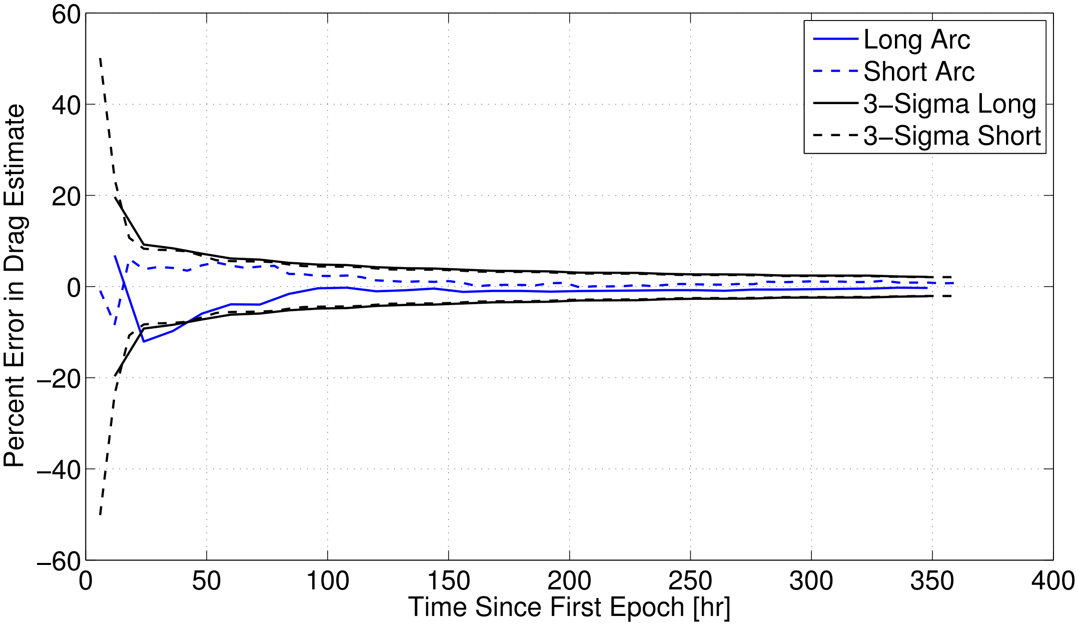

Figure 5.5: Percent error in the drag parameter estimate over time for LEO simulation. Blue represents the error of the actual estimates in these simulations and black represents the 3-σ envelope associated with these estimates. Long and short arcs are represented by solid and dashed lines, respectively.

where drag is nonexistent. As with the LEO example, state estimates are given on long and short arcs with 40 and 20 hour observation gaps, respectively. This is done for 1200 hours. State estimates are infused with 100m and 0.1 m/s Gaussian error in each direction.

The SRP parameter estimates for each pair of observation epochs are shown in Fig. 5.6. Even when SRP is the dominant perturbation it still has a large estimation spread because it is a weak force. Subtle changes in the SRP parameter over short observation gaps do not produce large state differences, which means the spread in the estimates is large in order to attain the levels of uncertainty in the boundary states. This is counteracted by one of two things: (1) reducing the uncertainty in the state estimates, and/or (2) introducing larger observation gaps. Considering the latter requires far less effort and is also reflective of astrodynamics applications, it is the preferred method. We can see this reduction in parameter spread for the long arc versus the short arc in Fig. 5.6 just as we saw in the LEO simulation.

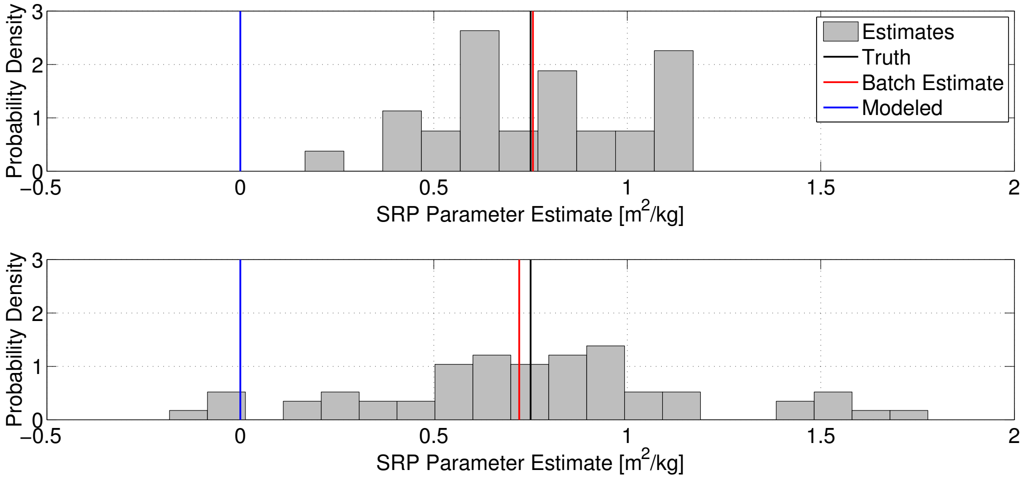

Figure 5.6: SRP parameter estimate histogram for GEO Simulation with long (top) and short (bottom) arcs. The true parameters, initial modeled values, and batch estimates are indicated.

A similar error study to the one performed for the LEO example is shown in Fig. 5.7. In these results we can make similar conclusions to the ones from the LEO simulation. First, the algorithm accurately estimates the SRP parameter using both the long and short arcs. The algorithm attains unity level percent deviation from truth (1-σ) after approximately 10 long arc observations, and it converges even more with further observation. In terms of observation gap results, we find comparable behavior over time between the arcs (with the short arc having double the number of state estimates). The long arc performs slightly better in terms of uncertainty metrics for equivalent state estimate uncertainties. Again we would expect to see larger uncertainties for longer observation gaps (relative to shorter observation gaps), but we can conclude that in general the increased observation gap performs better on a per estimate basis compared to shorter gaps when boundary uncertainty is comparable. Also the effect of increasing boundary uncertainty with increased observation gap time is mitigated by this improved performance.

From these LEO and GEO tracking simulations we have demonstrated the accuracy of this algorithm as a batch process, and how that accuracy changes as a function of the time gaps between those observations. This showed that this algorithm is well suited for data-sparse tracking

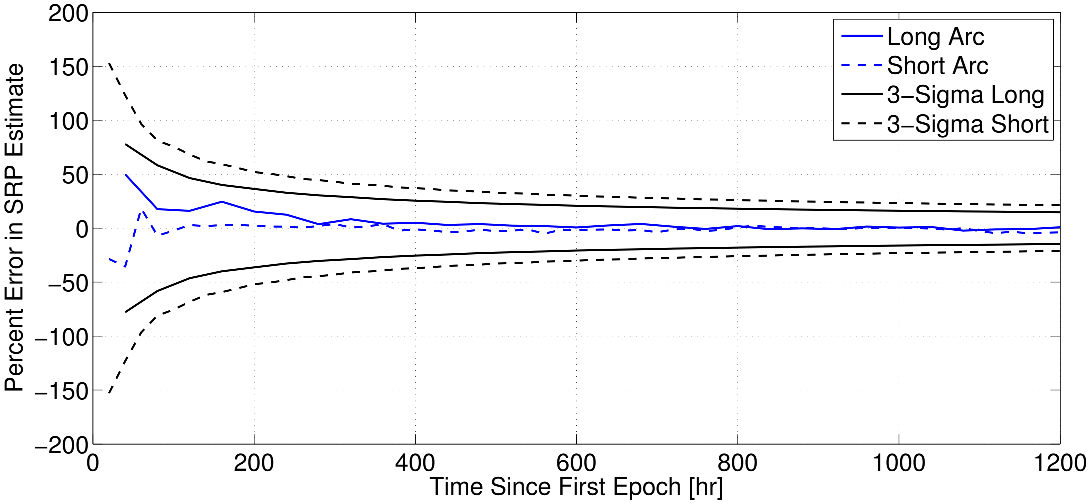

Figure 5.7: Percent error in the drag parameter estimate over time for GEO simulation. Blue represents the error of the actual estimates in these simulations and black represents the 3-σ envelope associated with these estimates. Long and short arcs are represented by solid and dashed lines, respectively.

applications, which is generally the case for astrodynamics tracking of defunct, natural, and active objects (especially broad SSA surveying). We have also demonstrated broad applicability of the algorithm with accurate results in LEO, GEO, and mid-altitude (as shown in the Monte Carlo results from the previous section) simulations.

5.6.2 Simulation II: Biased Dynamics and Unmodeled Maneuver

In the previous simulation, we saw how this algorithm operated in the presence of mismodeled natural dynamics. In this simulation there are also mismodeled drag and SRP perturbations, but additionally there is an unmodeled cross-track impulsive maneuver that occurs in one of the observation gaps. The initial conditions for this simulation are the same as the previous LEO case. The impulse parameters are summarized in Table 5.3. Similarly, one state estimate is given every 6 hours for 360 continuous hours with 100 m and 0.1 m/s Gaussian noise included in each ECI direction.

Parameter estimates for this simulation are shown in Fig. 5.8. In these results we see almost

Table 5.3: Timing and Impulse Values for Test Case IV

Parameter	Notation	Value	Units
Initial Time	t_0	0	hr
Impulse Time	t_{imp}	37.501	hr
Final Time	t_f	360	hr
Impulse Magnitude	ΔV_{man}	2.5	m/s

identical behavior to the LEO tracking case with the short arc observation gaps as is expected since the setups are largely the same other than the maneuver in this case. We still achieve accuracy in the drag estimate on the order of 1% deviation from truth (3-σ), and the spread in drag and SRP estimates is equivalent to the non-maneuver case. There is no clear outlier in the estimates that correspond to the maneuver for two reasons: (1) drag never acts in the cross-track direction and (2) SRP is weekly correlated with cross-track motions in the geometry and any effect is washed out in its large spread. In different geometries maneuvers may leave a clear trace in estimate space, and through this we can detect them, but there are additional ways of detecting them too.

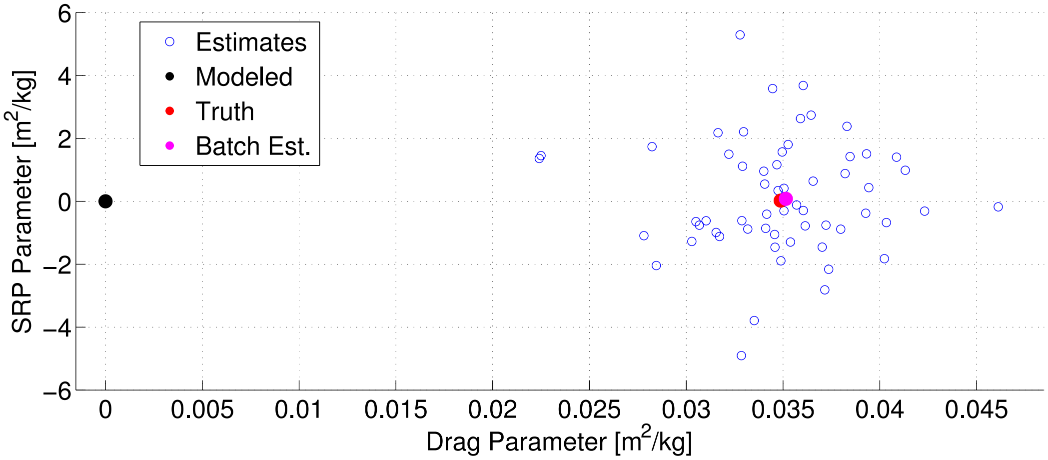

Figure 5.8: Drag and SRP parameter estimates for each pair of observation epochs for a tracked LEO object with mismodeled Drag and SRP perturbations and an unmodeled impulsive maneuver. True parameters, initial modeled values, and the batch estimate are indicated.

A maneuver's presence is most clearly seen in control distance metric-space. The distance metrics calculated between each observation gap are shown in Fig. 5.9 - these are the integrated control profiles for all pairs of observation epochs. Values are provided from both before and after dynamics parameter estimation. In general, the distance metrics are positively skewed with a small mean created by the boundary state uncertainty, as derived previously. Sensing a maneuver requires that its associated distance metric be beyond the threshold set by the boundary state uncertainty (indicated on the graph). As such, small maneuvers can get ignored, but we clearly see the maneuver as the right outlier in both the distributions. Consistent mismodeling presents itself as a positive shift in the distribution - the clear shift we see in the two distributions.

One-time maneuvers, on the other hand, will present as outliers in the control distance metric distribution. That is what we see in this distribution. The value of the distance metric also puts an upper bound on the maneuver (3.44 m/s after parameter estimation). By subtracting out the average due to boundary uncertainty, we can obtain an even more realistic value to characterize the maneuver in ΔV-space. In this case we can estimate the maneuver at 2.84 m/s after removing parameter mismodeling and boundary uncertainty effects, which is quite close to the true value of 2.5 m/s. Additionally, the OCP generated for this observation gap can be used to reconstruct the maneuver. It shows the maneuver as largely a cross-track acceleration, though the result is smooth as opposed to impulsive. With all this information we have shown this algorithm's ability to detect and characterize an unmodeled maneuver as well as consistent dynamics mismodeling.

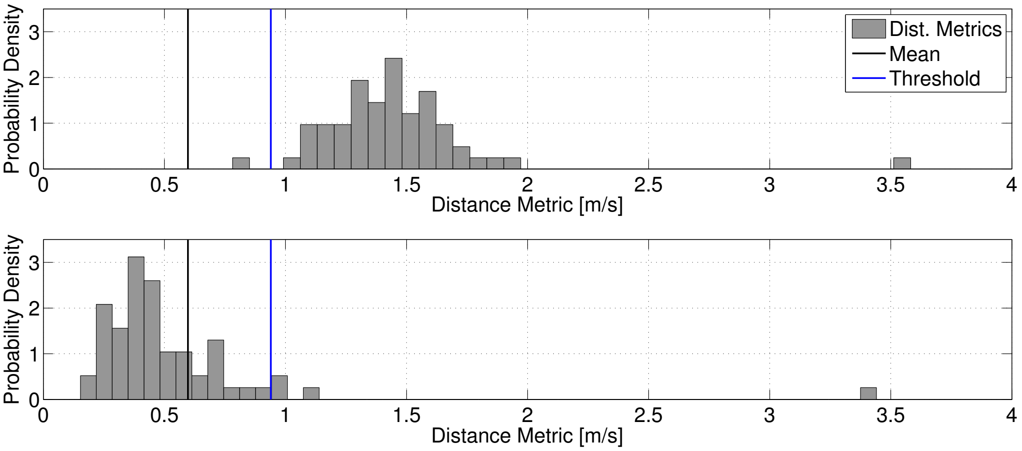

Figure 5.9: Control distance metrics between each measurement epoch for LEO simulation with unmodeled maneuver. Metrics from before estimation are provided (top) as well as from after parameter estimation (bottom).

5.7 Sample Maneuver Detection and Reconstruction with the OCBE

In the following sections, we provide the maneuver detection results from the LEO and GEO-based simulations using the BL-OCBE in Chapter 4. Since the simulations are the same we will not define the setup again, rather just skip to an analysis of the distance metrics that come out of the BL-OCBE.

5.7.1 Tracking a Spacecraft in LEO with Mismodeled Drag and an Unknown Maneuver

Recalling the simulation from Section 4.2, we have a spacecraft in LEO with atmospheric drag mismodeling and an unknown cross-track maneuver that is being observed once an hour for 150 consecutive hours with range and range-rate observations. In the original analysis we used postfit measurement residuals to motivate the selection of an appropriate assumed dynamic uncertainty, but in actuality these values are set using maneuver detection results. The associated maneuver detection results for the BL-OCBE and Nonlinear OCBE are presented in the following sections.

5.7.1.1 Tracking with the BL-OCBE

As with the original discussion, we first run the observations at a low assumed dynamic uncertainty ($\sigma_Q = 10^{-12}$ m/s^2) to determine the presence of mismodeling within the system. The resulting metric-to-threshold ratios are shown in Fig. 5.10. These results clearly indicate a slow build up of error, and then a large event that results in maneuvers being detected for all measurements afterward. As before, we make the hypothesis that the initial build up of error is due to a consistent mismodeling while the large deviation represents represents a one-time event.

To account for the initial mismodeling we increase the assumed dynamic uncertainty for all time to a new value such that the metrics before the large events are distributed appropriately without large detections. The resulting value is $\sigma_Q = 2 \times 10^{-8}$ m/s^2, and the corresponding metric-to-threshold ratios are depicted in Fig. 5.11. It is clear that the first group of metrics are distributed as would be analytically predicted, but it is impossible to accurately see past the large jump in the metrics because this likely represents an uncompensated maneuver that leads to filter divergence. To account for it we set the assumed dynamic uncertainty for the corresponding measurement epoch to $\sigma_Q = 7.3 \times 10^{-5}$ m/s^2 with the resulting distance metric-to-threshold ratios given in Fig. 5.12. The metrics are distributed as we would expect for a system with no uncompensated maneuvers, thus it is an indication that we have successfully addressed all statistically significant dynamic mismodeling within the system.

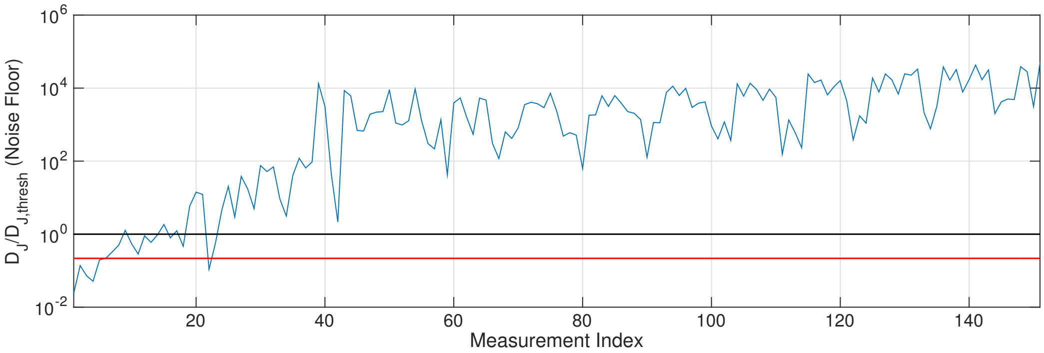

Figure 5.10: Distance metric to metric threshold ratio when running the BL-OCBE with $\sigma_Q = 10^{-12}$ m/s^2.

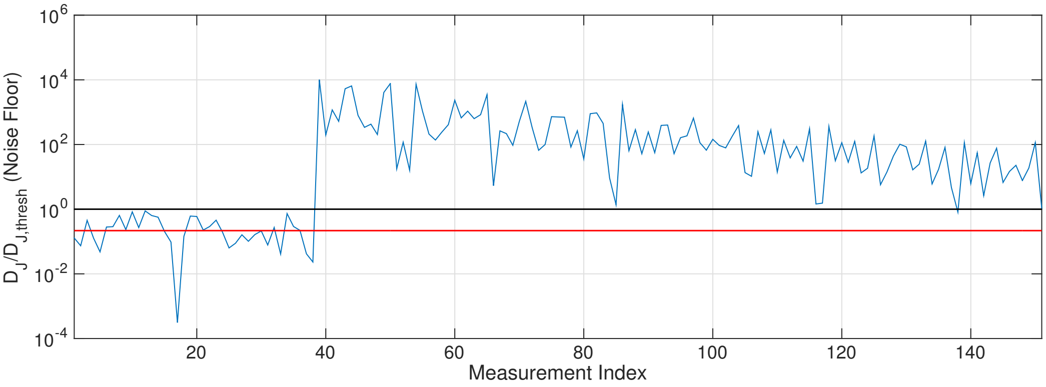

Figure 5.11: Distance metric to metric threshold ratio when running the BL-OCBE with $\sigma_Q = 2 \times 10^{-8}$ m/s^2.

Now that we compensated for all dynamic mismodeling, we plot the metric-to-threshold ratio relative to a constant dynamic uncertainty of $\sigma_Q = 2 \times 10^{-8}$ m/s^2. These ratios are not obtained by processing with a constant value, rather it just is used to identify any significant mismodeling relative to this value. These results are summarized in Fig. 5.13. It is clear from these results that we have identified the presence of a single maneuver, and all other epochs are subject to mismodeling on the order of 2×10^{-8} m/s^2. This completely agrees with truth, thus demonstrating the effectiveness of this method.

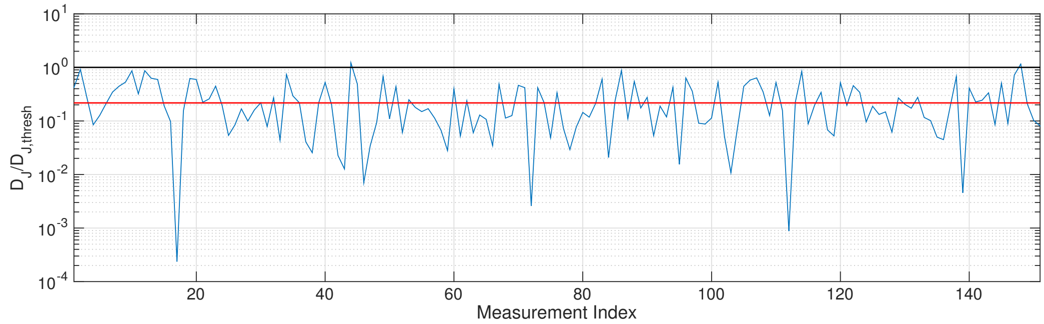

Figure 5.12: Distance metric-to-threshold ratio when running the BL-OCBE after accounting for the drag mismodeling and the remaining maneuver

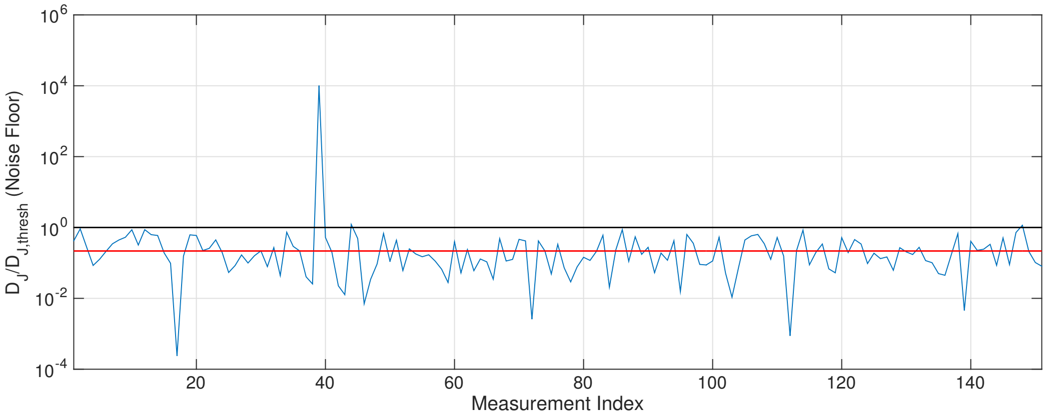

Figure 5.13: Distance metric-to-threshold when running the BL-OCBE after accounting for the drag mismodeling and the remaining maneuver. All ratios are taken with respect to an assumed dynamic uncertainty of $\sigma_Q = 2 \times 10^{-8}$ m/s^2

5.7.1.2 Tracking with the Nonlinear OCBE

The same maneuver detection process that was done with the BL-OCBE is completed with nonlinear OCBE. As such we now utilize all three distance metrics for analysis. The resulting distance metrics after the atmospheric drag and cross-track maneuver are addressed are shown in Fig. 5.14. It is clear through each of the three metrics that we have properly accounted for mismodeling in the system since the metrics remain below the threshold in general with no obvious correlation between measurement epochs.

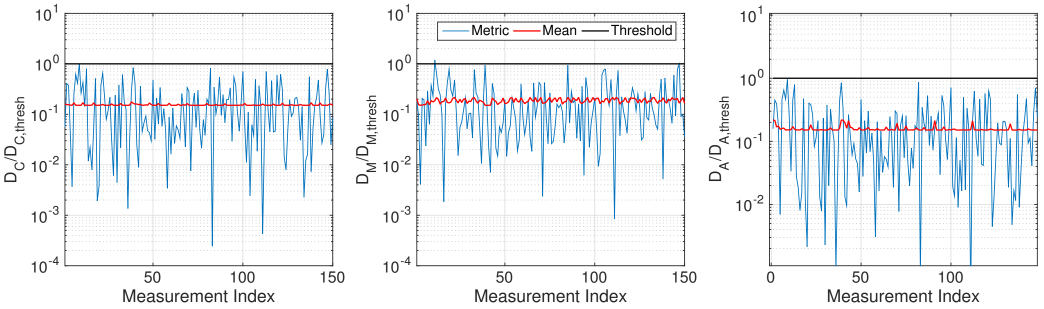

Figure 5.14: Distance metric-to-threshold ratio when running the Nonlinear OCBE after accounting for the drag mismodeling and the remaining maneuver.

We also provide the metrics with respect to an assumed dynamic uncertainty of $\sigma_Q = 2 \times 10^{-8}$ m/s^2 in order to demonstrate the detections that this method makes with respect to this level of mismodeling (Fig. 5.15). The one cross-track maneuver clearly stands out it this analysis in all three metrics. If we plotted these metric-to-threshold ratios relative to a smaller assumed dynamic uncertainty we would see a slight shift upward in the metrics as a whole to represent the presence of drag mismodeling, but this mismodeling is not large enough to detect consistently.

Between this analysis and that of the BL-OCBE, it is clear that this maneuver detection method is able to identify consistent mismodeling due to things like natural dynamics mismodeling in addition to seeing actuated maneuvers. The BL-OCBE results are good, but the diversity that results from using three metrics with the Nonlinear OCBE provides additional level of discrimination in any detection made. Thus, it is less likely that the Nonlinear OCBE makes a false detection for a given threshold percentile.

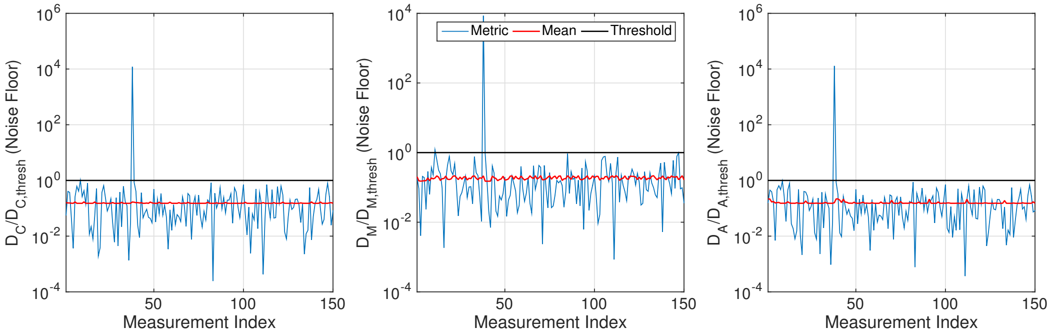

Figure 5.15: Distance metric-to-threshold when running the Nonlinear OCBE after accounting for the drag mismodeling and the remaining maneuver. All ratios are taken with respect to an assumed dynamic uncertainty of $\sigma_Q = 2 \times 10^{-8}$ m/s^2

5.7.2 Tracking a Spacecraft in GEO with Unknown Stationkeeping Maneuvers

Recalling the simulation from Section 4.3, we are observing a target in GEO that is undergoing unknown stationkeeping maneuvers. Observations include range and angles for two hours a night (every 100 seconds during that 2 hours). As with the previous simulation we will now discuss the maneuver detection results for this simulation using the BL-OCBE and the Nonlinear OCBE in the following two sections.

5.7.2.1 Tracking with the BL-OCBE

Following the development from Chapter 4, we originally process the measurements with a constant low value of the assumed dynamic uncertainty ($\sigma_Q = 10^{-10}$ m/s^2) in order to determine the presence of mismodeling above this level. The resulting distance metrics are plotted in Fig. 5.16. These results clearly indicate that the first 200 measurements are properly modeled with no sudden events or small mismodeling that builds over time. Just past the 200th measurement, there is a sudden even that leads to quick divergence in the metric, and the metric never recovers. This likely indicates a strong actuated maneuver or a similar type of event.

To account for this observed event we adjust the assumed dynamic uncertainty for that specific measurement epoch until the distance metric is pushed below the threshold, thus indicating we have compensated for the mismodeling. The resulting metrics are shown in Fig. 5.17. It is clear that the original detection was a quick event since compensation only requires adjusting the assumed dynamic uncertainty for that single epoch. However, it is clear an uncorrelated event occurs much further down in the observations. Just short of the 900th measurement there is a sudden jump in the distance metrics that vastly exceeds the metric threshold, and the metrics never recover after it. It exhibits similar behavior to the first detection.

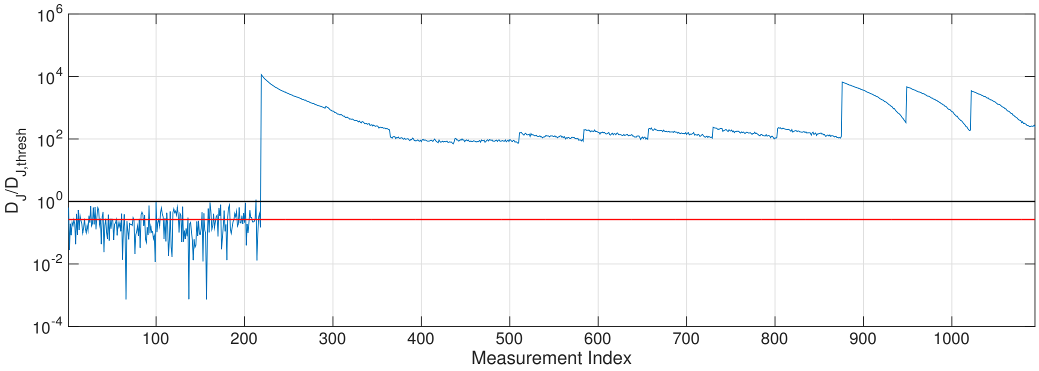

Figure 5.16: Distance metric to metric threshold ratio when running the BL-OCBE with $\sigma_Q = 10^{-10}$ m/s^2.

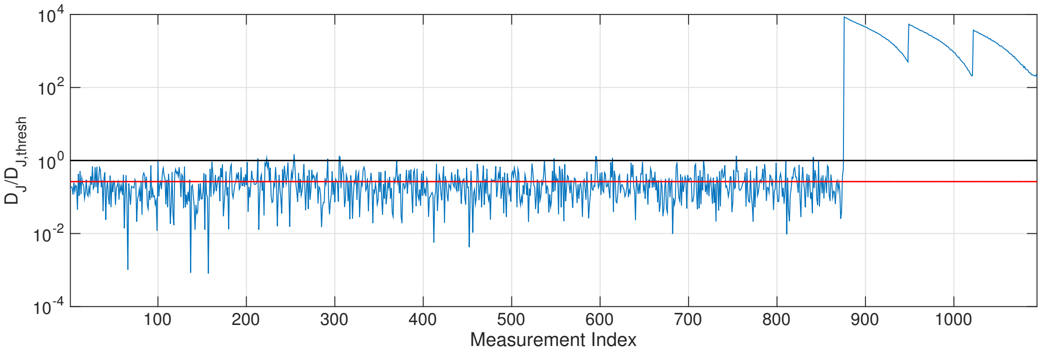

Figure 5.17: Distance metric to metric threshold ratio when running the BL-OCBE after accounting for the first maneuver.

Since this new detection behaves in a similar manner to the first, we compensate for it in a similar manner - by adjusting the assumed dynamic uncertainty for that specific measurement epoch until the metric is pushed below the threshold. The resulting distance metrics are plotted in Fig. 5.18. These results verify that we have compensated for all statistically significant dynamic mismodeling since the metrics have a distribution as analytically predicted. There are a total of 12 detections in this data (not including the two true detections), which corresponds to 1.10% of all epochs. For this analysis we use a threshold percentile of 99%, so this number of detections is expected. We can more clearly indicate the actual detections by plotting the metrics obtained with a constant low assumed dynamic uncertainty ($\sigma_Q = 10^{-10}$ m/s^2). These metrics are plotted in Fig. 5.19. The two maneuvers clearly stand out as single events that do not have a deterministic effect on the metrics directly after the detection. This indicates a successful compensation for the maneuvers. The results in Chapter 4 provide a full reconstruction of these two events.

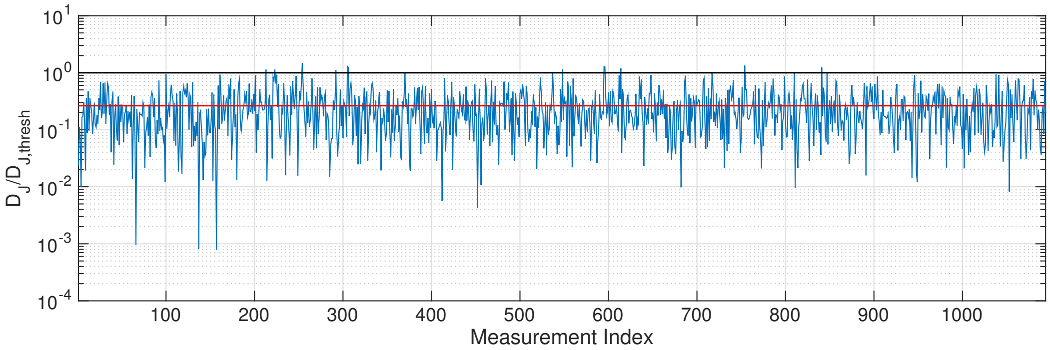

Figure 5.18: Distance metric-to-threshold ratio when running the BL-OCBE after accounting for the drag mismodeling and the remaining maneuver

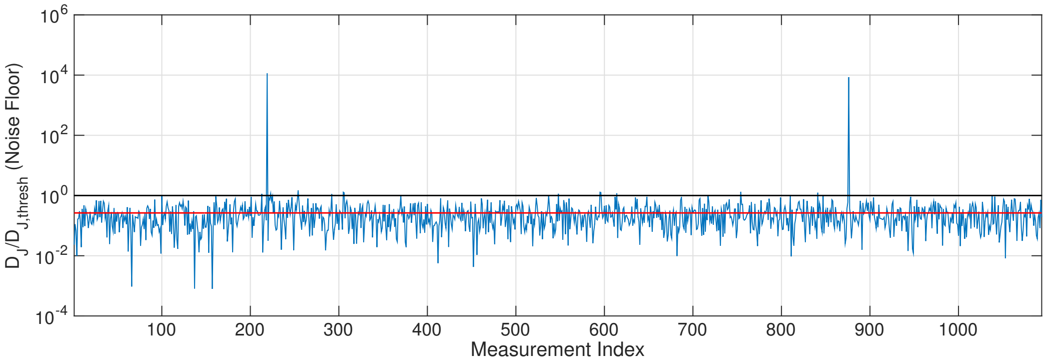

Figure 5.19: Distance metric-to-threshold when running the BL-OCBE after accounting for the drag mismodeling and the remaining maneuver. All ratios are taken with respect to an assumed dynamic uncertainty of $\sigma_Q = 10^{-10}$ m/s^2

These maneuver detection results clearly indicate the presence of the two maneuvers with all other detections being attributed to outliers in the measurements. Beyond the detections we are able to obtain full maneuver reconstructions through the control estimates as well. In Chapter 6, we discuss a method for eliminating these false detections.

5.7.2.2 Tracking with the Nonlinear OCBE

The BL-OCBE results clearly indicated successful detection and reconstruction of the two stationkeeping results, however there are false detections that accompany this due to the probabilistic nature of the hypothesis testing. We can limit these false detections within the Nonlinear OCBE by employing all three metrics and defining a detection as when all three metrics simultaneously exceed their thresholds.

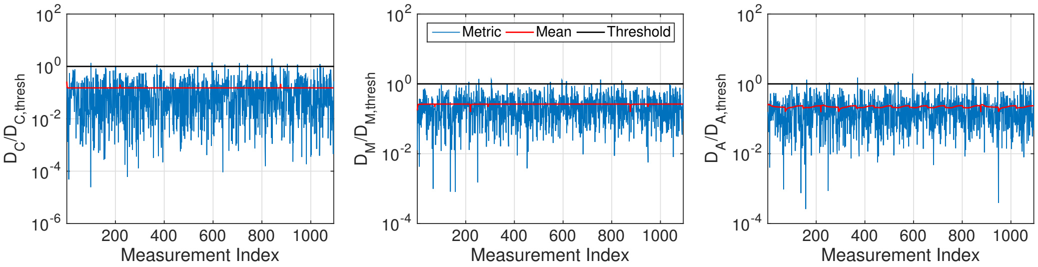

Figure 5.20: Distance metric-to-threshold ratio when running the Nonlinear OCBE after accounting for the drag mismodeling and the remaining maneuver.

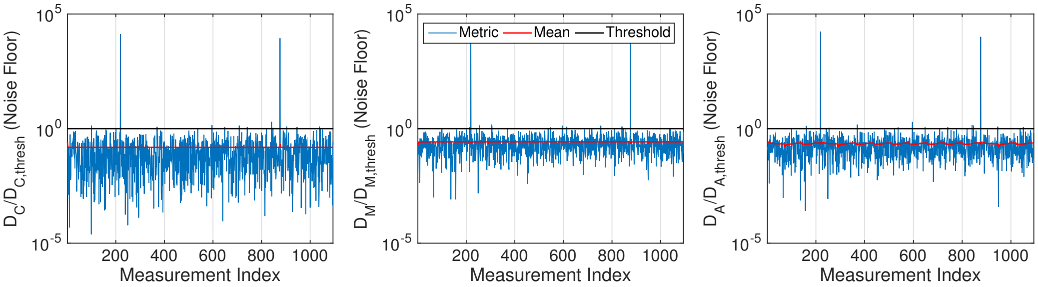

Figure 5.21: Distance metric-to-threshold when running the Nonlinear OCBE after accounting for the drag mismodeling and the remaining maneuver. All ratios are taken with respect to an assumed dynamic uncertainty of $\sigma_Q = 10^{-10}$ m/s^2.

Following the same process for the BL-OCBE, we are able to identify and compensate for the two stationkeeping maneuvers. Since we are using three separate metrics, the user needs to select one to focus on adjusting. This analysis focuses on adjusting the OCBE control distance metric. The resulting metrics after compensating for the two maneuvers are shown in Fig. 5.20. Not including the two true detections, the metrics make 11 (control metric), 10 (measurement metric), and 13 (a priori metric) detections each. This corresponds to 1.01%, 0.91%, and 1.19% of all epochs, respectively, which agrees well with the 99% threshold percentile. Defining a detection as when the metrics simultaneously exceed their thresholds, we can reduce the number of detections (not including the two true detections) to only 2. Thus, the diversity in metrics for the nonlinear OCBE is able to reduce the number of false detections from 12 for the BL-OCBE to only 2 for the Nonlinear OCBE. An additional detection criteria discussed in Chapter 6, can reduce this even further.

Finally, the two maneuvers can be clearly seen in the metrics when we plot them as functions of constant low value for the assumed dynamic uncertainty ($\sigma_Q = 10^{-10}$ m/s^2) as shown in Fig. 5.21. The metrics clearly stand out in all three metrics. The resulting maneuver reconstructions for these events are given in the analysis in Chapter 4. The successful detection and reconstruction of these stationkeeping maneuvers clearly indicates the abilities of this algorithm.

5.8 Conclusions

This chapter developed a maneuver detection method based on the control distance metric approach of Holzinger, Scheeres, and Alfriend [28]. The method was adapted to reflect the OCBE, such that the metrics chosen for the Nonlinear OCBE are the three portions of the OCBE cost functions and the BL-OCBE metric is chosen as the combined OCBE cost function. Using these metrics we perform a one-tailed χ^2 hypothesis test to determine the statistical significance of the estimates coming out of the OCBE. The method is easily implementable such that it can be applied in real-time as measurements come in. The process relies upon quantities already computed in the OCBE, thus the metrics and the associated maneuver detection method are natural fits for the OCBE algorithm. The resulting metrics clearly tell the user whether there are mismodelings that the user has to account for.

After establishing the theory and process behind this maneuver detection method, we demonstrated it through application to the LEO and GEO simulations described in Chapter 4. In both examples we were clearly able to detect the presence of both consistent mismodeling (e.g. error in atmospheric drag model) and the sudden mismodeling due to events like a short-term actuated maneuver. While we are able to successfully detect mismodeling there are also false detections due to the probabilistic nature of the hypothesis testing. We were able to reduce the effect for the Nonlinear OCBE by defining a detection as when all three metrics simultaneously exceed their respective thresholds. In the following chapter we will improve upon this false detection rejection method for both the Nonlinear OCBE and the BL-OCBE, while automating the process of compensating for detected mismodeling.

Chapter 6

Adaptive Optimal Control Based Estimator

The OCBE as discussed to this point is capable of compensating for mismodeled dynamics and estimating that mismodeling. However, this compensation requires the user to select a value for the assumed dynamic uncertainty with each new measurement. This value should reflect the level of mismodeling in the system, but that is not known a priori. As discussed in Chapter 5, the maneuver detection method can tell the user whether or not there exists any uncompensated mismodeled dynamics within the system. Iterating this procedure, the user can adjust the assumed dynamic uncertainty until a maneuver is no longer detected. This method is very manual, which precludes application to real-time systems, thus limiting the application of the OCBE. In this chapter, we discuss a method to automate the selection of the assumed dynamic uncertainty, such that it properly accounts for any mismodeled dynamics. The resulting algorithm is known as the Adaptive OCBE.

This discussion will start by defining the automation algorithm. This includes defining the criterion used to guide the automation, investigating the existence of a solution to this criterion, a method for obtaining this solution when it exists, and a discussion on when the automation should be implemeted. Next, we will provide a summary of the Adaptive OCBE in a flowchart form to allow for easier implementation of the algorithm. Following this we will provide results from applications of this algorithm to sample tracking scenarios to demonstrate its effectiveness in a Nonlinear OCBE and BL-OCBE context. Finally, a concluding discussion will summarize the development of this algorithm and its demonstrated properties. The Adaptive algorithm will be developed for the Nonlinear OCBE and BL-OCBE simultaneously since the automation methods are so similar. Where the methods differ notes, will be made in text.

6.1 OCBE Automation Algorithm

In this section we develop an algorithm that automatically selects the assumed dynamic uncertainty when applying the OCBE to an estimation problem. This method is heavily based on the maneuver detection algorithm as developed in Chapter 5. First we will define the criterion behind the automation. Next we will discuss the existence of a solution that satisfies this criterion. Following this, we will discuss methods to obtain a solution is it exists. Finally, we provide a discussion of when this automation should be applied. This discussion addresses the questions of how to distinguish between a maneuver and an outlier in the data. Making this distinction is important to ensuring the user does not overcompensate for mismodeling in the system that is not even present (which leads to degraded tracking), and also to lowering the false detection rate of this algorithm.

6.1.1 Automation Criterion

The accuracy of the OCBE is strongly linked to choosing an appropriate assumed dynamic uncertainty. The assumed dynamic uncertainty needs to reflect the actual level of dynamic mismodeling in the system. Setting it too high injects too much uncertainty in the system leading to degraded tracking performance. Setting it too low means mismodeled dynamics are not fully compensated for, so estimates will be biased and inaccurate. We need to find a level that compensates for mismodeling, but does not overcompensate. The mismodeling is unknown to the user, and it can change between measurement epochs, which makes it a difficult problem to solve by hand - especially for large observation sets from highly populated systems as is the case with SSA surveys.

While we have no knowledge of the mismodeled dynamics in the system we are able to detect their presence. Using the maneuver detection analysis we identified a method to detect maneuvers, and found that we can compensate for them by adjusting the assumed dynamic uncertainty. To automate this process we create an algorithm that selects the assumed dynamic uncertainty which forces the estimated distance metric to be equal to the mean of the distribution (Eq. 6.1), since this is the value we should expect when all uncertainties in the system are properly accounted for.

$$\tilde{Q}(t) : D_z(\tilde{Q}(t)) = \mu_z(\tilde{Q}(t)) \tag{6.1}$$

We make this definition of the automation criterion for an arbitrary distance metric (D_z) and its associated mean (μ_z). It should be noted that depending on the metric selected the mean may or may not be a function of the assumed dynamic uncertainty (e.g. the BL-OCBE metric mean is a constant, thus it is not a function of the assumed dynamic uncertainty).

It may be argued that a more appropriate choice is to set the metric to zero, since the Gaussian random vectors are zero-mean. However, doing so would require an infinite amount of dynamic uncertainty. This is unrealistic, thus we motivate this approach based on a metric formulation rather than a similar measurement residual based method. It could also be argued that the assumed dynamic uncertainty should just be chosen once the zero-mean Gaussian random quantities defining a metric are within a 3-σ envelope. However this approach is vague and does not give the user an exact metric assess estimator performance. Requiring the mean and metric to be equal provides an exact equality constraint that is physically significant. It also ensures that on average the OCBE does not under or over-compensate for detected maneuvers.

The constraint in Eq. 6.1 has many degrees of freedom. The only other constraints on the matrix are that it is symmetric positive definite for all $t \in \mathbb{R}$. To simplify the approach we will specify the matrix as being a constant across the measurement gap, and reduce it to a scalar quantity on the diagonals of the $p \times p$ matrix. We define this reduced automation criterion in Eq. 6.2.

$$\begin{aligned} \tilde{Q}(t) =& a\sigma_Q^2 I_{p\times p} \\ \sigma_Q :& D_z(\sigma_Q) = \mu_z(\sigma_Q) \end{aligned} \tag{6.2}$$

In this definition a is a positive scalar that corrects for units such that the assumed dynamic standard deviation (σ_Q) has the units of $\vec{u}(t)$. In practice we use the quantity $a = t_k - t_{k-1}$, which essentially averages out mismodeling across the measurement gap.

Though we have a clearly defined automation criterion we have not addressed the existence of a solution that satisfies this criterion. In the following section we will address existence of the solution, and what needs to be done when a solution is not available.

6.1.2 Existence of a Solution

In order to automate the algorithm in manner that satisfies Eq. 6.2 we must also verify solution existence, and if the solution does not exist in certain cases we must provide a default assumed dynamic uncertainty. A solution to this criterion is defined as a intersection between the mean and metric as functions of the assumed dynamic standard deviation. As shown in Fig. 6.1 there are clearly occasions when a solution exists. This is generally the case when there is deterministic mismodeling in the system that is large enough for the system to detect. It can also occur when there is no mismodeling and the measurement error is large enough. More generally if the the calculated metric exceeds the metric mean at small values of σ_Q, then a solution will exist.

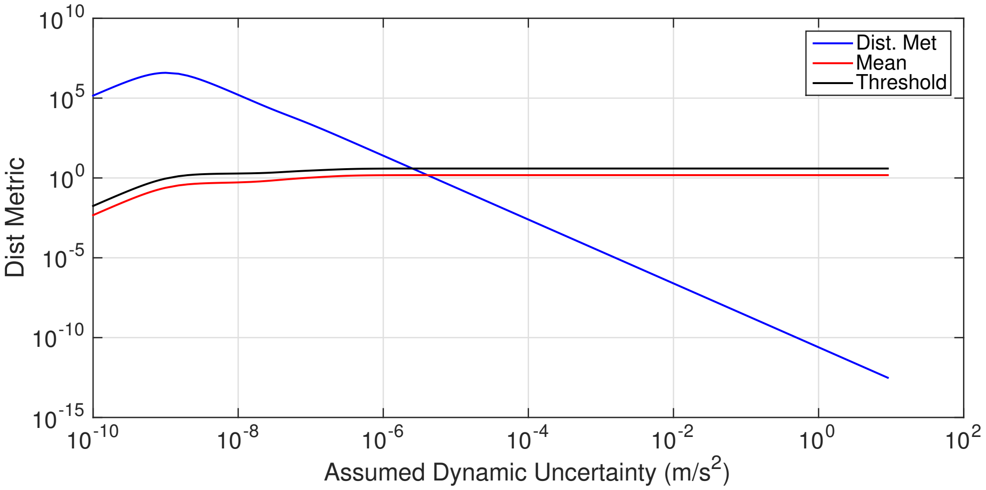

Figure 6.1: OCBE control distance metric, mean, and ratios as function of the assumed dynamic uncertainty for a case where the adaptive solution exists.

Figure 6.2 demonstrates a situation where no solution exists. As can be seen for small values of σ_Q the mean exceeds the metric, and this remains the case for the entire domain of assumed dynamic standard deviations. Clearly, since there are occasions where no solution exists there needs to be a solution to which to default.

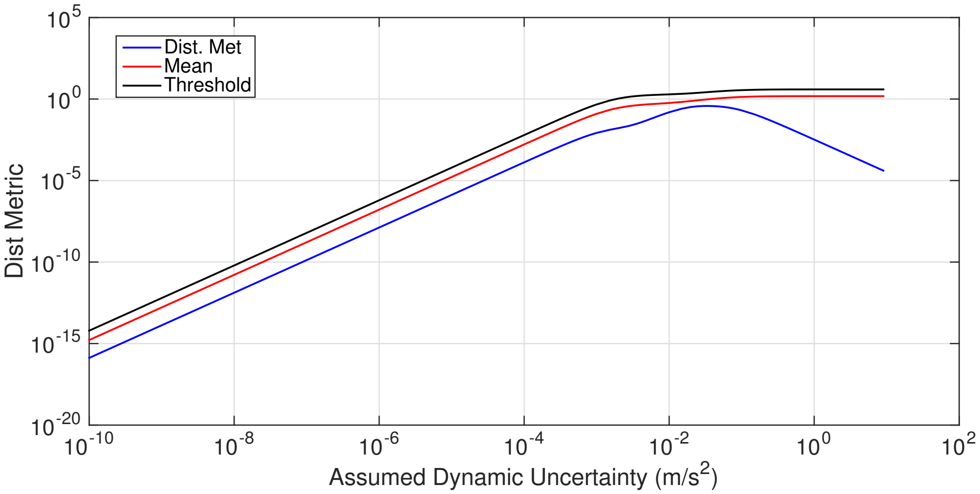

Figure 6.2: OCBE control distance metric, mean, and threshold as functions of the assumed dynamic uncertainty for a case where the adaptive solution does not exist.

.

To this point we have used the phrase “small values of σ_Q.” This just means values where the mismodeling is so small that it is impossible to detect because it is below the level of other errors within the estimation process. When a solution does not exist the algorithm should default to one of these small values since it represents the level of uncertainty within the estimation problem. We will define this default solution as the dynamic noise floor ($\sigma_{Q,NF}$). It represents the smallest amount of mismodeling the user cares about. Any mismodeling below this level is considered insignificant and negligible since it is dominated by other errors. Setting this value too high will result in missed detections and degraded tracking performance. Setting the value too low may result in spurious detections. In practice the user should select this value to correspond to what is detectable in the system based on the state uncertainties in the problem. For example the user could set the dynamic noise floor as the velocity uncertainty divided by the measurement gap or a multiple of this.

In order to address both the OCBE and BL-OCBE implementations Figs. **??** and **??** are provided as examples where the BL-OCBE distance metric has a solution that satisfies the automation criterion (the former) and when there is no solution satisfying the automation criterion (the latter). The difference between these results and the Nonlinear OCBE metrics is that the mean and threshold are not functions of the assumed dynamic uncertainty. The results are very similar, though. If a metric starts above the mean at the dynamic noise floor, then a solution will exist. If that metric starts below the metric, then a solution will not exist. In the latter case, the automation would default to the dynamic noise floor as a solution.

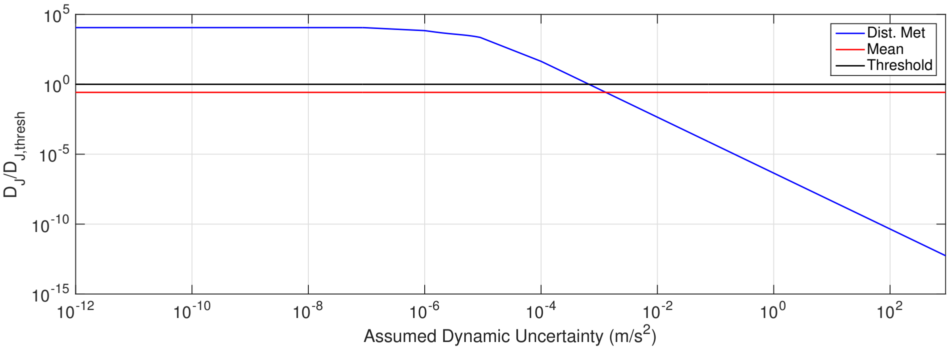

Figure 6.3: BL-OCBE distance metric, mean, and threshold as a function of the assumed dynamic uncertainty for a case where the adaptive solution exists.

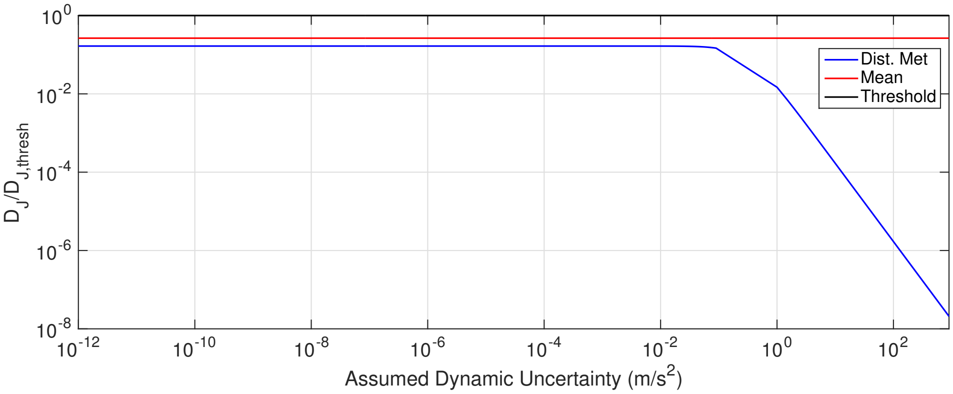

Figure 6.4: BL-OCBE distance metric, mean, and threshold ratios as functions of the assumed dynamic uncertainty for a case where the adaptive solution does not exist.

.

Having addressed the question of solution existence, and defining a default solution we have created an automation algorithm that works for any input. This automation only requires the user to first define a dynamic noise floor, and then it can process all measurements without a human in the loop. In the next section we will discuss how a solution may be calculated if it is determined that it exists.

6.1.3 Solution Method

After verifying that a solution exist (the distance metric is greater than or equal to the mean when evaluated at the noise floor), the next step is to calculate the solution. There is no invertible relation between the assumed dynamic standard deviation and the the distance metric or its mean, so the solution may not be obtained analytically. Instead we apply a standard nonlinear root finder algorithm. Many algorithms would work, but we will focus on application of a Newton-Secant solver.

As can be seen in Figs. 6.1 and 6.3, near the solution the difference in the mean and metric is very linear in log-log space. We take advantage of this by pursuing the solution in log-log space as well. The log-based assumed dynamic standard deviation and the function we are attempting to zero are defined below.

$$v = \log\left(\sigma_Q\right) \tag{6.3}$$

$$g(v) = \log\left[\frac{D_z(v)}{\mu_z(v)}\right] \tag{6.4}$$

To solve this nonlinear root finder problem the first step is to attain an upper and lower bound on the root. This is accomplished by starting with the dynamic noise floor as the lower limit and a scaled upper bound ($\sigma_{Q,U} = \alpha\sigma_{Q,NF}$ or in log-space $v_U = \log(\alpha) + v_{NF}$ where $v_{NF} = \log(\sigma_{Q,NF})$), evaluating the scaled upper bound, and iterating until $g(v_U) < 0$ since $g(v_{NF}) > 0$. Iterating entails setting the lower bound as the old upper bound and setting the upper bound as scaled version of the old upper bound when the inequalities constraints of upper and lower bounds are not yet achieved.

Once an upper and lower bound are achieved the next step is to employ the Newton-Secant method. A simple iterated Newton-Secant method is defined in Eq. 6.5.

$$v_{new}^{(i)} = v_L^{(i)} - \left(\frac{g\left(v_U^{(i)}\right)}{g\left(v_U^{(i)}\right) - g\left(v_L^{(i)}\right)} \right) \left(v_U^{(i)} - v_L^{(i)}\right) \tag{6.5}$$

This equations linearly interpolates between the upper and lower bounds to where the root of the linear interpolation (v_{new}). This value is then evaluated to see whether it is within the convergence tolerance of the iterative root finder. If so, the method stops with this as the solution. Otherwise, the method continues using this as the new upper or lower bound depending on whether the evaluation exceeds 0 or not. This process is continued until the new evaluation at the i$^{\text{th}}$ iteration is within a set tolerance ($|g(v_{new}^{(i)})| < \Delta_{tol}$). The result is then mapped into an assumed dynamic uncertainty, which is in turn set as an input for the OCBE evaluation.

When it comes to evaluating $g(v)$, this is where the BL-OCBE and the GL-OCBE differ. The GL-OCBE requires the user to essentially run the OCBE and take the metric and its statistics as outputs in order to make this evaluation. However, the BL-OCBE may be equated far more easily using the results of the OCBE outputs obtained when processing with the dynamic noise floor. The only term in the metric equation that is a function of the assumed dynamic uncertainty is the STM product in the propagated a priori uncertainty ($\Phi_{xp}\Phi_{xx}^T$). Using the equivalence this term has to continuous process noise we can easily express this STM product to be quadratic in the assumed dynamic uncertainty in the manner shown in Eq. 6.6.

$$\begin{aligned}\left[\Phi_{xp}\left(\sigma_Q\right)\Phi_{xx}^T\right] &= -\int_{t_{k-1}}^{t_k} \Phi_{xx}(t_k,\tau)\frac{\partial f}{\partial \vec{u}}\tilde{Q}(\tau)\frac{\partial f}{\partial \vec{u}}^T \Phi_{xx}^T(t_k,\tau)d\tau \\ &= \left(\frac{\sigma_Q}{\sigma_{Q,NF}}\right)^2 \left[\Phi_{xp}\left(\sigma_{Q,NF}\right)\Phi_{xx}^T\right]\end{aligned} \tag{6.6}$$

As we update this new matrix with each new $v^{(i)}$ (mapped into $\sigma_Q^{(i)}$), we can easily substitute the result into Eq. 5.43, which in turn is used to calculate the metric-mean deviation (Eq. 6.4). Being able to update this value analytically with each new iteration is ideal in a computational sense, thus making the BL-OCBE an even more streamlined version of the OCBE. Otherwise, the adaptive algorithm is identical between the different forms of the algorithm.

Having defined how an automated solution may be obtained, it is now important to discuss when this automation should be implemented. This is discussed fully in the following section.

6.1.4 When Automation Should be Employed

As discussed this algorithm is designed to adjust the assumed dynamic uncertainty with each new measurement where the calculated metric exceeds the calculated metric mean. However, in practice this may not always be best to do. Exceeding the metric mean or even the metric threshold is not completely indicative of a deterministic dynamic mismodeling - it could just be an outlier in the measurement error. If we compensate for every slight deviation from the mean we will overcompensate for non-existing maneuvers and as a result artificially degrade our tracking accuracy. To account for this we need a method to differentiate between deterministic mismodeling and outliers in the measurement error.

The method we propose here, is known as a maneuver compensation delay. When a metric exceeds its threshold, we flag this as a detection however we do not compensate for the detection immediately. Instead we wait until n_{delay} detections are made successively, where n_{delay} is a user defined integer number of successive detections. After this limit is hit the algorithm automatically returns to the first detection, compensates for it using the automation algorithm defined here and proceeds to following measurement. This approach attacks the two types of detections where they differ. Measurement outliers are unique events. The coupling with future estimates is limited, thus one detection is highly unlikely to trigger a second detection at the next measurement epoch. However, deterministic mismodelings are completely coupled. If the mismodeling is left uncompensated at one measurement epoch the next estimate will still have that deterministic error in it, thus it is far more likely to trigger a new detection. Applying this maneuver compensation delay ands another level of screening for detections. It allows us to segregate out false detections, thus improving the accuracy of the OCBE as a state estimate, a maneuver detection algorithm, and a maneuver reconstruction algorithm.

An additional level of screening for Nonlinear OCBE and GL-OCBE implementations is using multiple metrics to define a detection. Since the control, measurement, and a priori metrics are not completely coupled for these estimators it is possible for one to register a detection and others not for the same measurement. By defining a detection to be when all three metrics exceed their respective thresholds simultaneously, we reduce the chance of false detections. Such a method is not possible for the BL-OCBE since its three metrics are completely coupled. As such, to achieve similar false detection rejection efficiency the value of n_{delay} employed for the BL-OCBE will generally be higher than a similar GL-OCBE implementation.

When all metrics have exceeded their thresholds and the delay limit is reached, we now employ the automation algorithm discussed in this Chapter. In all other cases we stick to the dynamic noise floor. This method of implementation greatly reduces the chance of a false detection, but it delays maneuver reconstruction. While this is not ideal, the algorithm is still capable of real-time maneuver detection. The detections are made as new measurements are processed. At this point the detection may represent a false detection or a true maneuver, but it is still a real-time detection. The slight delay in detection verification and maneuver reconstruction are worthwhile with the level of accuracy that is achieved.

In the following the section we blend the OCBE algorithm, this maneuver detection algorithm, the maneuver compensation delay, and the automation method into a single algorithm known as the Adaptive OCBE. In this definition of the algorithm we provide a flowchart description of the algorithm that illustrates what steps the user must take to implement the algorithm and how it processes measurements automatically given a few inputs to initialize it.

6.1.5 Adaptive OCBE Algorithm Summary

To summarize the Adaptive OCBE we provide the flowcharts in Figs. 6.5 and 6.6 to identify how the algorithm operates once initialized by the user. Figure 6.5 details how the automation wraps around the actual OCBE in order to create the Adaptive OCBE. It focuses on the definition of a maneuver detection and how it should be handled within the algorithm.

Figure 6.6 details the actual automated assumed dynamic uncertainty selection process. Both

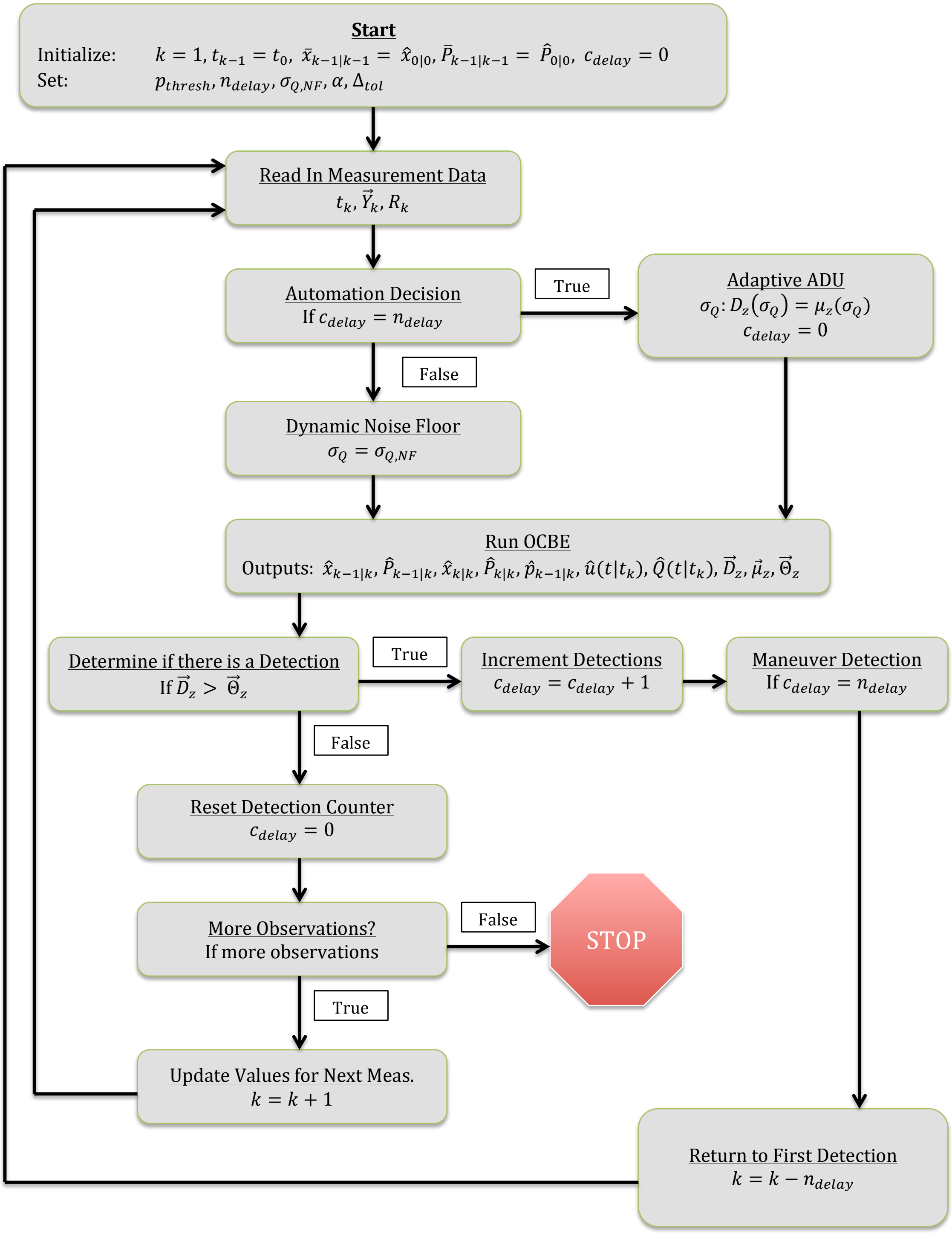

Figure 6.5: Flowchart illustrating how the Adaptive OCBE operates.

flowcharts apply regardless of which version of the core estimator is run (i.e. Nonlinear OCBE, GL-OCBE, or BL-OCBE), and they define all steps that must be taken to implement the algorithm. As defined in the flowchart, the user only needs to define five value, then the algorithm automatically processes all available measurements. The only additional values the user would need to set are tolerances for necessary condition convergence when implementing the Nonlinear OCBE as opposed to the linear versions.

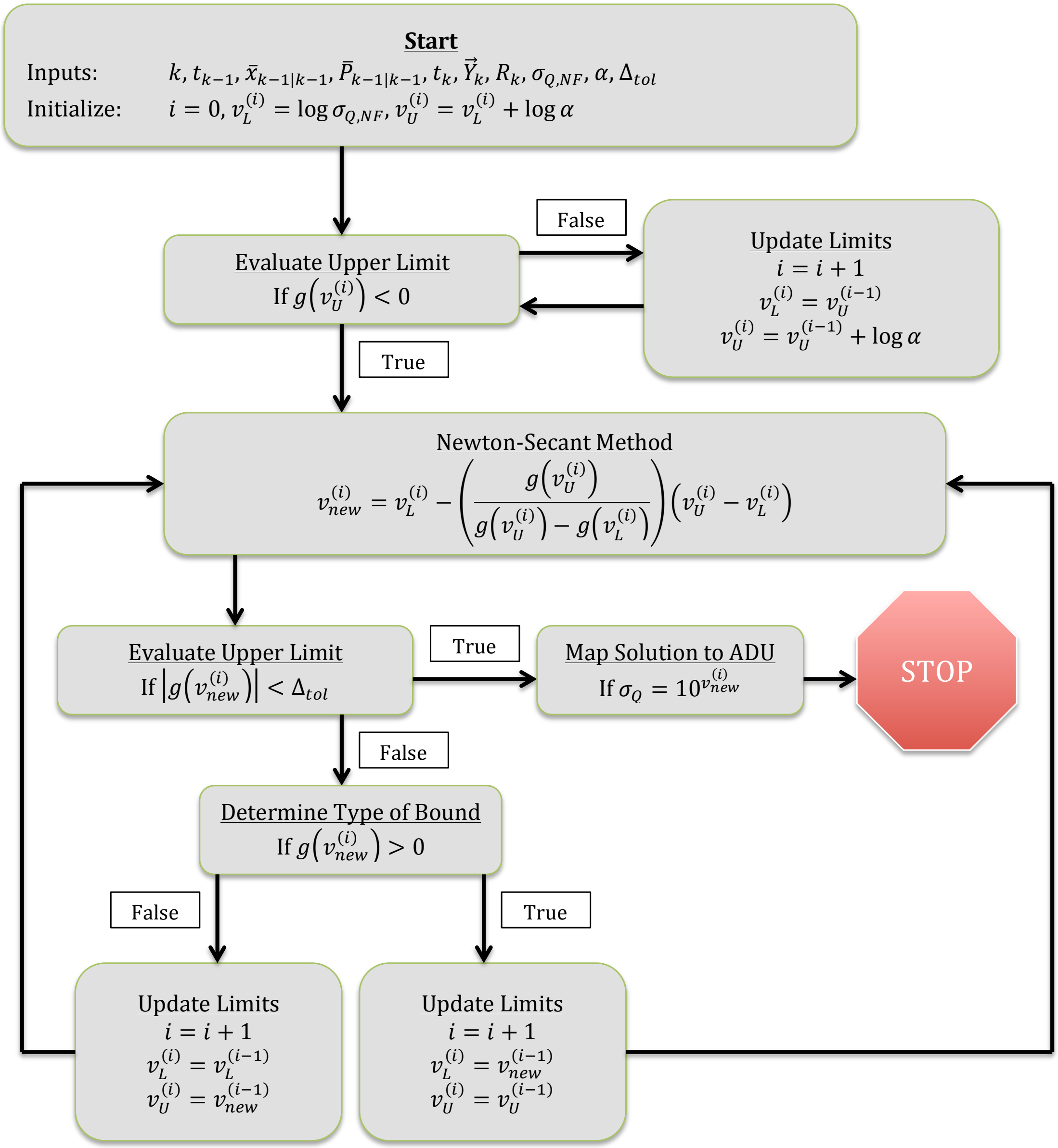

Figure 6.6: Flowchart illustrating how the Assumed Dynamic Uncertainty is automatically calculated in the Adaptive OCBE.

With these flowcharts, we have now fully defined the automation criterion that defines the

Adaptive OCBE, and how it wraps around the OCBE to create a fully integrated algorithm. In the following section we will apply this algorithm to sample tracking scenarios in order to demonstrate the algorithms effectiveness in terms of automatically detecting mismodeling, compensating for it, and tracking the maneuvering target.

6.2 Sample Applications of the Adaptive OCBE

In the following two sections we apply the Adaptive OCBE to the two problems we have addressed in Chapters 4 and 5 - tracking in LEO and GEO with mismodeled dynamics. We will focus on results obtained with the Nonlinear OCBE, but make comments about a BL-OCBE implementation where appropriate.

6.2.1 Tracking a target in LEO with Mismodeled Drag and an Unknown Maneuver

Recalling the simulation from Section 4.2, we have a spacecraft in LEO with atmospheric drag mismodeling and an unknown cross-track maneuver that is being observed once an hour for 150 consecutive hours with range and range-rate observations. In the original analysis we used postfit measurement residuals to motivate the selection of an appropriate assumed dynamic uncertainty, but in actuality these values are set using maneuver detection results. The associated maneuver detection results for the BL-OCBE and Nonlinear OCBE are presented in the following sections.

In this analysis we define a detection as when all three metrics exceed their thresholds simultaneously. We implement the compensation delay algorithm, requiring 2 successive detections before compensating for a given detection. The resulting distance metrics relative to dynamic noise floor ($\sigma_{Q,NF} = 2\times10^{-8}$ m/s^2) are plotted in Fig. 6.7. In these results there is a clear single detection made in each of the three metrics. This corresponds to the single impulsive cross-track maneuver. The metrics individually make 2 (control metric), 2 (measurement metric), and 1 (metric) detection. Combining them, only one detection is made in the total 150 measurements. This one detection corresponds to the one true maneuver, thus no false detections are made. The metrics relative to adaptive assumed dynamic uncertainty are shown in Fig. 6.8. There are no obvious detections here and the spread about the mean is as expected for a system with fully compensated mismodeled dynamics, thus indicating successful tracking is achieved.

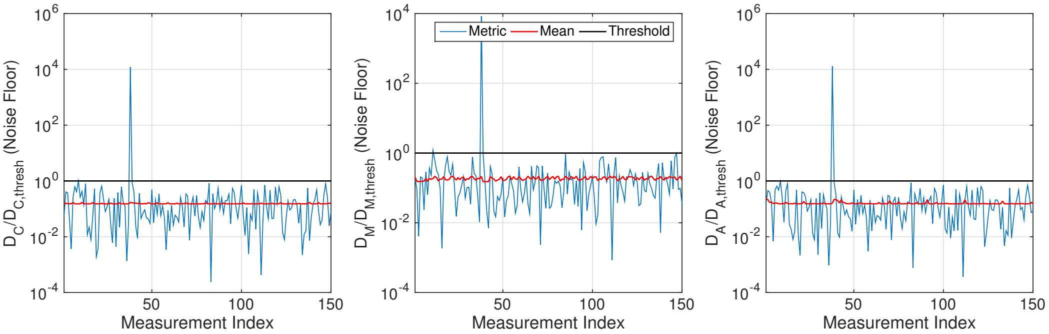

Figure 6.7: Distance metric-to-metric threshold ratio relative to dynamic noise floor when applying the Adaptive OCBE.

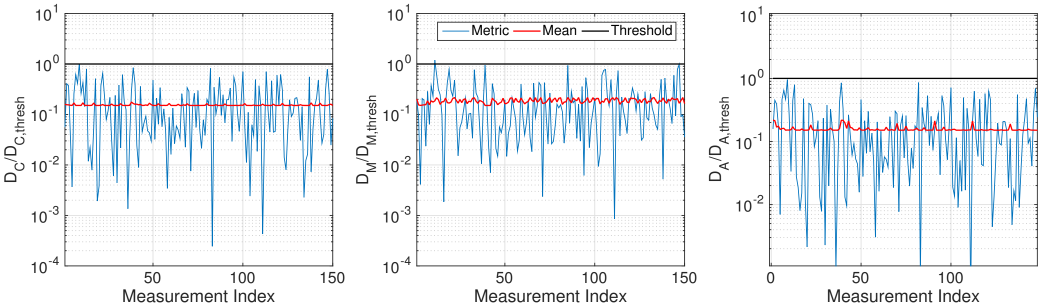

Figure 6.8: Distance metric to metric threshold ratio relative the adaptive assumed dynamic uncertainty when applying the Adaptive OCBE.

Having successfully detected the maneuver, we now focus on its reconstruction through the control estimates. These are shown as magnitudes in a Hill Frame as shown in Fig 6.9. The maneuver clearly stands out, amongst all other control estimates, though the directionality is not immediately evident due to the presence of atmospheric drag mismodeling. Application of the OCBE smoother would provide more accurate reconstructions, but this is done in post processing once more observations are taken post-maneuver. The other control estimates clearly show an along-track biasing that is consistent with the level of drag mismodeling we should expect.

To confirm the successful tracking we provide the state estimate deviations with respect to truth with a 3-σ envelope in Fig. 6.10. Remaining consistently below the uncertainty envelope,

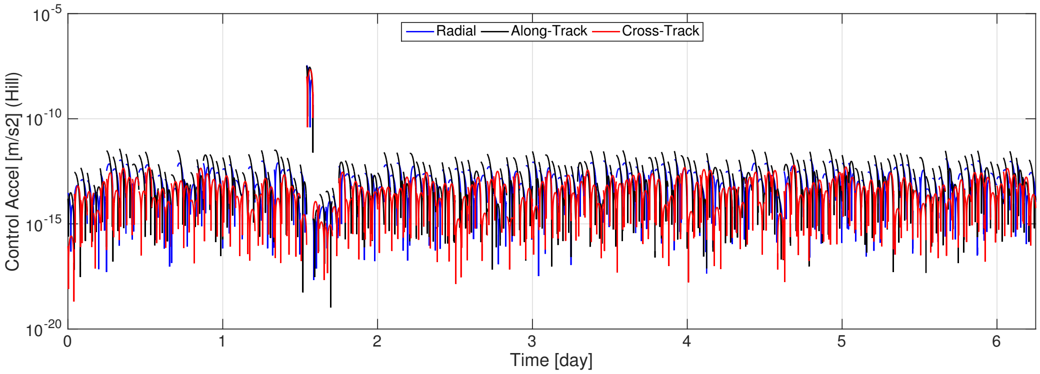

Figure 6.9: Magnitude of estimated controls in Hill frame when applying the Adaptive OCBE.

yet not too low to indicate overcompensation of mismodeling, indicates that we are maintaining tracking of the target. Position tracking is on the order of 1 m, but balloons to just under 1 km following the maneuver.

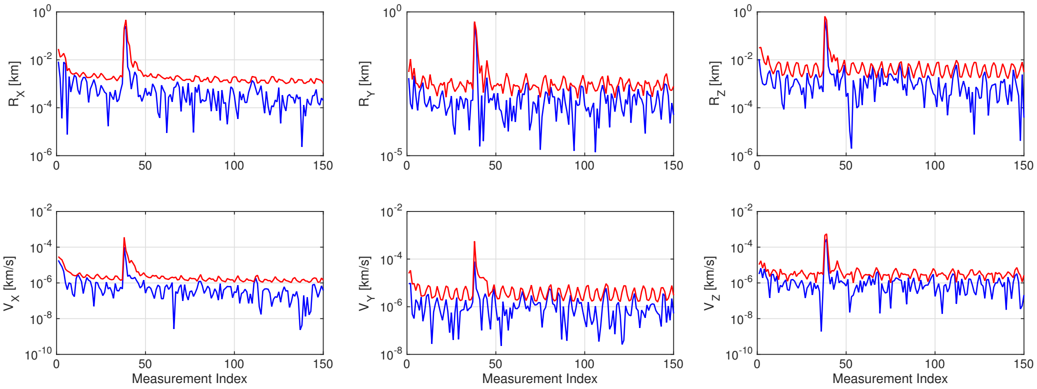

Figure 6.10: Cartesian state estimate deviations from truth against measurement index with a 3-σ envelope (red) when applying the Adaptive OCBE.

This example has shown the successful tracking of a target with mismodeled natural dynamics and an unknown actuated maneuver while obtaining information about those mismodelings through the control estimates. In this case setting the noise floor to level of mismodeling in the drag improves tracking, but setting it lower will not result in divergence. Rather, the Adaptive OCBE will make detections every so often to account for the accumulation of the mismodeling. This mismodeling can be identified in the distance metrics as correlation between the epochs, and it can be compensated for by increasing the dynamic noise floor.

6.2.2 Tracking a target in GEO with Unknown Stationkeeping Maneuvers

Recalling the simulation from Section 4.3, we are observing a target in GEO that is undergoing unknown stationkeeping maneuvers. Observations include range and angles for two hours a night (every 100 seconds during that 2 hours). As with the previous simulation we will now discuss the maneuver detection results for this simulation using the BL-OCBE and the Nonlinear OCBE in the following two sections.

As discussed in the algorithm development, detected maneuvers are defined as when all three metrics exceed their respective thresholds simultaneously. The delay algorithm requires two successive maneuvers be detected before addressing it with an adjusted dynamic uncertainty. This helps to differentiate between measurement outliers and true maneuvers so that the state uncertainty does not become artificially over inflated. This analysis uses a 99% threshold percentile for maneuver detection. When successive maneuvers are detected, an assumed dynamic standard deviation is chosen to ensure the mean of the control metric is equal to the calculated metric. The dynamic noise floor is set to $\sigma_{Q,NF} = 10^{-10}$ m/s^2.

Figure 6.11 shows the metric-threshold ratio for all three metrics. This is defined as the ratio of the distance metric to the distance metric threshold, thus anything exceeding one is a detected maneuver for that specific metric. For all three metrics we see the expected dispersion about the mean of the distribution with approximately one percent of the metrics exceeding the threshold (1.19% for the control metric, 1.10% for the measurement metric, and 1.37% for the a priori metric). In total there are 4 epochs where the three metrics simultaneously exceed their thresholds. However, when implementing the delay mechanism only two of these epochs stand out as true detected maneuvers. These correlate to the two true maneuvers. This tells us that the algorithm was able to successfully identify the only true maneuvers without any false detections in 1,094 observations.

While the previous metrics show maneuvers with respect to the noise floor, Fig. 6.12 shows maneuvers with respect to the adaptive assumed dynamic uncertainty. These results confirm the adaptive algorithm is working properly since the two maneuver detection events are removed. This indicates that the two detected maneuvers have been addressed with a proper level of dynamic uncertainty. For each metric some events still exceed the threshold, but these are because they were identified as being outliers rather than deterministic events via the combination of the three combined metrics and application of the delay mechanism.

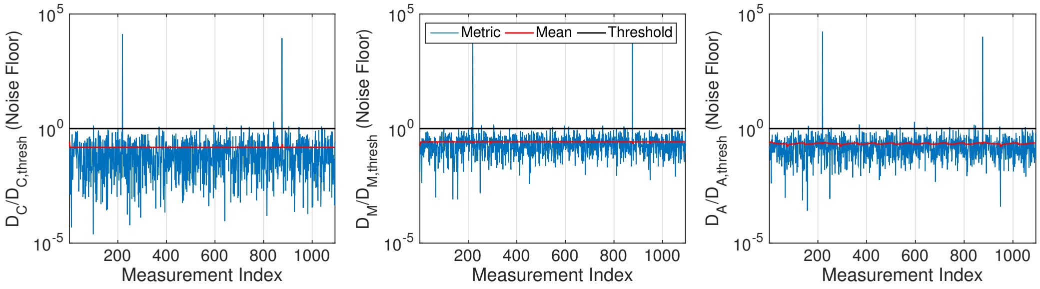

Figure 6.11: Distance metric-to-metric threshold ratio relative to dynamic noise floor when applying the Adaptive OCBE.

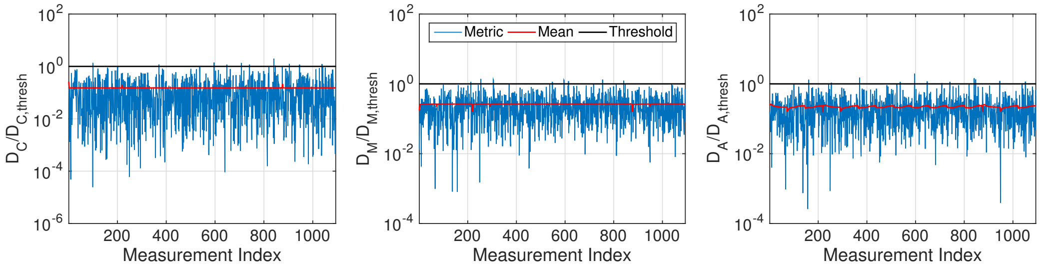

Figure 6.12: Distance metric to metric threshold ratio relative the adaptive assumed dynamic uncertainty when applying the Adaptive OCBE.

To this point it is clear that we successfully detected the presence of the only two maneuvers with no false detections. Our next step is to reconstruct these maneuvers to provide information on them. The first piece of information are the control estimates we obtained from the estimator. The magnitude of these controls in the Hill frame are shown in Fig. 6.13. The identified maneuvers clearly stick out in this plot with the rest of the estimated control being effectively zero. The first maneuver is heavily biased toward in plane accelerations with the radial and along-track directions approximately 2-3 orders of magnitude larger than the cross-track acceleration. This indicates that the maneuver is an EW maneuver. Similarly, the second maneuver is heavily biased toward the cross-track direction, which indicates that this is a NS maneuver. Additionally, we may use the metrics themselves to inform our reconstruction of the maneuvers. Because the maneuvers are one time events it becomes evident that they represent some non-natural process. This reinforces the hypothesis that the mismodeling is related to an actuated maneuver. We may also characterize the maneuvers based on these estimates as 0.525 m/s and 2.535 m/s maneuvers compared to the true values of 16.8652 m/s and 7.6552 m/s, respectively. Because these estimates are based on optimal controls they provide a lower bound on the true maneuver, but also give an order of magnitude estimate.

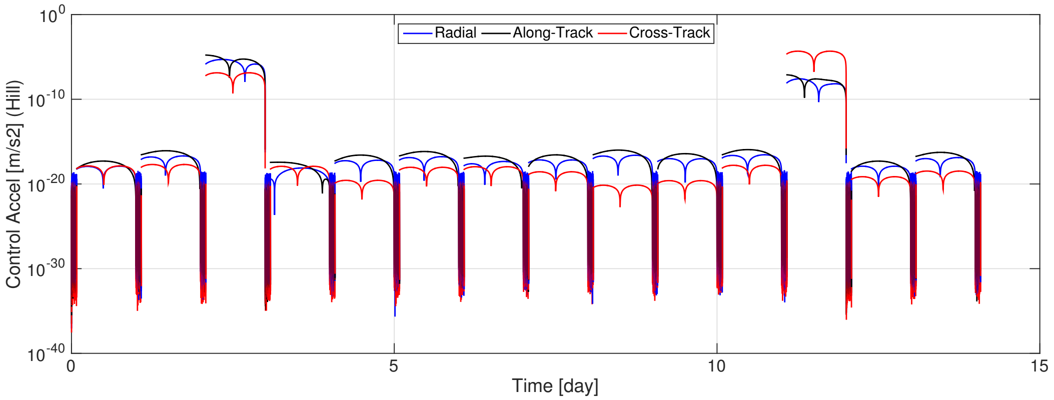

Figure 6.13: Magnitude of estimated controls in Hill frame when applying the Adaptive OCBE.

Finally, the results displayed in Fig. 6.14 show the level of tracking obtained with the OCBE. It is clear that the estimator maintains tracking of the spacecraft throughout both maneuvers and across all observation gaps. Tracking is attained on the 10 m level, which reflects the uncertainty in the measurements.

It should be noted that similar maneuver detection results are obtained with angles only observation. Fig. 6.15 shows the metric-to-threshold ratio results when the algorithm is run with angles only observation. Just as with the previous simulation, the only two events that are detected as maneuvers are the two true events. Tracking is not as good with fewer observations giving levels of approximately 1 km in position, rather than the 10 m level achieved with range. There are also observability issues that pop up as would be the case with a Kalman Filter. This does not prevent a solution, it just leads to tracking falling out of the 3-σ envelope more frequently.

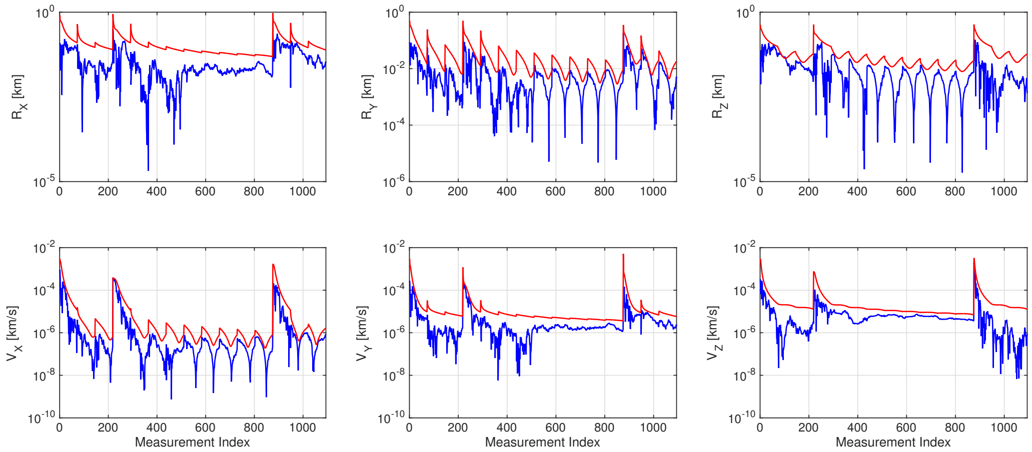

Figure 6.14: Cartesian state estimate deviations from truth against measurement index with a 3-σ envelope (red) when applying the Adaptive OCBE.

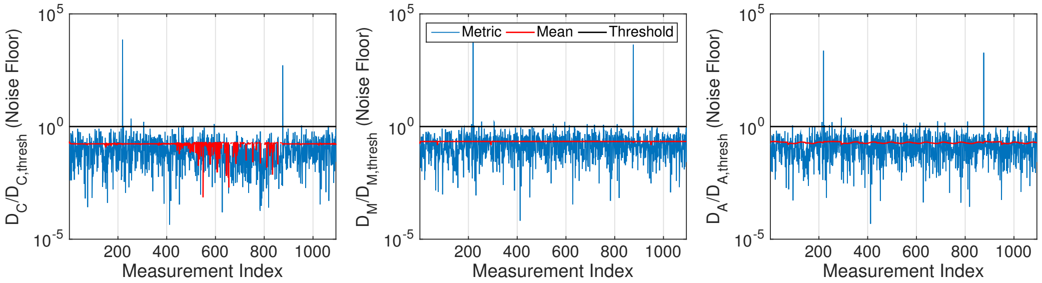

Figure 6.15: Distance metric-to-metric threshold ratio relative to the dynamic noise floor when applying the Adaptive OCBE with angles-only observation.

Application of the BL-OCBE yields very similar similar results except that there is only one metric to utilize. This means false detections are harder to reject. Using a delay of 2 consecutive detections, the BL-OCBE detects the true maneuvers and has one false detections. This false detection may be removed by increasing the delay to 3, though. In general the delay for the BL-OCBE should be slightly higher than the Nonlinear OCBE in order to promote an equivalent level of false detection rejection.

This simulation shows the Adaptive OCBE's ability to automatically track an object with mismodeled dynamics as well as detect and reconstruct that mismodeling. The algorithm correctly identified both maneuvers with no false detections in the 1,094 measurements processed. Even with fewer observation types the detection aspect of the work does not suffer, though tracking uncertainty increases due to a decrease in the amount of information.

6.3 Conclusions

In this chapter, we focused on automating the OCBE by developing a criterion to select the assumed dynamic uncertainty once a maneuver is detected. We defined a maneuver detection as when all metrics simultaneously exceed their thresholds over n_{delay} successive epochs. This method helps to eliminate false detections. Once the maneuver is detected we compensate for it by selecting an assumed dynamic uncertainty such that the calculated metric and the mean of its distribution are equal to one another. This method requires the user to set certain properties to initialize the estimator, but then all measurements are processed with the human out of the loop. Two flowcharts defining this processed were presented to illustrate how the algorithm is designed, and how it may be implemented.

We demonstrated the effectiveness of this algorithm via the same two simulations discussed in Chapter 4 and 5 - tracking targets in LEO and GEO. In both instances the algorithm is capable of automatically detecting and compensating for mismodeling. In the case of mismodeled drag, the mismodeling is not statistically significant over one measurement gap, thus detection and compensation is completed after several observations, but it never goes unaddressed. Adjusting the dynamic noise floor offers a solution, where the periodic detections are removed, though. In both examples the actuated maneuvers were successfully detected with no false detections. This demonstrates the ability of this algorithm to discern between true mismodeling and measurement outliers in an automated fashion. Being fully automated, this algorithm is far less tedious to apply and far more applicable to problems of real-time maneuver detection.

Chapter 7

Conclusions and Future Work

Throughout this thesis we have derived, developed, and discussed the Optimal Control Based Estimator (OCBE). This has included defining the motivation behind the work and where it fits in the existing literature, derived the estimator and its linear forms, discussed and proved important properties of the estimator and an accompanying smoother, developed a companion metrics-based maneuver detection method, automated the algorithm by using the maneuver detection results to adaptively adjust the assumed dynamic uncertainty, and demonstrated the algorithm through several sample applications of these algorithms. In this Chapter we will provide a more in depth summary and discussion of the results documented in this thesis. We will then conclude with some suggestions for future development of the algorithm, and its application to broader tracking problems.

7.1 Conclusions

Our development of OCBE started with defining our research goals and the motivation behind these goals, discussing the existing literature that addresses these research goals in some manner, and then defining why this research is unique and where it fits in the grander scheme of existing estimation methods. The OCBE is designed to be an algorithm that is capable state estimation in dynamically mismodeled systems with data sparse, non-cooperative observation sets while obtaining information about the mismodeling. In terms of information about the mismodeling, the method must be capable of identifying the presence of mismodeling, compensating for it, characterize it, and reconstruct it. This method must also be capable of automation for application to complex systems where it is infeasible to put a human in the loop. Additionally, though the algorithm should be written generally enough to be applied to any type of mechanical system that is observable, we specifically are looking for algorithms that are applicable to problems within the field of Space Situational Awareness (SSA) with generalization in terms of the Observer-Orbit setup. Existing literature provides many methods for attacking portions of this problem. Many different methods focus specifically on SSA, but these tend to be limited in application or even limited to a specific observer-orbit combination. Other methods from the fields of system identification and multiple model estimation are effective at approaching estimation in dynamically mismodeled systems, but non of the methods are able to achieve these results when being limited to data sparse, non-cooperative observation and having no control over the observed target. The OCBE is designed to satisfy this hole in the existing literature, which satisfies a need within the SSA community.

Following the definition of what the OCBE should be designed to accomplish, the next task was to discuss some necessary background information that would inform the development of the estimator. This background information included methods for functional optimization of a Bolza-type cost function, and the control distance metric approach of Holzinger, Scheeres, and Alfriend [28], which was designed for maneuver detection and object correlation in an SSA context. The former was necessary to introduce since the OCBE cost function must be optimized via functional methods. The latter informs the cost function of the OCBE and the maneuver detection method that is implemented with the OCBE, thus it is important to cover as context for the OCBE. Finally, the state and adjoint dynamics for SSA applications were defined since these would provided the basis almost all simulations presented in this thesis.

After defining this necessary background info, we defined and derived the OCBE. This included defining the cost function of the OCBE along with its physical and mathematical significance, deriving necessary conditions for a solution to the Nonlinear OCBE, and demonstrating its existence under certain conditions. Having found that no analytical solution exists for arbitrary nonlinear systems, next a linear version of the algorithm was derived and analyzed. The Generalized Linear

OCBE (GL-OCBE) was arranged into a Kalman-like formulation in order to make comparisons to this algorithm, which is a standard in the field of estimation theory and optimal in many respects. It was shown that the GL-OCBE operates like a biased Kalman filter, due to the biasing from a ballistic trajectory in its nominal trajectory. However it was found that the algorithm is ultimately unbiased. This means the expectations of its state estimates are truth, and the expectation of the control estimate is equal to the a priori control model, which indicates that the algorithm assumes no mismodeling other than what is already assumed in the a priori information - though errors in the system will induce a non-zero mismodeling estimate, which demonstrates the algorithm's robustness to dynamic mismodeling. The GL-OCBE equations were then reduced by assuming a ballistic nominal trajectory to form the Ballistic Linear OCBE (BL-OCBE). We demonstrated that this algorithm propagated dynamic uncertainty in a manner identical to continuous process noise, that the state estimate at the measurement epoch is equivalent to a Kalman filter estimate, and the state estimate at the a priori epoch is fully equivalent to a smoothed Kalman estimate. Put together this demonstrates that the BL-OCBE is a generalization of the Kalman algorithm, which means the BL-OCBE has all of the same optimality claims. Finally, we developed an algorithm that smoothed the OCBE solutions across all observations epochs such that the result was a smooth state trajectory and control estimates throughout the entire measurement arc. This derivation included Nonlinear, GL-OCBE, and BL-OCBE implementations with the latter being proven to be a generalization of Kalman smoother with the addition of an optimal control estimate.

Having defined and derived the OCBE, we next demonstrated its abilities through sample applications. This included three different applications: a mismodeled mass-spring-damper (MSD) system, observation of a target in Low Earth Orbit (LEO), and observation of a target in Geosynchronous Earth Orbit (GEO). Through the MSD example we demonstrated the algorithm on a linear level. Specifically, we demonstrated the ability of the algorithm to reconstruct both mismodeled natural dynamics and unmodeled perturbations. In the LEO example we showed that the algorithm was able to maintain track of target with sparse observation while detecting consistent natural dynamics mismodeling and an actuated maneuver. We found in this example that the

Nonlinear OCBE and BL-OCBE had very similar performance. This was because the observation gaps and the maneuvers were not large enough to require a nonlinear approach. Application of the smoother did successfully improve tracking by an order of magnitude. In the GEO example it was shown that the Nonlinear OCBE and BL-OCBE maintained tracking of the target across long observation gaps and large stationkeeping maneuvers The Nonlinear OCBE did have better performance overall, which is attributed to the fact that it tracked better through a large maneuver and long observation gaps. Coupled with the LEO example, we showed that the BL-OCBE tracks well in the face of dynamic mismodeling, but when the linear assumptions are stressed the Nonlinear OCBE provides better performance.

The uniqueness of the OCBE lies in the optimal control estimates that it outputs. These controls are models for the mismodeling within the system, and as such we may use them to detect the presence of statistically significant mismodeling as well as reconstruct it. We define three metrics for the OCBE that may be used to assess whether the estimates coming out of the OCBE are statistically significant to the point that represent deterministic mismodeling within the estimator. The defined method for maneuver detection uses these defined metrics as χ^2 statistics in a 1-tailed hypothesis test. Given that the OCBE operates via application of the GL-OCBE or the BL-OCBE, the metrics were linearized and simplified for application to these estimators. The three metrics for the BL-OCBE were shown to be completely dependent, thus a new combined metric was defined, that could be reduced to a form that is completely equivalent to a χ^2 statistic (with the requirement of any approximations). Beyond this a method for estimating natural dynamics using the estimated optimal controls was developed and demonstrated. Finally, the maneuver detection methods were demonstrated through numerical simulation via sample tracking applications.

To this point the OCBE was designed to be capable of state estimation and maneuver detection and reconstruction in dynamically mismodeled systems with data sparse and non-cooperative observation sets. However, application to SSA tracking problems is limited by the requirement of a human in the loop to manually adjust the assumed dynamic uncertainty with the introduction of each new measurement. To account for this we made the algorithm into an adaptive estimator by developing a method to automatically select the assumed dynamic uncertainty. This method uses the results of the maneuver detection method to automatically select an assumed dynamic uncertainty such that the resulting distance metric is equivalent to the mean of that metric's distribution. This method is only implemented when a maneuver is detected, which was defined to be when the distance metric simultaneously exceed their respective metrics for n_{delay} successive measurement epochs. Once the maneuver is detected, the algorithm automatically compensates for its presence and reconstructs in via the optimal control estimates. Flowcharts defining this combined algorithm, the Adaptive OCBE (OCBE with maneuver detection and automated assumed dynamics uncertainty selection), were provided to illustrate how the algorithm might be implemented for application to real-time state estimation and maneuver detection problems. Finally, the Adaptive OCBE was applied to sample tracking scenarios in order to demonstrate the algorithm's effectiveness at maintaining track of a maneuvering object and detecting mismodeled dynamics in a completely automated fashion.

This thesis detailed the complete development of the OCBE and all of its companion algorithms, with more detailed derivations provided in the Appendix for completeness. The derivation is kept general, so that it may be implemented for any mechanical system though the maneuver detection and adaptive developments do primarily focus on an SSA application. The resulting algorithm represents an algorithmic manifestation of the research goal given that it is an algorithm for real-time state estimation in dynamically mismodeled systems with data sparse and non-cooperative observation sets while obtaining information about any present mismodelings. In the next section we present ideas for logical extensions of this work, which would represent significant advancements in the theory and application of this algorithm.

7.2 Future Work

While the OCBE as designed successfully fulfills the goals of this research, there is always room to advance these goals to push for an even wider application of this algorithm along with improved effectiveness. Below, we present a list of logical extensions of the theory and application of this work with a specific emphasis on application to problems within SSA.

(1) More efficient numerical solution of nonlinear estimator: The numerical solution to the Nonlinear OCBE that we obtain is via iteration of the GL-OCBE until necessary converge within an accepted tolerance of zero. It is suggested that this method be improved by introducing more efficient nonlinear solvers.

(2) Distinguish maneuvers, measurement anomalies, and invalid observation-target correlation in real-time: When a mismodeling is detected it can represent dynamic mismodeling, an anomaly in the measurement (or a priori state estimate), or it may just be an invalid observation-target correlation (which is akin to a measurement anomaly, but from a different source). Measurement anomalies often look like maneuvers, but we remove them via maneuver compensation delay. To promote real-time application of this work, we suggest researching a method for distinguishing measurement anomalies from maneuver, so that they can be dealt with separately. The method could approach the problem from a multi-hypothesis foundation where the probability of each occurrence is assessed to determine the most likely cause of the detection.

(3) Compensate for measurement anomalies: The adaptive OCBE accounts for mismodelings as if they are dynamic in nature. In partnership with the previous suggestion, a method to compensate for measurement anomalies would offer improved estimator performance, and fewer false detections. This method would also account false measurement associations by removing the measurement from the observation set.

(4) Application to multi-target tracking with uncorrelated measurements: The OCBE is single target estimator, but for many SSA applications multi-target trackers are necessary where the observations taken are uncorrelated. Combining the previous suggestions to address measurement association, it would advance this estimator significantly to adapt it to problems with N targets and M uncorrelated measurements.

(5) Analytical relation between distance metrics and inputs (i.e. measurements and a priori estimates): To make the maneuver association problem more computationally feasible for systems with many targets, an analytical mapping between the estimator inputs and the OCBE distance metrics would allow for much faster maneuver association, thus allowing for application to multi-target tracking problems.

Bibliography

[1] B. S. Aaron. Geosynchronous Satellite Maneuver Detection and Orbit recovery Using Ground Based Optical Tracking. PhD thesis, Massachusetts Institute of Technology, Cambridge, MA, 2006.

[2] R. Adrain. Research concerning the probabilities of the errors which happen in making observations. The Analyst, 1(4):93–109, 1808.

[3] European Space Agency. Europe's envisat: Environment satellite.

[4] J. Ahmed, V. T. Coppola, and D. S. Bernstein. Asymptotic tracking of spacecraft attitude motion with inertia matrix identification. Journal of Guidance, Control, and Dynamics, 21(5):684–691, 1998.

[5] J. Aldrich. R.a. fisher and the making of the maximum likelihood 1912-1922. Statistical Science, 12(3):162–176, 1997.

[6] M. Athans and E. Tse. A direct derivation of the optimal linear filter using the maximum principle. IEEE Transactions on Automatic Control, 12(6):690–698, 1967.

[7] Y. Bar-Shalom and K. Birmiwal. Variable dimension filter for maneuvering target tracking. Transactions on Aerospace and Electronic Systems, 18(5):621–629, 1982.

[8] T. Bayes. An essay toward solving a problem in the doctrine of chances. Philosophical Transactions of the Royal Society of London, 53:370–418, 1763.

[9] G. J. Bierman. Comment on sequential estimation algorithm using a continuous udu^t covariance factorization. Journal of Guidance and Control, 4(4):444–446, 1980.

[10] R. Brincker, L. Zhang, and P. Andersen. Modal identification of output-only systems using frequency domain decomposition. Smart Materials and Structures, 10(3):441–445, 2001.

[11] Y. T. Chan, A. G. C. Hu, and J. B. Plant. A kalman filter based tracking scheme with input estimation. Transactions on Aerospace and Electronic Systems, 15(2):237–244, 1979.

[12] J. Chandrasekar and D. S. Bernstein. Position control using acceleration-based identification and feedback with unknown measurement bias. Journal of Dynamic Systems, Measurement, and Control, 130(1), 2007.

[13] H. D. Curtis. Orbital Mechanics for Engineering Students. Elsevier Academic Press, 2nd edition, 2010.

[14] L. Dieci and T. Eirola. Positive definiteness in the numerical solution of riccati differential equations. Numeriche Mathematik, 67:303–313, 1994.

[15] R. A. Fisher. On an absolute criterion for fitting frequency curves. Messenger of Mathematics, 41:155–160, 1912.

[16] R. A. Fisher. On the mathematical foundations of theoretical statistics. Philosophical Transactions of the Royal Society of London, 222:594–604, 1922.

[17] S.K. Flegel, J. Gelhaus, M. Mockel, C. Wiedmann, H. Krag, H. Klinkrad, and P. Vorsmann. Multi-layer insulation model for master-2009. Acta Astronautica, 69(11-12):911–922, December 2011.

[18] Z. J. Folcik, P. J. Cefola, and R. I. Abbot. Geo maneuver detection for space situational awareness. Advances in Astronautical Sciences, 129:1058–1074, 2007.

[19] K. F. Gauss. Theory of Motion of the Heavenly Bodies Moving About the Sun in Conic Sections: A Translation of Theoria Motus. Dover Phoenix Editions, 2004 (1809).

[20] G. M. Goff, J. T. Black, and J. A. Beck. Orbit estimation of a continuously thrusting spacecraft using variable dimension filters. In AIAA Guidance, Navigation, and Control Conference, January 2015.

[21] L. Grego. A history of anti-satellite programs. http://www.ucsusa.org/, January 2012.

[22] M.S. Grewal and A.P. Andrews. Applications of kalman filtering in aerospace 1960 to the present [historical perspectives]. Control Systems, IEEE, 30(3):69–78, June 2010.

[23] M. Gruss. Haney: U.s. partners to have indirect access to space fence data. http://spacenews.com/42619haney-us-partners-to-have-indirect-access-to-space-fence-data/, November 2014.

[24] A. Hald. A History of Parametric Statitical Inference From Bernoulli to Fisher, 1713-1935. Springer, 2007.

[25] P. D. Hanlon and P. S. Maybeck. Characterization of kalman filter residuals in the presence of mismodeling. IEEE Transactions on Aerospace and Electronic Systems, 36(1):114–131, 2000.

[26] J. Herzog and T. Schildknecht. Analysis of the long-term area-to-mass ratio variation of space debris. In Advanced Maui Optical and Space Surveillance Technologies Conference, September 2012.

[27] K. Hill. Maneuver detection and estimation with optical tracklets. In Advanced Maui Optical and Space Surveillance Technologies Conference, September 2014.

[28] M. J. Holzinger, D. J. Scheeres, and K. T. Alfriend. Object correlation, maneuver detection, and characterization using control distance metrics. J. Guidance, Control, and Dynamics, 35(4):1312–1325, 2012.

[29] D. S. Ingram. Orbit Determination in the Presence of Unmodeled Accelerations. PhD thesis, University of Texas, Austin, TX, 1970.

[30] A. H. Jazwinski. Stochastic Processes and Filtering Theory. Elsevier Academic Press, 1970.

[31] N. L. Johnson and S. Kotz. Leading Personalities in Statistical Sciences. Wiley, 1997.

[32] N. L. Johnson, E. Stansberry, D. O. Whitlock, K. J. Abercromby, and D. Shoots. History of on-orbit satellite fragmentations. Technical Report 14th Edition, National Aeronautics and Space Administration: Orbital Debris Program Office, June 2008.

[33] S. J. Julier and J. K. Uhlmann. New extension of the Kalman filter to nonlinear systems. In I. Kadar, editor, Signal Processing, Sensor Fusion, and Target Recognition VI, volume 3068 of Society of Photo-Optical Instrumentation Engineers (SPIE) Conference Series, pages 182–193, July 1997.

[34] R. E. Kalman. A new approach to linear filtering and prediction problems. Transactions of the ASME–Journal of Basic Engineering, 82(Series D):35–45, 1960.

[35] R. E. Kalman and R. S. Bucy. New results in linear filtering and prediction theory. Transactions of the ASME–Journal of Basic Engineering, 83(1):95–108, 1961.

[36] T. S. Kelso. Iridium 33/cosmos 2251 collision. http://celestrak.com/events/collision/, June 2012.

[37] T. S. Kelso. Chinese space debris maypp have hit russian satellite. http://blogs.agi.com/agi/2013/03/08/chinese-space-debris-hits-russian-satellite/, March 2013.

[38] P. M. Laplace. Theorie analytique des probabilits. Paris, Ve. Courcier, 1812.

[39] S. L. Lauritzen. Time series analysis in 1880. a discussion of contributions made by t.n. thiele. International Statistical Review, 49(3):319–331, 1981.

[40] S. L. Lauritzen. Thiele - Pioneer in Statistics. Clarendon Press, 2002.

[41] D. F. Lawden. Optimal Trajectories for Space Navigation. Butterworths Mathematical Texts, 1963.

[42] D. F. Lawden. Analytical Methods of Optimization. Dover Publications Inc., 1975.

[43] S. Lee and I. Hwang. Interacting multiple model estimation for spacecraft maneuver detection and characterization. In AIAA Guidance, Navigation, and Control Conference, January 2015.

[44] A. M. Legendre. Nouvelles mthodes pour la dtermination des orbites des comtes. F. Didot, 1805.

[45] S. Lemmens and H. Krag. Two-line-elements-based maneuver detection methods for satellites in low earth orbit. Journal of Guidance and Control, 2014.

[46] X. R. Li and V. P. Jilkov. Survey of maneuvering target tracking. part i: Dynamic models. IEEE Transactions on Aerospace and Electronic Systems, 39(4):1333–1364, 2005.

[47] X. R. Li and V. P. Jilkov. Survey of maneuvering target tracking. part v: Multiple-model methods. IEEE Transactions on Aerospace and Electronic Systems, 41(4):1255–1321, 2005.

[48] J. C. Liou and D. Shoots. Orbital debris quarterly news. National Aeronautics and Space Administration, 12(1), January 2008.

[49] J. C. Liou and D. Shoots. Orbital debris quarterly news. National Aeronautics and Space Administration, 15(3), July 2011.

[50] L. Ljung. System Identification:Theory for the User. Prentice Hall, 2nd edition, 1999.

[51] J. Mackey. Recent us and chinese antisatellite activities. Air and Space Power, 2009.

[52] R. Mandankan, P. Singla, T. Singh, and P. D. Scott. Polynomial-chaos-based bayesian approach for state and parameter estimations. Journal of Guidance and Control, 36(4):1058–1074, 2013.

[53] J. P. Marec. Optimal Space Trajectories. Elsevier Academic Press, New York, NY, 1979.

[54] A. M. Mathai and S. B. Provost. Quadratic Forms in Random Variables: Theory and Applications. Marcel Dekker, Inc., 1992.

[55] Jay W. McMahon. An Analytical Theory for the Perturbative Effect of Solar Radiation Pressure on Natural and Artificial Satellites. PhD thesis, University of Colorado, Boulder, CO, 2011.

[56] P. Del Moral. Nonlinear filtering: Interacting particle resolution. Markov Processes and Related Fields, 2(4):555–580, 1996.

[57] R. P. Patera. Space event detection method. Journal of Spacecraft and Rockets, 45(3):554–559, 2008.

[58] H. Pollard. Celestial Mechanics: The Carcus Mathematical Monographs, No. 18. Mathematical Association of America, 1976.

[59] J. E. Prussing. Optimal two- and three-impulse fixed-time rendezvous in the vicinity of a circular orbit. AIAA Journal, 8(7):1221–1228, 1970.

[60] J. E. Prussing and J. H. Chiu. Optimal multiple-impulse time-fixed rendezvous between circular orbits. AIAA Journal, 9(1), 1986.

[61] C. V. Rao, J. B. Rawlings, and D. Q. Mayne. Constrained state estimation for nonlinear discrete-time systems: Stability and moving horizon approximations. IEEE Transactions on Automatic Control, 48(2):246–258, 2003.

[62] G. W. Rosoborough and P. G. Antreasian. Radiation force modeling for the topex/poseidon spacecraft. AIAA Journal, pages 168–178, 1990.

[63] F. H. Schlee, C. J. Standish, and N. F. Toda. Divergence in the kalman filter. AIAA Journal, 5(6):1114–1120, 1967.

[64] D. Shoots and P. Anz-Meador. Orbital debris quarterly news. National Aeronautics and Space Administration, 19(3), July 2015.

[65] D. Simon. Optimal State Estimation. John Wiley and Sons, 2006.

[66] N. Singh, J. T. Horwood, and A. B. Poore. Space object maneuver detection via a joint optimal control and multiple hypothesis tracking approach. In 22nd AAS/AIAA Space Flight Mechanics Meeting. AAS/AIAA, January 2012.

[67] G. L. Smith, S. F. Schmidt, and L. A. McGee. Application of statistical filter theory to the optimal estimation of position and velocity on board a circumlunar vehicle. Technical Report R-135, National Aeronautics and Space Administration, 1962.

[68] M. C. Smitham. The need for a global space-traffic-control service: An opportunity for us leadership. Maxwell Paper No. 57, February 2010.

[69] E. Stansberry. Orbital debris: Frequently asked questions. http://orbitaldebris.jsc.nasa.gov/faqs.html, March 2012.

[70] R. F. Stengel. Optimal Control and Estimation. Dover Publications Inc., New York, NY, 1986.

[71] J. Stewart. Calculus: Single Variable. Thomson, 5th edition, 2005.

[72] S. M. Stigler. Gauss and the invention of least squares. The Annals of Statistics, 9(3):465–474, 1981.

[73] S. M. Stigler. The History of Statistics: The Measurement of Uncertainty Before 1900. Belknap Press, 1990.

[74] R. L. Stratonovich. On the theory of optimal nonlinear filtering of random functions. Theory of Probability and it Applications, 4:223–225, 1959.

[75] R. L. Stratonovich. Optimum nonlinear systems which bring about a separation of a signal with constant parameters from noise. Radiofizika, 2(6):892–901, 1959.

[76] R. L. Stratonovich. Application of the markov processes theory to optimal filtering. Radio Engineering and Electronic Physics, 5(11):1–19, 1960.

[77] R. L. Stratonovich. Conditional markov processes. Theory of Probability and it Applications, 5:156–178, 1960.

[78] S. C. Stubberud and K. A. Kramer. System identification using the neural-extended kalman filter for state-estimation and controller modification. In IEEE World Congress on Computational Intelligence, 2008.

[79] P. Swerling. First-order error propagation in a stagewise smoothing procedure for satellite observations. Technical Report RM-2329, U.S. Air Force: Project Rand, 1959.

[80] B. D. Tapley and D. Ingram. Orbit determination in the presence of unmodeled accelerations. IEEE Transactions on Automatic Control, 18(4):369–373, 1973.

[81] B. D. Tapley and J. G. Peters. Reply by authors to g.j. bierman. Journal of Guidance and Control, 4(4):446–448, 1980.

[82] B. D. Tapley and J. G. Peters. Sequential estimation algorithm using a continuous udu^t covariance factorization. Journal of Guidance and Control, 3(4):326–331, 1980.

[83] B. D. Tapley, B. E. Schutz, and G. H. Born. Statistical Orbit Determination. Elsevier Academic Press, 1st edition, 2004.

[84] D. A. Vallado. Fundamentals of Astrodynamics and Applications. Microcosm Press, 3rd edition, 2007.

[85] V. Viberg. Subspace-based methods for the identification of linear time-invariant systems. Automatica, 31(12):1835–1851, 1995.

[86] R. E. Walpole, R. H. Myers, S. L. Myers, and K. E. Ye. Probability and Statistics for Engineers and Scientists. Pearson, 9th edition, 2011.

[87] D. Wang and A. Haldar. System identification with limited observations and without input. Journal of Engineering Mechanics, 123(5):504–511, 1997.

[88] B. Weeden. Space situational awareness fact sheet. Secure World Foundation, September 2014.

Appendix A

Derivation of the GL-OCBE State, Adjoint and Control Estimates

In this appendix a full derivation for the GL-OCBE state, adjoint and control estimates. This will focus on steps that are not trivial in order to demonstrate how one obtains the estimates starting with the linearized nonlinear necessary conditions defined in Chapter 3 (Eqs. 3.19 - 3.21). This derivation starts with the state estimate at the measurement epoch ($\delta\hat{x}_{k|k}$), covers the state estimate at the a priori epoch ($\delta\hat{x}_{k-1|k}$) next, moves to the adjoint estimate at the a priori epoch ($\delta\hat{p}_{k-1|k}$), and concludes with optimal control estimate. In this section there is not teatment of the uncertainties in these estimate. These are reserved for Appendix B.

A.1 State Estimate at the Measurement Epoch

To obtain the GL-OCBE we start with the linearizations made in Theorem 3.1. While that analysis focuses on the state estimate at the a priori epoch, this derivation will focus on the state estimate at the measurement epoch since it is possible to draw parallels to existing estimators like the Kalman Filter. Taking the results of Eqs. 3.19 - 3.21, they are rearranged to solve for $\delta\hat{x}_{k|k}$ as shown below.

$$
\begin{aligned}
\delta\hat{x}_{k|k} =& M_k \left(\delta\bar{x}_{k-1|k-1} - \bar{P}_{k-1|k-1}\tilde{p}_{k-1}\right) + N_k \left[\tilde{p}_k + \vec{v}_p(t_k) + \tilde{H}_k^T R_k^{-1} \left(\delta\tilde{y}_k - \tilde{H}_k \vec{v}_x(t_k)\right)\right] + \vec{v}_x(t_k) \\
M_k =& \Bigg[\Phi_{xp} + \left(\Phi_{xx} - \Phi_{xp}\bar{P}^{-1}_{k-1|k-1}\right) \left[\left(\tilde{H}_k^T R_k^{-1} \tilde{H}_k \Phi_{xx} - \Phi_{px}\right) + \left(\Phi_{pp} - \tilde{H}_k^T R_k^{-1} \tilde{H}_k \Phi_{xp}\right) \bar{P}^{-1}_{k-1|k-1}\right]^{-1} \\
& \cdot \left(\Phi_{pp} - \tilde{H}_k^T R_k^{-1} \tilde{H}_k \Phi_{xp}\right)\Bigg] \bar{P}^{-1}_{k-1|k-1} \\
N_k =& \left(\Phi_{xx} - \Phi_{xp}\bar{P}^{-1}_{k-1|k-1}\right) \Bigg[\left(\Phi_{pp}\bar{P}^{-1}_{k-1|k-1} - \Phi_{px}\right) \\
& + \tilde{H}_k^T R_k^{-1} \tilde{H}_k \left(\Phi_{xx} - \Phi_{xp}\bar{P}^{-1}_{k-1|k-1}\right)\Bigg]^{-1}
\end{aligned}
\tag{A.1}
$$

We will now attempt to reduce this into a Kalman-like formulation by simplification of these gain matrices. This starts with the gain matrix on the measurement deviation vector, which should essentially be the Kalman Gain of this estimator (what we will refer to as the OCBE Gain).

$$
\begin{aligned}
L_k =& N_k \tilde{H}_k^T R_k^{-1} \\
=& \left[\left(\Phi_{pp}\bar{P}^{-1}_{k-1|k-1} - \Phi_{px}\right) \left(\Phi_{xx} - \Phi_{xp}\bar{P}^{-1}_{k-1|k-1}\right)^{-1} + \tilde{H}_k^T R_k^{-1} \tilde{H}_k\right]^{-1} \tilde{H}_k^T R_k^{-1}
\end{aligned}
\tag{A.2}
$$

Application of the Schur Identity and subsequent algebraic simplifications leads to the gain matrix below.

$$
\begin{aligned}
L_k =& \mathcal{P}_{k|k-1} \tilde{H}_k^T \left(R_k + \tilde{H}_k \mathcal{P}_{k|k-1} \tilde{H}_k^T\right)^{-1} \\
\mathcal{P}_{k|k-1} =& \left(\Phi_{xx}\bar{P}_{k-1|k-1} - \Phi_{xp}\right) \left(\Phi_{pp} - \Phi_{px}\bar{P}_{k-1|k-1}\right)^{-1}
\end{aligned}
\tag{A.3}
$$

This result seems very comparable to the Kalman Gain other than the $\mathcal{P}_{k|k-1}$ matrix. To have complete equality this matrix must be equivalent to the propagated a priori covariance at the measurement epoch. The properties of this matrix are discussed in section B.2. This matrix is referred to as the propagated a priori state quasi-covariance.

Now we will move on to the the gain on the a priori state deviation (M_k). Rearranging this matrix and subbing in the OCBE Gain.

$$
\begin{aligned}
M_k =& \Phi_{xp}\bar{P}^{-1}_{k-1|k-1} - L_k \tilde{H}_k \Phi_{xp}\bar{P}^{-1}_{k-1|k-1} \\
& + \left(\Phi_{xx} - \Phi_{xp}\bar{P}^{-1}_{k-1|k-1}\right) \left[\left(\Phi_{pp}\bar{P}^{-1}_{k-1|k-1} - \Phi_{px}\right) + \tilde{H}_k^T R_k^{-1} \tilde{H}_k \left(\Phi_{xx} - \Phi_{xp}\bar{P}^{-1}_{k-1|k-1}\right)\right]^{-1} \Phi_{pp}\bar{P}^{-1}_{k-1|k-1}
\end{aligned}
\tag{A.4}
$$

Making the temporary definitions in Eq. A.5, we expand and rearrange the equation to obtain the form shown below.

$$\begin{aligned} A =& \Phi_{pp}\bar{P}^{-1}_{k-1|k-1} - \Phi_{px} \\ B =& \tilde{H}^{T}_{k} R^{-1}_{k} \tilde{H}_{k} \\ C =& \Phi_{xx} - \Phi_{xp}\bar{P}^{-1}_{k-1|k-1} \end{aligned} \tag{A.5}$$

$$\begin{aligned} M_k &= \Phi_{xp}\bar{P}^{-1}_{k-1|k-1} + C\left(A+BC\right)^{-1}\left(A+\Phi_{px}\right) - L_k\tilde{H}_k\Phi_{xp}\bar{P}^{-1}_{k-1|k-1} \\ &= \Phi_{xp}\bar{P}^{-1}_{k-1|k-1} + \left(I+CA^{-1}B\right)^{-1}\left(\Phi_{xx} - \Phi_{xp}\bar{P}^{-1}_{k-1|k-1}\right) \\ &\quad + C\left(A+BC\right)^{-1}\Phi_{px} - L_k\tilde{H}_k\Phi_{xp}\bar{P}^{-1}_{k-1|k-1} \end{aligned} \tag{A.6}$$

Further rearranging leads to the form below. This requires rearranging the result and subbing in the OCBE Gain then canceling out both terms with OCBE Gain.

$$\begin{aligned} M_k &= \left[I - \left(I+CA^{-1}B\right)^{-1}\right]\Phi_{xp}\bar{P}^{-1}_{k-1|k-1} + \left(I+CA^{-1}B\right)^{-1}\Phi_{xx} \\ &\quad - L_k\tilde{H}_k\Phi_{xp}\bar{P}^{-1}_{k-1|k-1} + C\left(A+BC\right)^{-1}\Phi_{px} \\ &= \left(I+CA^{-1}B\right)^{-1}\Phi_{xx} + C\left(A+BC\right)^{-1}\Phi_{px} \end{aligned} \tag{A.7}$$

Application of the Schur identity to the second term with subsequent simplification leads to the first form below. Further simplification is shown, where the final step involves subbing in the relations for the OCBE Gain and $\mathcal{P}_{k|k-1}$.

$$\begin{aligned} M_k &= \left(I+CA^{-1}B\right)^{-1}\Phi_{xx} + \left(I+CA^{-1}B\right)^{-1}CA^{-1}\Phi_{px} \\ &= \left(I+CA^{-1}B\right)^{-1}\left(\Phi_{xx} + CA^{-1}\Phi_{px}\right) \\ &= \left(I+CA^{-1}B\right)^{-1}\left[\left(I+CA^{-1}B\right) - CA^{-1}B\right]\left(\Phi_{xx} + CA^{-1}\Phi_{px}\right) \\ &= \left[I - C\left(A+BC\right)^{-1}B\right]\left(\Phi_{xx} + CA^{-1}\Phi_{px}\right) \\ &= \left[I - L_k\tilde{H}_k\right]\left(\Phi_{xx} + \mathcal{P}_{k|k-1}\Phi_{px}\right) \end{aligned} \tag{A.8}$$

This result is very similar to the Kalman other than the trailing matrix $(\Phi_{xx}+\mathcal{P}_{k|k-1}\Phi_{px})$. Properties of this trailing matrix are discussed in the next subsection.

The final matrix to consider is N_k. Using the same definitions from A.5, this matrix may be rewritten and simplified as demonstrated below.

$$\begin{aligned} N_k &= \left(\Phi_{xx} - \Phi_{xp}\bar{P}^{-1}_{k-1|k-1}\right)\left[\left(\Phi_{pp}\bar{P}^{-1}_{k-1|k-1} - \Phi_{px}\right) + \tilde{H}^T_k R^{-1}_k \tilde{H}_k \left(\Phi_{xx} - \Phi_{xp}\bar{P}^{-1}_{k-1|k-1}\right)\right]^{-1} \qquad (A.9) \\ &= C\left(A + BC\right)^{-1} \\ &= \left(I + CA^{-1}B\right)^{-1} CA^{-1} \\ &= \left(I + CA^{-1}B\right)^{-1}\left[\left(I + CA^{-1}B\right) - CA^{-1}B\right] CA^{-1} \\ &= \left[I - C\left(A + BC\right)^{-1} B\right] CA^{-1} \\ &= \left[I - L_k\tilde{H}_k\right]\mathcal{P}_{k|k-1} \end{aligned}$$

This simplification involves applying the Schur identity, rearranging the result, and then subbing in the definitions for the OCBE Gain and $\mathcal{P}_{k|k-1}$.

Having completed all necessary simplifications we define the fully simplified state estimate at the measurement epoch as shown below.

$$\delta\hat{x}_{k|k} = \left(\delta\bar{x}_{k|k-1} + \tilde{b}_k + \vec{v}_x(t_k)\right) + L_k\left[\delta\tilde{y}_k - \tilde{H}_k\left(\delta\bar{x}_{k|k-1} + \tilde{b}_k + \vec{v}_x(t_k)\right)\right] \qquad (A.10)$$

$$\delta\bar{x}_{k|k-1} = \left(\Phi_{xx} + \mathcal{P}_{k|k-1}\Phi_{px}\right)\delta\bar{x}_{k-1|k-1} \qquad (A.11)$$

$$\tilde{b}_k = \mathcal{P}_{k|k-1}\left(\tilde{p}_k + \vec{v}_p(t_k)\right) - \left(\Phi_{xx} + \mathcal{P}_{k|k-1}\Phi_{px}\right)\bar{P}_{k-1|k-1}\tilde{p}_{k-1} \qquad (A.12)$$

The form of this estimate is quite similar to the Kalman Filter definition other than the biasing term ($\tilde{b}_k$). Analysis of these equations is provided in section 3.3.

A.2 State Estimate at the a priori Epoch

Having solved for the state estimate at the measurement epoch, the remaining estimates can be obtained by leveraging this already simplified form. The state estimate at the a priori epoch defined in terms of the state estimate at the measurement epoch is given below.

$$\delta\hat{x}_{k-1|k} = \left(\Phi_{xx} - \Phi_{xp}\bar{P}^{-1}_{k-1|k-1}\right)^{-1}\left[\delta\hat{x}_{k|k} - \Phi_{xp}\left(\bar{P}^{-1}_{k-1|k-1}\delta\bar{x}_{k-1|k-1} - \tilde{p}_{k-1}\right) - \vec{v}_x(t_k)\right] \qquad (A.13)$$

Using Eq. A.10, Eq. A.13 may be simplified to a form that is solely a function of the system inputs. This is shown in the following development.

$$\begin{aligned}\delta\hat{x}_{k-1|k} =& \left[I_{n\times n} + \bar{P}_{k-1|k-1}\left(\Phi_{pp} - \Phi_{px}\bar{P}_{k-1|k-1}\right)^{-1}\Phi_{px}\right]\delta\bar{x}_{k-1|k-1} \\ &+ \bar{P}_{k-1|k-1}\left(\Phi_{xx}\bar{P}_{k-1|k-1} - \Phi_{xp}\right)^{-1}\left(\tilde{b}_k + \Phi_{xp}\tilde{p}_{k-1}\right) \\ &+ \bar{P}_{k-1|k-1}\left(\Phi_{xx}\bar{P}_{k-1|k-1} - \Phi_{xp}\right)^{-1}L_k\left[\delta\vec{y}_k - \tilde{H}_k\left(\delta\bar{x}_{k|k-1} + \tilde{b}_k + \vec{v}_x(t_k)\right)\right] \\ =& \mathcal{I}_{k-1}\left(\delta\bar{x}_{k-1|k-1} + \tilde{b}_{k-1}\right) + L_{k-1}\left[\delta\vec{y}_k - \tilde{H}_k\left(\delta\bar{x}_{k|k-1} + \tilde{b}_k + \vec{v}_x(t_k)\right)\right]\end{aligned} \tag{A.14}$$

$$\mathcal{I}_{k-1} = I_{n\times n} + \bar{P}_{k-1|k-1}\left(\Phi_{pp} - \Phi_{px}\bar{P}_{k-1|k-1}\right)^{-1}\Phi_{px} \tag{A.15}$$

$$\begin{aligned}L_{k-1} =& \bar{P}_{k-1|k-1}\left(\Phi_{xx}\bar{P}_{k-1|k-1} - \Phi_{xp}\right)^{-1}L_k \\ =& \bar{P}_{k-1|k-1}\left(\Phi_{pp} - \Phi_{px}\bar{P}_{k-1|k-1}\right)^{-1}\tilde{H}_k^T\left(R_k + \tilde{H}_k\mathcal{P}_{k|k-1}\tilde{H}_k^T\right)^{-1}\end{aligned} \tag{A.16}$$

$$\begin{aligned}\tilde{b}_{k-1} =& \left[I_{n\times n} + \bar{P}_{k-1|k-1}\left(\Phi_{pp} - \Phi_{px}\bar{P}_{k-1|k-1}\right)^{-1}\Phi_{px}\right]^{-1}\bar{P}_{k-1|k-1}\left(\Phi_{xx}\bar{P}_{k-1|k-1} - \Phi_{xp}\right)^{-1}\left(\tilde{b}_k + \Phi_{xp}\tilde{p}_{k-1}\right) \\ =& \left[\left(\Phi_{xx}\bar{P}_{k-1|k-1} - \Phi_{xp}\right)\bar{P}_{k-1|k-1}^{-1} + \mathcal{P}_{k|k-1}\Phi_{px}\right]^{-1}\left(\tilde{b}_k + \Phi_{xp}\tilde{p}_{k-1}\right) \\ =& \left[\left(\Phi_{xx}\bar{P}_{k-1|k-1} - \Phi_{xp}\right)\bar{P}_{k-1|k-1}^{-1} + \mathcal{P}_{k|k-1}\Phi_{px}\right]^{-1}\Big(\mathcal{P}_{k|k-1}\left(\tilde{p}_k + \vec{v}_p(t_k)\right) \\ &- \left[\left(\Phi_{xx}\bar{P}_{k-1|k-1} - \Phi_{xp}\right)\bar{P}_{k-1|k-1}^{-1} + \mathcal{P}_{k|k-1}\Phi_{px}\right]\bar{P}_{k-1|k-1}\tilde{p}_{k-1}\Big) \\ =& \left[\left(\Phi_{xx}\bar{P}_{k-1|k-1} - \Phi_{xp}\right)\bar{P}_{k-1|k-1}^{-1} + \mathcal{P}_{k|k-1}\Phi_{px}\right]^{-1}\mathcal{P}_{k|k-1}\left(\tilde{p}_k + \vec{v}_p(t_k)\right) - \bar{P}_{k-1|k-1}\tilde{p}_{k-1} \\ =& \bar{P}_{k-1|k-1}\left(\Phi_{pp}^{-1}\tilde{p}_k - \tilde{p}_{k-1}\right)\end{aligned} \tag{A.17}$$

This fully defines the state estimate at the a priori epoch. A detailed analysis of the terms and their specific meanings is provided in section 3.3.

A.3 Adjoint and Optimal Control Estimates

The adjoint estimate is an intermediate value. We care about it only because it gives us the optimal control estimate, which has far more physical significance. As such we stick with an estimate of the adjoint at the a priori epoch that is a function of the state estimate at the a priori epoch.

$$\delta\hat{p}_{k-1|k} = \bar{P}^{-1}_{k-1|k-1}\left(\delta\bar{x}_{k-1|k-1} - \delta\hat{x}_{k-1|k}\right) - \tilde{p}_{k-1|k} \tag{A.18}$$

Via the results of the Pontryagin Minimum Principle (Eq. 3.9), we can provide a linearized estimate of the control vector as a function of time in terms of the state estimate at the a priori epoch. This linearization and solution process are shown below.

$$\begin{aligned}\delta\hat{u}(t) =& \hat{u}(t) - \tilde{u}(t) \qquad\qquad (A.19)\\ &= \left[\vec{w}(t) - \tilde{Q}(t)B(t)^T\vec{v}_p(t|t_{k-1}) - \Phi_{pp}(t,t_{k-1})\tilde{p}_{k-1}\right]\\ &\quad - \tilde{Q}(t)B(t)^T\left[\left(\Phi_{px}(t,t_{k-1}) - \Phi_{pp}(t,t_{k-1})\bar{P}^{-1}_{k-1|k-1}\right)\delta\hat{x}_{k-1|k} + \Phi_{pp}(t,t_{k-1})\bar{P}^{-1}_{k-1|k-1}\delta\bar{x}_{k-1|k-1}\right]\\ \tilde{u}(t) =& -\tilde{Q}(t)B(t)^T E\left[\phi_p(t;t_{k-1},\tilde{x}_{k-1},\tilde{p}_{k-1})\right] + E\left[\bar{u}(t)\right]\end{aligned}$$

With this solution we have covered estimates that come out of the OCBE. In Appendix B, there is a treatment of the uncertainties of the estimates in order to fully define the estimator. All analysis of these results is provided in Chapter 3.

Appendix B

Uncertainty Properties of the GL-OCBE

In this appendix we provide the through derivations of the uncertainties associated with the GL-OCBE. This will include the covariance of the propagated a priori state ($\bar{P}_{k|k-1}$), covariance of the state estimate at the a priori epoch ($\hat{P}_{k-1|k}$), covariance of the state estimate at the measurement epoch ($\hat{P}_{k|k}$), and the covariance of the control estimate ($\hat{P}_u(t|t_k)$).

B.1 Uncertainty of the Propagated a priori State

Presented here is a derivation of the covariance of the propagated a priori state ($\bar{P}_{k|k-1}$) for the GL-OCBE. The results may be simplified to also obtain the results for the BL-OCBE.

The covariance we are seeking is of the propagated a priori state with the added stochastic effects of the biasing term and the state process noise term. This combined metric is defined below.

$$\begin{aligned}\vec{z} &= \delta\bar{x}(t|t_{k-1}) + \tilde{b}(t|t_{k-1}) + v_x(t|t_{k-1}) \\ &= E\left[\vec{z}\right] + \bar{\eta}(t|t_{k-1})\end{aligned} \tag{B.1}$$

Subbing in all appropriate values, we solve for the zero mean error term ($\bar{\eta}(t|t_{k-1})$) as shown below.

$$\bar{\eta}(t|t_{k-1}) = \left[\Phi_{xx}(t,t_{k-1}) + \mathcal{P}(t|t_{k-1})\Phi_{px}(t,t_{k-1})\right]\bar{\eta}_{k-1|k-1} + \left[\mathcal{P}(t|t_{k-1})v_p(t|t_{k-1}) + v_x(t|t_{k-1})\right] \tag{B.2}$$

Following a development similar Tapley, Schutz, and Born [83], the covariance is derived via its dynamical equation. This requires having a dynamical equation for the zero mean error term. This is obtained by differentiating Eq. B.2 with respect to the final time.

$$\begin{aligned}\dot{\bar{\eta}}(t|t_{k-1}) = &\left[\dot{\Phi}_{xx}(t,t_{k-1}) + \dot{\mathcal{P}}(t|t_{k-1})\Phi_{px}(t,t_{k-1}) + \mathcal{P}(t|t_{k-1})\dot{\Phi}_{px}(t,t_{k-1})\right]\bar{\eta}_{k-1|k-1} \\ &+ \left[\dot{\mathcal{P}}(t|t_{k-1})v_p(t|t_{k-1}) + \mathcal{P}(t|t_{k-1})\dot{v}_p(t|t_{k-1}) + \dot{v}_x(t|t_{k-1})\right]\end{aligned} \tag{B.3}$$

This dynamical equation requires known derivatives of the state and adjoint process noise terms. These may be derived via application of the fundamental theorem of calculus [71]. The results are given below.

$$\begin{aligned}\dot{v}_x(t|t_{k-1}) = &\int_{t_{k-1}}^{t} \frac{d}{dt}\left(\Phi_{xx}(t,\tau)\right)B(\tau)\vec{w}(\tau)d\tau + \Phi_{xx}(t,t)B(t)\vec{w}(t) \\ =&A_{xx}(t)v_x(t|t_{k-1}) + A_{xp}(t)v_p(t|t_{k-1}) + B(t)\vec{w}(t)\end{aligned} \tag{B.4}$$

$$\begin{aligned}\dot{v}_p(t|t_{k-1}) = &\int_{t_{k-1}}^{t} \frac{d}{dt}\left(\Phi_{px}(t,\tau)\right)B(\tau)\vec{w}(\tau)d\tau + \Phi_{px}(t,t)B(t)\vec{w}(t) \\ =&A_{px}(t)v_x(t|t_{k-1}) + A_{pp}(t)v_p(t|t_{k-1})\end{aligned} \tag{B.5}$$

Subbing these results and the other required derivatives into Eq. B.3, a simplified version of the zero mean error term dynamics are obtained.

$$\dot{\bar{\eta}}(t|t_{k-1}) = \left[A_{xx}(t) + \mathcal{P}(t|t_{k-1})A_{px}(t)\right]\bar{\eta}(t|t_{k-1}) + B(t)\vec{w}(t) \tag{B.6}$$

The next step in this derivation is to formally define the covariance and its time derivative. These are defined below.

$$\bar{P}(t|t_{k-1}) = E\left[\bar{\eta}(t|t_{k-1})\bar{\eta}(t|t_{k-1})^T\right] \tag{B.7}$$

$$\begin{aligned}\dot{\bar{P}}(t|t_{k-1}) =&E\left[\dot{\bar{\eta}}(t|t_{k-1})\bar{\eta}(t|t_{k-1})^T + \bar{\eta}(t|t_{k-1})\dot{\bar{\eta}}(t|t_{k-1})^T\right] \\ =&\left[A_{xx}(t) + \mathcal{P}(t|t_{k-1})A_{px}(t)\right]E\left[\bar{\eta}(t|t_{k-1})\bar{\eta}(t|t_{k-1})^T\right] \\ &+ E\left[\bar{\eta}(t|t_{k-1})\bar{\eta}(t|t_{k-1})^T\right]\left[A_{xx}(t) + \mathcal{P}(t|t_{k-1})A_{px}(t)\right]^T \\ &+ B(t)E\left[\vec{w}(t)\bar{\eta}(t)^T\right] + E\left[\bar{\eta}(t)\vec{w}(t)^T\right]B(t)^T\end{aligned} \tag{B.8}$$

The final two expectation terms do not have an obvious solution. Subbing in Eq. B.2 we obtain the incomplete result below.

$$\begin{aligned}E\left[\bar{\eta}(t)\vec{w}(t)^T\right] = &\left[\Phi_{xx}(t,t_{k-1}) + \mathcal{P}(t|t_{k-1})\Phi_{px}(t,t_{k-1})\right] E\left[\bar{\eta}_{k-1|k-1}\vec{w}(t)^T\right] \\ &+ \mathcal{P}(t|t_{k-1})E\left[\vec{v}_p(t|t_{k-1})\vec{w}(t)^T\right] + E\left[\vec{v}_x(t|t_{k-1})\vec{w}(t)^T\right]\end{aligned} \tag{B.9}$$

This result has three expectations that must be evaluated, since there is no set definition for these random variables relation. The first expectation is identified to be zero since an instantaneous acceleration cannot effect a past state.

$$E\left[\bar{\eta}_{k-1|k-1}\vec{w}(t)^T\right] = 0 \tag{B.10}$$

The other two expectations are obtained via the definition of assumed dynamical uncertainty. The steps in the solution for each expectation are detailed below. The method involves linearization of time functions, but this is done over an infinitesimal time gap, thus results are exact.

$$\begin{aligned}E\left[\vec{v}_x(t|t_{k-1})\vec{w}(t)^T\right] &= \int_{t_{k-1}}^{t} \Phi_{xx}(t,\tau)B(\tau)E\left[\vec{w}(\tau)\vec{w}(t)^T\right]d\tau \\ &= \int_{t_{k-1}}^{t} \Phi_{xx}(t,\tau)B(\tau)\tilde{Q}(t)\delta(t-\tau)d\tau \\ &= \lim_{\epsilon\to 0}\left(\frac{1}{\epsilon}\right)\int_{t-\frac{\epsilon}{2}}^{t} \Phi_{xx}(t,\tau)B(\tau)\tilde{Q}(t)d\tau \\ &= \lim_{\epsilon\to 0}\left(\frac{1}{\epsilon}\right)\int_{t-\frac{\epsilon}{2}}^{t} \left[I_{n\times n} - A_{xx}(t)(t-\tau)\right]\left[B(t) - \dot{B}(t)(t-\tau)\right]\tilde{Q}(t)d\tau \\ &= \frac{B(t)\tilde{Q}(t)}{2}\end{aligned} \tag{B.11}$$

$$\begin{aligned}E\left[\vec{v}_p(t|t_{k-1})\vec{w}(t)^T\right] &= \int_{t_{k-1}}^{t} \Phi_{px}(t,\tau)B(\tau)E\left[\vec{w}(\tau)\vec{w}(t)^T\right]d\tau \\ &= \int_{t_{k-1}}^{t} \Phi_{px}(t,\tau)B(\tau)\tilde{Q}(t)\delta(t-\tau)d\tau \\ &= \lim_{\epsilon\to 0}\left(\frac{1}{\epsilon}\right)\int_{t-\frac{\epsilon}{2}}^{t} \Phi_{px}(t,\tau)B(\tau)\tilde{Q}(t)d\tau \\ &= -\lim_{\epsilon\to 0}\left(\frac{1}{\epsilon}\right)\int_{t-\frac{\epsilon}{2}}^{t} A_{px}(t)(t-\tau)\left[B(t) - \dot{B}(t)(t-\tau)\right]\tilde{Q}(t)d\tau \\ &= 0\end{aligned} \tag{B.12}$$

Plugging all of these results into Eq. B.8, the final dynamical equation of the covariance of the propagated a priori state is obtained.

$$\begin{aligned}\dot{\bar{P}}(t|t_{k-1}) = &\left[A_{xx}(t) + \mathcal{P}(t|t_{k-1})A_{px}(t)\right]\bar{P}(t|t_{k-1}) + \bar{P}(t|t_{k-1})\left[A_{xx}(t) + A_{px}(t)\mathcal{P}(t|t_{k-1})\right]^T \\ &+ B(t)\tilde{Q}(t)B(t)^T\end{aligned} \tag{B.13}$$

Furthermore, the solution to this dynamical equation (a differential Lyapunov equation) is obtained as defined below.

$$\bar{P}(t|t_{k-1}) = \Omega(t,t_{k-1})\bar{P}_{k-1|k-1}\Omega(t,t_{k-1})^T + \int_{t_{k-1}}^{t}\Omega(t,\tau)B(\tau)\tilde{Q}(\tau)B(\tau)^T\Omega(t,\tau)^T d\tau \tag{B.14}$$

$$\begin{gathered}\dot{\Omega}(t,t_{k-1}) = \left[A_{xx}(t) + \mathcal{P}(t|t_{k-1})A_{px}(t)\right]\Omega(t,t_{k-1}) \\ \Omega(t_{k-1},t_{k-1}) = I_{n\times n}\end{gathered} \tag{B.15}$$

This fully defines the covariance matrix of the propagated a priori state for GL-OCBE. While there is no known analytical solution to this equation in GL-OCBE implementation, there is an analytical solution for the BL-OCBE implementation (see next section).

B.2 Propagated a priori State Quasi-Covariance

The propagated a priori state quasi-covariance ($\mathcal{P}_{k|k-1}$) for the BL-OCBE is equivalent to the propagated a priori state covariance ($\bar{P}_{k|k-1}$), but this is not the case for the GL-OCBE. This is demonstrated in this section along with a summary of its special properties.

The definition of the propagated a priori state quasi-covariance where the measurement epoch is varied as t is given below.

$$\mathcal{P}(t|t_{k-1}) = \left[\Phi_{xx}(t,t_{k-1})\bar{P}_{k-1|k-1} - \Phi_{xp}(t,t_{k-1})\right]\left[\Phi_{pp}(t,t_{k-1}) - \Phi_{px}(t,t_{k-1})\bar{P}_{k-1|k-1}\right]^{-1} \tag{B.16}$$

Notice under this definition that the initial conditions are $\mathcal{P}(t_{k-1}|t_{k-1}) = \bar{P}_{k-1|k-1}$. Thus this matrix has the same initial conditions as $\bar{P}_{k|k-1}$. Differentiating this with respect to the final time t and simplifying the results, the form shown below is obtained.

$$\begin{aligned}\dot{\mathcal{P}}(t|t_{k-1}) =& A_{xx}(t)\mathcal{P}(t|t_{k-1}) - \mathcal{P}(t|t_{k-1})A_{pp}(t) - A_{xp}(t) + \mathcal{P}(t|t_{k-1})A_{px}(t)\mathcal{P}(t|t_{k-1}) \\ =& A_{xx}(t)\mathcal{P}(t|t_{k-1}) + \mathcal{P}(t|t_{k-1})A_{xx}(t)^T + B(t)\tilde{Q}(t)B(t)^T + \mathcal{P}(t|t_{k-1})A_{px}(t)\mathcal{P}(t|t_{k-1})\end{aligned} \tag{B.17}$$

It is interesting to note that this dynamical equation is a matrix Riccati differential equation given that $A_{px}(t)$ is symmetric by definition. This result is quite close to the dynamics of the propagated a priori state covariance (Eq. B.13) other than the final term. Defining the matrix $\Delta\bar{P}(t|t_{k-1}) = \bar{P}(t|t_{k-1}) - \mathcal{P}(t|t_{k-1})$, the following differenced dynamics are obtained.

$$\begin{aligned}\Delta\dot{\bar{P}}(t|t_{k-1}) =& \left[A_{xx}(t) + \mathcal{P}(t|t_{k-1})A_{px}(t)\right]\Delta\bar{P}(t|t_{k-1}) + \Delta\bar{P}(t|t_{k-1})\left[A_{xx}(t) + \mathcal{P}(t|t_{k-1})A_{px}(t)\right]^T \\ &+ \mathcal{P}(t|t_{k-1})A_{px}(t)\mathcal{P}(t|t_{k-1})\end{aligned} \tag{B.18}$$

The solution to the top line of this equation is $\Delta\bar{P}(t|t_{k-1}) = 0,\ \forall t \in \mathbb{R}$. However, because of the presence of the final term this is not the case. As such, we conclude that these two matrices are not equal for GL-OCBE. This term is zero for the BL-OCBE since $A_{px}(t) = 0,\ \forall t \in \mathbb{R}$, which is why these matrices are equivalent for that version of the estimator.

In general, we can conclude that $\mathcal{P}(t|t_{k-1}) = \bar{P}(t|t_{k-1})$ if and only if $A_{px}(t) = 0,\ \forall t \in \mathbb{R}$. We are able to draw other conclusions as well. As the solution to a matrix Riccati equation with a symmetric matrix for an initial condition, $\mathcal{P}(t|t_{k-1})$ is guaranteed to be symmetric for all time. Given the initial condition is positive definite, and $\tilde{Q}(t)$ also has this requirement, $\mathcal{P}(t|t_{k-1})$ is also guaranteed to be a positive definite matrix [14]. Because this matrix is symmetric positive definite, is solved via a matrix differential Riccati Equation, has a covariance as its initial conditions, and occupies the spot in the GL-OCBE where the propagated a priori state covariance would go for a Kalman Filter implementation it has very covariance-like properties. Thus, we term it the propagated a priori state quasi-covariance.

B.3 Uncertainty of the State Estimate at the a priori Epoch

The covariance of the state estimate at the a priori state epoch ($\hat{P}_{k-1|k}$) must be derived in a manner similar to the propagated a priori state covariance ($\bar{P}_{k|k-1}$) - meaning the presence of state and adjoint process noise terms requires the calculation of coupling with state propagation errors. This process start by defining this state estimate as a mean term summed with a zero mean error term. This error term may then be calculated via the definition of the state estimate at the a priori epoch (Eq. 3.37).

$$\begin{aligned}\delta\hat{x}_{k-1|k} &= E\left[\delta\hat{x}_{k-1|k}\right] + \hat{\eta}_{k-1|k} \\ \hat{\eta}_{k-1|k} &= \mathcal{I}_{k-1}\left(\bar{\eta}_{k-1|k-1} + \bar{P}_{k-1|k-1}\Phi_{pp}^{-1}\vec{v}_p(t_k)\right) + L_{k-1}\left(\epsilon_k - \tilde{H}_k\bar{\eta}_{k|k-1}\right)\end{aligned} \tag{B.19}$$

Using this error term, the associated covariance is defined as indicated below.

$$\hat{P}_{k-1|k} = E\left[\hat{\eta}_{k-1|k}\hat{\eta}_{k-1|k}^T\right] \tag{B.20}$$

Subbing in the appropriate relations we obtain the following solution.

$$\begin{aligned}\hat{P}_{k-1|k} =& \mathcal{I}_{k-1}\left(\bar{P}_{k-1|k-1} + \bar{P}_{k-1|k-1}\Phi_{pp}^{-1}E\left[\vec{v}_p(t_k)\vec{v}_p(t_k)^T\right]\Phi_{pp}^{-T}\bar{P}_{k-1|k-1}\right)\mathcal{I}_{k-1}^T \\ &+ L_{k-1}\left(R_k + \tilde{H}_k\bar{P}_{k|k-1}\tilde{H}_k^T\right)L_{k-1}^T \\ &+ \mathcal{I}_{k-1}E\left[\bar{\eta}_{k-1|k-1}\vec{v}_p(t_k)^T\right]\Phi_{pp}^{-T}\bar{P}_{k-1|k-1}\mathcal{I}_{k-1}^T + \mathcal{I}_{k-1}\bar{P}_{k-1|k-1}\Phi_{pp}^{-1}E\left[\vec{v}_p(t_k)\bar{\eta}_{k-1|k-1}^T\right]\mathcal{I}_{k-1}^T \\ &- \mathcal{I}_{k-1}E\left[\bar{\eta}_{k-1|k-1}\bar{\eta}_{k|k-1}^T\right]\tilde{H}_k^T L_{k-1}^T - L_{k-1}\tilde{H}_k E\left[\bar{\eta}_{k|k-1}\bar{\eta}_{k-1|k-1}^T\right]\mathcal{I}_{k-1}^T \\ &- \mathcal{I}_{k-1}\bar{P}_{k-1|k-1}\Phi_{pp}^{-1}E\left[\vec{v}_p(t_k)\bar{\eta}_{k|k-1}^T\right]\tilde{H}_k^T L_{k-1}^T - L_{k-1}\tilde{H}_k E\left[\bar{\eta}_{k|k-1}\vec{v}_p(t_k)^T\right]\Phi_{pp}^{-T}\bar{P}_{k-1|k-1}\mathcal{I}_{k-1}^T\end{aligned} \tag{B.21}$$

This solution has many expectations that must be calculated before it is complete and implementable. These expectations are evaluated below. Similar to the approach in Section B.1, the evaluation of Eqs. B.24 and B.25 requires linearization. The resulting equations are exact though, since the time gap over which the linearization takes place is infinitesimal. Also, the arguments from Eq. B.10 apply to Eqs. B.22 and B.23. The expectations are zero since an instantaneous acceleration has no effect on a previous state.

$$E\left[\vec{v}_p(t_k)\bar{\eta}_{k-1|k-1}^T\right] = \int_{t_{k-1}}^{t}\Phi_{px}(t,\tau)B(\tau)E\left[\vec{w}(\tau)\bar{\eta}_{k-1|k-1}^T\right]d\tau = 0 \tag{B.22}$$

$$E\left[\vec{v}_x(t_k)\bar{\eta}_{k-1|k-1}^T\right] = \int_{t_{k-1}}^{t}\Phi_{xx}(t,\tau)B(\tau)E\left[\vec{w}(\tau)\bar{\eta}_{k-1|k-1}^T\right]d\tau = 0 \tag{B.23}$$

$$\begin{aligned}
E\left[v_p(t_k)\vec{v}_p(t_k)^T\right] &= \int_{t_{k-1}}^{t}\int_{t_{k-1}}^{t} \Phi_{px}(t,\tau_1)B(\tau_1)E\left[\vec{w}(\tau_1)\vec{w}(\tau_2)^T\right]B(\tau_2)^T\Phi_{px}(t,\tau_2)^T d\tau_1 d\tau_2 \\
&= \int_{t_{k-1}}^{t}\int_{t_{k-1}}^{t} \Phi_{px}(t,\tau_1)B(\tau_1)\tilde{Q}(\tau_2)\delta(\tau_2-\tau_1)B(\tau_2)^T\Phi_{px}(t,\tau_2)^T d\tau_1 d\tau_2 \\
&= \lim_{\epsilon\to 0}\left(\frac{1}{\epsilon}\right)\int_{t_{k-1}}^{t}\int_{\tau_2-\frac{\epsilon}{2}}^{\tau_2+\frac{\epsilon}{2}} \Phi_{px}(t,\tau_1)B(\tau_1)d\tau_1\tilde{Q}(\tau_2)B(\tau_2)^T\Phi_{px}(t,\tau_2)^T d\tau_2 \\
&= \lim_{\epsilon\to 0}\left(\frac{1}{\epsilon}\right)\int_{t_{k-1}}^{t}\int_{\tau_2-\frac{\epsilon}{2}}^{\tau_2+\frac{\epsilon}{2}} \left[\Phi_{px}(t,\tau_2) - \left(A_{px}(t)\Phi_{xx}(t,\tau_2) + A_{pp}(t)\Phi_{px}(t,\tau_2)\right)(\tau_2-\tau_1)\right] \\
&\quad \times\left[B(\tau_2) - \dot{B}(\tau_2)(\tau_2-\tau_1)\right]d\tau_1\tilde{Q}(\tau_2)B(\tau_2)^T\Phi_{px}(t,\tau_2)^T d\tau_2 \\
&= \int_{t_{k-1}}^{t} \Phi_{px}(t,\tau_2)B(\tau_2)\tilde{Q}(\tau_2)B(\tau_2)^T\Phi_{px}(t,\tau_2)^T d\tau_2
\end{aligned} \tag{B.24}$$

$$\begin{aligned}
E\left[v_p(t_k)\vec{v}_x(t_k)^T\right] &= \int_{t_{k-1}}^{t}\int_{t_{k-1}}^{t} \Phi_{px}(t,\tau_1)B(\tau_1)E\left[\vec{w}(\tau_1)\vec{w}(\tau_2)^T\right]B(\tau_2)^T\Phi_{xx}(t,\tau_2)^T d\tau_1 d\tau_2 \\
&= \int_{t_{k-1}}^{t}\int_{t_{k-1}}^{t} \Phi_{px}(t,\tau_1)B(\tau_1)\tilde{Q}(\tau_2)\delta(\tau_2-\tau_1)B(\tau_2)^T\Phi_{xx}(t,\tau_2)^T d\tau_1 d\tau_2 \\
&= \lim_{\epsilon\to 0}\left(\frac{1}{\epsilon}\right)\int_{t_{k-1}}^{t}\int_{\tau_2-\frac{\epsilon}{2}}^{\tau_2+\frac{\epsilon}{2}} \Phi_{px}(t,\tau_1)B(\tau_1)d\tau_1\tilde{Q}(\tau_2)B(\tau_2)^T\Phi_{xx}(t,\tau_2)^T d\tau_2 \\
&= \lim_{\epsilon\to 0}\left(\frac{1}{\epsilon}\right)\int_{t_{k-1}}^{t}\int_{\tau_2-\frac{\epsilon}{2}}^{\tau_2+\frac{\epsilon}{2}} \left[\Phi_{px}(t,\tau_2) - \left(A_{px}(t)\Phi_{xx}(t,\tau_2) + A_{pp}(t)\Phi_{px}(t,\tau_2)\right)(\tau_2-\tau_1)\right] \\
&\quad \times\left[B(\tau_2) - \dot{B}(\tau_2)(\tau_2-\tau_1)\right]d\tau_1\tilde{Q}(\tau_2)B(\tau_2)^T\Phi_{xx}(t,\tau_2)^T d\tau_2 \\
&= \int_{t_{k-1}}^{t} \Phi_{px}(t,\tau_2)B(\tau_2)\tilde{Q}(\tau_2)B(\tau_2)^T\Phi_{xx}(t,\tau_2)^T d\tau_2
\end{aligned} \tag{B.25}$$

$$\begin{aligned}
E\left[\bar{\eta}_{k|k-1}\bar{\eta}_{k-1|k-1}^T\right] &= \left[\Phi_{xx} + \mathcal{P}_{k|k-1}\Phi_{px}\right]\bar{P}_{k-1|k-1} + \mathcal{P}_{k|k-1}E\left[v_p(t_k)\bar{\eta}_{k-1|k-1}^T\right] + \left[v_x(t_k)\bar{\eta}_{k-1|k-1}^T\right] \\
&= \left[\Phi_{xx} + \mathcal{P}_{k|k-1}\Phi_{px}\right]\bar{P}_{k-1|k-1}
\end{aligned} \tag{B.26}$$

$$\begin{aligned}
E\left[\bar{\eta}_{k|k-1}\vec{v}_p(t_k)^T\right] &= \left[\Phi_{xx} + \mathcal{P}_{k|k-1}\Phi_{px}\right]E\left[\bar{\eta}_{k-1|k-1}\vec{v}_p(t_k)^T\right] + \mathcal{P}_{k|k-1}E\left[v_p(t_k)\vec{v}_p(t_k)^T\right] \\
&\quad + \left[v_x(t_k)\vec{v}_p(t_k)^T\right] \\
&= \mathcal{P}_{k|k-1}\int_{t_{k-1}}^{t}\Phi_{px}(t,\tau)B(\tau)\tilde{Q}(\tau)B(\tau)^T\Phi_{px}(t,\tau)^T d\tau \\
&\quad + \int_{t_{k-1}}^{t}\Phi_{xx}(t,\tau)B(\tau)\tilde{Q}(\tau)B(\tau)^T\Phi_{px}(t,\tau)^T d\tau
\end{aligned} \tag{B.27}$$

Subbing all of these results into Eq. B.21, a final version of the covariance matrix is obtained. In the BL-OCBE implementation each of the integrals remaining in this solution is zero since

$\Phi_{px}(t,\tau) = 0,\ \forall t,\tau \in \mathbb{R}$. As such the BL-OCBE implementation does not require any integration beyond the nominal state and STM.

$$\begin{aligned}
\hat{P}_{k-1|k} =& \mathcal{I}_{k-1}\bar{P}_{k-1|k-1}\mathcal{I}_{k-1}^T + L_{k-1}\left(R_k + \tilde{H}_k\bar{P}_{k|k-1}\tilde{H}_k^T\right)L_{k-1}^T \\
&+ \mathcal{I}_{k-1}\bar{P}_{k-1|k-1}\Phi_{pp}^{-1}\left(\int_{t_{k-1}}^{t}\Phi_{px}(t,\tau)B(\tau)\tilde{Q}(\tau)B(\tau)^T\Phi_{px}(t,\tau)^T d\tau\right)\Phi_{pp}^{-T}\bar{P}_{k-1|k-1}\mathcal{I}_{k-1}^T \\
&- \mathcal{I}_{k-1}\bar{P}_{k-1|k-1}\left[\Phi_{xx} + \mathcal{P}_{k|k-1}\Phi_{px}\right]^T\tilde{H}_k^T L_{k-1}^T - L_{k-1}\tilde{H}_k\left[\Phi_{xx} + \mathcal{P}_{k|k-1}\Phi_{px}\right]\bar{P}_{k-1|k-1}\mathcal{I}_{k-1}^T \\
&- \mathcal{I}_{k-1}\bar{P}_{k-1|k-1}\Phi_{pp}^{-1}\left[\int_{t_{k-1}}^{t}\Phi_{px}(t,\tau)B(\tau)\tilde{Q}(\tau)B(\tau)^T\Phi_{px}(t,\tau)^T d\tau\mathcal{P}_{k|k-1}\right]\tilde{H}_k^T L_{k-1}^T \\
&- \mathcal{I}_{k-1}\bar{P}_{k-1|k-1}\Phi_{pp}^{-1}\left[\int_{t_{k-1}}^{t}\Phi_{px}(t,\tau)B(\tau)\tilde{Q}(\tau)B(\tau)^T\Phi_{xx}(t,\tau)^T d\tau\right]\tilde{H}_k^T L_{k-1}^T \\
&- L_{k-1}\tilde{H}_k\left[\mathcal{P}_{k|k-1}\int_{t_{k-1}}^{t}\Phi_{px}(t,\tau)B(\tau)\tilde{Q}(\tau)B(\tau)^T\Phi_{px}(t,\tau)^T d\tau\right]\Phi_{pp}^{-T}\bar{P}_{k-1|k-1}\mathcal{I}_{k-1}^T \\
&- L_{k-1}\tilde{H}_k\left[\int_{t_{k-1}}^{t}\Phi_{xx}(t,\tau)B(\tau)\tilde{Q}(\tau)B(\tau)^T\Phi_{px}(t,\tau)^T d\tau\right]\Phi_{pp}^{-T}\bar{P}_{k-1|k-1}\mathcal{I}_{k-1}^T
\end{aligned} \tag{B.28}$$

B.4 Uncertainty of the State Estimate at the Measurement Epoch

The covariance of the state estimate at the measurement epoch ($\hat{P}_{k|k}$) is a relatively easy quantity to obtain since there is no coupling between epochs that must be accounted for as is the case with the state estimate at the a priori epoch (see Section B.3). Defining this estimate as the summation of a mean and zero mean error term ($\hat{\eta}_{k|k}$), that error term can be calculated via the GL-OCBE definition of the state estimate at the a priori epoch (Eq. 3.41).

$$\begin{aligned}
\delta\hat{x}_{k|k} =& E\left[\delta\hat{x}_{k|k}\right] + \hat{\eta}_{k|k} \\
\hat{\eta}_{k|k} =& \bar{\eta}_{k|k-1} + L_k\left(\epsilon_k - \tilde{H}_k\bar{\eta}_{k|k-1}\right)
\end{aligned} \tag{B.29}$$

Using this error term we define the associated covariance as demonstrated below.

$$\hat{P}_{k|k} = E\left[\hat{\eta}_{k|k}\hat{\eta}_{k|k}^T\right] \tag{B.30}$$

By plugging Eq. B.29 in Eq. B.31, an analytical expression for the covariance of interest may be obtained using definitions of the involved error terms.

$$\hat{P}_{k|k} = \left(I_{n\times n} - L_k\tilde{H}_k\right)\bar{P}_{k|k-1}\left(I_{n\times n} - L_k\tilde{H}_k\right)^T + L_kR_kL_k^T \tag{B.31}$$

B.5 Uncertainty of the Control Estimate

The optimal control estimate from OCBE is one of the biggest things that separates it from other estimators. In order to provide a full estimate of the control, an uncertainty metric (the control estimate covariance - $\hat{Q}(t)$) will also be provided as derived in this section. This derivation starts with the linearization of the results of the Pontryagin Minimum Principle (Eq. A.19). Defining the solution as a mean summed with a zero mean error term ($\hat{w}(t)$), this error term may be used to define the desired covariance as shown below.

$$\begin{aligned}\delta\hat{u}(t) =& E\left[\delta\hat{u}(t)\right] + \hat{w}(t) \qquad \text{(B.32)}\\ \hat{w}(t) =& \left[\vec{w}(t) - \tilde{Q}(t)B(t)^T\vec{v}_p(t|t_{k-1})\right]\\ &- \tilde{Q}(t)B(t)^T\left[\left(\Phi_{px}(t,t_{k-1}) - \Phi_{pp}(t,t_{k-1})\bar{P}_{k-1|k-1}^{-1}\right)\hat{\eta}_{k-1|k} + \Phi_{pp}(t,t_{k-1})\bar{P}_{k-1|k-1}^{-1}\bar{\eta}_{k-1|k-1}\right]\end{aligned}$$

$$\hat{Q}(t) = E\left[\hat{w}(t)\hat{w}(t)^T\right] \tag{B.33}$$

This covariance may be solved for by subbing Eq. B.32 into Eq. B.33 and calculating all resulting expectations. The majority of these expectations were calculated in Sections B.1 and B.3.

$$\begin{aligned}
\hat{Q}(t) =& \tilde{Q}(t)\delta(t-\tau) + \tilde{Q}(t)B(t)^T E\left[\vec{v}_p(t|t_{k-1})\vec{v}_p(t|t_{k-1})^T\right] B(t)\tilde{Q}(t) \\
&+\tilde{Q}(t)B(t)^T \left(\Phi_{px}(t,t_{k-1}) - \Phi_{pp}(t,t_{k-1})\bar{P}^{-1}_{k-1|k-1}\right)\hat{P}_{k-1|k}\left(\Phi_{px}(t,t_{k-1}) - \Phi_{pp}(t,t_{k-1})\bar{P}^{-1}_{k-1|k-1}\right)^T B(t)\tilde{Q}(t) \\
&+\tilde{Q}(t)B(t)^T\Phi_{pp}(t,t_{k-1})\bar{P}^{-1}_{k-1|k-1}\Phi_{pp}(t,t_{k-1})^T B(t)\tilde{Q}(t) \\
&-E\left[\vec{w}(t)\vec{v}_p(t|t_{k-1})^T\right]B(t)\tilde{Q}(t) - \tilde{Q}(t)B(t)^T E\left[\vec{v}_p(t|t_{k-1})\vec{w}(t)^T\right] \\
&-E\left[\vec{w}(t)\hat{\eta}^T_{k-1|k}\right]\left(\Phi_{px}(t,t_{k-1}) - \Phi_{pp}(t,t_{k-1})\bar{P}^{-1}_{k-1|k-1}\right)^T B(t)\tilde{Q}(t) \\
&-\tilde{Q}(t)B(t)^T\left(\Phi_{px}(t,t_{k-1}) - \Phi_{pp}(t,t_{k-1})\bar{P}^{-1}_{k-1|k-1}\right)E\left[\hat{\eta}_{k-1|k}\vec{w}(t)^T\right] \\
&+\tilde{Q}(t)B(t)^T E\left[\vec{v}_p(t|t_{k-1})\hat{\eta}^T_{k-1|k}\right]\left(\Phi_{px}(t,t_{k-1}) - \Phi_{pp}(t,t_{k-1})\bar{P}^{-1}_{k-1|k-1}\right)^T B(t)\tilde{Q}(t) \\
&+\tilde{Q}(t)B(t)^T\left(\Phi_{px}(t,t_{k-1}) - \Phi_{pp}(t,t_{k-1})\bar{P}^{-1}_{k-1|k-1}\right)E\left[\hat{\eta}_{k-1|k}\vec{v}_p(t|t_{k-1})^T\right]B(t)\tilde{Q}(t) \\
&+\tilde{Q}(t)B(t)^T E\left[\vec{v}_p(t|t_{k-1})\bar{\eta}^T_{k-1|k-1}\right]\left(\Phi_{pp}(t,t_{k-1})\bar{P}^{-1}_{k-1|k-1}\right)^T B(t)\tilde{Q}(t) \\
&+\tilde{Q}(t)B(t)^T\left(\Phi_{pp}(t,t_{k-1})\bar{P}^{-1}_{k-1|k-1}\right)E\left[\bar{\eta}_{k-1|k-1}\vec{v}_p(t|t_{k-1})^T\right]B(t)\tilde{Q}(t) \\
&+\tilde{Q}(t)B(t)^T\left(\Phi_{px}(t,t_{k-1}) - \Phi_{pp}(t,t_{k-1})\bar{P}^{-1}_{k-1|k-1}\right)E\left[\hat{\eta}_{k-1|k}\bar{\eta}^T_{k-1|k-1}\right]\left(\Phi_{pp}(t,t_{k-1})\bar{P}^{-1}_{k-1|k-1}\right)^T B(t)\tilde{Q}(t) \\
&+\tilde{Q}(t)B(t)^T\left(\Phi_{pp}(t,t_{k-1})\bar{P}^{-1}_{k-1|k-1}\right)E\left[\bar{\eta}_{k-1|k-1}\hat{\eta}^T_{k-1|k}\right]\left(\Phi_{px}(t,t_{k-1}) - \Phi_{pp}(t,t_{k-1})\bar{P}^{-1}_{k-1|k-1}\right)^T B(t)\tilde{Q}(t)
\end{aligned} \tag{B.34}$$

$$\begin{aligned}
E\left[\hat{\eta}_{k-1|k}\vec{w}(t)^T\right] =& \mathcal{I}_{k-1}\left(E\left[\bar{\eta}_{k-1|k-1}\vec{w}(t)^T\right] + \bar{P}_{k-1|k-1}\Phi^{-1}_{pp}E\left[\vec{v}_p(t_k)\vec{w}(t)^T\right]\right) \\
&- L_{k-1}\tilde{H}_k E\left[\bar{\eta}_{k|k-1}\vec{w}(t)^T\right] \\
=& - L_{k-1}\tilde{H}_k\left(\Phi_{xx} + \mathcal{P}_{k|k-1}\Phi_{px}\right)E\left[\bar{\eta}_{k-1|k-1}\vec{w}(t)^T\right] - L_{k-1}\tilde{H}_k\mathcal{P}_{k|k-1}E\left[v_p(t_k)\vec{w}(t)^T\right] \\
&- L_{k-1}\tilde{H}_k E\left[v_x(t_k)\vec{w}(t)^T\right] \\
=& - L_{k-1}\tilde{H}_k E\left[v_x(t_k)\vec{w}(t)^T\right] \\
=& - \frac{1}{2}L_{k-1}\tilde{H}_k B(t)\tilde{Q}(t)
\end{aligned} \tag{B.35}$$

$$
\begin{aligned}
E\left[\hat{\eta}_{k-1|k}\vec{v}_p(t|t_{k-1})^T\right] =& \mathcal{I}_{k-1}\left(E\left[\bar{\eta}_{k-1|k-1}\vec{v}_p(t|t_{k-1})^T\right] + \bar{P}_{k-1|k-1}\Phi_{pp}^{-1}E\left[\vec{v}_p(t_k)\vec{v}_p(t|t_{k-1})^T\right]\right) \\
&- L_{k-1}\tilde{H}_k E\left[\bar{\eta}_{k|k-1}\vec{v}_p(t|t_{k-1})^T\right] \\
=& \left(\mathcal{I}_{k-1}\bar{P}_{k-1|k-1}\Phi_{pp}^{-1} - L_{k-1}\tilde{H}_k\mathcal{P}_{k|k-1}\right)E\left[\vec{v}_p(t_k)\vec{v}_p(t|t_{k-1})^T\right] \\
&- L_{k-1}\tilde{H}_k E\left[v_x(t_k)\vec{v}_p(t|t_{k-1})^T\right] \\
=& \left(\mathcal{I}_{k-1}\bar{P}_{k-1|k-1}\Phi_{pp}^{-1} - L_{k-1}\tilde{H}_k\mathcal{P}_{k|k-1}\right)\left[\int_{t_{k-1}}^{t}\Phi_{px}(t_k,\tau)B(\tau)\tilde{Q}(\tau)B(\tau)^T\Phi_{px}(t,\tau)^T d\tau\right] \\
&- L_{k-1}\tilde{H}_k\left[\int_{t_{k-1}}^{t}\Phi_{xx}(t_k,\tau)B(\tau)\tilde{Q}(\tau)B(\tau)^T\Phi_{px}(t,\tau)^T d\tau\right]
\end{aligned}
\tag{B.36}
$$

$$
\begin{aligned}
E\left[\hat{\eta}_{k-1|k}\bar{\eta}_{k-1|k-1}^T\right] =& \mathcal{I}_{k-1}\left(E\left[\bar{\eta}_{k-1|k-1}\bar{\eta}_{k-1|k-1}^T\right] + \bar{P}_{k-1|k-1}\Phi_{pp}^{-1}E\left[\vec{v}_p(t_k)\bar{\eta}_{k-1|k-1}^T\right]\right) \\
&- L_{k-1}\tilde{H}_k E\left[\bar{\eta}_{k|k-1}\bar{\eta}_{k-1|k-1}^T\right] \\
=& \mathcal{I}_{k-1}\bar{P}_{k-1|k-1} - L_{k-1}\tilde{H}_k\left(\Phi_{xx} + \mathcal{P}_{k|k-1}\Phi_{px}\right)E\left[\bar{\eta}_{k-1|k-1}\bar{\eta}_{k-1|k-1}^T\right] \\
&- L_{k-1}\tilde{H}_k\mathcal{P}_{k|k-1}E\left[v_p(t_k)\bar{\eta}_{k-1|k-1}^T\right] - L_{k-1}\tilde{H}_k E\left[v_x(t_k)\bar{\eta}_{k-1|k-1}^T\right] \\
=& \left[\mathcal{I}_{k-1} - L_{k-1}\tilde{H}_k\left(\Phi_{xx} + \mathcal{P}_{k|k-1}\Phi_{px}\right)\right]\bar{P}_{k-1|k-1}
\end{aligned}
\tag{B.37}
$$

$$
\begin{aligned}
\hat{Q}(t) =& \tilde{Q}(t)\delta(t-\tau) + \tilde{Q}(t)B(t)^T\left[\int_{t_{k-1}}^{t}\Phi_{px}(t,\tau)B(\tau)\tilde{Q}(\tau)B(\tau)^T\Phi_{px}(t,\tau)^T d\tau\right]B(t)\tilde{Q}(t) \\
&+\tilde{Q}(t)B(t)^T\left(\Phi_{px}(t,t_{k-1}) - \Phi_{pp}(t,t_{k-1})\bar{P}_{k-1|k-1}^{-1}\right)\hat{P}_{k-1|k}\left(\Phi_{px}(t,t_{k-1}) - \Phi_{pp}(t,t_{k-1})\bar{P}_{k-1|k-1}^{-1}\right)^T B(t)\tilde{Q}(t) \\
&+\tilde{Q}(t)B(t)^T\Phi_{pp}(t,t_{k-1})\bar{P}_{k-1|k-1}^{-1}\Phi_{pp}(t,t_{k-1})^T B(t)\tilde{Q}(t) \\
&+\frac{1}{2}\tilde{Q}(t)B(t)^T\tilde{H}_k^T L_{k-1}^T\left(\Phi_{px}(t,t_{k-1}) - \Phi_{pp}(t,t_{k-1})\bar{P}_{k-1|k-1}^{-1}\right)^T B(t)\tilde{Q}(t) \\
&+\frac{1}{2}\tilde{Q}(t)B(t)^T\left(\Phi_{px}(t,t_{k-1}) - \Phi_{pp}(t,t_{k-1})\bar{P}_{k-1|k-1}^{-1}\right)L_{k-1}\tilde{H}_k B(t)\tilde{Q}(t) \\
&+\tilde{Q}(t)B(t)^T E\left[\vec{v}_p(t|t_{k-1})\hat{\eta}_{k-1|k}^T\right]\left(\Phi_{px}(t,t_{k-1}) - \Phi_{pp}(t,t_{k-1})\bar{P}_{k-1|k-1}^{-1}\right)^T B(t)\tilde{Q}(t) \\
&+\tilde{Q}(t)B(t)^T\left(\Phi_{px}(t,t_{k-1}) - \Phi_{pp}(t,t_{k-1})\bar{P}_{k-1|k-1}^{-1}\right)E\left[\hat{\eta}_{k-1|k}\vec{v}_p(t|t_{k-1})^T\right]B(t)\tilde{Q}(t) \\
&+\tilde{Q}(t)B(t)^T\left(\Phi_{px}(t,t_{k-1}) - \Phi_{pp}(t,t_{k-1})\bar{P}_{k-1|k-1}^{-1}\right)\left[\mathcal{I}_{k-1} - L_{k-1}\tilde{H}_k\left(\Phi_{xx} + \mathcal{P}_{k|k-1}\Phi_{px}\right)\right] \\
&\quad\times\bar{P}_{k-1|k-1}\left(\Phi_{pp}(t,t_{k-1})\bar{P}_{k-1|k-1}^{-1}\right)^T B(t)\tilde{Q}(t) \\
&+\tilde{Q}(t)B(t)^T\left(\Phi_{pp}(t,t_{k-1})\bar{P}_{k-1|k-1}^{-1}\right)\bar{P}_{k-1|k-1}\left[\mathcal{I}_{k-1} - L_{k-1}\tilde{H}_k\left(\Phi_{xx} + \mathcal{P}_{k|k-1}\Phi_{px}\right)\right]^T \\
&\quad\times\left(\Phi_{px}(t,t_{k-1}) - \Phi_{pp}(t,t_{k-1})\bar{P}_{k-1|k-1}^{-1}\right)^T B(t)\tilde{Q}(t)
\end{aligned}
\tag{B.38}
$$

Subbing all of these results into Eq. B.34 (save for Eq. B.36 for space consideration) we obtain the final result in Eq. B.38. As is the case throughout this text, when the time arguments are not specified on STM quadrants and other values the assumption is they are evaluated between t_{k-1} and t_k.

B.6 Numerical Implementation of Process Noise Terms

The process noise terms discussed do not have analytical solutions in a GL-OCBE formulation. In this section we will provide alternate forms of these variables that allow for simpler numerical implementation.

The implementation issues hinge on requiring an STM of the form $\Phi(t_k, t)$ where t_k is greater than or equal to t. When numerically integrating the STM the form we have is $\Phi(t, t_{k-1})$. Thus, we want all portions of the STM to reflect this. Using the definition of the STM we and rewrite the bounds on the STM as shown below.

$$\begin{aligned}
\Phi(t_k, \tau) &= \Phi(t_k, t)\Phi(t, \tau) \\
\Phi_{xx}(t_k, \tau) &= \Phi_{xx}(t_k, t)\Phi_{xx}(t, \tau) + \Phi_{xp}(t_k, t)\Phi_{px}(t, \tau) \\
\Phi_{px}(t_k, \tau) &= \Phi_{px}(t_k, t)\Phi_{xx}(t, \tau) + \Phi_{pp}(t_k, t)\Phi_{px}(t, \tau)
\end{aligned} \tag{B.39}$$

Similarly, we may use symplectic properties of the STM inverse to rewrite the STM as shown below.

$$\begin{aligned}
\Phi(t, \tau) &= \Phi(t, t_{k-1})\Phi(\tau, t_{k-1})^{-1} \\
\Phi_{xx}(t, \tau) &= \Phi_{xx}(t, t_{k-1})\Phi_{pp}(\tau, t_{k-1})^T - \Phi_{xp}(t, t_{k-1})\Phi_{px}(\tau, t_{k-1})^T \\
\Phi_{xp}(t, \tau) &= \Phi_{xp}(t, t_{k-1})\Phi_{xx}(\tau, t_{k-1})^T - \Phi_{xx}(t, t_{k-1})\Phi_{xp}(\tau, t_{k-1})^T \\
\Phi_{px}(t, \tau) &= \Phi_{px}(t, t_{k-1})\Phi_{pp}(\tau, t_{k-1})^T - \Phi_{pp}(t, t_{k-1})\Phi_{px}(\tau, t_{k-1})^T \\
\Phi_{pp}(t, \tau) &= \Phi_{pp}(t, t_{k-1})\Phi_{xx}(\tau, t_{k-1})^T - \Phi_{px}(t, t_{k-1})\Phi_{xp}(\tau, t_{k-1})^T
\end{aligned} \tag{B.40}$$

Subbing these results into the definitions of $\vec{v}_x(t_k|t_{k-1})$ and $\vec{v}_p(t_k|t_{k-1})$, we obtain them as functions of $\vec{v}_x(t|t_{k-1})$ and $\vec{v}_p(t|t_{k-1})$ as shown below.

$$\begin{aligned}
\vec{v}_x(t_k|t_{k-1}) = &\int_t^{t_k} \Phi_{xx}(t_k,\tau)B(\tau)\vec{w}(\tau)d\tau \\
&+ \left[\Phi_{xx}(t_k,t_{k-1})\Phi_{pp}(t,t_{k-1})^T - \Phi_{xp}(t_k,t_{k-1})\Phi_{px}(t,t_{k-1})^T\right]\vec{v}_x(t|t_{k-1}) \\
&+ \left[\Phi_{xp}(t_k,t_{k-1})\Phi_{xx}(t,t_{k-1})^T - \Phi_{xx}(t_k,t_{k-1})\Phi_{xp}(t,t_{k-1})^T\right]\vec{v}_p(t|t_{k-1})
\end{aligned} \tag{B.41}$$

$$\begin{aligned}
\vec{v}_p(t_k|t_{k-1}) = &\int_t^{t_k} \Phi_{px}(t_k,\tau)B(\tau)\vec{w}(\tau)d\tau \\
&+ \left[\Phi_{px}(t_k,t_{k-1})\Phi_{pp}(t,t_{k-1})^T - \Phi_{pp}(t_k,t_{k-1})\Phi_{px}(t,t_{k-1})^T\right]\vec{v}_x(t|t_{k-1}) \\
&+ \left[\Phi_{pp}(t_k,t_{k-1})\Phi_{xx}(t,t_{k-1})^T - \Phi_{px}(t_k,t_{k-1})\Phi_{xp}(t,t_{k-1})^T\right]\vec{v}_p(t|t_{k-1})
\end{aligned} \tag{B.42}$$

This result allows us to easily caculuate the following expectations, which are required when computing $\hat{Q}(t)$.

$$\begin{aligned}
E\left[\vec{v}_x(t_k|t_{k-1})\vec{v}_x(t|t_{k-1})^T\right] = &\left[\Phi_{xx}(t_k,t_{k-1})\Phi_{pp}(t,t_{k-1})^T - \Phi_{xp}(t_k,t_{k-1})\Phi_{px}(t,t_{k-1})^T\right] \\
&\times E\left[\vec{v}_x(t|t_{k-1})\vec{v}_x(t|t_{k-1})^T\right] \\
&+ \left[\Phi_{xp}(t_k,t_{k-1})\Phi_{xx}(t,t_{k-1})^T - \Phi_{xx}(t_k,t_{k-1})\Phi_{xp}(t,t_{k-1})^T\right] \\
&\times E\left[\vec{v}_p(t|t_{k-1})\vec{v}_x(t|t_{k-1})^T\right]
\end{aligned} \tag{B.43}$$

$$\begin{aligned}
E\left[\vec{v}_x(t_k|t_{k-1})\vec{v}_p(t|t_{k-1})^T\right] = &\left[\Phi_{xx}(t_k,t_{k-1})\Phi_{pp}(t,t_{k-1})^T - \Phi_{xp}(t_k,t_{k-1})\Phi_{px}(t,t_{k-1})^T\right] \\
&\times E\left[\vec{v}_x(t|t_{k-1})\vec{v}_p(t|t_{k-1})^T\right] \\
&+ \left[\Phi_{xp}(t_k,t_{k-1})\Phi_{xx}(t,t_{k-1})^T - \Phi_{xx}(t_k,t_{k-1})\Phi_{xp}(t,t_{k-1})^T\right] \\
&\times E\left[\vec{v}_p(t|t_{k-1})\vec{v}_p(t|t_{k-1})^T\right]
\end{aligned} \tag{B.44}$$

$$\begin{aligned}
E\left[\vec{v}_p(t_k|t_{k-1})\vec{v}_x(t|t_{k-1})^T\right] = &\left[\Phi_{px}(t_k,t_{k-1})\Phi_{pp}(t,t_{k-1})^T - \Phi_{pp}(t_k,t_{k-1})\Phi_{px}(t,t_{k-1})^T\right] \\
&\times E\left[\vec{v}_x(t|t_{k-1})\vec{v}_x(t|t_{k-1})^T\right] \\
&+ \left[\Phi_{pp}(t_k,t_{k-1})\Phi_{xx}(t,t_{k-1})^T - \Phi_{px}(t_k,t_{k-1})\Phi_{xp}(t,t_{k-1})^T\right] \\
&\times E\left[\vec{v}_p(t|t_{k-1})\vec{v}_x(t|t_{k-1})^T\right]
\end{aligned} \tag{B.45}$$

$$\begin{aligned} E\left[\vec{v}_p(t_k|t_{k-1})\vec{v}_p(t|t_{k-1})^T\right] = &\left[\Phi_{px}(t_k,t_{k-1})\Phi_{pp}(t,t_{k-1})^T - \Phi_{pp}(t_k,t_{k-1})\Phi_{px}(t,t_{k-1})^T\right] \\ &\times E\left[\vec{v}_x(t|t_{k-1})\vec{v}_p(t|t_{k-1})^T\right] \\ &+ \left[\Phi_{pp}(t_k,t_{k-1})\Phi_{xx}(t,t_{k-1})^T - \Phi_{px}(t_k,t_{k-1})\Phi_{xp}(t,t_{k-1})^T\right] \\ &\times E\left[\vec{v}_p(t|t_{k-1})\vec{v}_p(t|t_{k-1})^T\right] \end{aligned} \tag{B.46}$$

Making the following definitions (Eqs. B.47 - B.49) we can reformulate the previous expectations into functions of values that are easily integrated in a numerical integration scheme.

$$\Theta_{pp,pp}(t|t_{k-1}) = \int_{t_{k-1}}^{t} \Phi_{pp}(\tau,t_{k-1})^T B(\tau)\tilde{Q}(\tau)B(\tau)^T \Phi_{pp}(\tau,t_{k-1})d\tau \tag{B.47}$$

$$\Theta_{px,px}(t|t_{k-1}) = \int_{t_{k-1}}^{t} \Phi_{px}(\tau,t_{k-1})^T B(\tau)\tilde{Q}(\tau)B(\tau)^T \Phi_{px}(\tau,t_{k-1})d\tau \tag{B.48}$$

$$\Theta_{px,pp}(t|t_{k-1}) = \int_{t_{k-1}}^{t} \Phi_{px}(\tau,t_{k-1})^T B(\tau)\tilde{Q}(\tau)B(\tau)^T \Phi_{pp}(\tau,t_{k-1})d\tau \tag{B.49}$$

$$\begin{aligned} E\left[\vec{v}_p(t|t_{k-1})\vec{v}_x(t|t_{k-1})^T\right] = &\Phi_{px}(t,t_{k-1})\Theta_{pp,pp}(t|t_{k-1})\Phi_{xx}(t,t_{k-1})^T \\ &- \Phi_{pp}(t,t_{k-1})\Theta_{px,pp}(t|t_{k-1})\Phi_{xx}(t,t_{k-1})^T \\ &- \Phi_{px}(t,t_{k-1})\Theta_{px,pp}(t|t_{k-1})^T\Phi_{xp}(t,t_{k-1})^T \\ &+ \Phi_{pp}(t,t_{k-1})\Theta_{px,px}(t|t_{k-1})\Phi_{xp}(t,t_{k-1})^T \end{aligned} \tag{B.50}$$

$$\begin{aligned} E\left[\vec{v}_p(t|t_{k-1})\vec{v}_p(t|t_{k-1})^T\right] = &\Phi_{px}(t,t_{k-1})\Theta_{pp,pp}(t|t_{k-1})\Phi_{px}(t,t_{k-1})^T \\ &- \Phi_{pp}(t,t_{k-1})\Theta_{px,pp}(t|t_{k-1})\Phi_{px}(t,t_{k-1})^T \\ &- \Phi_{px}(t,t_{k-1})\Theta_{px,pp}(t|t_{k-1})^T\Phi_{pp}(t,t_{k-1})^T \\ &+ \Phi_{pp}(t,t_{k-1})\Theta_{px,px}(t|t_{k-1})\Phi_{pp}(t,t_{k-1})^T \end{aligned} \tag{B.51}$$

$$\begin{aligned} E\left[\vec{v}_x(t|t_{k-1})\vec{v}_x(t|t_{k-1})^T\right] = &\Phi_{xx}(t,t_{k-1})\Theta_{pp,pp}(t|t_{k-1})\Phi_{xx}(t,t_{k-1})^T \\ &- \Phi_{xp}(t,t_{k-1})\Theta_{px,pp}(t|t_{k-1})\Phi_{xx}(t,t_{k-1})^T \\ &- \Phi_{xx}(t,t_{k-1})\Theta_{px,pp}(t|t_{k-1})^T\Phi_{xp}(t,t_{k-1})^T \\ &+ \Phi_{xp}(t,t_{k-1})\Theta_{px,px}(t|t_{k-1})\Phi_{xp}(t,t_{k-1})^T \end{aligned} \tag{B.52}$$